

ABSTRACT

Title of Dissertation: PLANETARY SEISMOLOGY USING
SINGLE-STATION AND SMALL
APERTURE ARRAYS: IMPLICATIONS FOR
MARS AND OCEAN WORLDS

Angela Giuliano Marusiak, Doctor of
Philosophy, 2020

Dissertation directed by: Associate Professor, Nicholas C Schmerr,
Geology Department

Studying geophysical station deployment on Earth is essential preparation for future geophysical experiments elsewhere in the solar system. Here, I investigated how single-station seismometers and small-aperture seismic arrays in analog settings can quantify instrument capabilities, develop methodologies to detect and locate seismicity, and constrain internal structure. First, I used a single-station seismometer in Germany to study how the NASA InSight mission could constrain core depth. I showed that InSight could recover the Martian core within ± 30 km if ≥ 3 events are located within an epicentral distance uncertainty of $< \pm 1$ degree. Increasing the number of detected events reduces core depth uncertainty, and higher signal-to-noise events will not affect core depth uncertainty or recovery rate.

Next, I used environmental analogs in Earth's cryosphere to quantify how seismometer placement on a mock-lander would affect instrument performance and

seismic science results for a future surface mission to an icy ocean world. If mock-lander instruments were unprotected from the wind, noise levels were 50 dB higher than those on the ground. However, once seismometers were shielded via burial, noise performances were similar to the ground-coupled seismometers, although spacecraft resonances were found at frequencies ~ 100 Hz. For icy ocean worlds lacking atmospheres, I showed that deck-mounted flight-candidate seismometers recorded ground motion comparably to surface-deployed instrumentation, with responses similar to terrestrial seismometers at frequencies > 0.1 Hz.

Finally, I investigated seismicity detection capabilities of single-station and small-aperture seismic arrays. Small-aperture arrays were more effective at distinguishing low-frequency seismic events from noise and had fewer false positive events than a single-station. The Greenland site detected a higher percentage of teleseismic and regional tectonic events while the Gulkana Glacier, Alaska site observed more high frequency events. The high frequency seismicity was interpreted as originating from moulins, drainage events, icequakes, and rockfalls. Both sites had very high frequency events (> 100 Hz) that came from poles left in the field. These studies inform landing site selection criteria, such that there were trades between detecting local seismicity at the expense of seeing more distant events, and detecting larger teleseismic events that inform on deeper internal structure.

PLANETARY SEISMOLOGY USING SINGLE-STATION AND SMALL-
APERTURE ARRAYS: IMPLICATIONS FOR MARS AND OCEAN WORLDS

by

Angela Giuliano Marusiak

Dissertation submitted to the Faculty of the Graduate School of the
University of Maryland, College Park, in partial fulfillment
of the requirements for the degree of
Doctorate of Philosophy
2020

Advisory Committee:

Professor Nicholas Schmerr, Chair

Dr. Terry Hurford

Associate Professor Vedran Lekic

Professor Laurent Montesi

Professor Derek Richardson, Dean's Representative

© Copyright by
Angela Giuliano Marusiak
2020

Foreword

Some of the work presented in this thesis has been published in peer-reviewed journals. *Icarus* and *Seismological Research Letters* have allowed figures and text to appear in this dissertation. All co-authors have provided consent for use of figures in this dissertation.

Chapter 2 was published as:

Marusiak, A. G., Schmerr, N. C., Banks, M. E., & Daubar, I. J. (2020). Terrestrial single-station analog for constraining the Martian core and deep interior: Implications for InSight. *Icarus*, 335, 113396.
<https://doi.org/10.1016/j.icarus.2019.113396>

Chapter 3, Section 2 was published as:

Marusiak, A. G., Schmerr, N. C., DellaGiustina, D. N., Pettit, E. C., Dahl, P. H., Avenson, B., et al. (2020). The Deployment of the Seismometer to Investigate Ice and Ocean Structure (SIOS) on Gulkana Glacier, Alaska. *Seismological Research Letters*. <https://doi.org/10.1785/0220190328>

Chapter 3 Section 3 is being prepared as:

Marusiak, A. G., Schmerr, N. C., Avenson, B., Bailey, S. H., Bray, V.J., DellaGiustina, D. N., et al. The Deployment of the Seismometer to Investigate Ice and Ocean Structure (SIOS) in Northwest Greenland. (in prep) *Seismological Research Letters*.

Dedication

To my parents

Acknowledgements

This document would not be possible without several influential people in my life including family, friends, and colleagues.

First and foremost, I need to thank my family. My parents have been incredibly supportive throughout my life. They sacrificed so my education could be a priority. I would not be where I am without them. My older brother, Nick, has always provided kind words and a healthy-ish sibling rivalry. My two aunts who have also always encouraging and supportive. Lastly, my late grandparents provided words of wisdom and guidance. To my grandfather, I hope I can live up to your nickname, “Little Genius”.

Next, I would like to thank my friends especially Rachel Fees for listening to my rants about grad school while reminding me there is life outside of the academic bubble. Thank you to the other graduate students, in particular, Erin Cunningham for helping me throughout grad school. A special thanks Joe Schools and Kayleigh Harvey for keeping me sane during a global pandemic and self-quarantine. Thank you to Joe Schools for keeping my spirits up and always making me laugh.

I would also like to thank members of Team SIIOS and the InSight Science Team. SIIOS has taken me to the edges of the Earth with the most amazing people. Thank you to the students and post-docs of the seismology groups and UMD Geology.

I’d also like to thank my funding sources. Most of this thesis was made possible by NASA PSTAR Grant #80NSSC17K0229, NASA MFRP Grant #NNX14AQ92G and NASA NESSF Grant # 80NSSC18K1260. The NASA Earth and Space Science Fellowship for provided the funding for the final two years of my work and reminded

me that my writing and research ideas may not be as terrible as I think. Thank you to the Seismological Society of America (SSA), Goldhaber travel grant, and the Earth-Systems Science Interdisciplinary Center (ESSIC) for providing travel funds so I could attend conferences and InSight meetings.

Lastly, to my advisor Nick. Your time and efforts made a big difference in my life. Your guidance and advice have helped me tremendously. Thank you for accepting me into your group.

Table of Contents

Foreword.....	ii
Dedication.....	iii
Acknowledgements	iv
Table of Contents	vi
List of Tables.....	ix
List of Figures.....	x
List of Abbreviations.....	xii
Chapter 1: Introduction to Planetary Seismology	1
1.1 Terrestrial Seismology.....	1
1.2 Planetary Seismology	5
1.2.1 Apollo-Era and Early Planetary Seismology.....	6
1.2.2 InSight Mission	8
1.2.3 Icy Ocean World Seismology and Future Missions	10
1.3 Analog Studies.....	12
1.4 Single-Station and Small-Aperture Array Approaches	15
Chapter 2: Terrestrial Single-Station Analog for Constraining the Martian Core and Deep Interior: Implications for InSight	21
Abstract.....	21
2.1 Introduction	22
2.2 Dataset	28
2.2.1 Constructing a Mars-like Database	28
2.2.2 Event SNR Determination.....	32
2.2.3 Core Models	34
2.3 Methods	37
2.3.1 Event Selection.....	37
2.3.2 Stacking.....	39
2.3.3 Core Recovery	43
2.4 Results	44
2.4.1 Synthetic Tests.....	44
2.4.2 Quantity and SNR effects of Real Events	47
2.4.3 Location Alteration of Real Events	48
2.4.4 ScS Multiples.....	50
2.4.5 Mantle Heterogeneities.....	55
2.5 Analysis and Discussion.....	58
2.5.1 Comparison to Mars	59
2.5.2 Detecting mantle heterogeneities	62
2.5.3 Benefit/Negatives of using Multiples	64
2.5.4 Blind Test	64
2.6 Conclusions	70
2.7 Acknowledgements	71
2.8 Datasets.....	71
Chapter 3: The Deployment of the Seismometer to Investigate Ice and Ocean Structure (SIIOS).....	72

Abstract.....	72
3.1 Introduction	73
3.2 Gulkana Glacier, Alaska.....	74
3.2.1 Analog Setting	75
3.2.2 Instrument Deployment	75
3.2.3 Data Quality and Availability.....	80
3.2.4 Initial Observations	87
3.2.5 Summary.....	90
3.3 Northwest Greenland.....	91
3.3.1 Analog Setting	91
3.3.2 Instrument Deployment	92
3.3.4 Data Quality and Availability.....	94
3.3.4 Initial Observations	95
3.3.5 Summary.....	99
3.4 Data and Resources	100
3.5 Summary.....	100
3.5 Acknowledgements	102
3.7 Appendices	104
Chapter 4: Detecting Passive Signals on Icy ocean World Analogs	110
Abstract.....	110
4.1 Introduction	111
4.2 Analogs and Data	120
4.3 Methods	123
4.3.1 Short-Term Average/Long-Term Average.....	124
4.3.2 Template Detection	129
4.4 Results	131
4.4.1 Regional and Teleseismic.....	131
4.4.2 HF event	136
4.4.3 VHF Anomalies.....	141
4.5 Discussion.....	143
4.5.1 Regional and Teleseismic Detections.....	144
4.5.2 HF Detections.....	146
4.5.3 VHF Detections	149
4.5 Summary.....	153
4.6 Acknowledgements and Data Resources.....	154
Chapter 5: Conclusions and Future Work	156
Overview	156
5.1 Summary of Conclusions	156
5.1.1 Deep Interior Structure Constraints with a Single-Station Seismometer	157
5.1.2 Lessons Learned and Recommendations for Deployments on Icy Ocean Worlds	158
5.1.3 Advantages and Recommendations for Single-Station and Small-Aperture Array Seismology.....	160
5.2 Continued Work	162
5.2.1 Applications to InSight mission	162
5.2.3 Future Icy Ocean World Deployments and Investigations.....	163

5.4 Summary.....	164
Appendices	166
Bibliography	190

List of Tables

- Table 2.1 Recovery Rate, Mean Core Depth, and Uncertainty by Event Quality and Quantity.
- Table 2.2 Effects of Source Location Errors on Recovery Rate, Mean Core Depth and Uncertainty
- Table 2.3 Effects of adding ScS multiples
- Table 2.4 Martian Velocity Models
- Table 3.1 Station Name, Location, and Final Azimuth for Gulkana
- Table 3.2 Operational Days, Instrument Type, Saturation of Sand, and Components for Gulkana
- Table 3.A.1 Active source location and timings for Gulkana experiment
- Table 3.3 Station Names and Locations for Greenland
- Table 3.2 Operational Days, Instrument Type, and Components for Greenland
- Table 3.A.2 Active source location and timings for Greenland
- Table 4.1 Comparison of Event Detection capabilities using Single-Station and Small-Aperture Array Approaches
- Table A.1 Catalog of Tectonic events from the Passive Experiment at Gulkana
- Table A.2 Catalog of Tectonic events from the Passive Experiment at Greenland

List of Figures

- Figure 1.1 Arrival Times and Travel Paths of S and P
- Figure 1.2 Deep Interior Structure of the Earth, constrained by Seismology
- Figure 1.3 Martian Seismicity as measured by InSight in its First Year
- Figure 1.4 Apollo Seismic Deployments on a) a Global and b) for Apollo 17
- Figure 2.1. Travel Paths of ScS and its multiples
- Figure 2.2 Distribution of events by a) Epicentral Distance b) Magnitude and c) Geographic Location
- Figure 2.3 Event catalog plotted by Epicentral Distance and Magnitude
- Figure 2.4 Moveout of ScS and its multiples on a distance vs time plot
- Figure 2.5 Examples of a) Low b) Average and c) High Quality Events
- Figure 2.6 Diagram of Event Selection Algorithm
- Figure 2.7 Example of selected events a) plotted with predicted moveouts and b) at PREM's expected arrival time
- Figure 2.8 Stacked Amplitudes for 5 example models
- Figure 2.9 a) Stacked Amplitudes and b) Mean Offset Times for all models with uncertainties
- Figure 2.10 Selection Frequency of each model for various event qualities
- Figure 2.11 a) Recovery Rate, b) Mean Core Depth and c) Core Depth Uncertainty recovered by various quantities and qualities of events
- Figure 2.12 Effects of Source Location Uncertainty
- Figure 2.13 a) Recovery Rate b) Mean Core Depth and c) Core Depth Uncertainty when ScS multiples are used
- Figure 2.14 a) Tomographic Map at 2800 km depth and its affect on b) Recovered Core Depth
- Figure 2.15. Moveout of ScS and its Multiples for several Martian Velocity Models
- Figure 2.16. a) Martian Velocity Models and b) Resulting Moveouts of ScS
- Figure 2.17. Stacked Amplitude Results for Martian Interior Models
- Figure 2.18 Recovered Martian Core Depths
- Figure 3.1 Map of SIIOS Array location relative to a) Alaska and b) Gulkana Glacier. c) Photo and d) Schematic of SIIOS array
- Figure 3.2 a) Schematic of Active Source locations relative to SIIOS. b) Photo of active source experiment
- Figure 3.3 Instrument Response Functions
- Figure 3.4. Power Density Functions of vertical component for all seismic stations
- Figure 3.5 Direct Comparison of a) vertical PDFs b) Spectrograms during High Wind and c) Spectrograms during Low Wind
- Figure 3.6 Examples of Time-series and Spectrogram for a) Teleseismic Event b) Regional Event and c) Local/Background Noise
- Figure 3.7 Distance-Time Moveout Plot for Active Source Experiment
- Figure 3.A.1 PDF's for Component 1
- Figure 3.A.2 PDF's for Component 2
- Figure 3.8 Greenland Deployment a) Map b) Photo and c) Schematic
- Figure 3.9 Greenland Active Source Location
- Figure 3.10 PDF of vertical Component for Greenland

Figure 3.11 Event examples of a) Regional Tectonic Event and b) Local Signals and Background

Figure 3.12 Active Source Moveout of Greenland

Figure 3.A.3 PDF's for Component 1 in Greenland

Figure 3.A.4 PDF's for Component 2 in Greenland

Figure 4.1 Interior Structure of Europa

Figure 4.2 Map of SIIOS locations in Alaska and Greenland

Figure 4.3 Time-Series and resulting STA/LTA values for a large event (Mw 7.1)

Figure 4.4 Example of Anthropogenic Signal in the Temporal and Spectral Domains

Figure 4.5 Example of Detected Low-frequency Event from ComCat catalog

Figure 4.6 Example of Detected Low-frequency event not in known catalog

Figure 4.7 Final Catalog of Events from a) Gulkana and b) Greenland datasets

Figure 4.8 Comparison of catalogs with wind speed

Figure 4.9 Gulkana HF Events Catalog compared to a) temperature and b) change in temperature. c) High Wind likely caused increased background noise

Figure 4.10 Gulkana's HF Event Cluster analysis

Figure 4.11 Gulkana Map with recorded azimuths of HF and VHF events

Figure 4.12 Catalog of Greenland HF Events

Figure 4.13 Greenland Cluster analysis of HF Events

Figure 4.14 Greenland map with recovered azimuths of HF and VHF events

List of Abbreviations

ANSS- Advanced National Seismic System
BFO- Black Forest Observatory
CLPS- Commercial Lunar Payload Services
CMB- Core Mantle Boundary
ComCat- Comprehensive Catalog
DMC- Data Management Center
GSN- Global Seismic Network
HF- High Frequency
InSight- Interior Exploration using Seismic Investigations, Geodesy, and Heat Transport
IPR- Ice Penetrating Radar
IRIS- Incorporated Research Institutions for Seismology
LGN- Lunar Geophysical Network
LLSVP- Large Low Shear Velocity Provenance
LSPE- Lunar Seismic Profiling Experiment
MQS- Mars Quake Service
MSS- Mars Structure Service
NASA- National Aeronautical and Space Agency
NEIC PDE- National Earthquake Information Center, Preliminary Determination of Epicenters
NHNM- New High Noise Model
NLNM- New Low Noise Model
PASSCAL- Portable Array Seismic Studies of the Continental Lithosphere
PDF- Power Density Function
PSD- Power Spectral Density
PREM- Preliminary Earth Reference Model
SAC- Seismic Analysis Code
SIES- Seismic Experiment for Interior Structure
SIIOS- Seismometer to Investigate Ice and Ocean Structure
SNR- Signal to Noise Ratio
SP- Short Period
STA/LTA- Short Term Average/ Long Term Average
TC- Trillium Compact
TPH- Trillium Post-hole
UAF- University of Alaska Fairbanks
ULVZ- Ultra-Low Velocity Zone
USGS- United States Geological Survey
VBB- Very Broadband
VHF- Very High-frequency
WWSSN- World-wide Standard Seismograph Network

Chapter 1: Introduction to Planetary Seismology

1.1 Terrestrial Seismology

Seismology has been vital for the interior exploration of our planet. Beginning in the 19th century, the development of new types of seismometers allowed early seismologists to interpret recorded ground motions. By studying the seismograms from only a few stations and events, the early seismologists began to reveal the internal structure of the Earth. By studying the travel times of *P* and *S* waves, Mohorovičić was able to determine the depth of the discontinuity between the crust and mantle (Mohorovicic, 1909). By recognizing the core shadow zone, and appearance of *P* waves refracted through the core, Gutenberg and Oldham established the presence of a core-mantle boundary in the Earth (Gutenberg, 1914; Oldham, 1906). Lehmann was able to determine the presence of a solid inner core by identifying *P* waves that refracted through the inner core (Lehmann, 1936). These important studies demonstrated that the Earth had differentiated into layers and provided the backbone for future seismic studies.

Early seismologists relied on simplifying assumptions to determine internal structure. Initial models presented Earth as a one-dimensional velocity structure, meaning there were no lateral heterogeneities. To determine structure as a function of depth, the arrival times of key phases were compared to the distances at which the events occurred. More distant events showed that seismic phases bent or refracted through the Earth, indicating velocity must increase with depth throughout most of the mantle (Fig. 1.1). In the case of Lehmann, she was able to detect a deviation from this pattern, associated with

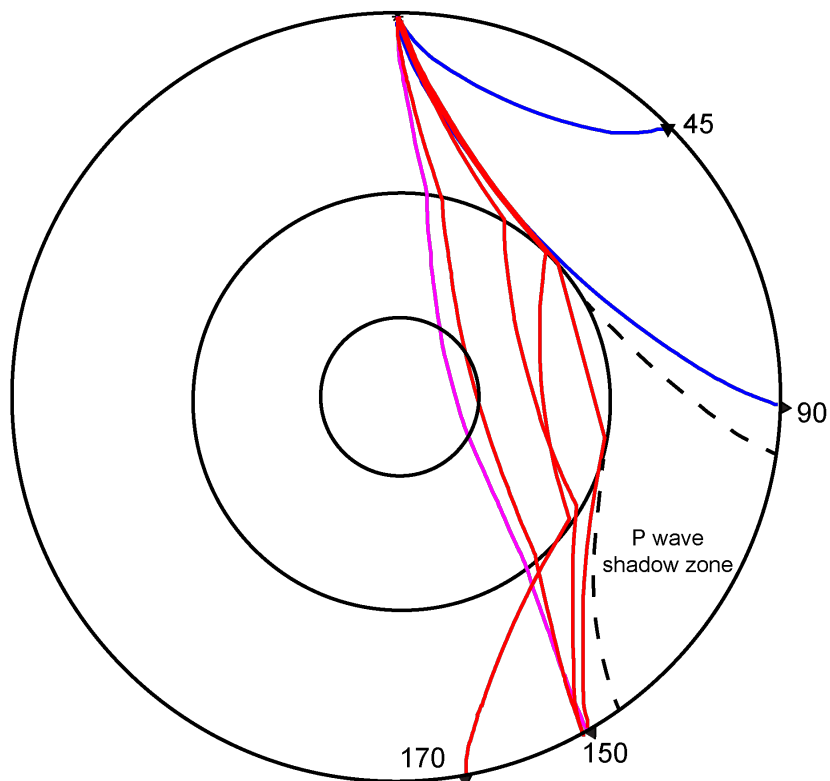
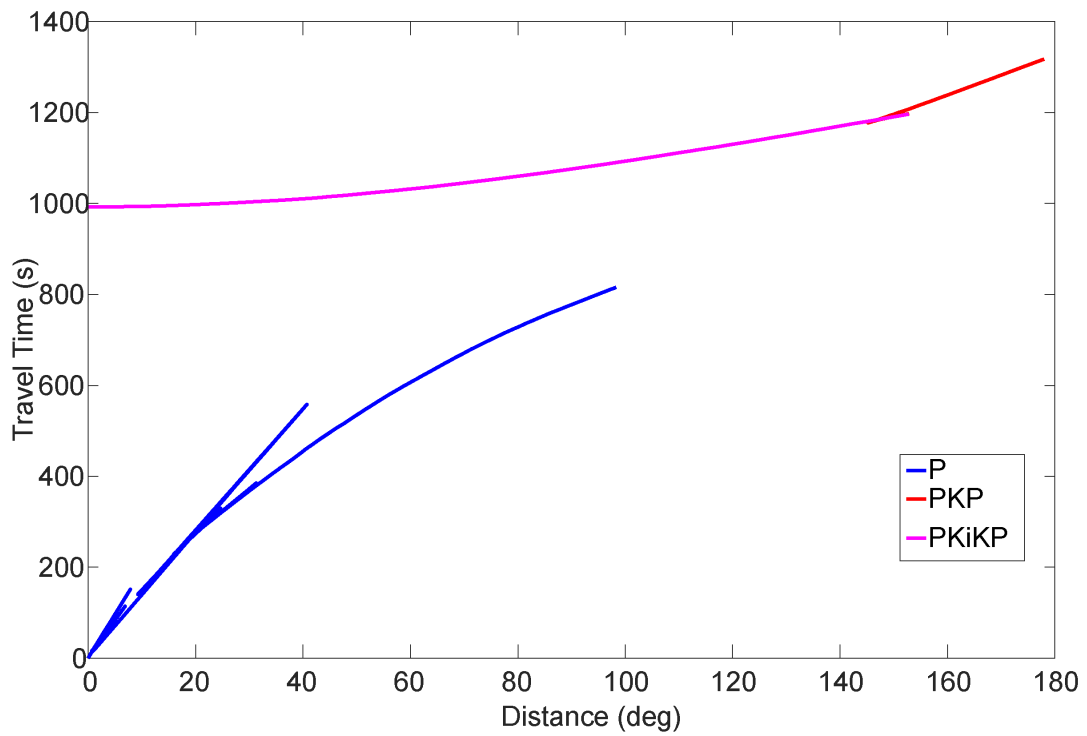


Figure 1.1 Loosely based on Oldham, 1906. Oldham noted the arrivals of *P* wave arrivals versus distance and noticed a sudden change in arrival time for distances 100°. Lehmann later discovered a new phase *PKiKP* (pink/purple). Figures were created using TauP software (Crotwell *et al.*, 1999) and the PREM model (Dziewonski & Anderson, 1981).

the arrival of an unknown phase, *PKiKP* and *PKIKP* (she called it *P'*). As the depth, velocity, and density of the layers became better constrained, updates to velocity structure were improved.

Early seismic studies typically relied on single-stations or sparsely deployed networks operated by academic geophysical observatories. The first modern, standardized global network deployed in the 1960's was the World-Wide Standard Seismograph Network (WWSSN) (Agnew et al., 1976; Bondár & Engdahl, 2019; Oliver & Murphy, 1971). This network was developed to monitor nuclear tests (Barker et al., 1998; Grover, 1979; Hannon, 1985; Murphy, 1977; Romanowicz & Dziewonski, 1986) and to determine if countries, specifically the USSR, were violating the nuclear test ban treaty. Although the intention of the network was to detect explosions, by continuously recording data, naturally earthquakes were recorded allowing seismologists to build catalogs of worldwide earthquakes and assemble datasets of seismograms. In the 1970's and 1980's the first digital seismograms were recorded with stations part of the Global Seismic Network (GSN). The advent of large datasets led to numerous studies on the interior of the Earth with higher resolution than previously possible.

Concurrently in the 1960's, the theory of plate tectonics rapidly became a new paradigm in the geosciences (Isacks et al., 1968; Mckenzie & Parker, 1967; Molnar & Sykes, 1969; Morgan, 1968; Le Pichon, 1968). Seismology was a key piece of evidence for the plate tectonics paradigm shift, as it showed that the locations and depths of earthquakes were not random, but instead concentrated along the boundaries of what are now called Earth's tectonic plates. For example, deep earthquakes preferentially occurred in subduction zones while extensional faulting tended to occur at shallow depths. The focal

mechanisms further showed the directionality of plate motions along the boundaries. Seismology provided additional evidence for convection's role in mantle dynamics (Davies & Richards, 1992; Hager & Clayton, 1989; Morgan, 1972; Schubert et al., 2001). Mantle anomalies were typically found by comparing the arrival times of body waves travelling along different paths within the mantle. As more stations were installed and events were recorded, reference models of the Earth were constructed from the newly acquired large datasets (Anderson, 1965; Dziewonski & Anderson, 1981; Gutenberg, 1959; Kennett & Engdahl, 1991). These models used not only seismic constraints, but also constraints from the mean mass and radius of Earth, moment of inertia measurements, and geochemical measurements of Earth's crust and mantle. In the case of the Preliminary Reference Earth Model (PREM), thousands of body wave arrivals and normal mode observations were used to refine the Earth's compressional (P) and shear (S) wave velocities, densities, and seismic quality factor, the inverse of attenuation. From these one-dimensional models, any variations in the arrival times of body phases indicated either a variation in layer thickness or a velocity heterogeneity (Anderson & Dziewonski, 1984; Dziewonski et al., 1977; Iyer & Hirahara, 1993).

Seismic velocity variations have been used to show regions of faster-than-average velocities which have indicated the presence of subducting slabs (Grand et al., 1997; Ritsema et al., 2020). Slower-than-average velocities were associated with Large Low Shear Velocity provinces (LLSVPs) and Ultralow Velocity Zones (ULVZs)(Garnero & McNamara, 2008; Williams et al., 1998; Williams & Garnero, 1996) (Fig. 1.2). By paring seismic observations with geochemical observations (Kellogg et al., 1999) and geodynamic modeling, the core-mantle boundary has been established as a region of enhanced

heterogeneity with complexity similar to that of Earth's crust (Cammarano et al., 2005; Garnero, 2000; van der Hilst et al., 1997; Lay et al., 1998). Specifically, seismic data has linked LLSVPs and ULVZs to mantle plumes and hot spots (Garnero et al., 1998; Williams et al., 1998; Yuan & Romanowicz, 2017). Seismology is unique in its ability to image the interior of the Earth, especially the deep interior of the Earth. Through tomography and waveform analysis, we can get an enticing glimpse of the current state of the Earth's interior. When coupled with modeling and other geophysical and geochemical constraints, we can begin to understand how the interior of a planet influences the surface of the planet.

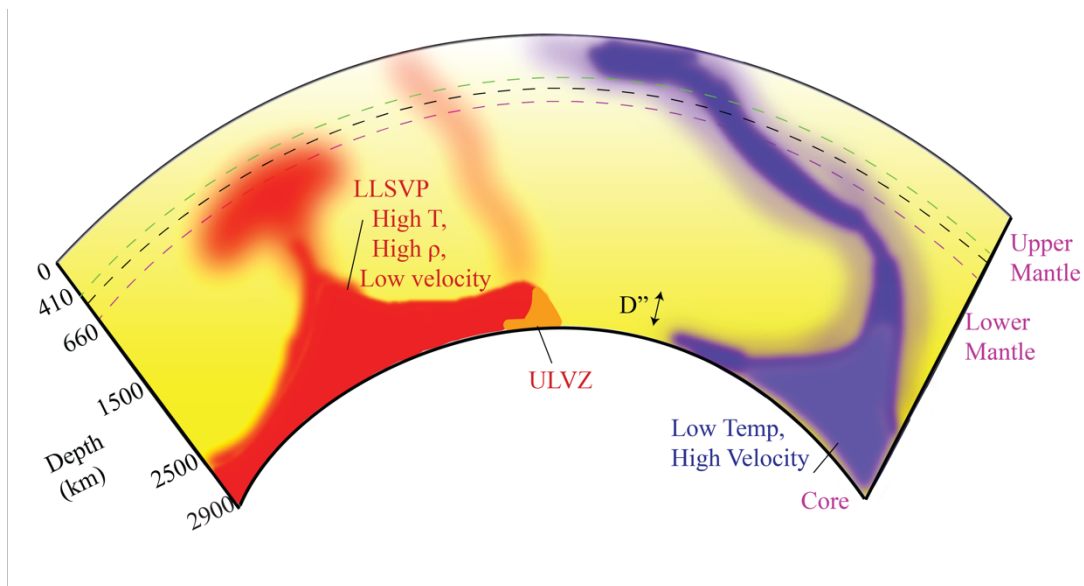


Figure 1.2 Based on Garnero and McNamara (2008). Variations in velocity structure indicate subducting slabs (blue) and LLSVPs or ULVZs (red). The slower-than-average velocities could be caused by the increase in temperature and densities inside the LLSVPs and ULVZs.

1.2 Planetary Seismology

As seismology has yielded critical information on the interior of Earth, there have been several seismometer deployments to other planetary bodies. In the following section, I outline the history of planetary seismology. I focused on larger duration missions on the Moon and Mars but seismometers have also been deployed briefly on Venus (Ksanfomaliti

et al., 1982), with the Ranger missions to the Moon (Hall, 1977), and to small bodies such as comets (Kochan et al., 2000).

1.2.1 Apollo-Era and Early Planetary Seismology

In 1969, the Apollo 11 astronauts landed on the Moon and one experiment that they deployed was a seismic experiment. Although the initial Apollo 11 experiment only last one lunar day (~ 2 Earth weeks), the results paved the way for future seismic installations on the Moon. Seismometers and geophone instruments were installed by astronauts at Apollo 12, 14, 15, 16, and 17 landing sites. The experiments included active source tests and passively recorded data (Latham et al., 1970a, 1970b; Watkins & Kovach, 1972).

The active source experiments on Apollo performed with geophone lines and explosives were critical for determining the lunar near-surface properties. Notably, these experiments established that the highly fractured sub-surface of the Moon, called the megaregolith, caused significant scattering of seismic data. This scattering effect was likely enhanced by a lack of fluids in the pore space of deeply seated fractures in the Moon (Nakamura, 1976, 1977b; Pandit & Tozer, 1970). The scattering effects greatly reduced the signal quality of detected moonquakes which impeded the science return (Weber et al., 2017). Despite the complications of scattering effects, the Apollo seismic experiments yielded a wealth of information about the lunar interior and seismicity.

A primary result of the Apollo experiments was their recording of thousands of moonquakes. The most common type of event were the deep moonquakes. Deep moonquakes occurred in clusters 700-1000 km deep (Latham et al., 1970a; Nakamura, 2003) and were likely caused by tidal interactions with the Earth (Bulow et al., 2007; Gouly, 1979; Kawamura et al., 2017). Notably, deep moonquakes were not detected on

the far-side of the Moon (Khan et al., 2014; Nakamura, 2005). The lack of far-side detections of deep moonquakes could be an artifact from the Apollo stations all being installed on the near-side of the Moon coupled with internal properties that prevented the detection of far-side quakes (Garcia et al., 2019). The lack of detection could also indicate lack of source, meaning deep moonquakes may only occur on the near-side.

In addition to the deep moonquakes, shallow tectonic events were detected (Nakamura, 1977a). The shallow events were associated with high stress states (Binder & Oberst, 1985; Oberst, 1987) and were likely caused by contractional cooling of the lunar interior (Watters et al., 2019). Additionally, there were thermal moonquakes caused by the heating and cooling of the lunar near-surface and equipment left on the lunar surface (Duennebier & Sutton, 1974; Weber et al., 2018). Lastly, the Apollo experiment recorded signals from impacts (Latham et al., 1970a; Oberst & Nakamura, 1991).

The Apollo seismic experiments definitively proved the moon is a differentiated body and is currently seismically active. Another major achievement was the constraint of the lunar interior structure and the detection of the lunar core (Garcia et al., 2011; Weber et al., 2011). As additional datasets have become available, such as gravity data from the GRAIL mission (Zuber et al., 2013a, 2013b), uncertainties in the lunar interior have been reduced through joint inversion of the two datasets (Garcia et al., 2019). Seismic constraints on the size and state of the core and lower mantle allowed for better modeling of the lunar dynamo evolution (Laneuville et al., 2014; Weiss & Tikoo, 2014). The seismicity of the Moon serves as a potential end-member when considering the seismic activity of a planetary body.

Seismometers were sent to Mars on the Viking missions (Anderson et al., 1976), with each Viking lander was equipped with a seismometer. However, the seismometer aboard Viking 1 failed to properly uncage, thus did not record any useable data (Anderson et al., 1976). The cages were designed to protect the internal masses during vibrations associated with launch, descent, and landing, but were supposed to then release upon safe landing to then allow the seismometers to record vibrations from Mars. The seismometer aboard Viking 2 did successfully uncage and was able to record and send back seismic data. However, since the seismometer was coupled to the lander deck and did not have any isolation from wind or thermal variations, most of the signals are attributed to wind and/or lander noise (Lorenz et al., 2017; Nakamura & Anderson, 1979). There was one plausible event, but the pressure sensors were not recording, thus wind noise could not be definitively ruled out (Lorenz et al., 2016). For several decades, there were no operational seismometers on other planetary bodies, although several missions were unsuccessfully proposed and launched (Lognonné et al., 2000), until the landing of InSight in late 2018.

1.2.2 InSight Mission

On 26 November 2018, the Interior Exploration using Seismic Investigations, Geodesy, and Heat Transport (InSight) mission landed on Elysium Planitia. InSight was tasked with several science objectives, nearly all focused on Martian geophysics. Two of its primary objectives were to investigate Martian seismicity and the interior structure of Mars (Lognonné et al., 2019; Panning et al., 2017). Other objectives include making meteorological and geologic observations, as well as heat flow measurements.

The Mars Quake Service (MQS) was designed to detect, and if possible, locate seismic sources. Several hundred events have already been detected in the first (Earth)

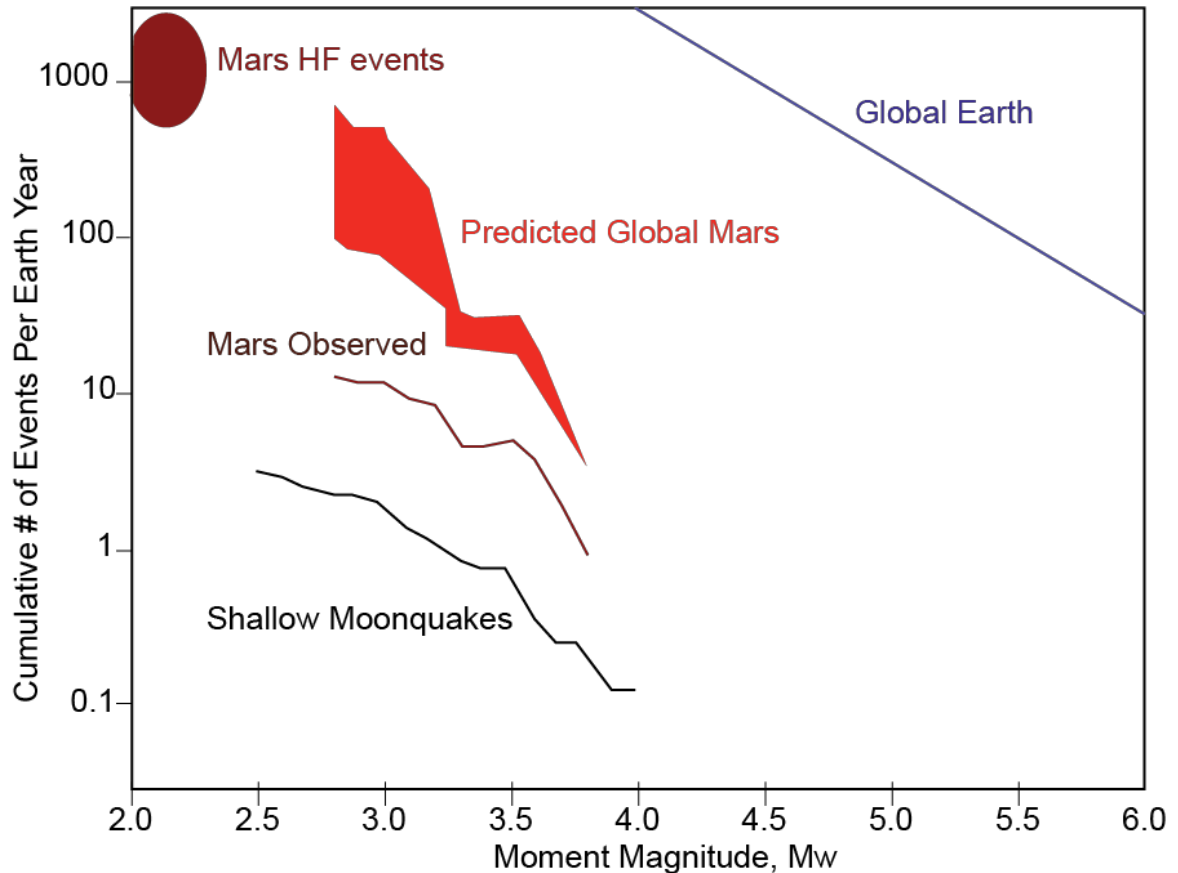


Figure 1.3. Adapted from Banerdt et al., 2020. The first year of Martian seismicity show high frequency (HF) are most common and about a thousand are predicted to occur each year. The number of observed Martian events is about an order of magnitude greater than the number of shallow moonquakes (grey) and well below Earth’s global seismicity rate (blue).

year on Mars (Banerdt et al., 2020; Giardini et al., 2020) (Fig. 1.3). Previous estimates predicted Martian seismicity would fall between Earth’s intraplate seismicity and lunar seismicity. Based on the first year, the observed rate was about an order of magnitude greater than shallow moonquakes. When considering an observational bias due to location, Mars has a seismicity rate similar to Earth’s stable intraplate seismicity rate, a bit higher than original predictions. This translates to a predicted Mw 4.5 occurring somewhere on Mars once per Earth year, and InSight observing ~ 10 Mw 3.0 events every Earth year. The most frequently occurring event were high frequency (HF) events which tended to have equivalent magnitudes of $M_w < 2.5$. Roughly 1000 of these events

are predicted to occur each Earth year. To date, three events with $M_w > 3.0$ have been detected and originated from the Cerebus Fossae region.

These marsquake events are being used to constrain internal structure through the Mars Structure Service (MSS)(Panning et al., 2017). The MSS is tasked with developing a one-dimensional velocity model similar to Earth's PREM. Like PREM, MSS will utilize seismic data along with geochemical, moment of inertia, and tidal measurements. Specifically, the InSight team will determine the crustal thickness, investigate if there is a mantle low-velocity zone or transition zone, and finally, determine the size and state of the Martian core. In my dissertation, Chapter 2 addresses the final task by studying the predicted uncertainty from an *ScS* stacking approach for a single seismometer like InSight, by using a terrestrial single-station seismometer as a planetary analog.

The results of the MQS and MSS will allow planetary scientists to quantitatively compare the Earth, Moon and Mars in terms of seismicity and internal structure, providing constraints on planetary evolution. Investigations on core size and state help model the evolution of the Martian magnetic dynamo and help answer questions on the lack of strong magnetic field at Mars. The structure of Mars will be a guideline to model internal convection or lack thereof, which has implications for the lack of active plate tectonics. The findings of the InSight team will have implications for not only Mars, but for terrestrial planets in general. For this reason, there is continued interest in returning seismometers to the Moon and to other bodies in the solar system.

1.2.3 Icy Ocean World Seismology and Future Missions

Although Mars and the Moon were shown to have seismicity rates below those of Earth, there are places in the solar system that may have higher seismicity rates (Hurford

et al., 2020; Panning et al., 2018). Icy ocean worlds are bodies in the outer solar system that may be currently seismically active due to tidal interactions with their parent planet and surrounding moons. Icy ocean worlds are of high interest to the planetary community due to their potentially active surfaces and the presence of subsurface liquid water oceans. These oceans, which may lie tens to hundreds of km beneath the surface, might support habitable environments (Parkinson et al., 2008; Reynolds et al., 1983; Vance et al., 2018a, 2018b). There are several concept, proposed, and planned missions to icy ocean worlds including the Europa Clipper (Phillips & Pappalardo, 2014), Europa lander (Hand et al., 2017), several Enceladus investigations (Konstantinidis et al., 2015; Razzaghi et al., 2008; Vance et al., 2019), and Dragonfly, a mission to Titan (Turtle et al., 2017). The proposed Europa lander and planned Dragonfly (Lorenz et al., 2019) missions both have seismic payloads.

These seismometers would have similar tasks to those of the InSight and Apollo seismic missions. The seismic data would be used to determine seismicity rates, detect and identify seismic sources, and constrain the interior structure. Determining the interior structure will likely be possible only through the use of seismometers (Kovach & Chyba, 2001; Lee et al., 2003). Given that their ice shells are tens of kilometers or greater in thickness, radar will not be able to penetrate deep enough to constrain the depth of a deep ocean. However, terrestrial seismology has been used in arctic conditions to detect subsurface aquifers and lakes beneath the ice (Isanina et al., 2009; Peters et al., 2008). Determining the thickness of the ice layer, and whether or not there is evidence of convection within the ice shell, can reveal how easily material from the subsurface ocean can reach the surface. Seismicity within the ice shell may also reveal the presence of dikes

or propagating fluid intrusions where future mission may more readily sample the ocean. Seismically detected active regions would not only reveal where tidal forces are creating fractures within the ice shell but could also reveal activity related to subsurface pockets of liquid water, cryovolcanism, and ice-water interactions within the ice shell. Chapters 3 and 4 of my dissertation focus on icy ocean world exploration approaches and methods using terrestrial analog locations.

1.3 Analog Studies

Analog studies and field work can be vital to the preparation of future missions. Here I define analog studies as terrestrial locations on Earth that mimic other planetary bodies in certain regards. The use of terrestrial analogs to prepare for future missions has been a common approach for over 50 years (Léveillé, 2010). Previous studies have used terrestrial analogs to prepare for crewed missions to the Moon (Young, 2007), determine if surface features have impact or volcanic origins (Beals et al., 1956), assess potential conditions for habitability (Horowitz et al., 1972; Kooistra et al., 1958; Navarro-González et al., 2003), and test the fidelity of instrumentation and analytical approaches (Marusiak et al., 2020; Panning & Kedar, 2019; Stone et al., 2019). For this dissertation I focused on environmental analogs selected to replicate natural variations in predicted seismic sources as well as mimic the properties of wave propagation in relevant planetary structures.

Although laboratory or synthetic experiments can precisely control environments, experiments in natural environments realistically recreate all effects at once. For example, synthetics can recreate anisotropy, internal structure, and lateral heterogeneity, but do not recreate some specific source mechanisms and unexpected instrument anomalies such as glitches or tilting effects. It can also be time consuming and cost ineffective to

systematically model every possible effect at once. Laboratory experiments can perfectly control most environmental factors but are often limited in scale. While geophysical analogs can be imperfect due to surface gravity or atmospheric effects and cannot achieve the same level of control over their environment that synthetics or laboratory experiments can, environmental analogs can replicate environments and instrumental effects on a greater scale.

For this reason, the InSight science team relied on a combination of synthetics and a terrestrial analog station, the Black Forest Observatory (BFO), which was used as an analog station for predicting the signals that would be recorded by the InSight seismometer on Mars. The seismic analog studies at BFO were used to develop methods and investigate uncertainties in event location and internal structure (Bose et al., 2017; Khan et al., 2016; Panning et al., 2015). In Chapter 2, I discuss how studying the detection of a core-reflected wave, ScS , on a single-station on Earth can be used to estimate the depth and uncertainty in the core-mantle boundary on Mars.

Although geophysical analogs environments or stations are not perfect matches for their target bodies, they can replicate expected conditions and help to anticipate unexpected results. One result of Chapter 2 was that high signal-to-noise events are not inherently better at retrieving core size. While this seems counterintuitive, it makes sense when you consider large events were still subjected to anisotropy, mantle and crustal heterogeneities, core topography, and location bias. Through the single-station geophysical analog work, I was able to show mantle-heterogeneities on Earth are detectable with a even a single seismometer like InSight.

In addition to global-scale investigations, geophysical analogs can be used to investigate the effects on seismic waves for specific local environments. Arctic environments, like ice shelves, ice sheets, and glaciers, can be used to simulate future missions to icy ocean worlds (Lorenz et al., 2011). While the ice in these environments is not as thick or as cold as the ice in the outer solar system, Antarctica, Greenland, and glaciers have been used in analog studies to test equipment fidelity (Marusiak et al., 2020; Stone et al., 2019), hypotheses on surface feature formation (Greeley et al., 1998; Hurford & Brunt, 2014; Pappalardo & Coon, 1996), as well as approaches and methods for constraining chemical composition (Gleeson et al., 2010) and searching for biosignatures (Gleeson et al., 2012). In Chapter 3, I present the results for seismometer deployments on environmental analogs to icy ocean world field sites. The field work was able to provide a unique approach to quantitatively compare deployment mechanisms and instruments. Since icy environments experience distinctive signals, such as icequakes, moulins, and basal motion, that are complex and higher frequency that can be easily modeled, field work is the best way to anticipate such signals for future missions. By mimicking robotic deployments, the instruments were subjected to similar conditions they would experience on an icy ocean world. In Gulkana, the instruments experienced tilting and rotation due to the active glacier surface. In Greenland, direct coupling to a mock-lander revealed lander resonances which help are being used to develop approaches to remove such effects. Instrumental anomalies also occurred which are common with all seismic instrumentation.

In addition to simply testing equipment, deployment strategies, or analysis methods, spacecraft and environmental analog studies can reveal potential pitfalls that would add risk to a mission, degrading the science return. It is better to identify these

problems on Earth rather than on a distant robotic spacecraft with fewer options for recovery. In Chapter 4, different sources from the passively recorded experiment illustrated the ability of a single-station and small-aperture array to detect, locate, and identify several seismic sources. Tectonic event detections were compared to known catalogs to determine when the algorithm failed to detect events. Through field testing, the algorithm can be adjusted to improve efficiencies, reduce false positives, and increase true positive detections. This fieldwork revealed cultural and instrumental sources were possible and had a significant effect on passively recorded data. Future missions would want to reduce unintended anthropogenic noises and sources so that naturally occurring sources can be detected and used for analysis.

1.4 Single-Station and Small-Aperture Array Approaches

Future missions will likely rely on a single-station or small-aperture arrays of seismometers for their seismic studies. In the early days of terrestrial seismology, instruments typically operated as single-stations or were sparsely dispersed across the globe. Despite the challenges, early seismologists were able to investigate large scale structure and begin to understand the geologic nature of our planet. More modern terrestrial studies have shown that single-station seismic approaches were capable of determining earthquake location and magnitude (Magotra et al., 1989; Wu et al., 2006). By placing several seismometers in close proximity (meters to kilometer scale) in an array, similar to telescope arrays or radio antennae, we can study the directivity and incoming angle of seismic waves. Here we define aperture as the largest distance between individual stations in the array. Kilometer-scale small-aperture arrays have been deployed to monitor volcanoes and better determine local structure (Chaput et al., 2015; Rivera et al., 2008;

Scarpetta et al., 2005). In the 1960's the Canadian Yellowknife array illustrated the capabilities of a small array (kilometer-scale) to detect and locate local and regional seismicity (Manchee & Weichert, 1968). Single-stations and small-aperture arrays depend on differential arrival times of body waves and surface waves to determine distance (Bose et al., 2017; Khan et al., 2016; Panning et al., 2015). While this is most accurate when the velocity structure is well constrained, as more data becomes available, the structure can become better understood and locations can be updated. The azimuth of the event is typically calculated using the polarization of surface waves or *P* waves (de Franco & Musacchio, 2001; Schimmel & Gallart, 2004; Stachnik et al., 2012; Vidale, 1986). For small-aperture arrays, beamforming approaches can be used to better constrain azimuth (Edelmann & Gaumont, 2011). These methods require good signal-to-noise ratios in order to properly identify the onsets surface waves and *P* waves.

The Apollo-era seismic experiments were a mixture of small-aperture array active source experiments, and a large-aperture 1000 km triangular array of passive seismic experiments positioned on the near-side of the Moon. The Viking and InSight missions carried single-stations to Mars and operated when there was no other working seismometer on the planet. The Venera mission also acted as a single-station seismometer due to its limited lifetime (less than one Earth day)(Ksanfomaliti et al., 1982). One driving factor for single-station deployments has been cost. Because planetary missions are often costly (several hundred million to billions of dollars), a single-station approach may be the most economically reasonable method for seismic investigations. The current mission InSight was designed as a single-station as funding for a global Martian network is currently unavailable (Harri et al., 1999). Even if cost was not a factor, competing science objectives

and desired investigations mean there would be limited space and opportunities to fly to distant bodies. Future missions to icy ocean worlds are also unlikely to consist of more than a single-station station or small-aperture array due to the ability to send large data volumes in a timely manner. While data can be relayed relatively easily from the Moon or from Mars in a timely fashion, a mission to Europa would face difficulties sending all collected data back before instrumentation dies from radiation exposure (Hand et al., 2017; Pappalardo et al., 2013). While typically more data is a good thing once it is archived on Earth, transmitting large data volumes may be a challenge (Hand et al., 2017).

Even if arrays are deployed, there are still associated challenges. An event may only be detected by a single-station, in which case single-station approaches would need to be implemented. Larger arrays have the disadvantage of extra mass, additional power constraints, and the environmental dangers (e.g. radiation) that single-stations still face. Precise timing among stations in the array is also required in order to perform many science tasks. Each station would also be subjected to the deployment mechanism which may have its own risk associated with it. Seismometer deployments on lander or rover decks may be contaminated by wind noise and lander or rover resonances (Marusiak et al., 2020; Nakamura & Anderson, 1979; Panning et al., 2020; Panning & Kedar, 2019). Ideally seismometers would be deployed to the surface or subsurface via robotic arm, effectively decoupling the instrument from the spacecraft. However, such deployments would introduce additional complexity and risk to the overall mission.

One advantage of a large network of seismometers is the global coverage of stations. When numerous stations are able to detect the same event, better constraints on

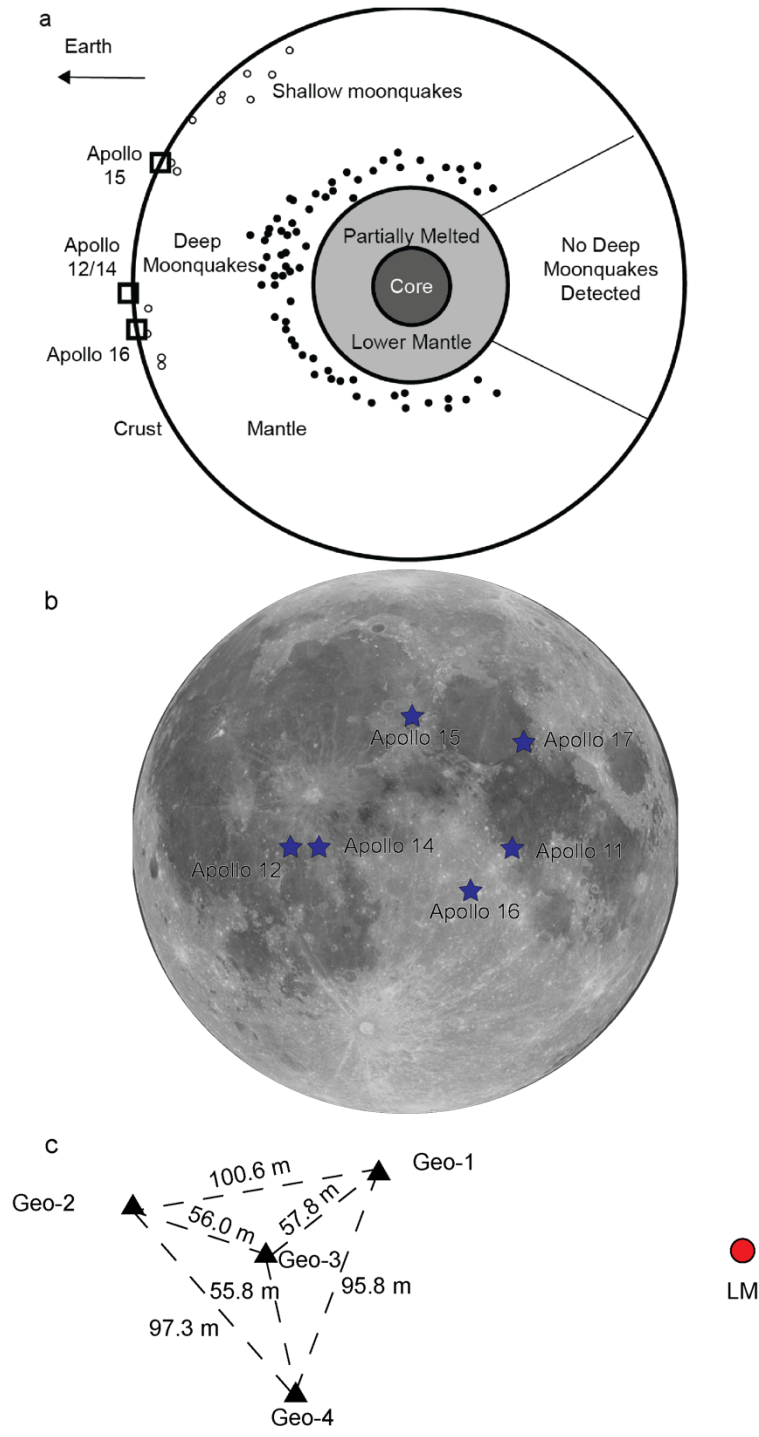


Figure 1.4 a) Based on Khan et al., 2014. Most of the Apollo seismometers were placed on the near-side of the Moon and near the lunar equator. This created a possible shadow zone where far-side deep moonquakes cannot be detected. The shallow moonquakes were also relatively close to the deployed stations. b) All of the Apollo sites were located on the near-side of the Moon and mostly close to the equator. c) Based on Heffels et al., 2017. A small array was set up at the Apollo 17 landing site near the lunar module (LM) which helped constrain the local structure.

the location can be made. Wide coverage also allows for the detection of smaller events that may become undetectable at large distances. The individual stations within the Apollo array functioned as a network from 1972-1977 (Fig. 1.4a). The Apollo 17 mission was able to deploy a 4 station small-aperture array, the Lunar Seismic Profiling Experiment (LSPE), that allowed seismologists to better constrain the local near-surface structure (Dimech et al., 2017; Heffels et al., 2017; Kovach & Watkins, 1973; Tanimoto et al., 2008). The Apollo-era stations were all deployed on the near-side of the Moon, and most were close to the lunar equator (Fig 1.4b). The location bias of the lunar network created a shadow zone on the far-side where no quakes were detected. This could be due to a lack of sources but was likely due to a lack of stations on the far-side. For this reason, the Lunar Geophysical Network (LGN) proposes to create a modern network, with stations on the far-side of the Moon (Lunar Exploration Roadmap Steering Committee, 2016; The National Academy of the Sciences, 2011).

My dissertation describes methods and approaches that single-station seismometers and small-aperture arrays can exercise to explore terrestrial bodies and icy ocean worlds. It is worth noting the small-aperture arrays in this dissertation were limited to meter-scale deployments, rather than the tens of meters of LSPE or kilometer-scale terrestrial arrays. Here I quantify advantages and disadvantages of deployment schemes and analytical approaches for meeting key science goals. The findings of Chapter 2 have helped the InSight team better understand potential pitfalls and uncertainties in core detection using core-reflected body waves. The results of Chapter 3 can inform future missions on lander configurations, and deployment schemes on icy ocean worlds. Chapter 4 illustrates the

importance of landing sites and potential tradeoffs. My conclusions show that single-stations and small-aperture arrays are powerful tools for planetary exploration and can help a mission achieve critical science objectives. Environmental and instrument deployment analog studies were vital for proper investigations of local conditions, seismic sources, and instrument responses.

Chapter 2: Terrestrial Single-Station Analog for Constraining the Martian Core and Deep Interior: Implications for InSight

Marusiak, A. G., Schmerr, N. C., Banks, M. E., & Daubar, I. J. (2020). Terrestrial single-station analog for constraining the Martian core and deep interior: Implications for InSight. *Icarus*, 335, 113396. <https://doi.org/10.1016/j.icarus.2019.113396>

Abstract

We used a terrestrial single-station seismometer to quantify the uncertainty of InSight (INterior explorations using Seismic Investigations, Geodesy and Heat Transport) data for determining Martian core size. To mimic Martian seismicity, we formed a catalog using 917 terrestrial earthquakes, from which we randomly selected events. We stacked *ScS* amplitudes on modeled arrival times and searched for where *ScS* produced coherent seismic amplitudes. A core detection was defined by a coherent peak with small offset between predicted and user-selected arrival times. Iterating the detection algorithm with varying signal-to-noise (SNR) ranges and quantity of events determined the selection frequency of each model and quantified core depth uncertainty. Increasing the quantity of events reduced core depth uncertainty while increasing the recovery rate, while increasing event SNR had little effect. Including *ScS2* multiples increased the recovery rate and reduced core depth uncertainty when we used low quantities of events. The most-frequent core depths varied by back azimuth, suggesting our method is sensitive to the presence of mantle heterogeneities. When we added 1° in source distance errors, core depth uncertainty increased by up to 11 km and recovery rates decreased by $<5\%$. Altering epicentral distances by 25% added ~ 35 km of uncertainty and reduced recovery rates to $<50\%$ in some cases. From these experiments, we estimate that if InSight can detect five events with

high location precision (<10 % epicentral distance errors), that there is at least an 88% chance of core depth recovery using *ScS* alone with uncertainty in core depth approaching 18 km and decreasing as more events are located.

2.1 Introduction

Seismology is a vital tool for investigating Earth's deep interior. Despite a limited number of seismic stations, early seismologists were able to determine the basic internal structure of Earth and constrain the size of the outer core (Oldham, 1906), the physical properties of the boundary between the outer core and mantle (Gutenberg, 1913), and the size of the inner core (Lehmann, 1936). These studies were achieved by noting arrival times of core traversing or interacting seismic phases and measuring the travel-time versus epicentral distance moveouts to identify these body waves. Body wave studies have been essential for the creation of one-dimensional models of the seismic velocity layering, density, and shear and bulk moduli throughout the Earth (Dziewonski & Anderson, 1981).

More recently, travel time observations of body waves such as *P* (Dziewonski, 1984; Dziewonski et al., 1977; Wysession et al., 1992), *PcP* (Garcia & Souriau, 2000; Morelli & Dziewonski, 1987; Tanaka, 2010), *PKP* (Creager & Jordan, 1986; Morelli & Dziewonski, 1987; Schlaphorst et al., 2016), *PKKP* (Doornbos & Hilton, 1989), *S*, *SS*, and *ScS* (Garnero, 2000; Russell et al., 1999; Su et al., 1994) indicated that the core-mantle boundary (CMB) may have topography of up to ± 4 km and exhibit variations from a one-dimensional velocity model. These studies compared the arrival times of body waves to predicted arrivals or used the residual times between seismic phases from the same event. In addition to travel time deviations, normal mode investigations indicated the presence of

large-scale variations in seismic velocities in the mantle above the CMB (Ishii & Tromp, 2004; Krüger et al., 1995; Li et al., 1991; Mégnin & Romanowicz, 2000; Moulik & Ekstrom, 2014)

The seismic phase *ScS* wave has been used extensively to study the core-mantle boundary region of Earth (Mitchell & Helmberger, 1973; Wysession et al., 1992; Young & Lay, 1987) placing constraints on anisotropy (Fukao, 1984; Kendall & Silver, 1996; Russell et al., 1999), thermal structure (Hernlund et al., 2005; van der Hilst et al., 2007), the fate of subducted slabs (Hutko et al., 2006), and the source of mantle plumes (Lay et al., 1998; Schubert et al., 2004a; Yuan & Romanowicz, 2017). These studies investigated anomalies by comparing *ScS-S* arrival times, and how *ScS* arrivals differed from predictions by one-dimensional seismic models (e.g. Preliminary Reference Earth Model) (Dziewonski & Anderson, 1981). Waveform studies of precursory and postcursory scattered arrivals near *ScS* have also been used to investigate the mantle above the CMB. For example, delayed precursors, reduction in amplitude of the main phase, and delayed postcursors indicated the presence of low-velocity zones. *ScS* is sensitive to the properties of ultra-low velocity zones (ULVZs) lying above the CMB (Li et al., 2017; Simmons & Grand, 2002; Thorne & Garnero, 2004), the shape and properties of large low-shear velocity provinces (LLSVPs) (Burke et al., 2008; Garnero & McNamara, 2008) and other layered features such as the thickness of the thermal boundary layer, or deposits of denser material above the core (Buffett et al., 2000). In addition to studies on LLSVPs and ULVZs, *ScS* has been used to investigate the fate of subducted lithosphere “slabs” in the deep mantle (Hutko et al., 2006; Rost et al., 2008). Seismic velocities constrained by *ScS* have led to better constraints of the Earth’s chemical composition (Kellogg et al., 1999), dynamics

(Garnero & McNamara, 2008; Lay et al., 1998) and structure (Lay & Garnero, 2004) of the CMB. Although *ScS* provides extensive evidence for complex structure and dynamics in the Earth, the interiors of the other terrestrial bodies in our solar system remain virtually unknown.

We can investigate the interiors of other terrestrial bodies, by placing seismometers on their surface. Even a single-station seismometer can detect and locate seismicity, measure internal layers, and be used to determine the depth to the CMB. From 1969-1972, five of NASA's Apollo missions installed seismometers on the lunar surface enabling both active and passive experiments (Nakamura et al., 1982). The lunar experiments revealed seismic waves with unusually long codas compared to those on Earth (Latham et al., 1970b). This effect was explained by scattering in the lunar near surface layer (Toksöz et al., 1974) that is heavily cratered and without atmosphere or currently active plate tectonics. The lunar megaregolith is highly porous and fractured creating large velocity gradients in the upper 20 km of the crust (Toksöz et al., 1974). Diffusive scattering effects played a strong role on the Moon owing to the lack of sufficient atmosphere (Pandit & Tozer, 1970), and are weaker on Earth and presumably Mars. Despite the difficulties in identifying body waves the passive experiment found clusters of deep moonquakes that coincided with tides from the Earth and Sun (Bulow et al., 2007; Kawamura et al., 2017; Weber et al., 2011). Rarer, shallower events (<200 km) were thought to be tectonic or meteoritic in origin (Binder & Oberst, 1985; Oberst, 1987). Although only five stations were installed, seismologists were able to invert travel times to begin constraining the shallow internal structure of the moon (Hartmann, 1973; Latham et al., 1970a, 1970b). Owing to the strong scattering in the near surface, constraining the deep interior of the

Moon required the stacking of numerous core-reflected phases with additional constraints from geophysical data (Garcia et al., 2011; Weber et al., 2011). These investigations revealed layering within the lunar core that would not have been observed using tidal or gravity data alone. As on Earth, seismology is a vital tool for constraining the deep lunar interior, and seismology will be essential to investigate the Martian deep interior.

In 2018, NASA launched the Interior explorations using Seismic Investigations, Geodesy and Heat Transport (InSight) a Discovery class mission with the goal of investigating the interior structure and processes of Mars (Banerdt et al., 2017; Lognonné et al., 2012). The mission payload included a short period seismometer, the Seismic Experiment for Interior Structure (SEIS-SP) and a 3-component very broadband seismometer (SEIS-VBB) to record seismic waves across a range of frequencies (~1 mHz to 10 Hz) (Panning et al., 2017). The data from these seismometers are used to constrain the interior structure of Mars. With an array of seismometers, a single event can yield several seismograms from multiple distances which help constrain the location and depth of the event. A single-station will only yield a single set of 3 component seismograms; thus, the location and depth of the event is more difficult to determine. Despite difficulties, terrestrial single-stations have detected events and determined their locations (Magotra et al., 1987; Roberts et al., 1989) and magnitudes (Wu et al., 2006) and have also been studied for use in early warning systems (Lockman & Allen, 2005). In preparation for InSight's landing, several studies have examined InSight's ability to identify events from impacts (Schmerr et al., 2016; Teanby, 2015; Teanby & Wookey, 2011) or tectonic events (Bose et al., 2017; Khan et al., 2016; Panning et al., 2015), and determine interior structure (Banerdt & Landis, 2010; Lognonné et al., 2012; Panning et al., 2015, 2017). This study aims to

build on previous work and determine the efficacy of a single-station in detecting the core and investigating the deep interior.

Currently the interior of Mars is only constrained by a few geophysical parameters and geochemical measurements. Smrekar et al. (2018) present a comprehensive discussion on interior structure constraints and models for Mars. Interior structure models (Folkner et al., 1997; Gudkova & Zharkov, 2004; Khan et al., 2017) and seismic velocity models (Folkner et al., 1997; Nimmo & Faul, 2013; Rivoldini et al., 2011; Sohl & Spohn, 1997) rely on tidal dissipation measurements (Bills et al., 2005; Smith & Born, 1976), moment of inertia (Yoder & Standish, 1997), gravity data (Konopliv et al., 2011, 2016), and geochemical constraints from the recent rover missions (Gellert et al., 2004; Hecht et al., 2009; McLennan et al., 2014; McSween et al., 2009) and Martian meteorites (McSween, 1985, 1994). These models utilized assumptions for the deep interior composition and inferred core depths ranging between 1470-1860 km. For example, Sohl and Spohn (1997) presented two possible end-member models of the Martian interior. One model was optimized to fit the Fe/Si ratio of 1.71, and the second was optimized to fit a moment of inertia equal to 0.366. The first model has a core depth of 1922 km while the other has a core depth of 1723 km. Since then, the moment of inertia measurements have improved and tidal love numbers have been measured (Konopliv et al., 2016) but the estimates of core depth still range between 1531-1797 km (Khan et al., 2017; Nimmo & Faul, 2013; Rivoldini et al., 2011). Numerous forthcoming seismic studies are expected to provide additional constraints on internal layering and better resolve the deep interior to within several tens of kilometers.

To seismically image the core and explore the possible uncertainty in core size, we used the seismic phases; S , ScS and ScS multiples. The ScS phase is a shear wave (S) that travels down to the core (c) where it reflects and returns to the surface as a shear wave (S) (Fig. 2.1). ScS is particularly sensitive to the impedance contrasts at the CMB and has been used to constrain the lunar CMB (Weber et al., 2011). Its multiples include $ScSScS$ ($ScS2$), $ScSScSScS$ ($ScS3$) and $ScSScSScSScS$ ($ScS4$), which reflect off the core at multiple points and are observed over a larger range of epicentral distances. To quantify the uncertainty in obtaining core depth with only InSight, we implemented a terrestrial single-station analog of seismic events to test a ScS - S stacking method for constraining the depth to the terrestrial CMB. Our study utilized a database of seismic events recorded at the Black Forest Observatory (BFO) (Fig. 2.2) to 1) investigate the quality and quantity of events required to identify core reflected ScS arrivals sensitive to the size of the terrestrial core, 2) estimate the uncertainty in core size obtained from a plausible Mars-like distribution of events, 3)

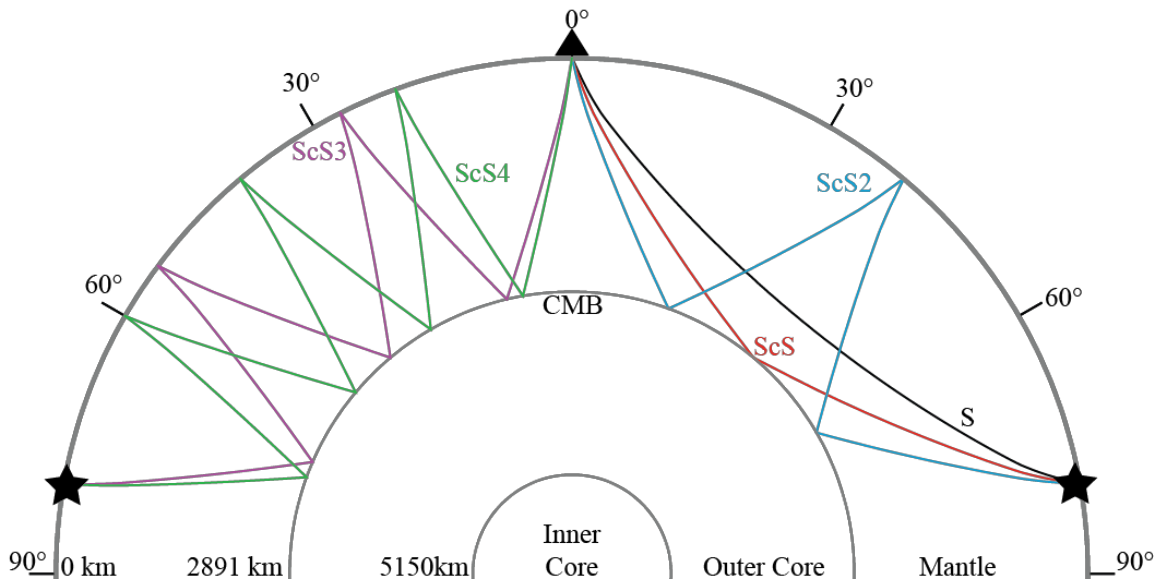


Figure 2.1. Travel paths of S (black), ScS (red), $ScS2$ (blue), $ScS3$ (purple) and $ScS4$ (green) through Earth. Sources (black stars) occur 80° from the receiver (black triangle). Raypaths were generated using the TauP toolkit (Crotwell et al., 1999).

investigate if the single-station InSight can detect mantle heterogeneities and deviations from a one-dimensional velocity structure.

2.2 Dataset

2.2.1 Constructing a Mars-like Database

We built our analog database using earthquake data collected from the Incorporated Research Institutions for Seismology (IRIS) Data Management Center. We select events from those identified in the National Earthquake Information Center, Preliminary Determination of Epicenters (NEIC PDE) catalog (Guy et al., 2015). BFO was chosen as our single-station seismometer because 1) it has previously been used as an analog station for InSight (Bose et al., 2017; Panning et al., 2015) and 2) its intraplate location in Germany approximates InSight’s landing site on Mars due to BFO’s location far from plate

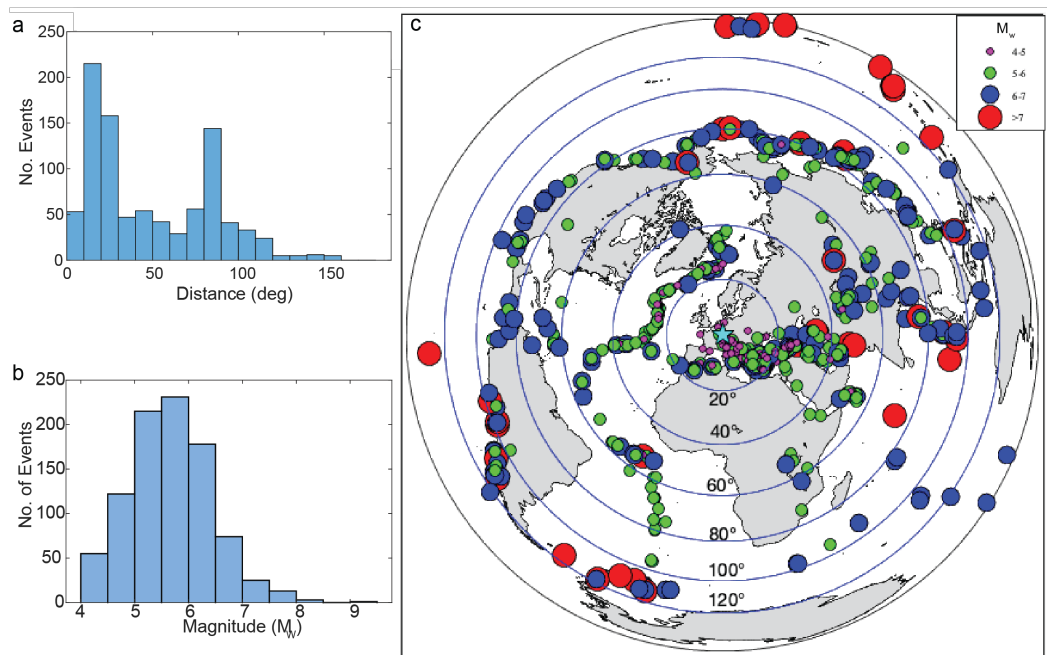


Figure 2.2. Distribution of the 917 events based on a) Magnitude, b) Distance and c) on an epicentral distance map projected with equal azimuths centered at BFO. The smallest M_w magnitude shown is 4.0 where the greatest is 9.08 (2011 Tohoku). The blue star at the center of the map represents BFO.

boundaries, large population centers, and the coast/ocean, the main producer of microseism noise on Earth (Ardhuin et al., 2001; Stutzmann et al., 2009).

BFO's local seismicity was modeled to be on the same order of magnitude as Mars (Golombek, 2002; Knapmeyer et al., 2006; Plesa et al., 2018) due the scarcity of local events that the catalog reports. The SEIS VBB instrument has an observational limit of about $10^{-9} \text{ m/s}^2/\sqrt{\text{Hz}}$ in the 0.01-1 Hz range (Lognonné et al., 2019). This range allows for potential observations of multiple orbit surface waves on Mars for events with moments greater than 10^{16} - 10^{17} Nm (M_w 4.6-5.3) and regional (distance $< 60^\circ$) detection of events with moments as low as 10^{13} Nm (M_w 2.5) (Mimoun et al., 2017; Panning et al., 2017). To have an observable *S* and *ScS* phase, the minimum required moment is estimated to be about 10^{16} Nm. From seismicity estimates (Knapmeyer et al., 2006; Panning et al., 2017; Plesa et al., 2018) this would translate to ~ 10 detectable *ScS* events over the duration of InSight's mission lifetime (one Martian year or approximately two Earth years).

Although Mars will experience fewer seismic events than Earth, Mars has less noise due to the absence of oceans and thick atmosphere, which will improve signal-to-noise for the detectability of body wave phases (Panning et al., 2015). Attenuation effects are expected to be smaller owing to the smaller planet radius and travel path lengths (Panning et al., 2015). For example, core-reflecting waves (e.g. *ScS*) from an event at an epicentral distance of 60° on Earth travel about 6700 km, while on Mars they would only travel about 3900 km, or $\sim 40\%$ less than the Earth distance. Although the Martian mantle is expected to have lower seismic quality factors (Q) than Earth (Lognonné & Mosser, 1993; Nimmo & Faul, 2013) overall attenuation could be lower than Earth due to the thicker Martian thermal lithosphere with higher Q and the smaller planetary radius (Panning et al., 2015).

Lower attenuation, or higher Q , would allow InSight to detect smaller magnitude events at greater distances than would be detected on Earth. For this reason, we began searching for terrestrial events with a minimum moment magnitude (M_w) of 4.0.

To build our *ScS* database, all seismograms from teleseismic events occurring between 2010 and 2016 with $M_w > 4.0$ and depths less than 100 km were downloaded and individually visually inspected using the Seismic Analysis Code (Goldstein et al., 2003). We do not expect deep events on Mars due to the lack of plate tectonics that produce deep subduction zones on Earth (Barazangi & Isacks, 1976). Due to the scarcity of events that occur within 80° of BFO, we further downloaded events from 2000-2009 to create a more

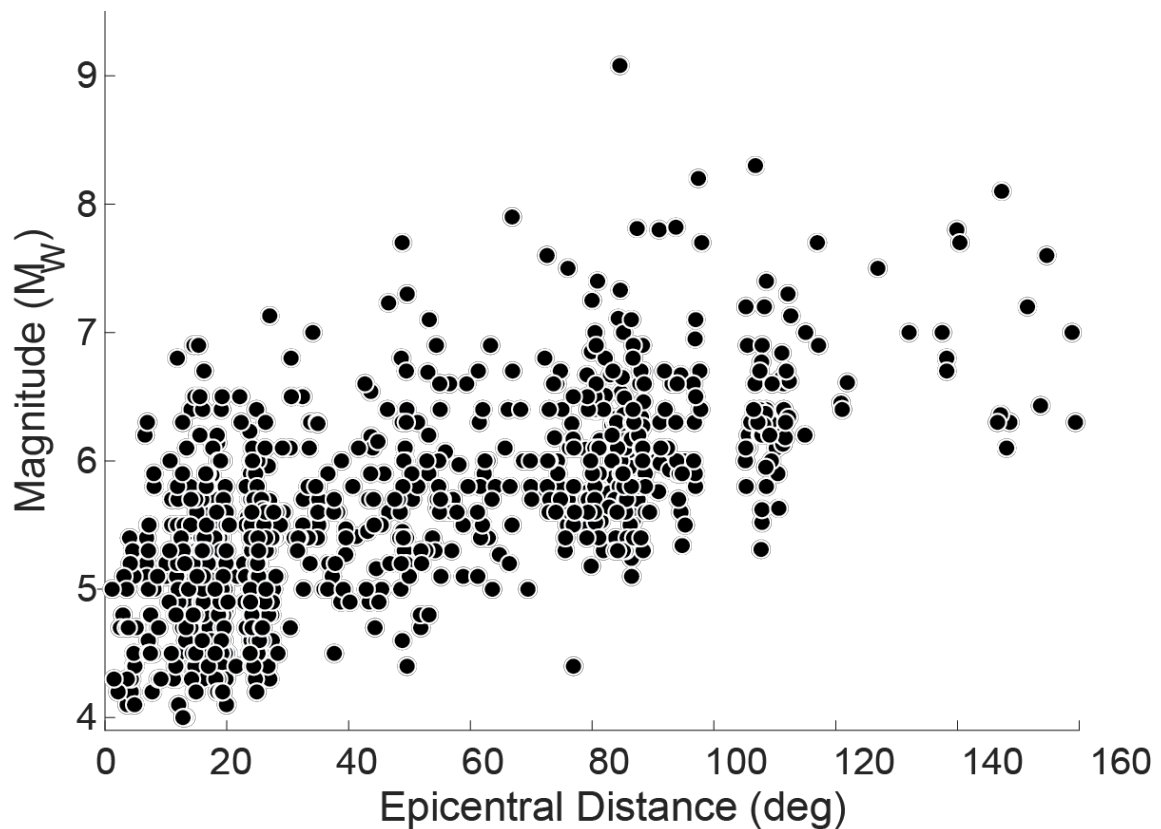


Figure 2.3. Our event catalog plotted by distance and magnitude. At distances greater than 169° , we did not identify any events due to the lack of detectable seismic activity in that region. This plot also demonstrates that the catalog was biased to high magnitude events ($M_w 5.0$) at large distances.

robust catalog. Since we designed our algorithm to pick events based on distance bins, we preferred a larger number of events of similar magnitude within those bins. Initially we found that the selection algorithm (Fig. 2.6, Section 2.3.1) had limited options for choosing smaller events (i.e. tended to select the same event in every iteration), which could have created a bias during our analysis. By adding more events, specifically those with low magnitudes ($M_w < 5$), we were able to create a more diverse dataset that could help remove biases from source location and travel paths (Fig. 2.3).

Our chosen station, BFO, has an STS-2 seismometer, that recorded events in three components; vertical (BHZ), East (BHE) and North (BHN). We converted the horizontal components to radial and transverse orientations using the source location published in the NEIC PDE catalog to rotate the horizontal components to the back azimuth of the event. We chose to use acceleration, rather than displacement or velocity, to avoid issues with the polarity of the S and ScS signals. We take advantage of a phase shift relative to displacement, that can produce a coherent positive peak. We used a time window that began 600 seconds before the start of the event and ended up to 10,000 seconds after the source origin time to capture any ScS multiples reverberations in our analysis. We immediately excluded seismograms with multiple earthquake signals within this time window and those with signal-to-noise ratios (SNR) below 0.5, on the assumption that the Martian database would not include such events in a core depth analysis due to poor signal quality. Here we defined the SNR ratio as the maximum amplitude of the first arriving S wave divided by the absolute value of the maximum background noise measured in a window 30-80 seconds prior to the S wave arrival.

2.2.2 Event SNR Determination

We visually inspected the transverse component of each event in the initial catalog of 12,754 events to determine if body waves could be identified and used in our analysis. To enhance the S and ScS signals, we applied a bandpass filter of 0.05-0.1 Hz (Loper & Lay, 1995). Our first visual criterion in event selection was the presence of a distinct S wave. Without a well-formed reference S phase, ScS will be difficult to identify, thus we excluded these events from our database. Next, we made a preliminary travel time pick on S and ScS (where possible) based upon the PREM predicted arrival time window for each phase. We then assigned the events a SNR rank based on the SNR ratio and whether ScS was identified to assess their quality for stacking. We excluded events from ScS stacking if the event occurred beyond the propagation distance of ScS or another wave obscured ScS . In particular, we did not stack ScS for events located between ~ 18 - 30° where the ScS arrival coincides with the arrival of surface waves. However, we are still able to use these events for stacking ScS multiples, thus we assigned a ranking to the multiples; either low ($SNR < 4.0$) or high-SNR ($SNR > 4.0$) rank and directed our algorithm to select these events only when investigating ScS multiples. The same quality ranking system applied where the S and ScS waves merge around 100° , with S beginning to interfere with ScS around 80° . Another important constraint on the size of the core is where S and ScS merge, but identification of this distance would require events to have sufficient distance sampling near the merging of S and ScS . Our shallow core models predict a merger at $\sim 98^\circ$ while deeper core models predicted the merger at $\sim 106^\circ$, thus Mars would need to produce multiple events that sample approximately every degree from 95 - 110° to properly distinguish between models.

To determine approximate distance ranges where ScS and its multiple could be utilized, we generated synthetics using the GEMINI code (Friederich & Dalkolmo, 1995)(Fig. 2.4). The synthetics show that ScS cannot be stacked between $\sim 18-30^\circ$ and beyond $\sim 80^\circ$. The synthetics also show that $ScS2$ is useable up to epicentral distances of 145° before other body waves such as S multiples (SS , SSS , etc.) interfere. We excluded distances of $60-115^\circ$ where there was interference between surface wave trains and the

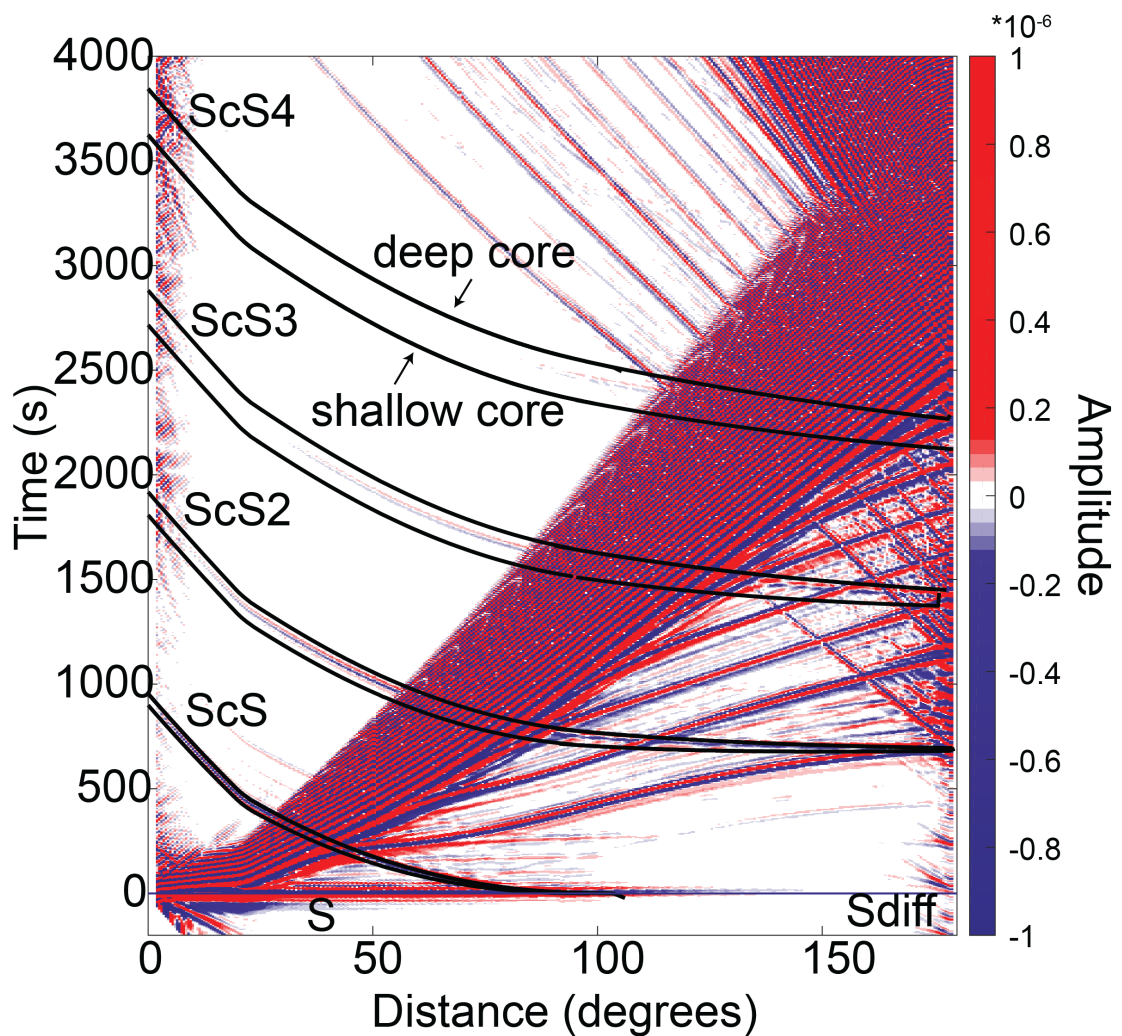


Figure 2.4. Moveout of ScS and its multiples relative to S arrival time illustrating the windows used to study ScS and its multiples. Synthetic seismograms based on PREM (Dziewonski & Anderson, 1981) with depths of 0 km and moment magnitude (M_w) of 6.0 were generated using the GEMINI code (Friederich & Dalkolmo, 1995). Solid black lines near ScS moveout indicates the range of predicted arrival times from 22 velocity models.

multiple. We stacked *ScS3* up to 150° before the phase is interfered with by multiple body waves, with an additional exclusion zone of $\sim 85\text{-}140^\circ$ due to surface waves. *ScS4* was stacked up to 110° before a combination of body and surface waves interact with *ScS4*. We were not able to use multiples *ScS5* and higher due to the low amplitudes of the phase.

In cases where we observed *ScS*, we categorized the events as low, average, or high SNR events. Low SNR events were defined by low *SNR* ratios (< 3), with a median value for this category of 1.4 (Fig. 2.5a). These events had an emergent *ScS* that can be difficult to distinguish from background noise. Average SNR events were defined by a larger *SNR* ratio (3-6), with a mean value for this category of 3.4 (Fig. 2.5b). *ScS* was more readily identified, with low uncertainty (< 8 seconds) in the arrival time. High SNR events were classified by having large *SNR* ratios (> 5), with a mean *SNR* ratio for this category of 8.5, and a maximum of 62 (Fig. 2.5c). In these events the *ScS* waveform was evident in the seismogram and emerged above the background noise; these waveforms represented the top 10% of *SNR* values. Our final database contained 917 events. Through visual inspection and our criteria above, we found 502 events where *ScS* was not identified (289 were low SNR, 213 were high SNR). Among the remaining events where *ScS* was identified, 254 were low SNR, 78 average SNR, and 83 high SNR. Each event was assigned a quantitative signal quality factor equal to the square root of the *SNR* ratio.

2.2.3 Core Models

We created 22 models based on the PREM 1D model (minus the ocean) (Dziewonski & Anderson, 1981) with core depths between 2791 km and 2991 km (true core depth ± 100 km) in increments of 10 km. PREM was selected as the reference model

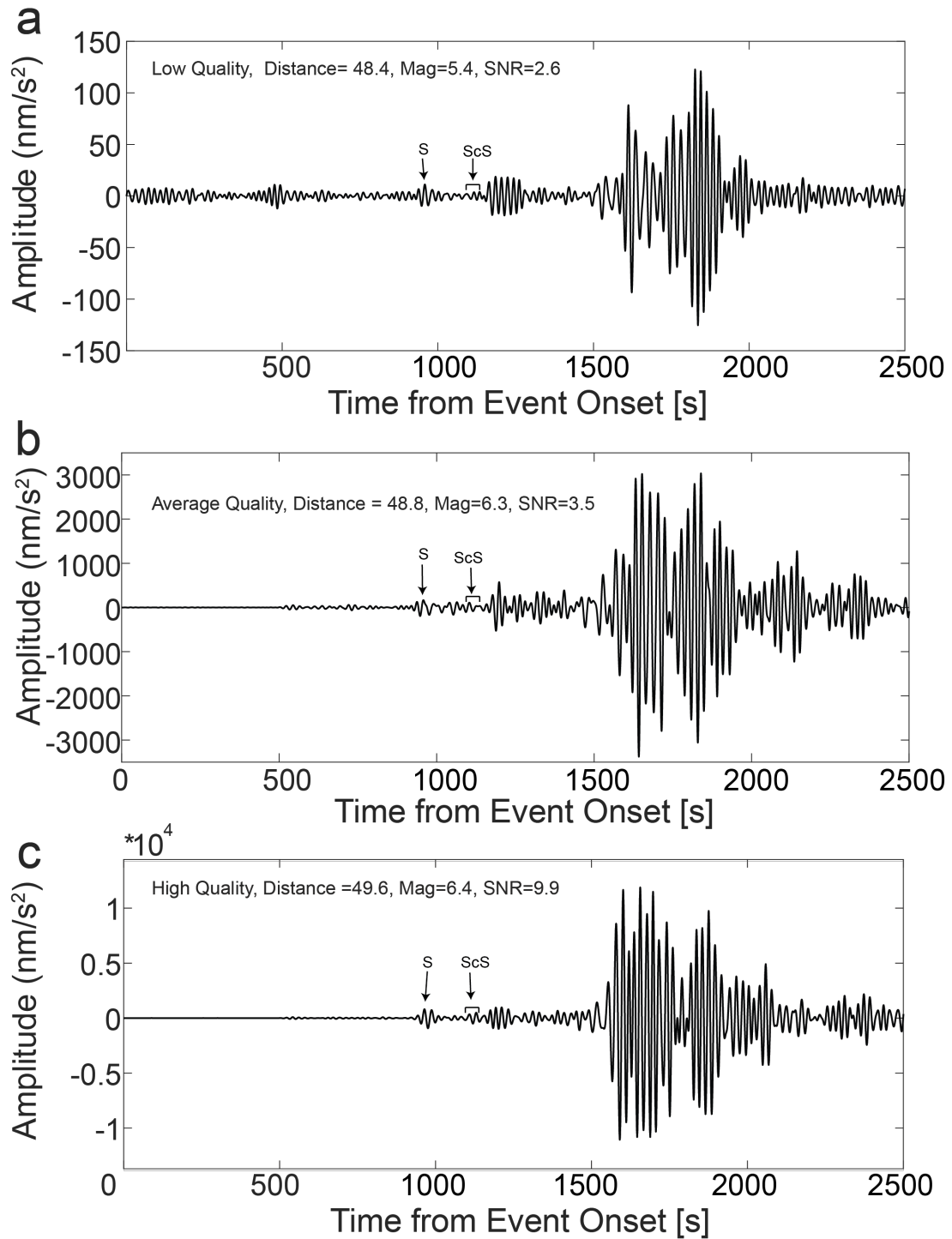


Figure 2.5. Examples of a) Low, b) Average, and c) High SNR events in our seismicity catalog. The events occur at about the same distance but have different amplitude ranges. Arrows indicate the S wave arrival and brackets indicate the ScS time window.

because it was built around geochemical and geophysical constraints similar to those that will be used for construction of a reference model for Mars (Panning et al., 2017). These constraints include moment of inertia, mean mass, and mean radius (Khan et al., 2017; Mocquet et al., 1996). PREM is one-dimensional, with seismic velocities constrained by arrival times of both seismic body waves, surface waves, and normal modes. PREM also represents one of the first self-consistent models that was widely accepted as a reference model. Newer models (e.g. ak135 (Kennett et al., 1995)) were similar to PREM and vary most in the inner core with ScS travel times varying by ± 0.2 seconds between the models. This variation is low enough to not affect our analysis of ScS. Finally, PREM has also been invoked in previous terrestrial analog studies for constraining Martian uncertainties (Bose et al., 2017; Khan et al., 2016; Panning et al., 2015), making our results readily comparable to those in the literature. To determine the moveout of ScS relative to S for each model, we used the TauP toolkit (Crotwell et al., 1999) (Fig. 2.4). For shallower cores, we preserved gradients in PREM's shear wave velocity and density and extended the core to shallower depths. For the deeper cores, we linearly extrapolated the shear velocity and density gradients in PREM to approximate what those properties would be for a deeper CMB. The extrapolation used the deepest 200 km, near the PREM CMB, and resulted in a maximum shear wave velocity of 7.26486 km/s. The change in velocity at the base of the terrestrial mantle is very minor but helps mimic Martian models where deeper cores tend to exhibit faster seismic velocities in the mantle at the CMB (Smrekar et al., 2018).

2.3 Methods

To determine the size of the core, we stacked seismograms on the model predicted moveout of the *ScS* phase relative to the *S* phase. We chose to use *ScS* only, as the phase has an amplitude ~10-40% of the *S* wave and was greater than *PcP* (Garnero, 2000; Woodward & Masters, 1991). *PcP* was not used because it is a low amplitude phase and is poorly detected on Earth. Furthermore, *ScS* does not rely on us knowing the core velocity like *PKP* or *SKS* to determine core depth. Our stacking process aligns individual wavelets along the predicted moveout based on the interior structure model to produce a higher signal-to-noise ratio than using a single event (Lay et al., 2004; Vidale & Benz, 1992). To avoid errors from using absolute travel time, we chose to stack along the *ScS-S* moveout rather than *ScS* relative to the origin time moveout. This helps remove any error caused by onset time and local crustal geology and removed the need for an accurate source onset time. Since *S* and *ScS* have similar travel paths through the crust and upper mantle, their travel times were similarly affected by the event depth and local crustal thickness, thus isolating travel time differences to the lowermost mantle.

The algorithm began by drawing events from our database to simulate a Martian, or intraplate, distribution of earthquake seismicity. We selected events using our weighted probability designed to mimic the range of magnitudes and epicentral distances for a planet without the strong signature of plate tectonics (Knapmeyer et al., 2006) (Fig. 2.3).

2.3.1 Event Selection

Since our terrestrial database of *ScS* events was not complete in magnitude or distance, we developed an algorithm to populate the Mars seismicity catalog with the

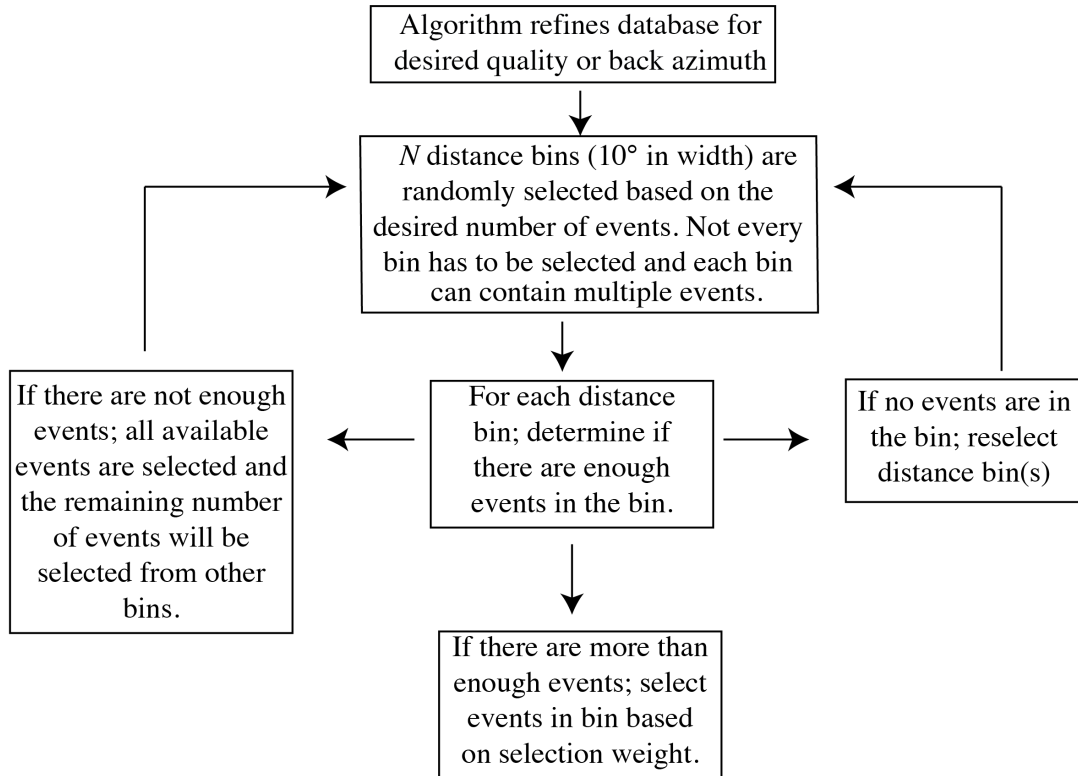


Figure 2.6. Diagram of event selection algorithm. The desired quantity, SNR, and back azimuth of event were predetermined and used to refine which and how many events were picked from the Mars-like database.

desired number of events for analysis (Fig. 2.6). We first specified the number of events (N) produced by Mars. This parameter was arbitrary and will be dependent upon the quality of data returned from Mars, and we explore it in more detail in Section 2.4. We then broke our database into subpopulations of events, separated into bins of 10° in epicentral distance. The bin size was chosen to provide a sufficient number of events at each magnitude. We randomly selected N source location distance bins and used this to determine which subpopulation to draw the events from. We then selected events from the distance bins the Gutenberg-Richter law assuming a b value of 1.05 (Ceylan et al., 2017; Knapmeyer et al., 2006). The b -value for Mars is still speculative, but 1.05 serves as a good approximation. The Gutenberg-Richter law states that for every decrease in magnitude, the number of

observed events increases roughly tenfold, thus smaller magnitude events are more likely to be selected than larger magnitude events. For a given moment (M_w) the selection weight (W) was equal to $10^{-(6.37+1.05M_w)}$. In the circumstance that a subpopulation was exhausted, we redrew the remaining number of events from other distance bins. With this algorithm, we were able to create and evaluate a dataset with mixed SNR events, examine subsets of events based on SNR range or source location, and discern back azimuth or location bias.

Initially we evaluated five events with any SNR and no added source location errors, but we adjusted the algorithm to choose three, ten and then fifteen events to see the effect quantity of events had on the algorithm's ability to constrain core depth. We based the quantity of events on lower estimates of Martian seismicity (Plesa et al., 2018) the probability of those events occurring at useable distances, and empirical tests. For the *ScS* multiple study that could utilize all distance bins, the number of events was set at 9, 15, 30 and 45. The average number of *ScS* events was 3, 6, 12, and 18, respectively, which we rounded to 3, 5, 10, and 15 events. We tested three *ScS* events to determine the minimum number of events required for core recovery.

2.3.2 Stacking

The algorithm chose a set of seismograms based on the desired quantity, SNR restrictions, and the selection weights. We then normalized each seismogram by the *S* wave amplitude and multiplied the amplitude of each seismogram by its quality factor (square root of the *SNR* ratio). This ensured higher SNR data were weighted more heavily than poor SNR data during stacking. We used the square root instead of just the *SNR* ratio to prevent a single event from dominating the analysis. Once the quality factor was applied, the algorithm isolated a section of the seismogram based on the visually inspected arrival

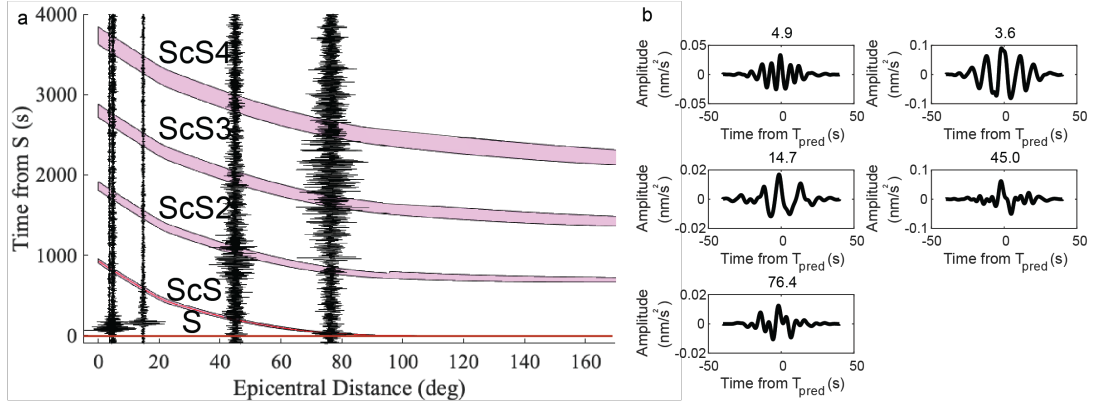


Figure 2.7. a) Example of selected events plotted along the moveout of ScS relative to the predicted arrival of S . The distances of the events are the cited distances in the catalog. The shaded region indicates the range in arrival times from the models. Please note two events have similar distances ($\sim 4^\circ$) and overlap on the plot. b) Same events plotted in panel a) after a taper and window has been applied. The time on the horizontal axis is time from predicted arrival time (T_{pred}). The plots are labeled by their distances.

of S and the predicted time of ScS and/or its multiples (Fig. 2.7b).

For each model, the algorithm applied a Gaussian taper to 40 seconds surrounding the predicted time of ScS relative to the S arrival to decrease the amplitude as it got further from the predicted arrival time of ScS (Fig. 2.7b). The taper reduced ambient noise and other waveforms that occurred near this interval. The same method applied to ScS multiple arrivals, but S_{diff} was used as the reference phase instead of S if the event occurred within the shadow zone of the core.

We distinguished the ScS arrival from other seismic energy by aligning on predicted travel time (T_{pred}) and used the phase-weighted stacking approach (Schimmel & Paulssen, 1997) to produce stacked amplitudes for each model (Fig. 2.8). In this approach we raised the phase coherence to the power of 2 so that higher SNR seismograms are weighted more. Stacked amplitudes that constructively interfere were indicative of a seismic phase arrival at the predicted moveout. We calculated the offset time (T_{off}) of each model by subtracting the time between T_{pred} and the visually selected arrival time of ScS (T_{vs}). This calculation

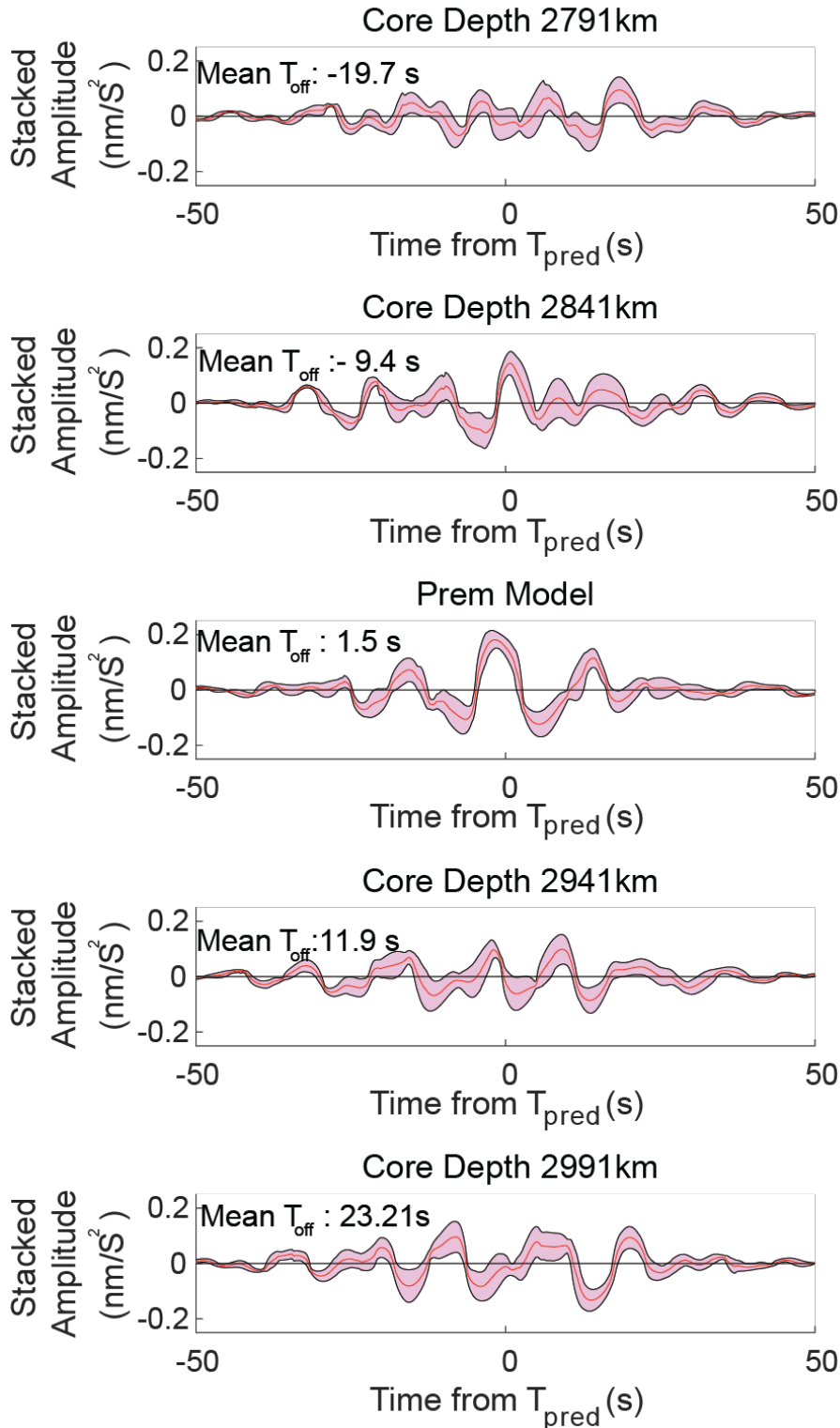


Figure 2.8. Examples of ScS stacked amplitudes (red lines) and uncertainties (pink shaded regions) using the bootstrap technique. The events are the same as those in the previous plots, and no ScS multiples were stacked in this example. As expected, the model with a core depth of 2891 km, PREM's core depth, has a large peak centered near the estimated time of arrival.

was repeated for each event, then averaged to calculate the mean value of T_{off} .

We determined confidence bounds on the stacked amplitudes and derived the uncertainty in amplitudes using the bootstrap technique (Efron & Tibshirani, 1997) with 100 resamples. Because we squared the phase coherence during the phase-weighted stack, some resamples produced anomalously large amplitudes that would skew the mean and standard values. To avoid this, we took the square root of the absolute value of each resample and multiplied by the sign of the original resample. This produced stacks that had a more normal or Gaussian distribution, thus calculating uncertainty using mean and standard deviation was appropriate.

In Fig. 2.8, the PREM model produced a coherent peak in amplitude of ScS at T_{pred} and had a small mean T_{off} , while perturbed core models defocused the stacked ScS arrivals. Fig. 2.9 shows the mean stacked amplitudes with uncertainty at T_{pred} for all 22 models with uncertainties equal to the shaded region of Fig. 2.8. The model with a core depth of 2891

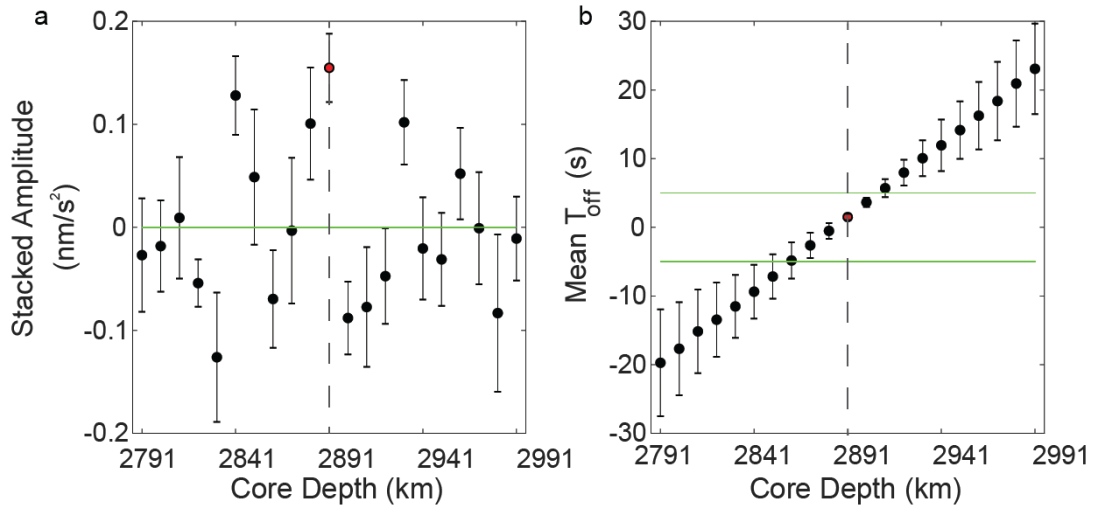


Figure 2.9. Criteria for evaluating core detection. Panel a) shows the mean stacked amplitude with certainty at T_{pred} for each model. Panel b) shows the average time between T_{pred} and the visually selected ScS arrival, T_{VS} . The dashed line indicates the PREM core depth for reference and the red points indicate the maximum amplitude (a) and smallest mean offset time (T_{off}) (b). The green line indicates the bounds for the models that can be considered. Errors bars must fall above green line (a) and offset times must fall between the green lines representing ± 8 seconds (b).

(the correct value) had the greatest amplitude (Fig. 2.9a) and the smallest mean T_{off} (Fig. 2.9b).

2.3.3 Core Recovery

A robust detection of the core had a large peak at T_{pred} with relatively low uncertainty, such that lower bound of uncertainty was still above zero at the 95% confidence bound, and a small value for mean T_{off} . We therefore selected the core depth using the maximum amplitude of models with amplitude certainty above zero with the additional criterion that the absolute value of T_{off} be less than 8 seconds. By ensuring lower uncertainty bounds were positive, we can be confident there is an arrival at T_{pred} . We used a cutoff T_{off} of 8 seconds because it typically eliminated about half of the model outliers left in consideration and corresponded to about half the width of the *ScS* waveform. This avoided spurious selection of *ScS* sidelobes and arrivals at the edge of the stacked predicted *ScS* time window. The cutoff also ensured we did not consider models that consistently failed to predict the arrival time of *ScS*. We could recover a core depth using only the maximum amplitude, but we found that by adding the time criterion, we reduced the uncertainty in the core depth by nearly half in some cases. The combination of time and amplitude restrictions typically left fewer than five core depth models for consideration. Using this combination of criteria also eliminated all models in some iterations, meaning the algorithm failed to recover a core depth, returning a null value for core depth.

We repeated this algorithm in over 1000 iterations to explore how data SNR, quantity, and location uncertainty each affected the outcomes. During each iteration, the event database was resampled for the desired criteria. Some events were rarely or never selected, like the large M_w 9.0 Tohoku, Japan event, because of low selection weights. We

selected some smaller events more frequently but verified that an event was never selected in more than 50% of the iterations so each iteration would represent a mostly unique combination of events. This was only a problem when selecting many events from a more restricted database (i.e. 15 high SNR *ScS* events) but the median event selection rate was always below 70 out of 1000 iterations.

2.4 Results

We used the 1000-fold ensemble of stacked *ScS* data to generate histograms showing the selection frequency of each core depth model and derived the mean core depth and uncertainty, here defined as the 1 sigma (σ) value assuming a Gaussian distribution (Fig. 2.10, Table 2.1). In addition to varying the number of events, we also investigated event SNR, using 1) only low SNR events or, 2) any SNR events or, 3) average SNR events or 4) excluding low SNR events or 5) only the highest SNR events.

2.4.1 Synthetic Tests

In addition to terrestrial events, we created PREM synthetic seismograms using the GEMINI code (Friederich & Dalkolmo, 1995). This allowed us to independently quantify

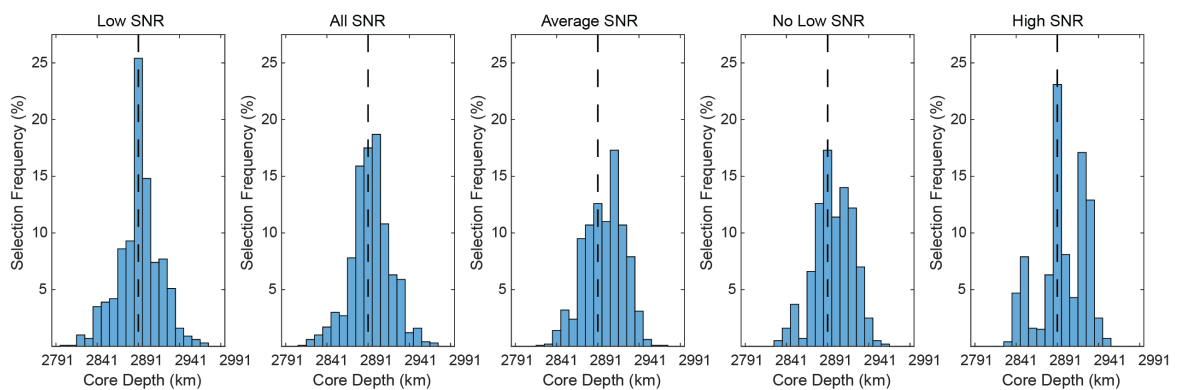


Figure 2.10. Selection Frequency based on SNR of events. Dashed Grey lines indicate the PREM core depth for reference. These plots represent core recovery using five *ScS* stacks. Results are without added source location errors.

SNR	3 events			5 events			10 events			15 events		
	Recovery Rate (%)	Mean PREM-Core Depth [km]	Uncertainty[km]	Recovery Rate (%)	Mean PREM - Core Depth [km]	Uncertainty[km]	Recovery Rate (%)	Mean PREM - Core Depth [km]	Uncertainty[km]	Recovery Rate (%)	Mean PREM - Core Depth [km]	Uncertainty[km]
Low	94.8	0.9	26.7	93.4	1.8	26.1	96.4	1.1	22.2	96.4	2.8	20.3
Average	94.9	7.5	25.9	90.9	7.8	24.1	90.3	9.3	23.7	90.9	7.8	24.1
High	86.8	5.1	30.1	87.7	6.7	27.9	92.5	6	25.8	93.8	6.4	23.4
All	95.1	2.9	25.9	95.5	3.4	24.3	94.7	2.4	20	96.4	1.82	18
No Low	93.1	6	25.5	90.8	7.4	23.3	88.6	7.4	21.7	91.3	8.5	21.5

Table 2.1. Table showing the recovery rate (%), mean core depth, and the 1σ confidence level based on SNR and quantity of seismograms. No source location errors were added.

how noise and source location errors affected core recovery while eliminating errors from mantle heterogeneities, crustal variations, and source location errors. To test how SNRs may affect our results we added noise to the synthetic seismograms. White noise was added using a random number generator and adding the resulting values to the amplitude of the seismogram. We used white noise because a Martian noise model is currently unavailable. The white noise model assumed equal amounts of energy at all frequencies, which for our purposes allowed us to evaluate the detectability of the synthetics for a given SNR without having to establish a noise model at each frequency. We always recovered the PREM core depth when the maximum value of added noise was comparable to the *ScS* amplitude. When noise increased to about half of the *S* amplitude ($SNR \sim 2$, comparable to the lowest event SNR we used) the algorithm still recovered a core, but the core depths had an uncertainty of ± 14 km.

We altered the location of events to test the effects of location uncertainty and origin time using five *ScS* events. It should be noted that InSight is predicted to have less location uncertainty ($\sim 0.5-1^\circ$) compared to terrestrial single-stations owing to the lack of oceans and anthropogenic noise (Bose et al., 2017; Khan et al., 2016). Changes in source location caused changes in the expected arrival time of the models such that a now closer event (i.e. 29° versus 30°) had greater time differences between *S* and *ScS* arrivals (Fig. 2.4). This results in a mismatching of the visually selected time (T_{VS}) and an incorrect value for the offset time between T_{VS} and the predicted arrival time (T_{pred}). The rotation of BHE and BHN components to radial and transverse required a precise source location, meaning source location errors will cause the radial component to contaminate the transverse.

We attempted to quantify location uncertainties here by randomly changing the

epicentral distance by up to 1° (Bose et al., 2017; Khan et al., 2016; Panning et al., 2015) representing low source location errors, 10% epicentral distance, a moderate source location error, and 25% of the epicentral distance, corresponding to larger errors in location but still meeting the mission goals of InSight (NASA, 2018). We also altered the back azimuth by up to 10° (Panning et al., 2015). During an iteration of the algorithm, we altered the source location of each event which modified the predicted arrival times of S and ScS and affected the rotation of the horizontal components. The new location was not permanent; we recalculated an adjustment in the location for subsequent iterations. For example, a source location could be closer in one iteration, but farther in another iteration. The errors were randomized such that the error function could select a value between -1 and 1 (for 1° error) and add that value to the cited epicentral distance, then select a value between -10 and 10 and add that value to the cited back azimuth value. When we added $\pm 1^\circ$ errors in distance, the core depth uncertainties increased by ~ 8 km. When we altered epicentral distances by $\pm 25\%$, the algorithm only recovered a core in $\sim 61\%$ of the iterations, and the uncertainty in core depth was over 55 km. Since most of these errors were smaller than our terrestrial data errors (discussed in the following paragraphs), this suggests that a combination of factors affected our algorithm's ability to recover the core depth.

2.4.2 Quantity and SNR effects of Real Events

Event SNR had less effect on core recovery than anticipated (Fig. 2.11). Low SNR events had higher recovery rates, more accurate core depths, and tended to have lower core

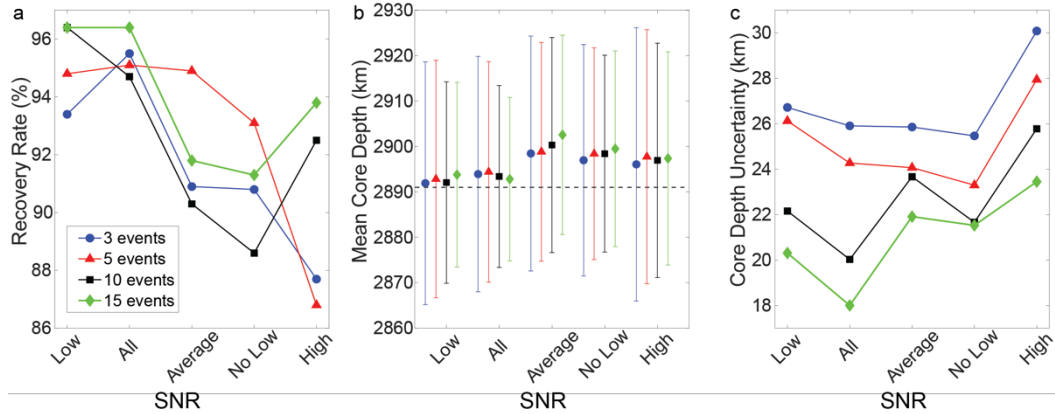


Figure 2.11. The effects of different SNR and quantity of events for a) recovery rate of a core depth b) mean core depth recovered with uncertainty and c) uncertainty in core depth. The dashed line in panel b) represents the PREM core depth for reference.

depth uncertainties than high SNR data. This suggests that any event where S and ScS can be identified is useful in core detection. It also implies that by applying our signal-quality index and using phase-weighted stacking, as opposed to linear stacking, we are sufficiently weighting higher SNR data. Higher SNR events tended to be from larger M_w events, and as a result may be limited in their event locations. For a lengthier discussion on the effects of location biases see Section 2.4.4. Increasing the quantity of events reduced the core depth uncertainty but did not necessarily increase recovery rate or improve core depth accuracy. When stacking events with no SNR limitations, the core depth uncertainty dropped from 25.9 to 18.0 km.

2.4.3 Location Alteration of Real Events

For the purposes of this study we assumed the distances reported in the NEIC PDE catalog are accurate (minimal location error), thus we considered any alterations to the cited distance and/or back azimuth as errors in locating the source. Smaller magnitude events inherently were less constrained than larger events on Earth because fewer stations detected them. Since InSight will be a single-station seismometer, this effect is absent on

Mars.

We attempted to quantify location uncertainties here by randomly changing the cited epicentral distance by up to 1° (Bose et al., 2017; Khan et al., 2016; Panning et al., 2015) representing low source location errors, 10% epicentral distance, a moderate source location error, and 25% of the epicentral distance, corresponding to larger errors in location but still meeting the mission goals of InSight (NASA, 2018). We also altered the back azimuth, as cited by the catalog, by up to 10° (Panning et al., 2015). During an iteration of the algorithm, we altered the source location of each event which modified the predicted arrival times of S and ScS and affected the rotation of the horizontal components. The new location was not permanent; we recalculated an adjustment in the location for subsequent iterations. For example, a source location could be closer in one iteration, but farther in another iteration. The errors were randomized such that the error function could select a value between -1 and 1 (for 1° error) and add that value to the cited epicentral distance, then select a value between -10 and 10 and add that value to the cited back azimuth value.

Adding error to the location affected the selection frequency of core models and

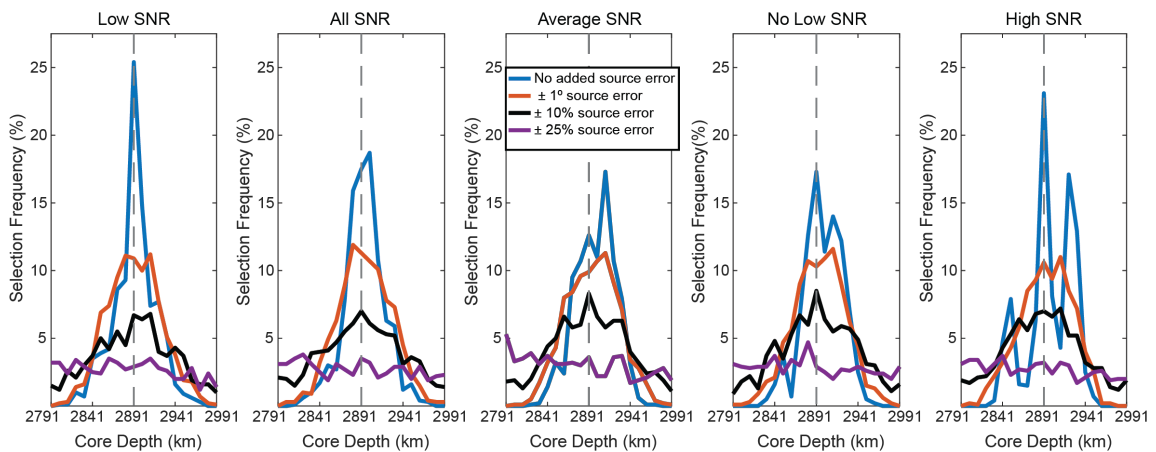


Figure 2.12. The effects of added 1° (red), 10% epicentral distance (black) and 25% epicentral distance errors compared to known locations (blue). The known core depth (2891 km) is indicated by the dashed vertical line. Five, ScS only, events were used to generate to recover the core depth.

the uncertainty in core depth (Fig. 2.12). In contrast to results from synthetic seismograms, but in line with real events, event SNR did not have any affect but increasing the quantity of events increased core depth recovery and decreased core depth uncertainty. When we altered the source epicentral distance by $\pm 1^\circ$ the core recovery rate dropped by 0-3% depending on the quantity and SNRs of events stacked (Table 2.2). The uncertainty in core depth increased by up to 11 km. Increasing source errors to up to $\pm 10\%$ epicentral distance further reduced recovery rates by $\sim 4-19\%$ and increased uncertainty in core depth by 14-28 km compared to using cited locations.

When we modified the epicentral by $\pm 25\%$, the recovery rate dropped to 40-75%. The selection frequency distribution no longer resembled a Gaussian distribution; all models had similar selection rates until 15 events were used, and then accurate core depth become the most selected model. Increasing the number of events increased the recovery rate and allowed some models to become selected more frequently than others, but the uncertainty in core depth was still greater than 50 km.

These experiments indicate that if the number of events recorded by InSight is limited, then source location errors will need to be low to accurately recover a core depth through stacking *ScS*. Higher quantities of events produce stacks that are more resistant to the effects of source location errors. InSight may be limited by the number of events it can observe, but more data can be made available if *ScS* multiples are also stacked.

2.4.4 *ScS* Multiples

Table 2.0 Effects of adding source location errors. Both have $\pm 10^\circ$ back azimuth errors and either $\pm 1^\circ$, $\pm 10\%$ or $\pm 25\%$ epicentral distance errors.

SNR	Source Distance Error	3 Events		5 events		10 events		15 events	
		Recovery Rate (%)	Uncertainty(km)						
Low	1°	93.9	37.4	95.3	32.5	95.8	30.7	95.9	29.4
	10%	75.8	53.4	75.0	47	71.8	44.2	71.7	38.7
	25%	50.0	64.3	56.1	57.7	67.6	53.8	70.2	53.8
Average	1°	92.6	35.5	92.5	31.4	91.2	29.2	90.0	25.9
	10%	86.0	51.7	86.4	46.3	86.7	39.2	87.4	35.9
	25%	52.6	62.3	63.4	60.5	73.8	54.2	75.5	52.6
High	1°	88.0	37.5	88.6	31.3	88.4	28.1	89.4	26.7
	10%	80.5	50.9	83.7	46.6	84.0	39.6	83.9	37.4
	25%	47.6	62.7	56.5	59.4	68.2	55.2	71.1	53.9
All	1°	93.4	36	94.3	32	94.4	29.2	95.8	28.0
	10%	79.5	53.2	80.3	48.3	77.4	40.4	76.8	39.0
	25%	49.0	62.5	57.4	60.4	71.1	57.3	70.3	51.0
No Low	1°	92.0	34	91.3	31	89.3	27.7	89.6	26.3
	10%	85.2	52.3	83.7	45.7	84.1	39.4	85.1	35.7
	25%	52.9	59	59.7	59.4	71.1	54.3	74.6	54.5

In addition to the *ScS* wave, we also investigated if the addition of *ScS* multiples to the stacked data could aid in the recovery of the core depth. Based on synthetics, we found that the amplitude ratio of *ScS* to its multiples was distance-dependent. For example, at a

distance of 16° , the ratio of $ScS:ScS2$ was 5.2:1, but at 56° , the ratio was 3.1:1. Synthetics also indicated that the multiples should decrease in amplitude. The $ScS2:ScS3$ amplitude ratio was typically around 3:1, while the $ScS2:ScS4$ was about 7:1. This was caused by the loss of energy when reflecting off the CMB and due to attenuation in the crust and mantle. In addition to the loss of energy, background noise also affected amplitudes of multiples. In many cases, the background noise of terrestrial events caused the amplitudes of $ScS2$, $ScS3$, and $ScS4$ to become comparable. Unlike ScS , the arrival times of most multiples could not be uniquely visually identified on individual seismograms due to poor signal-to-noise at the time of their arrival. $ScSn$ multiples also see the crust $2*n$ times, meaning $ScS2$ sees the crust 4 times, while $ScS4$ sees the crust 8 times. The crust can create offset in travels times that our stacking algorithm does not take into account, defocusing the $ScSn$ arrival. For these reasons, we determined mean offset times (T_{off}) using only ScS events and did not attempt to visually select the arrival of multiples.

The addition of $ScS2$ slightly increased recovery rates when the number of events was limited (<15 events) (Fig. 2.13a) and reduced core depth uncertainty (Fig. 2.13c). Stacking beyond $ScS2$ reduced the recovery rate, especially when stacking numerous events. Multiples did not have a consistent effect on recovering an accurate core (Fig.

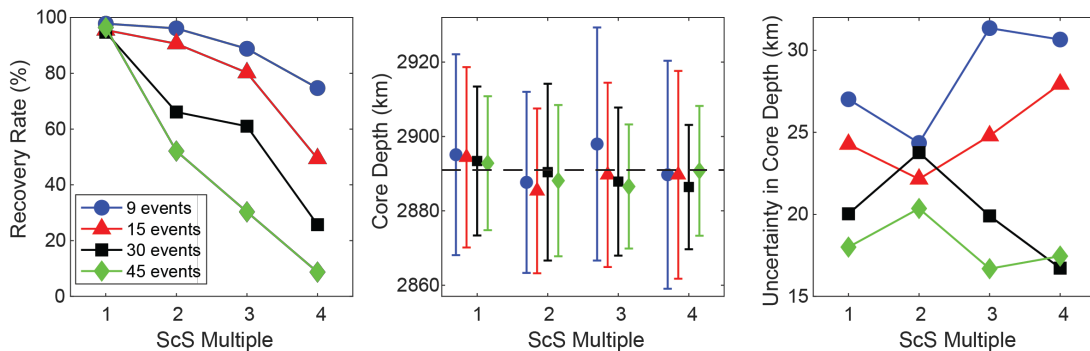


Figure 2.13. Results from ScS multiples experiments with the dataset. Comparison of (a) Recovery Rate (b) Mean Core Depth and (c) Uncertainty using different ScS multiples. Algorithm was not limited by event SNR.

2.13b) or reduction in core depth uncertainty (Fig. 2.13c). As mentioned earlier, multiples had much lower signal-to-noise ratios than *ScS* and *S*. After stacking, the stacked amplitude tended to remain above zero, but the poor signal of the multiple meant the uncertainty in the stack was relatively large, thus a coherent peak was not formed. The very low signals of the multiples had insufficient signals to create a coherent stack with 95% confidence bounds. If the number of *ScS* events is limited to less than five, then *ScS2* could be used to recover the core depth, but there is no advantage to stacking additional multiples.

For *ScS* multiples, we also investigated how SNR and quantity affected the recovery of the core (Table 2.3). To investigate SNR effects, we only selected events that we considered average or above SNR and thus were more likely to have stronger multiple signals compared to the background noise. Like *ScS*, SNR did not have a significant effect on recovery rate or mean core depth. However, using high SNR data did tend to reduce core depth uncertainty, especially once more than 15 events were stacked. However, the recovery rate for those quantities were still below the recovery rates using only *ScS*. Thus, we maintain, *ScS2* is only beneficial if there are less than 5 stackable *ScS* events.

We also tested source location errors when including multiples to see if they were still beneficial. When quantities of events were limited (<15 events), *ScS2* increased the recovery rate and decreased core depth uncertainty compared to using only *ScS*. For 9 events (~3 could stack *ScS*) the recovery rate increased by 1%, 9%, and 9% and core depth uncertainty was reduced by 5km, 5km, and 3 km for 1°, 10%, and 25% errors, respectively. Stacking *ScS3* produced similar results to stacking only *ScS* but stacking *ScS4* greatly reduced the recovery rate. For 15 events, *ScS2* reduced the recovery rate, but for 10% and 25% distance errors, also reduced core depth uncertainty. As with no added source location

Table 2.3. Results of stacking ScS multiples. *ScS values are given for comparison, but refer to 3, 5, 10 and 15 events using only ScS.

ScS Multiple	9 events			15 events			30 events			45 events		
	Recovery Rate (%)	Mean PREM - Core Depth [km]	Uncertainty[km]	Recovery Rate (%)	Mean PREM- Core Depth [km]	Uncertainty[km]	Recovery Rate (%)	Mean PREM - Core Depth [km]	Uncertainty[km]	Recovery Rate (%)	Mean PREM - Core Depth [km]	Uncertainty[km]
ScS*	95.1	2.9	25.9	95.5	3.4	24.3	94.7	2.4	20	96.4	1.82	18
No Low SNR	93.1	6	25.5	90.8	7.4	23.3	88.6	7.4	21.7	91.3	8.5	21.5
ScS2	96.1	-3.3	24.4	90.6	-5.6	22.2	66.1	-0.6	23.8	52.1	-2.9	20.4
No Low SNR	97	-6.2	24.2	87.6	-0.2	18.4	76.6	-0.4	16.3	51.3	1.2	16.7
ScS3	88.8	7	31.4	80.2	-1.32	24.8	61	-3.1	19.9	30.3	-4.5	16.7
No Low SNR	90.1	-2.9	26.2	70.4	2.8	23.5	59.1	4	10.4	32.8	-3	8.8
ScS4	74.7	-1.3	30.7	49.4	-1.3	27.9	25.7	-4.6	16.7	8.7	-0.2	17.5
No Low SNR	72.3	0.7	28.3	51.1	-0.7	24	17	-0.2	17.4	5.7	-2.9	16.6

errors, once there were more than 5 ScS events, there were no benefits of stacking ScS2 or any additional multiples. The recovery rates were much lower than using ScS alone.

2.4.5 Mantle Heterogeneities

A key result of our investigations is that the core was not always found to be at the PREM depth, and the mean core depth could be up to 9 km from the PREM core depth (Fig. 2.10). There are several possible causes for this discrepancy 1) the presence of mantle shear velocity heterogeneities within the Earth, 2) source location errors, including event depth, 3) crustal thickness variations, and 4) possible CMB topography. As previously discussed, using the *ScS-S* differential travel times eliminated many travel time perturbations from source origin times, as well as crustal thickness variations on the source and receiver sides of the *ScS* path. The *S* and *ScS* waves have similar raypaths, especially for large epicentral distances, and thus both were affected similarly by event depth and crustal variations. For local and regional events (within 30°) where the *S* raypath is shallow, and *ScS* travels nearly vertically, crustal variations are still able to affect travel times. Thicker continental crust would exhibit slower velocities than the PREM average crustal values and cause *ScS* to arrive later than predicted (Christensen & Mooney, 1995; Rudnick et al., 1998). If the source locations cited in the catalog (NEIC PDE) are accurate to within 1° then the travel time uncertainty from source location errors translates to ~ 15 km in core depth errors. Furthermore, topography at the CMB can vary up to 2 km (Morelli & Dziewonski, 1987; Schlaphorst et al., 2016; Tanaka, 2010), adding to the uncertainty in core depth.

To determine if there were any systematic effects arising from mantle heterogeneity, we stacked events as a function of back azimuth quadrant and examined variations in core depth and recovery. Seismic waves traveling through an area with velocities higher than PREM resulted in the core reflected phase arriving earlier than

predicted. This translates in our analysis of the ScS travel times to a shallower core depth. We used a tomographic shear-wave velocity model (S362ANI+M) of the mantle (Moulik & Ekstrom, 2014) to determine travel time heterogeneities along our sampled paths. We first computed the raypaths of ScS through the earth using the TauP Toolkit for each of our events. We used the tomographic velocity model along the path to compare the travel time delay or advance relative to the PREM one-dimensional travel time. We then show the location where the reflection off the core occurs, to determine the amount velocity varied from the average (Fig. 2.14a). Many of the travel paths in our dataset reflected off the CMB where shear velocities are relatively high (+1-2%).

The algorithm was re-run using only events within certain back azimuth ranges (Fig. 2.14b) and we compared the results to a tomography map of V_S near the core-mantle boundary. Although the map indicated that the northern hemisphere exhibits predominately faster velocity zones, we found that the most common bounce points (where ScS reflects off the core) tended to occur where the shear velocity was close to average. Therefore, the

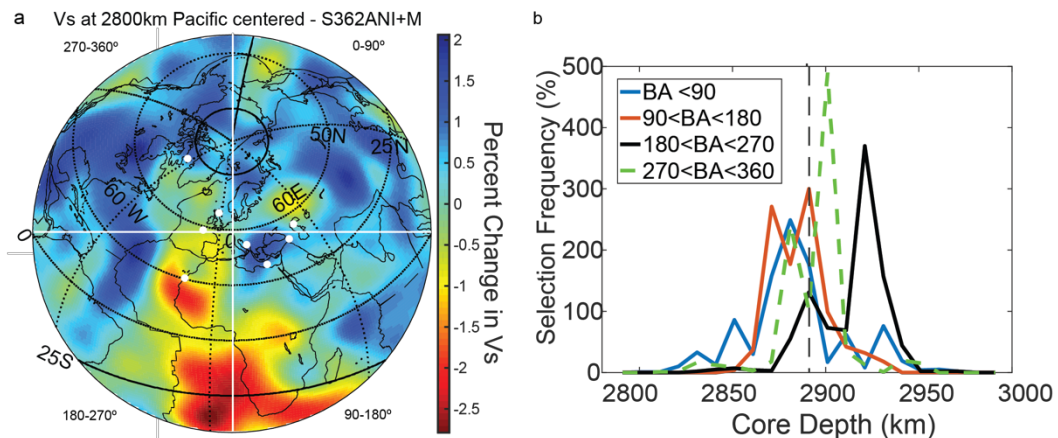


Figure 2.14 Possible sources of discrepancies in core depth measurements. a) Tomographic map of shear velocities heterogeneity near the CMB (2800 km) from (Moulik & Ekstrom, 2014). White points indicate points where ScS bounce points at the CMB for 8 common paths in our ScS dataset. b) Back azimuth (BA) stacks of the ScS dataset using five ScS events with any SNR.

algorithm for 0-90° (blue in Fig. 2.14b) selected core depths only 10 km shallower than PREM most often and the overall mean was 7.5 km shallower than PREM. The quadrant of 90-180° produced similar results where common bounce points occur in regions of faster than average shear velocities, thus result in a mean core depth of 5 km shallower than PREM. The tomography model suggested that events with origins near the Mediterranean (Greece, Turkey, Italy) should have travel times that arrived ~4 seconds earlier than PREM corresponding to a ~15 km shallower core depth model. Events originating near the East African Rift passed through regions that closely matched PREM's velocities resulting in travel time distances that were within 1 second of PREM. However, CMB topography and crustal variations could have caused the selection of PREM or deeper core depth models. The CMB was deeper than average (~2.5 km) underneath Northeast Africa and the Mediterranean Sea where many of the bounce points occur (Morelli & Dziewonski, 1987). A 2.5 km deeper core would cause errors of 1 s or about 4 km. The fast area around the Mediterranean has also been disputed (Lekic et al., 2012), thus the region may experience velocities closer to average values than suggested in the figure. These combinations of effects would explain why a deeper core depth was recovered, despite the faster than average velocities in Figure 2.14a.

In the 270-360° quadrant (green dashed), the algorithm selected many models deeper than PREM, but also selected a handful of models much shallower than PREM. Many events in this range originated in the Pacific Northwest with a bounce point in a relatively fast shear velocity area while events that occurred along the Mid-Atlantic Ridge tended to reflect off in regions of average or slower than average velocities. An event originating in Aleutians would recover a core depth nearly 70 km shallower than PREM

but events originating near Iceland or the Mid-Atlantic Ridge would pick core depths within 10 km of PREM.

In the 180-270° region (solid black), some bounce points occurred in or around the large-low shear velocity province (LLSVP) situated beneath Africa which slowed the *ScS* wave causing the algorithm to select deeper core depths. For example, an event that occurs along the Mid-Atlantic Ridge (near approximately 0°N, 30°W) would pick a core about 30 km deeper than PREM. As indicated in Fig. 2.14b, that back azimuth range consistently picked deep core depths and the most selected core depth range was 40 km deeper than PREM. Core topography could also have influenced our results by up to 5 km (Morelli & Dziewonski, 1987; Schlaphorst et al., 2016; Tanaka, 2010). The CMB under the South Atlantic had slower than average velocities combined with a deeper core depth, both of which would cause delays in the *ScS* arrival, leading to the recovery of a deeper core depth.

2.5 Analysis and Discussion

Our experiments showed that the depth of the terrestrial core was recovered by stacking at least three *ScS* recordings on a single-station, with an uncertainty in core depth of less than 31 km. This requires that the sources are well located ($<1^\circ$ error in distance), and the velocity model derived from other types of data is reasonably constrained. Increasing the quantity of events consistently led to decreases in core depth uncertainty and tended to increase the recovery rate. We found that low SNR events were able to recover the core better than requiring only high SNR events. For InSight, this implies that any event where *S* and *ScS* can be identified will be invaluable for core depth analysis. Small source location errors ($<1^\circ$) caused core depth uncertainty to increase by <10 km and decreased

the chances of recovering a core depth by $<3\%$. Larger uncertainties (25%) in source location reduced the chances of core recovery down to a minimum of 49%. The addition of *ScS2* helped reduce the effects of source location errors when the number of *ScS* events was limited. However, *ScS* multiples should be avoided once there are more than 5 *ScS* events. The following section delineates how to extrapolate our terrestrial results to Mars.

2.5.1 Comparison to Mars

We chose PREM as our Earth reference model because it is a relatively simple one-dimensional velocity model with a single average crustal thickness and no topography at the CMB, which are the same assumptions made by existing Martian models (Sohl et al., 2005; Sohl & Spohn, 1997; Zheng et al., 2015). More importantly, PREM was based on seismological and geodetic constraints including seismic velocity, attenuation, and density, the same constraints that InSight will provide. The InSight team plans to produce an initial model of Mars as velocity information from seismic events becomes available during the science monitoring phase of the mission (Panning et al., 2017). Impacts with known source locations will provide V_p - V_s differential profiles, and large events will provide Rayleigh and Love wave group velocities that constrain S velocity. Multiple surface wave orbits allow for more precise source locations that reduce error during velocity inversions. The dispersion of surface waves from small events may not be as precise but can still provide data for inversion of Martian crustal structure. A Bayesian inversion approach (Drilleau et al., 2013; Khan et al., 2000; Khan & Connolly, 2008; Panning et al., 2015) will be implemented with a limited dataset of arrival times and surface wave dispersions to derive shear and compressional wave velocities at greater depths. The inversions will use additional constraints from mineral physics modeling and geophysical constraints such as

moment of inertia and tidal love numbers (Khan et al., 2016; Rivoldini et al., 2011). As more data is collected, it is anticipated that the interior structure model can be updated and refined to become more accurate. If the scientific goal for interior models is met (within 5% accuracy) (NASA, 2018) then the velocity models would be comparable to the variation of velocities seen in tomographic models on Earth (~3% velocity variation) (Moulik & Ekstrom, 2014). The recovery of the Martian core will rely on the InSight mission's ability to produce an accurate model of the crust and mantle velocities.

The recovery of the Martian core using *ScS* stacking is dependent upon the SNR of the *ScS* waveforms. We anticipate that many of the sources we stack will come from double-couple events with identifiable *S* wave energy. For Mars, we assume scattering will be less than that of the Moon due to the lack of megaregolith. As exemplified by the lunar data, even highly scattered signals can produce a result. If the scattering effects are closer to the Moon than Earth, our approach still resembles the approach used by Weber et al. (2011) that recovered the lunar core. If scattering on Mars is large, recovery of the core will likely be more difficult and may require a larger number of events that can be stacked. The addition of a polarization filter, similar to what was used for the Apollo seismic data on the Moon (Weber et al., 2011) could be implemented to mitigate scattering effects if present on Mars.

Core recovery will also be more difficult if attenuation on Mars is higher than on Earth. On Earth, mantle attenuation has been constrained using *ScS* and *ScS* multiples (Kovach & Anderson, 1964; Lawrence & Wyssession, 2006; Mitsuru & Tsujiura, 1975) and *ScS* or *ScS* multiples may be used to constrain Martian mantle attenuation. Seismic quality factor (Q) on Mars will be lower in the mantle compared to Earth's (130 compared to

Earth's 312) (Lognonné & Mosser, 1993; Nimmo & Faul, 2013) but higher in the crust compared to Earth (Panning et al., 2015). Mars has a radius equal to about half of Earth's thus greatly reducing the travel path length, and consequently reducing the geometric spreading, overall attenuation, and scattering of raypaths. The decay of the ScS (or its multiples) amplitude is a function of the depth of each layer divided by the product of the layer's velocity and seismic quality factor. On Mars, the lithosphere is thicker than on Earth while the Q is greater, and the reverse is true for the mantle. Core reflected waves will be more affected by attenuation in the mantle than the crust, but since the mantle of Mars is about half the thickness of Earth's mantle, Q of Mars would have to be less than half of Earth's Q to begin degrading ScS . This agrees with Panning et al., (2017) who found attenuation can be an order of magnitude higher than expected without significant detriment to the recovery of V_s and the detection of events.

Ultimately, the recovery of the core may depend on the number of detected events, and core phases. If InSight records several high SNR events in which scattering is minimal and source locations are well constrained, then not only will the core be recoverable, but we will also be able to investigate the lowermost mantle. Although impacts would provide numerous sources with low location errors, their source mechanism is not well suited for producing S_H energy for stacking purposes (Banks et al., 2015; Schmerr et al., 2016). Our experiments show that core retrieval requires non-impact events with $M_w > 4.0$. Ideally, we need several large events for core retrieval, but Martian seismicity estimates indicate InSight is unlikely to record any events with $M_w > 6.0$ (Panning et al., 2017), thus we avoided selection of large events in our algorithm. Furthermore, in our analysis, we assume events occurred at the surface and further excluded deep seismicity events from our

catalog. For Mars, we expect many of the marsquakes will be relatively shallow (<100 km) compared to deep terrestrial events. On Earth, deep quakes are caused by subducting slabs, a feature more than likely absent on Mars. On the Moon, deep moonquakes were caused by tides from the Earth and Sun (Bulow et al., 2007; Kawamura et al., 2017) Mars is unlikely to experience similar tidal effects due to the smaller size of its moons; Deimos and Phobos, although the thicker lithosphere would expand the brittle/ductile transition to great depths (Montési & Zuber, 2003).

2.5.2 Detecting mantle heterogeneities

The back-azimuth study revealed that a range in the core may be indicative of the presence of crustal and mantle heterogeneities as the core would occur at similar depths around the planet, barring significant CMB topography (small for the Earth). For example, if InSight detects events originating in both the northern and southern hemispheres of Mars, it is possible to compare the travel times for each direction to determine if the surface dichotomy extends deeper into the planet. On Mars the crustal thickness varies greatly between the Northern and Southern hemisphere possibly due to mantle convection or from a giant impact (Andrews-Hanna et al., 2008; Golabek et al., 2011; Smith & Zuber, 1996; Thiriet et al., 2018; Wilhelms & Squyres, 1984; Zuber, 2001). If the events from different hemispheres retrieve different best fitting models for the core, this could indicate core topography, but such discrepancies are more likely caused by mantle heterogeneities.

On Earth, temperature and density increases reduce seismic velocities and are the implied mechanism for Large Low Shear Velocity Provinces (LLSVPs). Ultra-Low Velocity Zones (ULVZs) may further reduce seismic velocities due to increased melt, enhancement of MgO concentrations, core leakage, or other compositional variations.

Alternatively, cold material from sinking slabs increases seismic velocities. In our back-azimuth study, the most frequently selected core depth was up to 40 km deeper than the PREM depth but in the region of 90-270° (which contains the African LLSVP) less than 10% of the recovered core depths were 50 km or deeper than PREM. This suggests few raypaths sampled the LLSVP. The identification of such features on Mars would require careful study of pre and post-cursory waveform effects. For example, the postcursors, *Scd* and *Sab* (Thorne et al., 2007) along with precursors from reflections off D'' (Hernlund et al., 2005) have been used to investigate the thermal boundary layer above the CMB.

Investigations into the lower mantle of Mars will have important implications in understanding the thermal evolution of Mars. A layer of bridgmanite might exist if lowermost Martian mantle temperatures are high enough and the core is sufficiently small (Elkins-Tanton et al., 2003; Nimmo & Stevenson, 2000; Ruedas et al., 2013). Such a feature would have a shear velocity 4-5% higher than the shallower mantle in similar fashion to the Earth's seismic discontinuity at depths of 660 km. Like Earth, a high temperature plume source region beneath Tharsis and/or Elysium would produce seismic velocities slower than the rest of the planet. Alternatively, sinking cold material would create regions of faster than average velocities. With sufficient seismicity and good source locations, these lowermost mantle features could be identified using the same back azimuth approach we used for *ScS* in this study. InSight would need to detect 3-5 events located over multiple back azimuths to examine the existence of any travel time heterogeneity.

2.5.3 Benefit/Negatives of using Multiples

ScS2 was helpful in increasing the recovery rate and reducing core depth uncertainty when there was a limited number of events or source locations were uncertain. *ScS3* and *ScS4* had weak signals that created large uncertainties in the stacked amplitude. These uncertainties prevented the recovery of the core and for that reason, stacking *ScS3* and *ScS4* should be avoided unless a method is developed to correct for their defocusing. *ScS2* also stopped being beneficial once there were five or more *ScS* events for similar reasons. Since the multiple can occur at a wider range of distances, and can also occur when *ScS* occurs, it was not uncommon for the number of *ScS2* stacks to outnumber *ScS* stacks.

Table 2.4. Possible Interior Models for the blind test constructed by Clinton et al. 2017

Model Name	Source	Core Depth [km]	Moho Depth [km]
DWAK	Khan et al. (2016)	1704	66
EH45ThotCrust2	Rivoldini et al. (2011)	1594	85
EH45Tcold	Rivoldini et al. (2011)	1539	90
EH45TcoldCrust1	Rivoldini et al. (2011)	1671.5	85
EH45TcoldCrust1b	Rivoldini et al. (2011)	1671.5	85
EH45ThotCrust2b	Rivoldini et al. (2011)	1594	85
DWThot	Rivoldini et al. (2011)	1634	90
DWThotCrust1	Rivoldini et al. (2011)	1584	90
DWThotCrust1b	Rivoldini et al. (2011)	1584	90
Gudkova	Zharkov and Gudkova (2005)	1591	50
LFAK	Khan et al. (2016)	1659	56
MAAK	Khan et al. (2016)	1808	69
SANAK	Khan et al. (2016)	1870	32
TAYAK	Khan et al. (2016)	1597	77

2.5.4 Blind Test

In preparation for the data collected by InSight, a blind test was constructed using synthetic seismogram for expected Martian seismicity and noise (Ceylan et al., 2017; Clinton et al., 2017). This blind test consisted of one year of continuous seismic data

calculated using one of postulated fourteen internal structure models with core depths ranging from 1539-1870.4 km (Table 2.4). The input model, EH45Tcoldcrust1b, had a core depth of 1671.5 km. The seismic data were disturbed with seismic noise as predicted by Mimoun et al. (2017). The test was designed so that participants could attempt to detect, locate, and identify sources of seismicity and ultimately try to determine which interior model was used to construct the blind test. The creators of the blind test have since released the interior model used to create the synthetic series, which allowed us to verify if our method worked. We used the InSight blind test data to determine if our method could recover the correct internal structure model. We used the true source locations to select onset times to pick *S*, and if possible, *ScS* arrivals. The blindtest source locations were

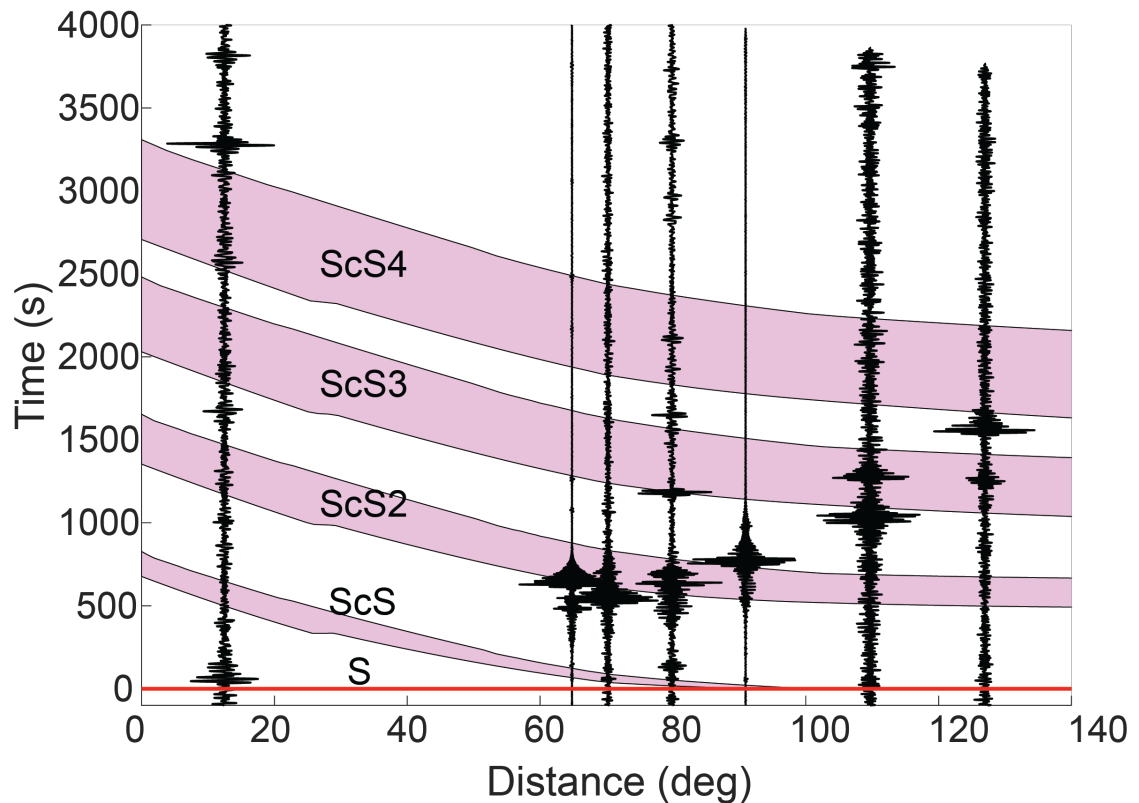


Fig. 2.15. Transverse component seismograms from the InSight blind test aligned on the where we picked the *S* or *Sdiff* phases. The shaded regions indicate the range of arrival times for *ScS* across the 14 potential interior structure models of Mars calculated using TauP. Seismograms were normalized for viewing purposes.

publicly released after the end of the test, and during the mission the Mars Quake Service will provide source location estimates (Panning et al., 2017) with the expected uncertainty discussed above. We used the geographic locations to compute source receiver azimuths, and rotate the three component seismograms into radial, transverse and vertical components. We initially used a bandpass filter mimicking that of Earth (10-20 s) but tested additional filters. The sampling rate of the blind test (2 Hz) is lower than BFO's sampling rate (1000 Hz) but is the same as that of the continuous data channel from Mars and reduces the Nyquist frequency to 1 Hz. Reducing the lower bandpass below 10 s allowed high frequency noise that can make it more difficult to identify *S*. Longer periods beyond 25 s tend to make it more difficult to separate *S* from *ScS* when they get close to merging. Therefore, we chose to adjust our filter from 10-20 seconds for terrestrial data to 10-25 seconds for synthetic Martian data. This allowed us the opportunity to stack events over a larger distance range and enhanced the *S* arrival relative to the background. We can further adjust our filters and tapers once the background noise of Mars has been established. Of the 204 events in the blind test, we were able to identify *S* in 7 events and *ScS* in 3 of those events (Fig. 2.15), knowing the true event location. *ScS*₂ and *ScS*₃ are predicted to appear without coincident phases in 3 events and 6 events, respectively. We used the provided models to determine a range over which *S* was predicted to occur. We then selected *S* based on the waveform and picked the amplitude maximum. The range of predicted time of arrivals was calculated for *ScS*. If any of the predicted times fell within the arrival of the surface wave, we did not use the event for *ScS* stacking. We also chose not to stack for *ScS*

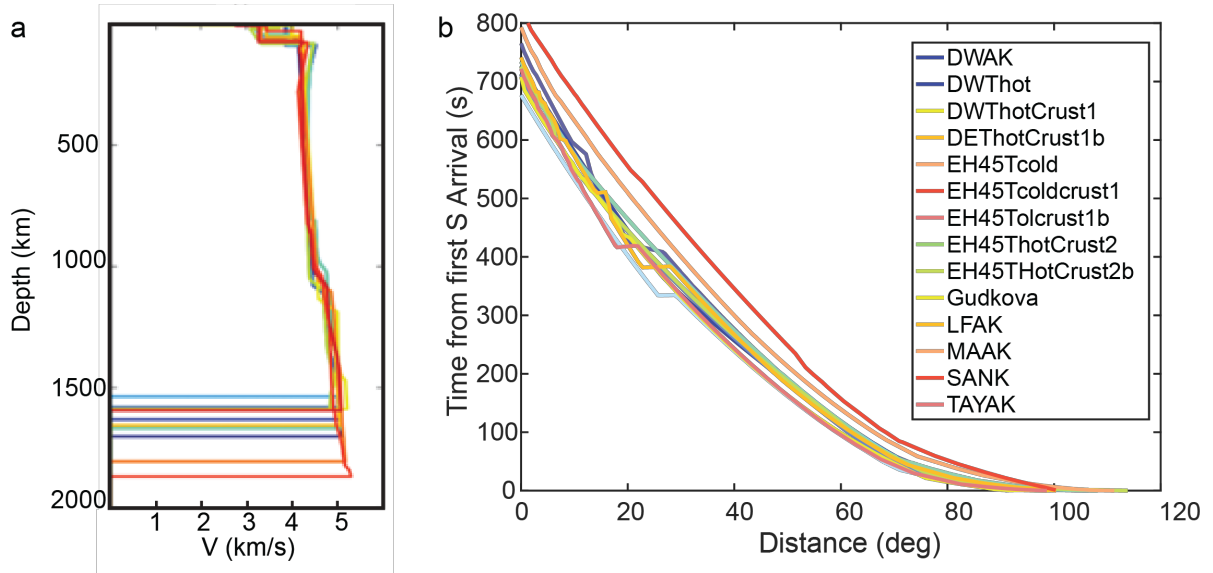


Fig. 2.16 a) S velocities through the crust, mantle and core. Figure is adapted from (Clinton et al., 2017). b) We used TauP to generate arrival times of ScS relative to S for each of the 14 models. When triplication of S occurred, the first arriving S time was chosen. If TauP predicted a shadow zone for S , we interpolated the S time arrival.

if the arrival windows of S and ScS overlapped. This was caused when shallow core depths would predict an early ScS arrival compared to slower moving S waves of other models.

One complication of the Martian blind test compared to the terrestrial test is the presence of shadow zones. In Fig. 2.16b, many models don't show smooth ScS - S arrival times. Part of this is due to triplication of the S wave following an immediate shadow zone. As with the terrestrial data, if triplication occurred, we chose the first arriving S wave as our S arrival time. To compensate for the shadow zone, we linearly interpolated to approximate when S would have arrived for the purposes of plotting the anticipated time difference. Some models like EH45ThotCrust had large shadow zones spanning over 40° , while models like Gudkova had shadow zones smaller than 5° . To avoid selecting SS or another body wave instead of S we chose not to stack events that occurred within any model's shadow zone.

We followed our terrestrial algorithm by applying a bandpass filter (10-25 seconds,

instead of 10-20 seconds for reasons stated above) and calculating a signal quality factor using the same procedure in Section 3.3. We stacked along the predicted moveout of ScS and $ScS2$ relative to S for each velocity model. Following our terrestrial analog results, when only three ScS events are available, $ScS2$ aids in core depth recovery. When stacking ScS alone, six out of the fourteen models produced positive amplitudes within the bootstrap derived uncertainty (Fig. 2.17). The model with the greatest stacked amplitude was EH45TColdCrust1b followed by EH45TColdCrust1, DWThot, DWAK, EH45Tcold, and TAYAK. Note that EH45TColdCrust1b and EH45TColdCrust1 vary only in the crust where 1b has a 1km thick slow velocity zone at the surface. The accurate core depth was 1671.5 km, and the models with coherent peaks had core-depths ranging from 1539 km - 1704 km. If we also considered a maximum value of T_{off} (average time between visually selected arrival and model's predicted arrival) then only DWThot, EH45TcoldCrust1 and Eh45TcoldCrust1b could be considered. This would reduce the range in core depths down to 1634-1671.5 km. When $ScS2$ was added, EH45TColdCrust1 and TAYAK no longer had positive amplitudes within uncertainty. DWThot now had the greatest stacked amplitude.

We used the six models with positive values at T_{pred} to quantify the uncertainty in core depth. We found the width of the signal peak at T_{pred} and converted time to core depth. By assuming the reference velocity model used to create the stacks, we converted the time at our reference distance to a core depth. This reference model would need to be derived from other seismic phases, including body waves that sample the crust and mantle (Panning et al., 2017). For each model we were able to recover a range of core depths that would create a coherent ScS peak (Fig. 2.17). The distribution of core depths results in an overall recovery rate of 1630.9 ± 58.2 km. The core depth range of 1670-1680 km including the

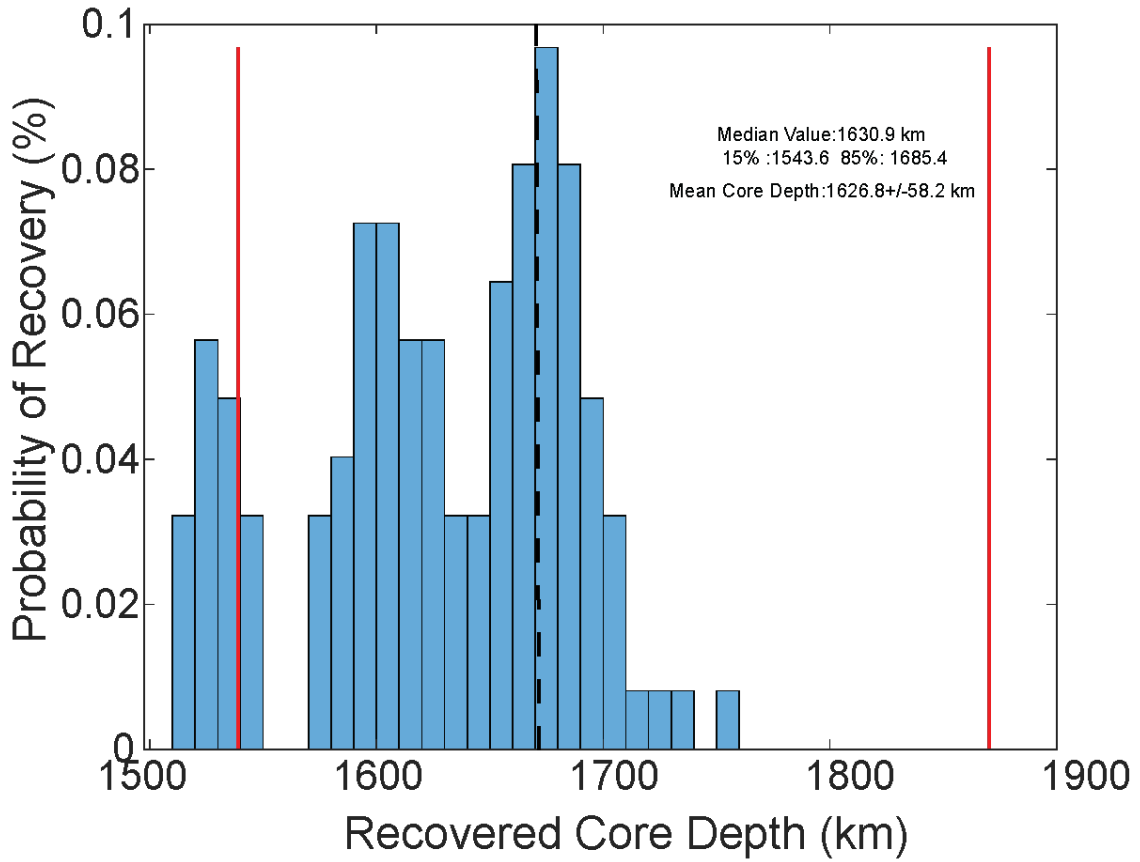


Fig. 2.18. Recovered core depths using models with coherent stacks around T_{pred} . Most recovered models fall within the red lines indicating the maximum and minimum core depths of all interior models. The dashed line indicates the input model's core depth (1671.5 km). In addition to the mean and standard deviation we also report the median with 15th and 85th percentiles, as the distribution is not a normal gaussian.

inputted (accurate) depth of 1671.5km, was the most selected core depth, suggesting recovery of the core depth. The uncertainty of 58 km is larger than our predicted core depth uncertainty of 26 km for 3 events. Using *ScS2*, would have increased the uncertainty to 66 km and retrieved a shallower core depth (1639 km).

The main difference between the terrestrial analog study, and the blind test is the use of accurate interior models. When the inputted interior model was used in the blind test stack, a clear coherent peak was present at the time of arrival. In addition to changes in the core depth, the models also had variations in Moho depths and velocities within the crust

and mantle (Fig. 2.18). For example, SANAK has a Moho depth of 32 km with S velocities ranging from 1.9-3.4 km/s. At 45° it takes ScS about 23.1 seconds, versus 52.6 seconds it takes EH45TcoldCrust1b, to travel through the crust. SANAK also has a much deeper core (1870 versus 1671 km). It takes about 884 seconds for ScS to travel through the mantle based on the SANAK model, but only 762 seconds based on the correct model. Because the models vary in crustal and mantle velocities, the moveouts of the different models can cross each other. For example, at 10° the model DWThot predicts ScS should arrive ~ 580 seconds after S , about 5 seconds after than the correct model. However, at 45° the model DWThot predicts ScS should arrive ~ 220 seconds after S , about 12 seconds sooner than the correct model. Depending on the epicentral distance of the event, more than one model may accurately predict the arrival of ScS relative to S . For the reason, it is important to consider the moveout of ScS and not just the arrival of a single event.

2.6 Conclusions

Our approach shows that it is possible to correctly recover the size of the terrestrial core with as few as three ScS events recorded at a single-station seismometer, assuming relatively precise source locations ($<1^\circ$) and an accurate reference background 1D crust and mantle velocity model. Given estimates of Martian seismicity and uncertainty in mantle structure we anticipate we can recover the Martian core within 40 km if the errors in source location are small ($<10\%$ epicentral distance). Larger source location errors ($>25\%$) would require larger quantities of events to constrain the core depth. A blind test of synthetic Martian seismograms indicated core depth uncertainties could be larger by 20 km if inaccurate internal models are used.

In addition to locating the depth of the CMB, our analysis shows how the single-station seismometer provided by InSight can be used to infer mantle heterogeneities on Mars. Both topography at the CMB and velocity heterogeneities in mantle would cause changes in travel times and waveforms for seismic phases traveling along different raypaths. Investigating these variations based on back-azimuth could reveal if the Martian mantle and CMB are more or less heterogeneous than the Earth.

2.7 Acknowledgements

AGM, MEB, ID and NCS were supported by NASA MFRP grant: NNX14AQ92G and 80NSSC18K1628. A portion of this research (ID) was carried out at the Jet Propulsion Laboratory, California Institute of Technology, under a contract with the National Aeronautics and Space Administration. We thank S. Ceylan, M. Drilleau, M. van Driel and B. Kendar for their work on preparing the blindtest dataset. We also thank Jessica Irving, Simon Stähler, and Renee Weber for their helpful comments and discussions. This paper is InSight contribution number 90.

2.8 Datasets

Terrestrial Events were downloaded from IRIS DMC using National Earthquake Information Center, Preliminary Determination of Epicenters (NEIC PDE) catalog (Guy et al., 2015). Blindtest data and internal models were downloaded from <http://blindtest.mars.ethz.ch/>.

Chapter 3: The Deployment of the Seismometer to Investigate Ice and Ocean Structure (SIIOS)

Abstract

The Seismometer to Investigate Ice and Ocean Structure (SIIOS) is a NASA funded analog mission program to test flight-candidate instrumentation on icy ocean world analog sites. In September 2017, a SIIOS experiment was deployed on Gulkana Glacier. In June 2018, a second SIIOS experiment was deployed in Northwest Greenland. The instrumentation included a Nanometrics Trillium 120 sec Posthole seismometer, four Nanometrics Trillium Compact seismometers, four Mark Products L28 geophones, and five each of Silicon Audio 203P-15 and 203P-60 seismometers. The Silicon Audio sensors served as our flight-candidate instruments. The instrumentation was arranged in a small (<2 m) aperture array with most sensors deployed in the ice. At the Gulkana site we also placed five of the Silicon Audio seismometers on top of a mock-lander to simulate placement on a lander deck. At the Greenland site, two Silicon Audio sensors were coupled to the legs and two were coupled to the mock-lander deck. The instrumentation recorded an active source experiment immediately after deployment and then passively for ~ 2 weeks at each location. We conducted an active source experiment using a sledgehammer striking an aluminum plate at thirteen locations, with nine to thirteen shots occurring at each location. During the passive observation of the Gulkana site, the experiment recorded one large Mw 7.1 event that occurred in Mexico and four other teleseismic events with Mw > 6.0. The Greenland site did not record any teleseismic events greater than Mw 6.0. The active and passive source signals are being used to constrain the local glacial

hydrological structure, environmental seismicity, to develop algorithms to detect and locate seismic sources, and to quantify the similarities and differences in science capabilities between sensors. Initial results indicate the flight-candidate instrumentation performs comparably to the Trillium Posthole up to periods of 3 seconds after which the flight-candidate performs more comparably to the Trillium Compacts.

3.1 Introduction

This field experiment was supported by a NASA-funded project, the Seismometer to Investigate Ice and Ocean Structure (SIIOS) that has the goal to develop instrumentation for a future mission to an icy ocean world, such as Europa or Enceladus. Icy ocean worlds are bodies in our solar system with icy shells and subsurface oceans (e.g. Carr et al., 1998; Nimmo & Pappalardo, 2016). Due to the potential habitability of these postulated oceans, icy ocean worlds have become a target for future mission development (Hand et al., 2017; Pappalardo et al., 2013, 2015; Raulin, 2008; Vance et al., 2018a). One major task of an icy ocean world mission is to determine the thickness of the overlying ice shell, and also the properties of the underlying ocean layer.

Missions to Europa, or any icy ocean world, would face many environmental and technical challenges. Due to its distance from the Sun, the surface of Europa is approximately 86-132 K (Spencer et al., 1999) and power necessities for a mission would require a non-solar power source such as a battery or radioactive power source (Hand et al., 2017). Ice shells could be several kilometers to tens of kilometers thick which limits the efficacy of orbital constraint of thickness through gravity, or flown ground or ice penetrating radar measurements (Kovach & Chyba, 2001; Lucchetti et al., 2017; Nimmo

& Schenk, 2006; Turtle & Pierazzo, 2001). Europa has a harsh radiation environment that would likely damage or destroy any stationary electronics within a few weeks (Paranicas et al., 2007). To increase the lifespan of electronic equipment, a lander's payload may be contained in a vault on the deck of a lander (Hand et al., 2017). These hardships would limit a lander carrying only a single-station seismometer, although it is possible a lander could also deploy a small-aperture array (<10 m²) of seismometers. Ideally, any flown instrumentation would have a small mass and volume to reduce flight costs. Here we used analog environments on Earth to investigate how ice shell thickness can be constrained via seismology, a technique that has proven useful for studying subglacial structures (Isanina et al., 2009; Kapitsa et al., 1996; Peters et al., 2008).

A primary goal of SIIOS was to investigate the ability of seismometers to meet planned science goals in preparation for a future mission to an icy ocean world. To test the efficacy of seismic studies in icy ocean world like environments, we deployed traditional and flight-candidate instrumentation side-by-side for approximately 13 days at each site. Both sets of instruments were buried in a small-aperture array on Gulkana Glacier's surface and within a vault on the Greenland ice sheet. The flight-candidate instruments were also placed on top of a mock-lander table to simulate an in-vault placement that would be coupled to the surface via lander legs (Fig. 3.1).

3.2 Gulkana Glacier, Alaska

Marusiak, A. G., Schmerr, N. C., DellaGiustina, D. N., Pettit, E. C., Dahl, P. H., Avenson, B., et al. (2020). The Deployment of the Seismometer to Investigate Ice and Ocean Structure (SIIOS) on Gulkana Glacier, Alaska. *Seismological Research Letters*. <https://doi.org/10.1785/0220190328>

3.2.1 Analog Setting

For our analog site, we selected Gulkana Glacier located in the Alaska Range as an analog site because of site accessibility, past characterization of the local geological setting (March, 2000; March & Trabant, 1997), and the presence of relatively thick ice (~130 m) (Josberger et al., 2007; March, 2000; Ostenso et al., 1965). Numerous studies over the past decades have been conducted on Gulkana Glacier (Baker et al., 2018; Van Beusekom et al., 2010; Josberger et al., 2007; March, 2000; Ostenso et al., 1965) establishing it as a USGS benchmark glacier. Although Gulkana's ice is thinner and warmer than the expected ice shells of an icy ocean world in the outer solar system, the glacier provided an opportunity to study the seismicity and diurnal signal influence in an icy structural setting that mimics that of the frozen surface of these objects. Furthermore, a nearby weather station (USGS station 15478038) provided context for correlating seismically detected signals with local weather events. An ideal analog for Europa's interior would have a kilometers thick layer of ice overlying an ocean, with no atmosphere, and strong tidal forces tectonically perturbing the ice. While no perfect analog location for Europa exists on Earth, Gulkana's seismic environment and local ice/bedrock structure allowed us to test our instrumentation and analytical approaches in an ice-dominated physical environment that could be present at depth within the European ice shell.

3.2.2 Instrument Deployment

A field team of researchers from the University of Alaska Fairbanks, University of Arizona, University of Maryland, University of Washington Applied Physics Laboratory, and Silicon Audio began deployment on 7 September 2017. Our instrumentation consisted of a Trillium Posthole seismometer (TPH), four Trillium Compact (TC) seismometers, and

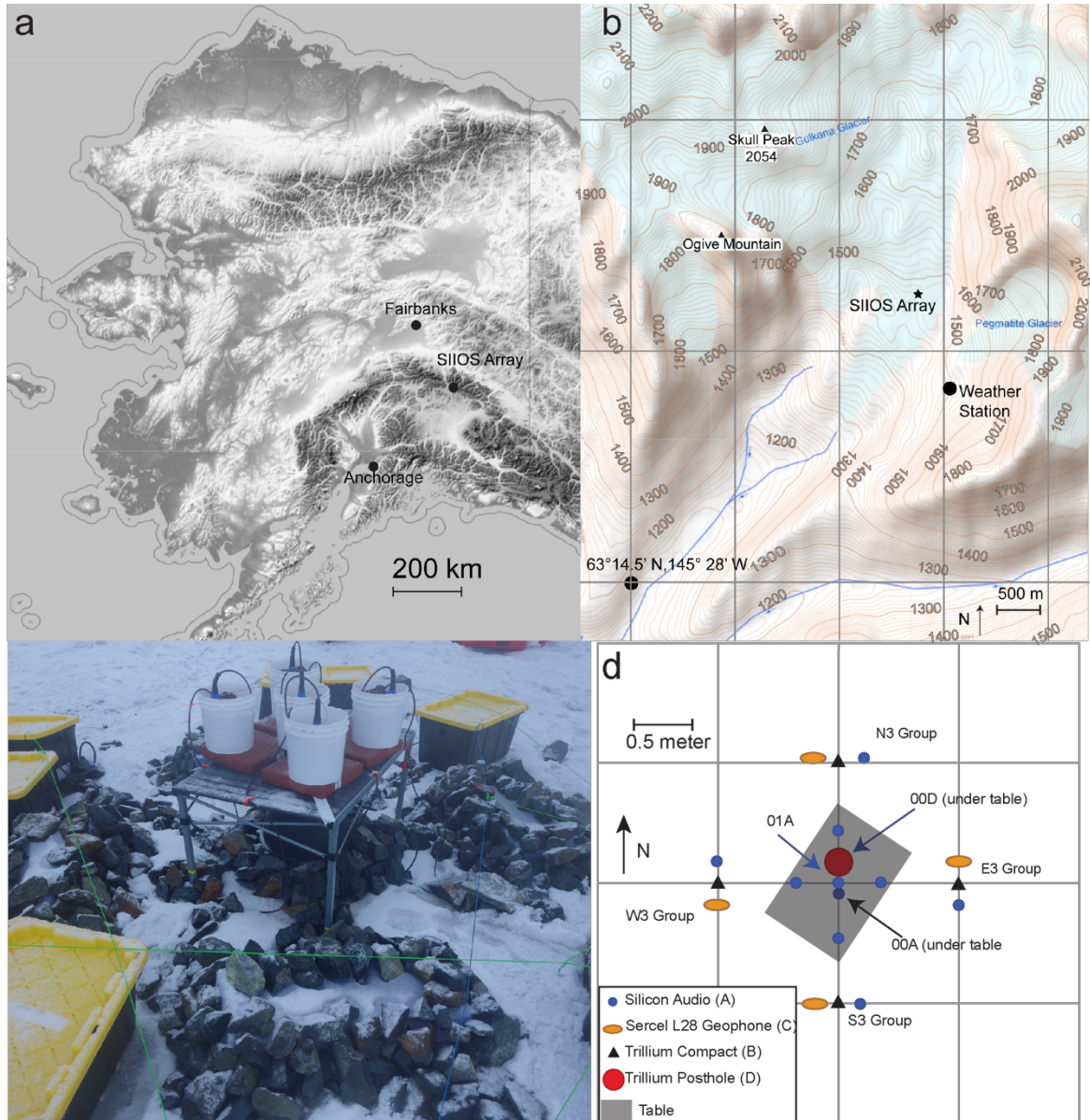


Figure 3.1. a) Map of Gulkana Glacier and SIIOS array site relative to Fairbanks, AK and Anchorage, AK. b) Local topography of Gulkana Glacier with coordinates of the center of the SIIOS array. The gray grid represents 1.5' spacing. Maps were generated using the National Elevation Dataset (Gesch et al., 2009) c) Photo taken in field of deployed equipment. Ground-based instrumentation are buried in sand, covered with a protective plastic vault, and then rocks are placed on top of the vaults. Yellow action packers held the Reftek recording units. Photo credit: N. C. Schmerr d) Schematic of photo in c) with stations labelled. Stations, 01AG/R, E2AG/R, N2A, S2A, and W2AG/R were placed in buckets on top of a mock-lander. The remaining instruments were placed on the ground and then covered by plastic vaults and rocks.

four Mark Products L28 Geophones lent by the Incorporated Research Institutions for Seismology Portable Array Seismic Studies of the Continental Lithosphere (IRIS-

PASSCAL) facility (Table 3.1). Four of the ten Silicon Audio sensors were programmed

Table 3.1 Station geometry relative to the center of the small-aperture array.

Station Name ¹	Easting (m)	Northing (m)	UTM Easting (m)	UTM Northing (m)	Lat (°N)	Lon (°W)	Final Azimuth ² (°)
00D	0	0.8	579657	7016330	63.267055	145.412750	350
00A	0	-0.2	579657	7016329	63.267047	145.412750	335
01AG*	0	0	579657	7016329	63.267048	145.412750	345
01AR [◊]	0	0	579657	7016329	63.267048	145.412750	345
E2AG*	0.35	0	579657	7016329	63.267048	145.412743	355
E2AR [◊]	0.35	0	579657	7016329	63.267048	145.412743	355
E3A	1.0	0.2	579659	7016329	63.267049	145.412710	330
E3B	1.0	0	579659	7016329	63.267048	145.412710	335
E3C	1.0	-0.2	579659	7016329	63.267045	145.412710	358
N2A	0	0.38	579657	7016329	63.267051	145.412750	335
N3AG*	-0.2	1.0	579657	7016330	63.267056	145.412753	350
N3AR [◊]	-0.2	1.0	579657	7016330	63.267056	145.412753	350
N3B	0	1.0	579657	7016330	63.267056	145.412750	15
N3C	0.2	1.0	579657	7016330	63.267056	145.412746	7
S2A	0	-0.42	579657	7016329	63.267044	145.412750	330
S3AG*	-0.2	-1	579657	7016328	63.267039	145.412754	346
S3AR [◊]	-0.2	-1	579657	7016328	63.267039	145.412754	346
S3B	0	-1	579657	7016328	63.267039	145.412750	352
S3C	0.2	-1	579657	7016328	63.267039	145.412747	350
W2AG*	-0.37	0	579657	7016329	63.267048	145.412757	340
W2AR [◊]	-0.37	0	579657	7016329	63.267048	145.412757	340
W3A	-1	0.2	579656	7016329	63.267050	145.412770	330
W3B	-1	0	579656	7016329	63.267048	145.412770	310
W3C	-1	-0.2	579656	7016329	63.267046	145.412770	340

¹Network Code: YH

²Starting Azimuths were due true north (0/360°) and are the value reported in the metadata

*Silicon Audios with high gain settings (Gain= 32 m/s²)

[◊]Silicon Audios with no gain settings (Gain= 1.53353 m/s²)

to record with unity gain (denoted with R) or high gain (G) simultaneously, resulting in one station producing 2 separate three-component data outputs (e.g. 01AG and 01AR). The instruments were deployed in a small-aperture array and five were placed on the top of a mock-lander (Fig. 3.1, Table 3.1). The small-aperture array consisted of four groups, each with a Trillium Compact, Silicon Audio, and L28 Geophone. We buried the instruments in a ~25 cm deep hole in the ice with a layer of sand between the ice and the instrument, and covered each group of instruments with a plastic vault to reduce the effects of wind and precipitation. Rocks were placed on top of the vaults to provide stability and create an insulating effect from winds and movement due to surface melting. Instruments on the mock-lander deck were placed in buckets and buried with sand. The buckets were placed on top of bricks, then placed on a table (Fig. 3.1c). The sand and buckets provided stability for the instruments, and the bricks added friction between the table and buckets to reduce sliding if the table became tilted.

We then performed an active source experiment on 9 September 2017. A 9 kg sledgehammer striking a 1.3 cm thick aluminum plate served as the active source. Timing for each of the hammer strikes was obtained using a GPS Synchronizer with a precision of 1-2 microseconds, along with GPS timing for the RefTek data recorders. We measured the location of each source relative to the center of the small-aperture array using a handheld laser-range finder and found the azimuth to the array with a Bruton compass. We conducted the active source experiment over 13 locations (Fig. 3.2). At each location between nine and thirteen hammer strikes were executed, with timing captured by the GPS Synchronizer, to allow for the stacking of shots to improve signal-to-noise ratios. See Table 3.A.1 in the

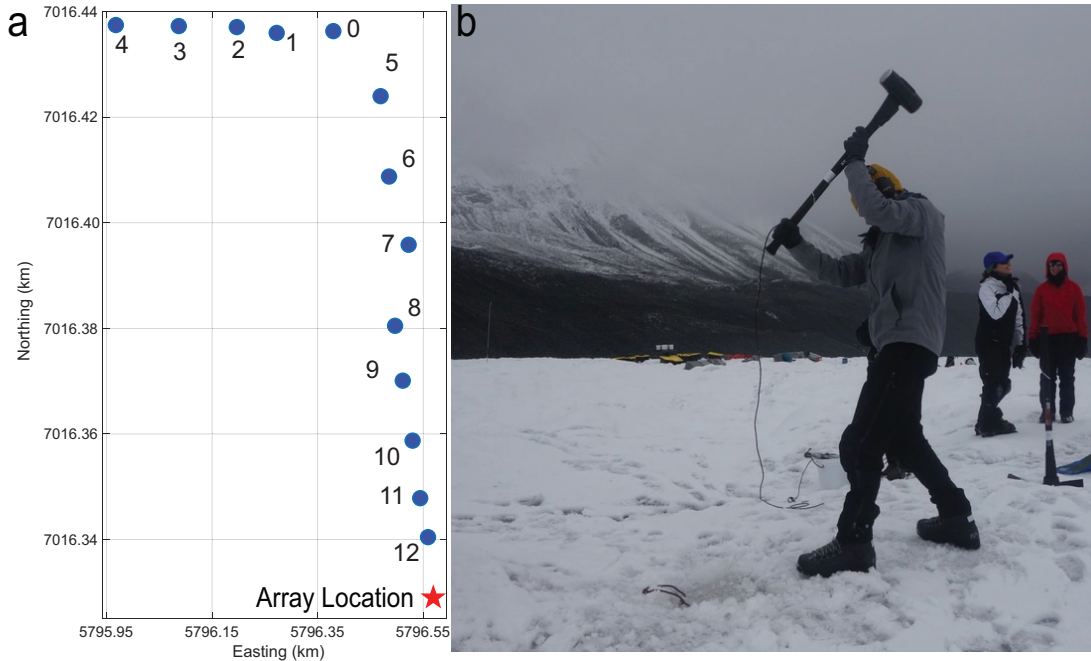


Figure 3.2. a) Position of each active source location (blue circle) relative to the center of the array (red star). Grid shows 20 m spacing. The active source locations are labelled and correspond to the numbering system in Appendix, Table 1. b) Photo of active source experiment courtesy of Nicholas Schmerr. A 9.1 kg sledgehammer striking a 1.3 cm inch aluminum plate serves as the seismic source.

appendix which contains details on the locations, timings, and number of hammer strikes of the active source experiment.

The passive recording portion of the experiment lasted 13 days spanning 10-22 September 2017. For details on the operational length for each instrument see Table 2. The instruments were retrieved from the field on 22 September 2017 by UAF students. The conditions (orientation, tilt, any damage, etc.) of the instruments were recorded upon retrieval. All but four of the instruments were still recording. Upon demobilization, four instruments had recently stopped recording due to power loss (Table 3.2).

The passive recording portion of the experiment lasted 13 days spanning 10-22 September 2017. For details on the operational length for each instrument see Table 3.2. The instruments were retrieved from the field on 22 September 2017 by UAF students. The

conditions (orientation, tilt, any damage, etc.) of the instruments were recorded upon retrieval. All but four of the instruments were still recording. Four instruments had recently stopped recording due to power loss (Table 3.2).

3.2.3 Data Quality and Availability

Data were recorded continuously from ~04:00 9 September through ~19:00 22 September 2017 UTC. Data from the experiment are available under the network code YH and are archived at the IRIS Data Management Center (IRIS DMC). All stations were set to record continuously with a sampling rate of 1000 Hz. As we were interested in understanding what signals would be recorded by different instrumentation across a range of frequencies, we used a suite of instrument types in the small-aperture array. The response functions of each instrument can be viewed in Fig. 3.3 (Thomas & Frechette, 2003). The Trillium Compacts have the highest sensitivities (along with the Posthole) at long periods, but the Silicon Audio instrumentation have greater sensitivity at high frequencies. Occasionally, due to site conditions, the GPS satellite lock was lost, resulting in gaps in timing. The data gaps were short lived and in some cases were less than 1 sampling interval (0.001 s) and did not affect the overall quality of the data. cases were less than 1 sampling interval (0.001 s). This was a rare occurrence and did not affect the overall quality of the data.

The demobilization team recorded any changes to the environment between deployment and retrieval. During initial data quality checks, while the deployment team was still in the field, a tilt was detected in the Trillium Compacts beyond design specifications (tilt angle $< \pm 2.5^\circ$)(Nanometrics, 2015), and was corrected by re-leveling

Table 3.2 Description of operational days, instrument type, sampling rate, and component for each station in our array.

Station Name^{1,2}	Operational Days in Sept 2017	Instrument Type	Saturation	Components
00D	08-23	Trillium Post Hole 120	Dry	FH1, FH2, FNZ
00A	08-23	Silicon Audio	Dry	FN1, FN2, FNZ
01AG*	09-21	Silicon Audio	Damp	FN1, FN2, FNZ
01AR[◇]	09-23	Silicon Audio	Damp	FN1, FN2, FNZ
E2AG*	09-22	Silicon Audio	Damp	FN1, FN2, FNZ
E2AR[◇]	09-23	Silicon Audio	Damp	FN1, FN2, FNZ
E3A	09-23	Silicon Audio	Damp	FN1, FN2, FNZ
E3B	09-23	Trillium Compact	Damp	FH1, FH2, FHZ
E3C	09-23	Mark Products L28 Geophone	Saturated	GH1, GH2, GHZ
N2A	09-23	Silicon Audio	Damp	FN1, FN2, FNZ
N3AG*	09-23	Silicon Audio	Saturated	FN1, FN2, FNZ
N3AR[◇]	09/23	Silicon Audio	Saturated	FN1, FN2, FNZ
N3B	09-23	Trillium Compact	Saturated	FH1, FH2, FHZ
N3C	09-23	Mark Products L28 Geophone	Saturated	GH1, GH2, GHZ
S2A	09-20	Silicon Audio	Damp	FN1, FN2, FNZ
S3AG*	09-23	Silicon Audio	Saturated	FN1, FN2, FNZ
S3AR[◇]	09-23	Silicon Audio	Saturated	FN1, FN2, FNZ
S3B	09-23	Trillium Compact	Saturated	FH1, FH2, FHZ
S3C	09-23	Mark Products L28 Geophone	Saturated	GH1, GH2, GHZ
W2AG*	09-23	Silicon Audio	Damp	FN1, FN2, FNZ
W2AR[◇]	09-23	Silicon Audio	Damp	FN1, FN2, FNZ
W3A	09-20	Silicon Audio	Damp	FN1, FN2, FNZ
W3B	09-23	Trillium Compact	Damp	FH1, FH2, FHZ
W3C	09-23	Mark Products L28 Geophone	Damp	GH1, GH2, GHZ

¹Network Code: YH

²All instruments recorded with a sampling rate of 1000 Hz

*Silicon Audios with high gain settings (Gain= 32 m/s²)

[◇]Silicon Audios with no gain settings (Gain= 1.53353 m/s²)

the instruments. Notably, Trillium Compacts are not self-centering and require manual leveling. The following day, the team found that this tilt was continuing, with the re-leveled instruments once again tilting in the local glacial environment. The team suspected that the instruments would continue to tilt after leaving the site. Upon returning to the site, the demobilization team found that most of the ground-based instruments were in water-

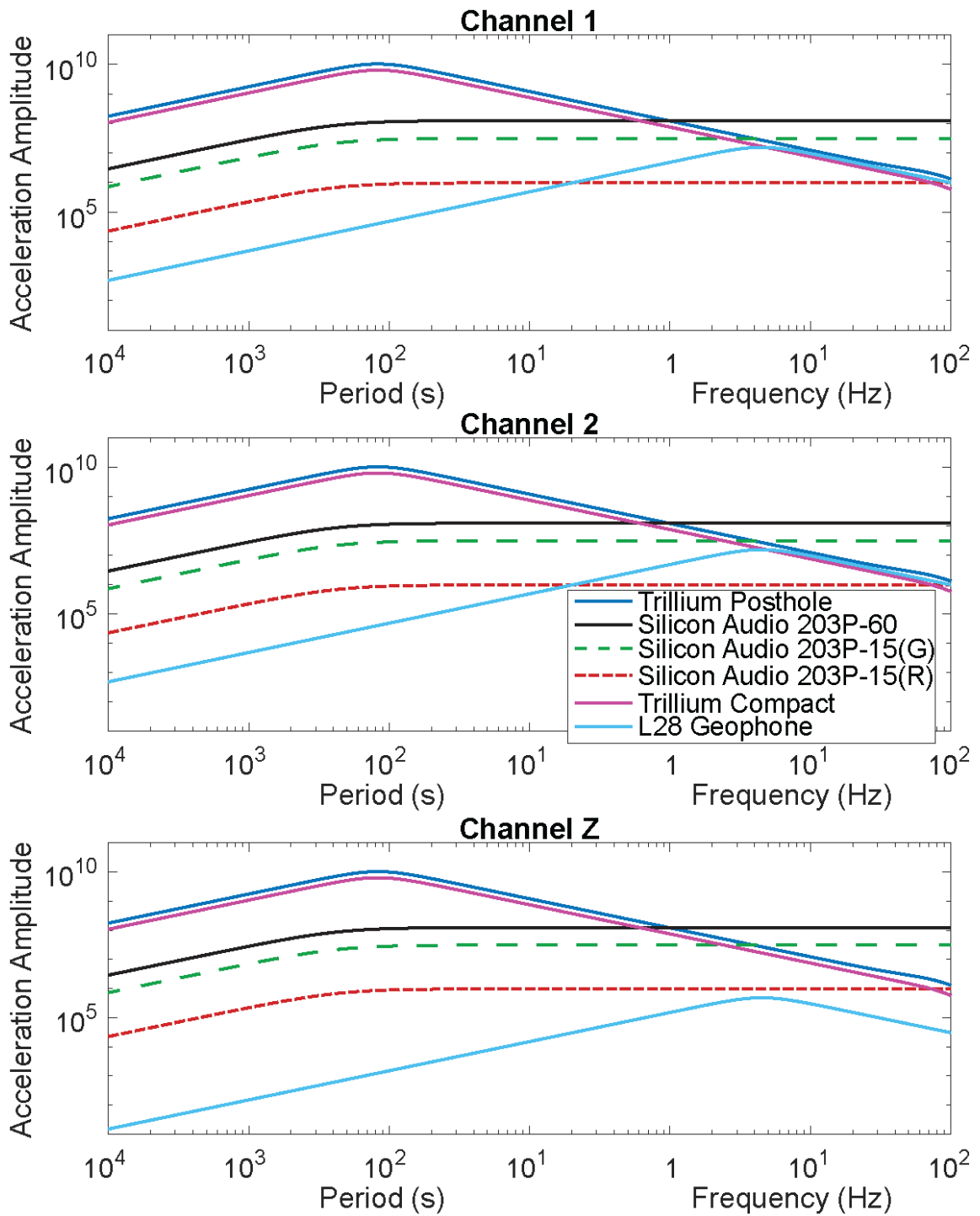


Figure 3.3. Instrument responses showing acceleration amplitude for the instruments deployed on Gulkana Glacier. The Trillium Posthole and Trillium Response functions were generated using metadata provided by IRIS DMC and JEvalResp, an open Java based code (E. Thomas & Frechette, 2003).

saturated sand, with the water level visible when the instruments were removed from the sand. The instruments on the table were in damp sand. The retrieval team found that the table serving as the mock-lander had also tilted, causing some of the bricks and buckets to slide toward the edge of the table. Likewise, they found that most of the ground-based instruments became tilted over the duration of the experiment, with the Trillium Compacts exceeding their tilt tolerance, although they continued to provide data. The Trillium Posthole (00D) was the only instrument that remained level, and station 00A (Silicon Audio) was only slightly tilted toward the south, downslope of the glacier. The remaining stations were primarily tilted downslope except for station N2A, a Silicon Audio, which tilted west, and station N3C, a Mark Products L28 Geophone, and station S3A, a Silicon Audio, that tilted east. In addition to tilting, all instruments underwent some rotation over the duration of the experiment. The original azimuths were set to true north ($0/360^\circ$) using a Brunton compass. The final azimuths, also measured with a Brunton compass during demobilization, are presented in the final column of Table 3.1. Some instruments were rotated by less than 5° , many by less than 15° , and at most by 50° .

The tilt and rotation experienced by many of the stations was detrimental to the recording quality of both the horizontal and vertical channels. In particular, the Trillium Compacts record in the Galperin arrangement, using channels UVW, with the vertical component consisting of a blend of the channels. Thus, having one axis beyond specification range affects both the horizontal and vertical components. All but one of the Trillium Compacts exceeded the dynamic range for two channels. By 17 September, all the Trillium Compacts had at least one channel cease to record useable data. Apart from the 2nd channel for N2A, all of the Silicon Audios placed on the mock lander, which

underwent the most tilt, were able to record on all 3 channels for the duration of the experiment. Stations 00A, N3AR, and W3A recorded on all 3 channels for the entire passive experiment. Stations E3A, N3AG, S3AG/R stopped recording useable horizontal data prior to end of the experiment. Figures 3.A.2 and 3.A.3 contain the power density functions for the horizontal components and the time and date at which the horizontal channels stopped recording useable data.

The effects of the tilt and rotation on the vertical channels are exhibited in Figure 3.4 where 3 out of 4 Trillium Compact instruments (Fig. 3.4a-d) show flat background noise measurements between 10s and 10 Hz. The L28 geophones (Fig. 3.4e-h) were less affected by instrument tilt. We infer that the short and elongated physical shape of the geophones helped mitigate them against tilt and rotation effects, while the vertical cylindrical shape of the other instruments did not protect them from these effects.

To evaluate the sensitivity and noise conditions at the Gulkana experiment, we compared the instrument noise level performances to those of the New High Noise Model (NHNM) and New Low Noise Model (NLNM) (Peterson, 1993) by calculating the probability density functions of the power spectral density of each instrument. The L28 geophones noise levels were consistently at or above the NHNM (Fig. 3.4e-h). At long periods (> 1 s) the geophones recorded noise ~ 75 dB higher than the NHNM. The Trillium Posthole seismometer, station 00D, (Fig. 3.4i) recorded noise mostly between the NHNM and the NLNM. Silicon Audios on the ground (Fig. 3.4j-p) recorded noise at similar levels to the Trillium Posthole at periods below 3 s. At longer periods, Silicon Audio, instrumentation recorded noise levels ~ 50 dB higher than the Trillium Posthole (Fig. 3.5a). Notably, stations coupled to the ground had lower background noise (up to 50 dB) than the

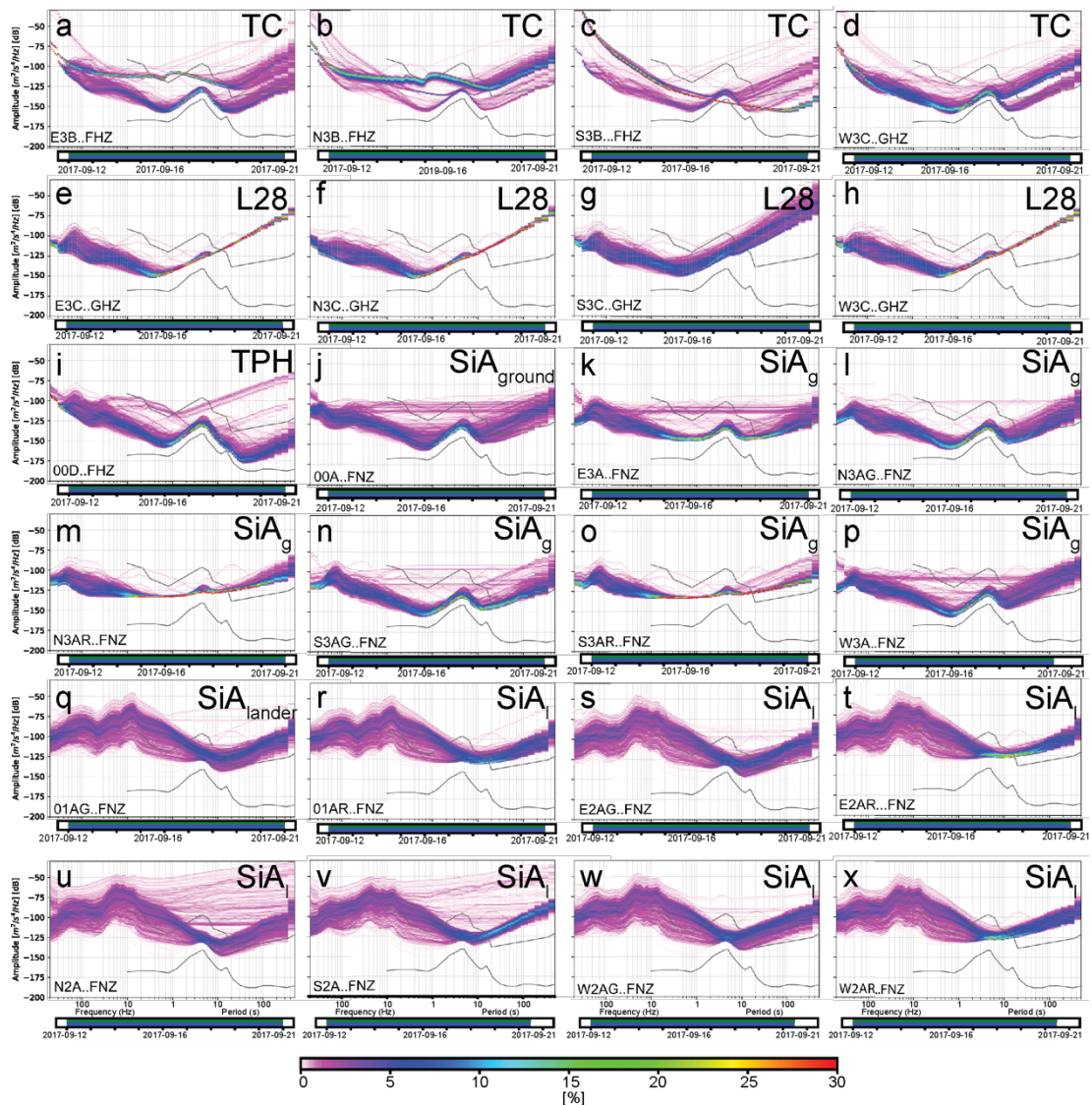


Figure 3.4. Instrument Noise Performance. A time period of 12-20 September 2017 was used to calculate the Power Density Functions (PDFs) based on Power Spectral Densities (PSDs) for the vertical component (McNamara & Buland, 2004). The time segments were divided following the approach of McNamara and Buland, 2004 and correspond to roughly 17 minutes each. The color bars indicate the likelihood of the noise occurring at each period. The colorbar saturates at 30% meaning a value greater than 30% is represented by red. The solid gray lines are the new high noise model (NHHM) and new low noise model (NLNM)(Peterson, 1993). Plots were generated using ObsPy's PPSD code (Beyreuther et al., 2010).

instruments placed on the mock lander (Fig. 3.4q-x) particularly at high frequencies (~10 Hz) (Fig. 3.5a). At long periods (>10 s), the Silicon Audio instrumentation, regardless of

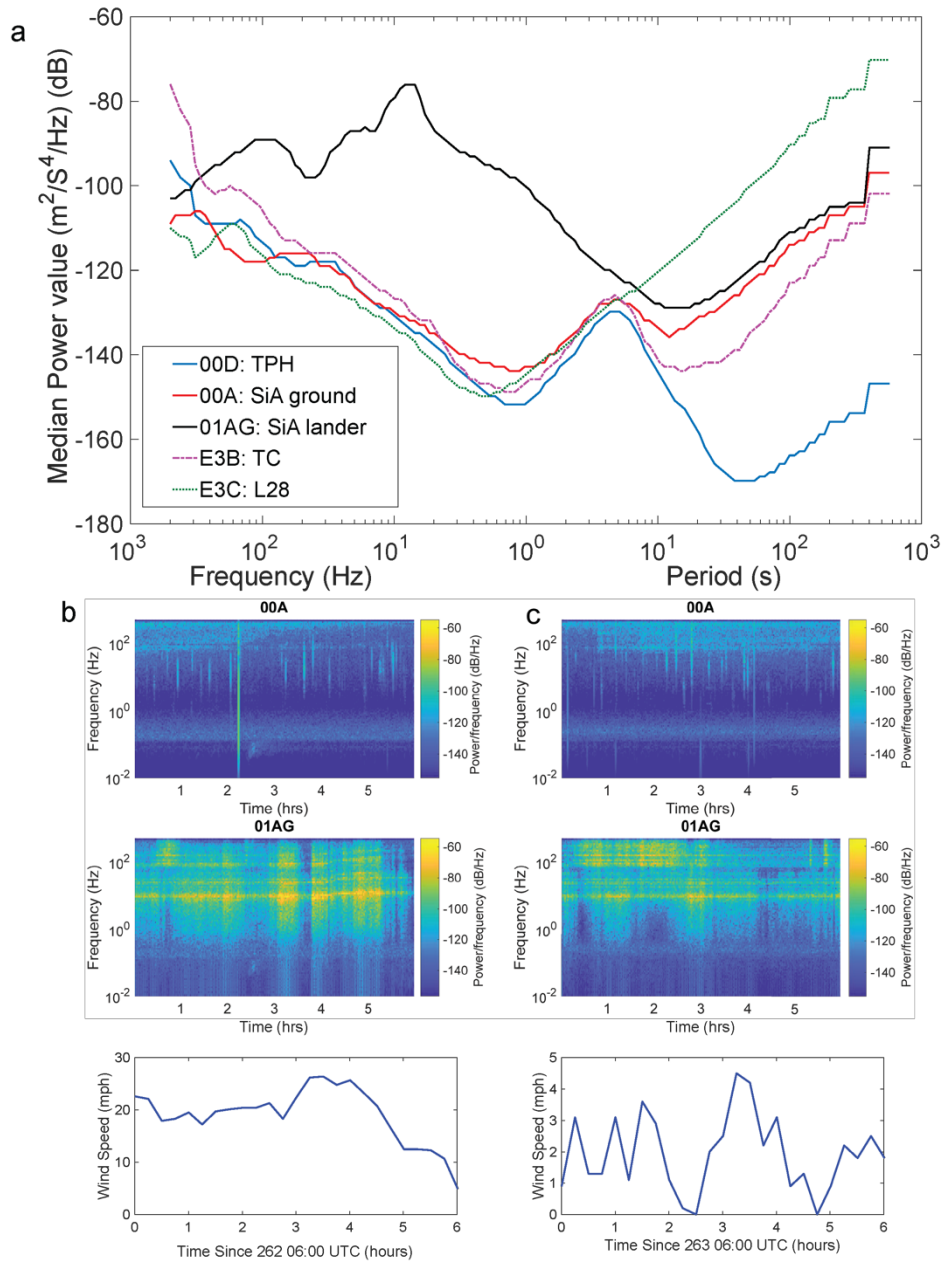


Figure 3.5. a) Median values of PSDs from Figure 4. The Trillium Posthole 00D (blue) is the most sensitive instrument at periods above 1 s. With the exception of the Silicon Audio coupled to the mock-lander (black), the instruments have comparable performance at frequencies above 0.3 Hz (below 3 seconds). Silicon Audios deployed on the ground (red) stay within 10 dB of Trillium Compacts (dashed purple) across all periods and frequencies. b) Example spectrogram of Silicon Audio on the ground (top) and on the mock-lander (middle) during a period of high-wind (bottom). Table resonance can be seen around 10 Hz. c) Example spectrograms during low wind speeds. Table resonances are still excited, but to a lesser extent. Wind speeds provided by USGS station #15478038.

placement, performed comparably to Trillium Compacts (within 10 dB), and was ~50 dB noisier than the Trillium Posthole. This suggests the deck-mounted instruments were contaminated by noise at frequencies above 0.1 Hz. Presumably, instruments on the mock-lander were subjected to increased noise from wind (Dybing et al., 2019; Marusiak et al., 2019a), precipitation, and the motion and resonance of the mock-lander table. During periods of high wind (Fig. 3.5b), the instruments on the mock-lander demonstrably showed increased noise compared to the ground-based instruments. When wind speeds were lower, the instruments performed more comparably across most frequencies (Fig. 3.5c). The table resonance(s) are observed as the peaks around 10-100 Hz. Overall, the ground-based flight-candidate instruments performed as well as the Trillium Posthole (station 00D) at periods below 3 s, and comparable to the Trillium Compacts (Fig. 3.4a-d) at periods greater than 3 s (Fig. 3.5a).

3.2.4 Initial Observations

The small-aperture seismic array recorded numerous types of seismic events during its deployment. Examples of teleseismic, regional seismicity, and local seismicity are shown in Figure 6. Seismograms shown in Figure 6 are bandpass filtered using corners of 1-50 s, 0.02-1 s, and 1-500 s, for teleseismic, regional, and local events, respectively. We generated the spectrograms by calculating the short-time Fourier transform of unfiltered data spanning 200 s, 2 s, and 1 s for teleseismic, regional, and local signals, respectively.

Local signals dominated at high frequencies (>10 Hz) while regional and teleseismic events dominated at 1-50 Hz, and .001-0.1 Hz, respectively. The largest event was a M_w 7.1 earthquake that occurred near Ayutla, Mexico on 19 September 2017 (Fig. 3.6a). There were three additional teleseismic events with $M_w > 6.0$ that all occurred on 20 September 2017: A M_w 6.4 in Vanuatu, a M_w 6.1 south of New Zealand and another M_w 6.1 off the Japanese coast. In addition to large teleseismic events, the array detected smaller regional events (Fig. 3.6b). The National Earthquake Information Center, Preliminary Determination of Epicenters (NEIC PDE) catalog (Guy et al., 2015), indicates there were

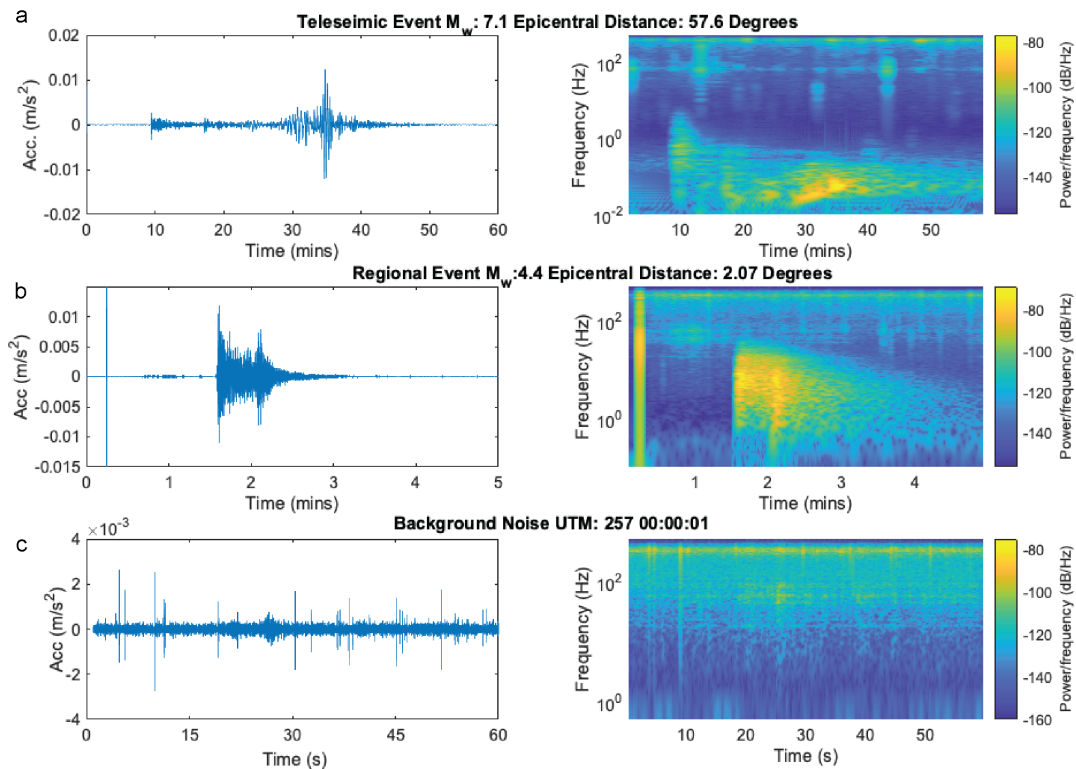


Figure 3.6. Examples of events recorded by station 00A, vertical component. a) The largest magnitude (M_w) event that occurred during deployment. Most of the energy is concentrated in frequencies below 1 Hz. b) An example of a regional event. The spike around 15 seconds is due to the instrument, not the event. The event's energy is concentrated between 1- 50 Hz. c) A sample of the background noise shows there are ~25 small local events that occur per minute. Around 25 seconds there is a possible rockfall or icequake. The background noise is most prominent at high frequencies > 100 Hz. The spectrograms for the regional and local events cannot resolve frequencies below 1 Hz due to the time window used to generate the spectrograms.

over 100 $M_w > 2.5$ earthquakes within 2500 km of our array during our deployment. Analysis on the detection rate of these events is currently under study. The array recorded many smaller but more frequent local events (Fig. 3.6c), source mechanisms for these events could include icequakes, rockfalls, and ice-water interactions like water flow in moulins and surface melt runoff. We estimate that station 00A, the central ground-based Silicon Audio, recorded roughly 20-25 potential high frequency local events per minute, totaling $\sim 300,000$ events over the duration of the passive experiment.

In addition to the passive experiment, we also collected data from the active source experiment. A distance-time moveout was made using the precise timings and measured

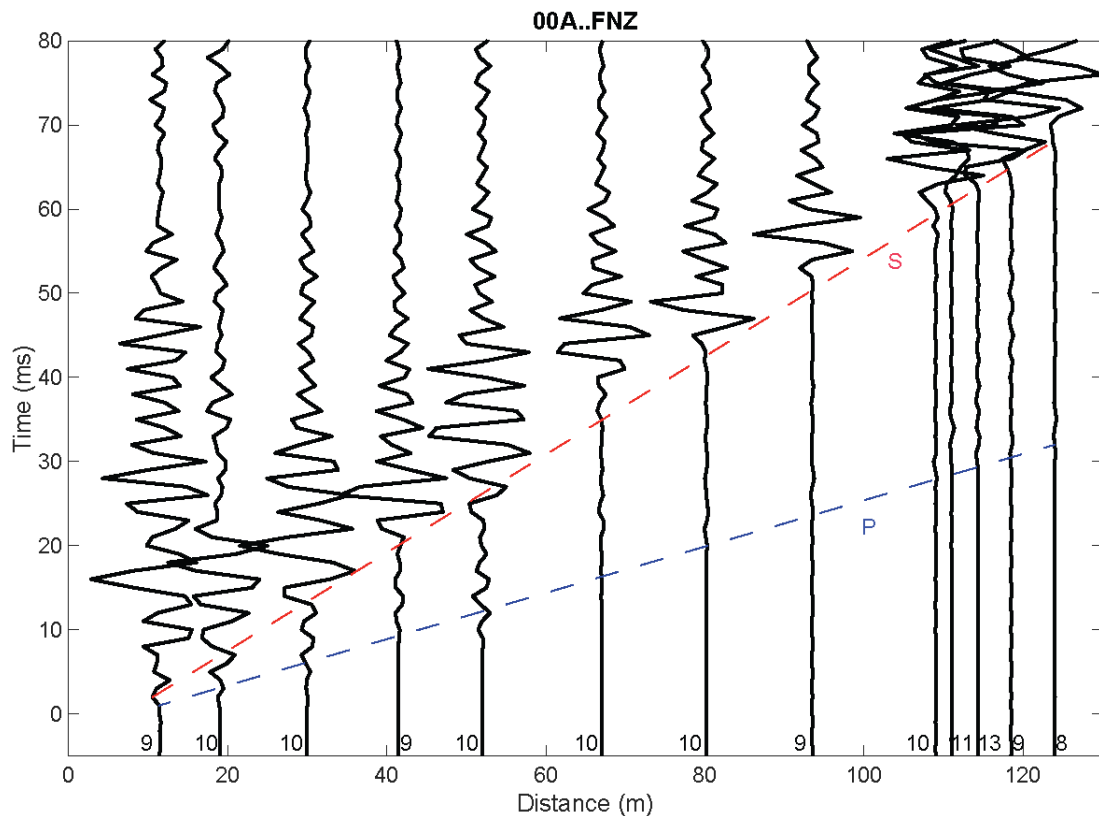


Figure 3.7. Example of the active source experiment distance-time moveout. The distance refers to the distance between the active source and the center of the array. The seismograms are a result of stacking individual shots (number next to seismogram along x-axis) and using acceleration. The instrument response has been removed but no filter was applied. Acceleration amplitudes have been normalized to the maximum value within the first 80 milliseconds.

locations of the events (Fig. 3.7). Both passive and active source tests were used to quantify the performance of the Silicon Audio instrumentation, compared to the other equipment, and quantify the science capabilities of the instruments placed on the mock-lander (Bray et al., 2017). For the active source experiment, the increased background noise degraded the signal-to-noise ratios for the instruments mounted to the deck. In some cases, we could not identify the active source generated body waves in deck-mounted seismometers. The added uncertainties in arrival times propagated to larger uncertainties in the recovered velocity structure resulting in uncertainties increasing by ~ 200 m/s for primary wave velocities (Marusiak et al., 2018a). Future and ongoing work with the active source will be used to determine the local structure of the ice and calibrate a location algorithm (Marusiak et al., 2019b).

3.2.5 Summary

The SIIOS field experiment recorded both active source and passive source experiments on Gulkana Glacier, Alaska in a simulated lander geometry while in an analog location for icy ocean worlds. We showed that our flight candidate seismometer performs comparably to other terrestrial-based instrumentation. We further show mock-lander-coupled instruments record up to 50 dB higher levels of background noise compared to their ground-coupled counterparts at frequencies above 1 Hz, although the source of this noise is primarily atmospheric effects and resonances within the mock lander structure. Surface conditions of the glacier including surface melt, saturation of sand, and motion of the glacier, caused several of our instruments to become tilted, degrading data quality. Flight-candidate instrumentation tended to have noise level performance comparable to Trillium Posthole Seismometer at periods below 3 s. At periods greater than 3 s, the Silicon

Audios noise level performance is comparable to Trillium Compacts, and lower than Mark Products L28 geophones. The results of our experiment have implications for future geophysical missions to ocean-worlds. Both the active and passive source experiment data will be used to quantify the science return of a small-aperture array for recovering local seismicity and structure of the ice versus a single-station seismometer. The data will further be used to quantify the disadvantages of placement of seismometers on top of or within a mock-lander.

3.3 Northwest Greenland

3.3.1 Analog Setting

We selected a site in Northwest Greenland north of Thule Air Force Base at approximately 78.06360° N and 68.43335° W (Fig. 3.8). Like Gulkana, the ice is thinner and warmer than an icy ocean world, but Greenland's ice is thick by terrestrial standards. At our field site the ice is approximately 800-950 m thick (Paden et al., 2010). Also, like Gulkana, we expected the seismicity of the Greenland site to mimic ocean worlds. A major difference with the Gulkana is the presence of a subglacial lake approximately 900 m below the surface (Bowling et al., 2019; Palmer et al., 2013). This lake acts as an analog for trapped liquid water within an icy shell. Due to our position near the ice divide, the ice velocity was less than 10 m a year (Joughin et al., 2018). In addition to the seismic studies, we also performed an Ice-Penetrating Radar (IPR), and GPS experiment. We also installed a weather station that recorded temperature, wind, and air pressure for the duration of the experiment. Our weather station recorded temperatures between $259 - 271^{\circ}$ K and wind speeds between 1- 25 mph.

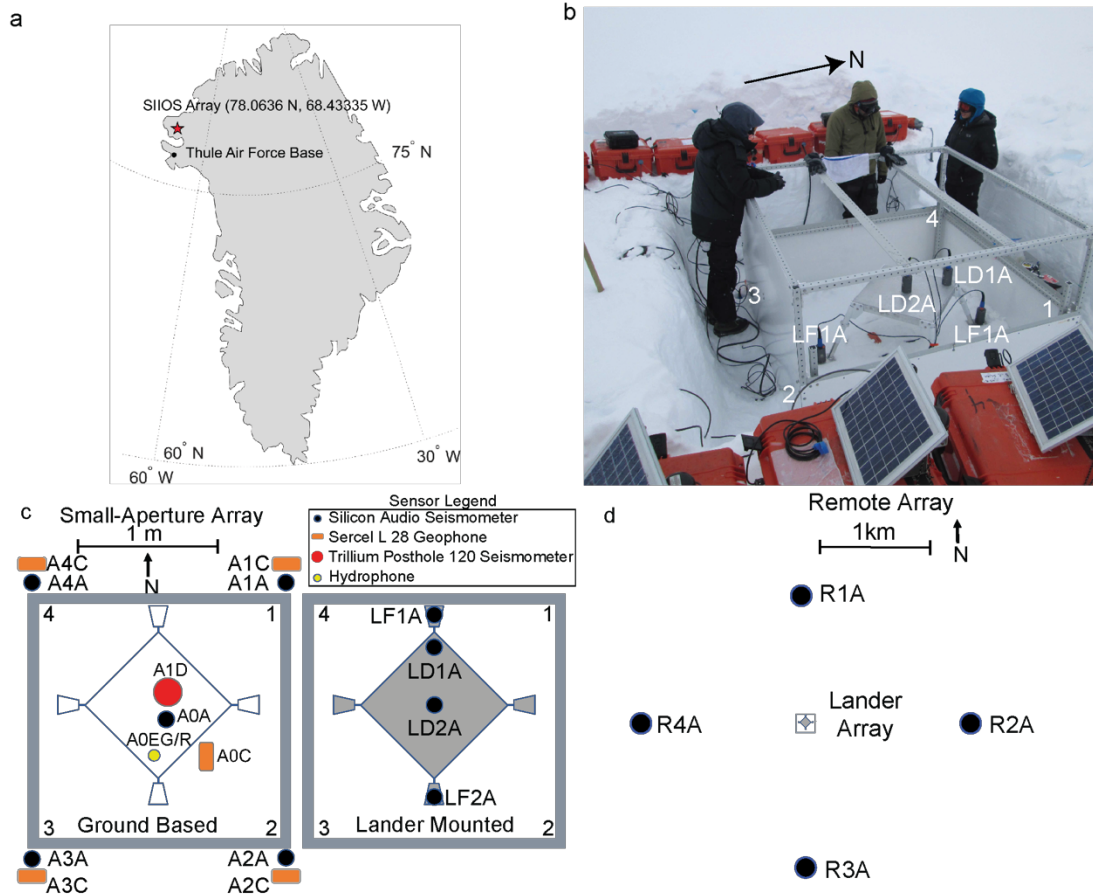


Figure 3.8 a) Map of SIOS's array location (red star) relative to Thule Air Force Base (black point). Coordinates are the location of the lander array. b) Image of the lander with station LD1A, LD2A, LF1A, and LF2A visible. Image credit: Susan Detweiler. c) Schematic of vault (gray box) with ground-based instrumentation (left) and instruments mounted to mock-lander (right). d) Remote array with instruments not and lander not to scale. We deployed 13 Silicon Audios (black), 5 geophones (orange), 1 hydrophone (yellow) and 1 Trillium Posthole (red).

3.3.2 Instrument Deployment

A field team deployed the SIOS array in Northwest Greenland on 01 June 01 2018. The instrumentation consisted of thirteen Silicon Audio seismometers, five Mark Products L28 geophones, one Trillium Posthole seismometer (TPH), and one High-Tech Inc 96 minute hydrophone. A mock-lander was placed at the center of the array. Two Silicon Audios were coupled to the legs of the lander, and another two were coupled to the deck

(Fig. 3.8). The remaining Silicon Audio were placed in a larger array, with each seismometer approximately 1 km from the center of the small array.

Station Name	Easting (m)	Northing (m)	UTM easting (m)	UTM northing (m)	Lat (°)	Lon (°)
A0A [†]	0	0	513087.350	8664481.630	78.05420	-68.43360
A0C	0.1	0	513087.450	8664481.630	78.05420	-68.43360
A0D	0	0.1	513087.350	8664481.730	78.05420	-68.43360
A1A [‡]	0.899	0.841	513088.249	8664482.471	78.05421	-68.43356
A1C	0.919	0.771	513088.269	8664482.401	78.05421	-68.43356
A2A [†]	0.889	-1.110	513088.239	8664480.520	78.05419	-68.43356
A2C	0.929	-1.010	513088.279	8664480.620	78.05419	-68.43356
A3A [‡]	-1.048	-1.110	513086.302	8664480.520	78.05419	-68.43365
A3C	-1.108	-1.010	513086.242	8664480.620	78.05419	-68.43365
A4A [†]	-1.048	0.728	513086.302	8664482.358	78.05421	-68.43365
A4C	-1.098	0.781	513086.252	8664482.411	78.05421	-68.43365
LD1A [†]	0	0.332	513087.350	8664481.962	78.05420	-68.43360
LD2A [†]	0	0	513087.350	8664481.630	78.05420	-68.43360
LF1A [‡]	0	0.791	513087.350	8664482.421	78.05421	-68.43360
LF2A [‡]	0	-0.567	513087.350	8664481.063	78.05419	-68.43360
R1A [†]	-4	1049	513083	8665531	78.06360	-68.43335
R2A [†]	984	89	514070	8664571	78.05491	-68.39102
R3A [†]	13	-932	513100	8663550	78.04585	-68.43345
R4A [†]	1002	58	512085	8664540	78.05481	-68.47697

Table 3.3 Station Name and Location for Greenland Array. UTM are accurate to the mm for the small array and to the meter for the remote array.

Unlike Gulkana, where the instruments were shielded only by a plastic vault, in Greenland we used an aluminum vault. We dug a hole that could fit the mock-lander, and all of the stations for the small-aperture array. The hydrophone, TPH, and center Silicon Audio were buried beneath the mock-lander. The mock-lander was designed and built by the University of Arizona to better mimic a plausible lander. Four Silicon Audios could be

directly coupled to the mock-lander, rather than sit on top or near it. Once the stations were installed, the vault was sealed and buried in snow. The combination of vault and burial insulated the instruments from thermal variations and wind noise.

We performed the active source test on 01 June 2018. Like Gulkana, we used a GPS Synchronizer to record timings to within 1-2 microseconds. The location of each source was measured relative to the center of the array. A 9 kg sledgehammer striking a 1.3 cm thick aluminum plate served as the source. We conducted the experiment at 10 locations (Fig. 3.9), with 10-12 shots occurring at each location. See Table 3.A.3 in this chapter's appendix for a list of the timings and location of each shot.

The passive experiment lasted approximately two weeks until the solar panels became buried beneath snow and stopped providing power. The instruments stopped recording on 13-18 June 2018. See Table 3.4 for the operational days for each instrument. Unlike Gulkana there was no tilting or rotations.

3.3.4 Data Quality and Availability

Data will be made available through the IRIS DMC using network code 9C (2018). Data were recorded continuously at 1000 Hz from 01 June 2018 until ~14 June 2018. The demobilization team noted the solar panels supplying power had become buried beneath snow. Some of the remote stations had power cords disconnected from the instruments. It is unclear when the disconnection happened. The instruments inside the aluminum vault were recovered without any major incidents. Unlike Gulkana, there was not significant tilting or rotation, nor were Trillium Compacts used, thus all three components recorded until power was lost. We compared the instrument noise performance to the NHNM and

the NLNM (Peterson, 1993) using the approach of (McNamama and Buland, 2004) (Fig.

3.10). The Trillium Posthole (TPH) was the most sensitive instrument. Silicon Audio

Table 3.4 Station Name with operation days, instrument type, and components recorded. Station Code 9C (2018). All stations recorded using a sampling rate of 1000 Hz.

Station Name	Operational Days in 2018	Instrument Type	Components
A0A	June 01- June 15	Silicon Audio	FN1, FN2, FNZ
A0C	June 01- June 15	Geophone	GH1, GH2, GHZ
A1D	June 01- June 13	Trillium Posthole 120	FH1, FH2, FH3
A0EG	June 01- June 15	Hydrophone	GDH
AOER	June 01- June 15	Hydrophone	GDH
A1A	June 01-J June 15	Silicon Audio	FN1, FN2, FNZ
A1C	June 01- June 15	Geophone	GH1, GH2, GHZ
A2A	June 01- June 15	Silicon Audio	FN1, FN2, FNZ
A2C	June 01- June 15	Geophone	GH1, GH2, GHZ
A3A	June 01- June 13	Silicon Audio	FN1, FN2, FNZ
A3C	June 01- June 13	Geophone	GH1, GH2, GHZ
A4A	June 01- June 15	Silicon Audio	FN1, FN2, FNZ
A4C	June 01- June 15	Geophone	GH1, GH2, GHZ
LD1A	June 01- June 13	Silicon Audio	FN1, FN2, FNZ
LD2A	June 01- June 15	Silicon Audio	FN1, FN2, FNZ
LF1A	June 01-June 15	Silicon Audio	FN1, FN2, FNZ
LF2A	June 01- June 13	Silicon Audio	FN1, FN2, FNZ
R1	May 29- June 18	Silicon Audio	FN1, FN2, FNZ
R2	May 30- June 13	Silicon Audio	FN1, FN2, FNZ
R3	May 30- June 14	Silicon Audio	FN1, FN2, FNZ
R4	May 30- June 15	Silicon Audio	FN1, FN2, FNZ

showed comparable noise levels at periods below 3 s. The aluminum enclosure and improved mock-lander improved the noise levels of on-deck instrumentation, compared to Gulkana. Instruments coupled to the lander showed a resonance around 100 Hz, but power at the remaining frequency ranges were within 10 dB. The instruments coupled to the legs were always within 10 dB of those on the ground. The remote stations were also comparable to the small-aperture array.

3.3.4 Initial Observations

The passive experiment was conducted for approximately 12 days spanning June 03 2018 until the instruments lost power around 13 June 2018- 18 June 2018. During that

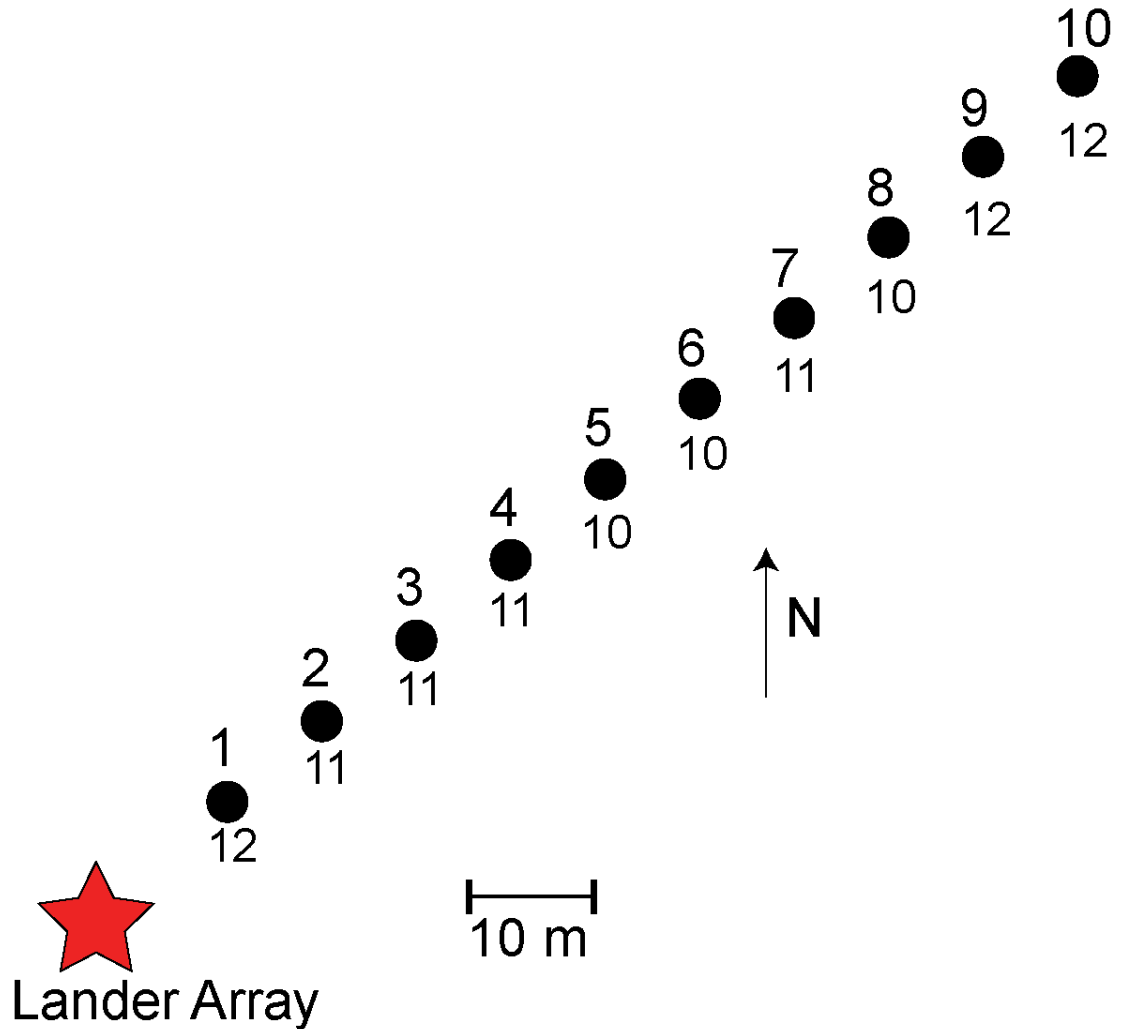


Figure 3.9 Active source experiment conducted at Greenland site. Each source (black circle) location was approximately 10 m away in the northeast direction from the previous location. The small number beneath the circle indicates the number of shots at each location.

time span, the array recorded various seismic signals. According to the NEIC catalog (Guy et al., 2015), the largest teleseismic event was a Mw 5.9 that occurred near Indonesia on 12 June 2018. Unlike Gulkana, which recorded numerous regional activity, the Greenland site only recorded ~ 5 events nearby, all with magnitudes < Mw 5 (Fig. 3.11a). For regional events, a bandpass filter of 0.02-1 second was applied. The subsequent spectrograms were calculated using the short-time Fourier transform of unfiltered data spanning 2 seconds. The regional signals dominant around 1 Hz.

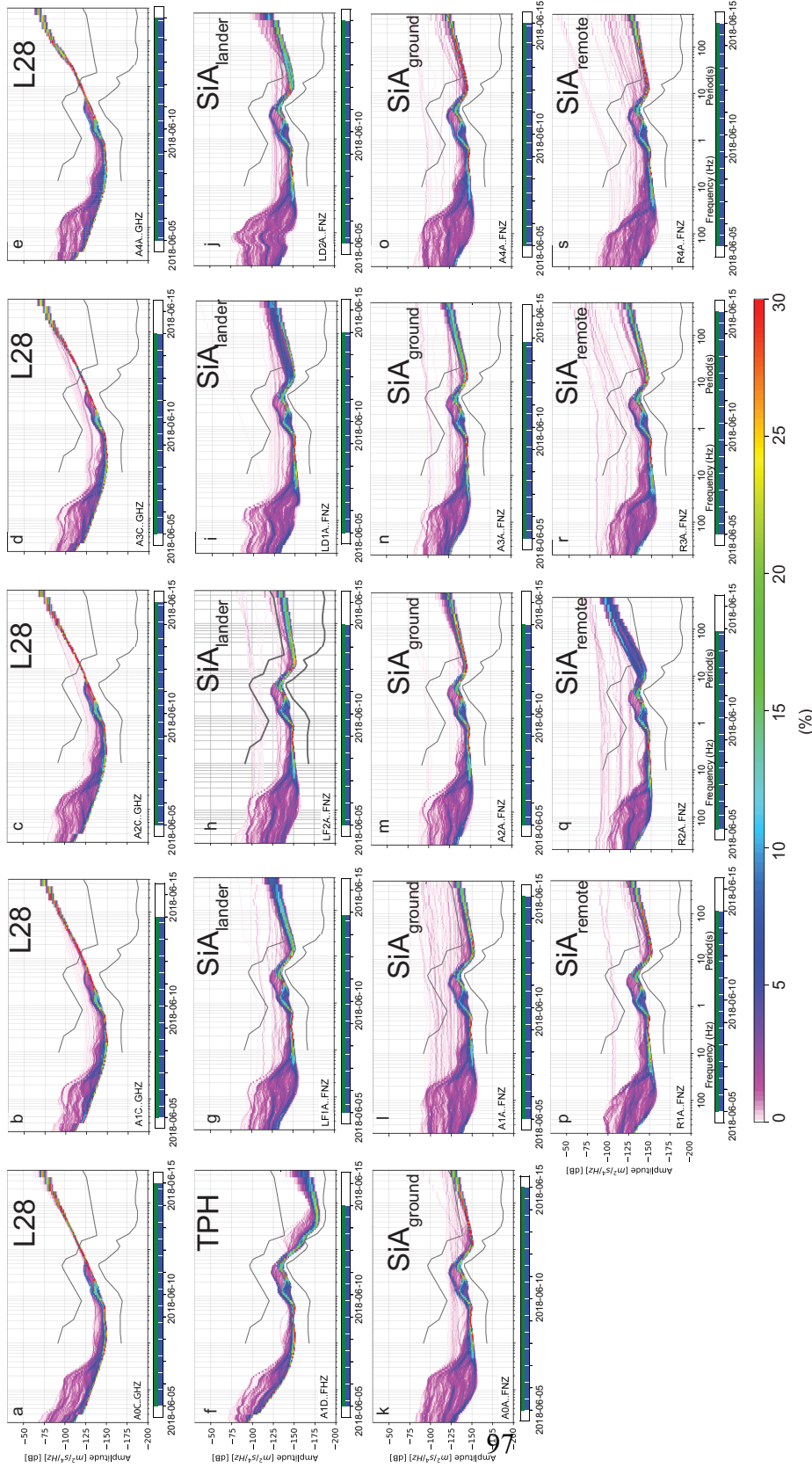


Figure 3.10. Power Density Functions (PDF) for vertical component of Greenland Array. Grey lines are NHNM and NLNM (Peterson et al., 2003). Probability saturates at 30%, meaning all values above 30% are red.

In addition to teleseismic events, the array recorded small local events (Fig. 3.11b). To generate this spectrogram, a short-time Fourier transform was calculated from unfiltered data spanning 1 second. Due to the vault, burial of array, and environmental conditions, the local events were not correlated with temperature. However, we did record a signal that was correlated with periods of high winds. These events showed strong spectral features around ~ 320 Hz which corresponds to the 4th harmonic of a 1 meter-long cylinder open at one end and closed at the other. The seismic signal was turned into an audio signal which confirmed that the signal was caused by the bamboo poles near the seismic stations. For details regarding the ambient signals see Chapter 4.

In addition to the passively recorded event, an active source experiment was conducted. A distance-time moveout (Fig. 3.12) can be used to quantitatively compare instruments, and constrain local structure (Marusiak et al., 2018b). Due to the low levels of background noise and better coupling to the mock-lander, compared to the Gulkana

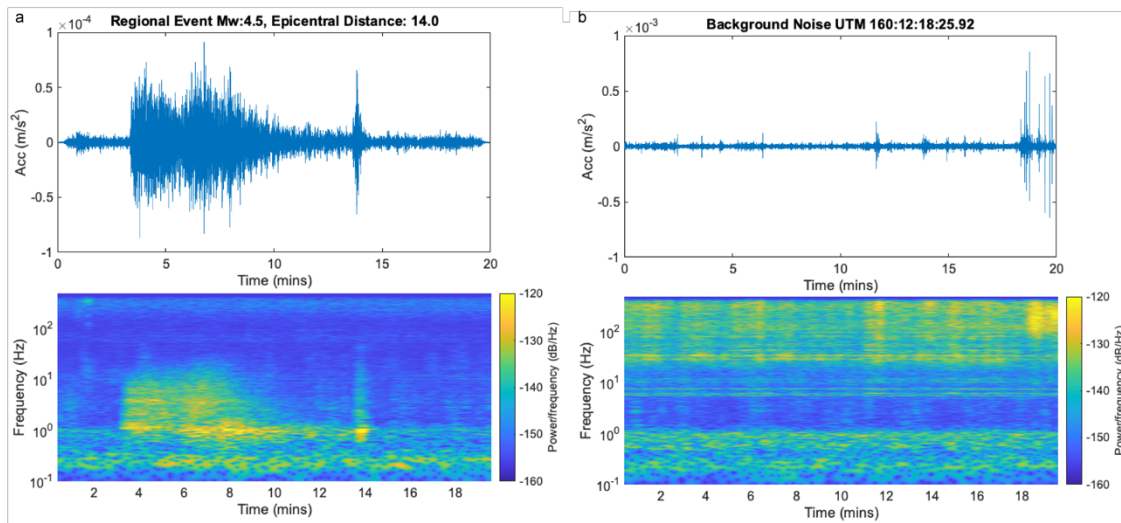


Figure. 3.11 a) example of a regional event in the time domain (top) and spectral domain (below). b) Example of background noise and local events. Wind-driven events are seen in the last ~ 2 minutes.

deployment, the instruments coupled to the mock-lander recorded signals with comparable

signal-to-noise ratios. P waves were relatively easy to detect, but S waves were more challenging as they are more easily scattered due to the properties of snow in the near surface. Picking arrivals could be performed for all stations, thus the recovered structures had very similar uncertainties (Marusiak et al., 2018b).

3.3.5 Summary

The SIOS experiment was able to successfully record active and passive source experiments on the Greenland ice sheet. Not only did the flight-candidate record comparably to traditional equipment, but the mock-lander coupled instrumentation were also able to perform comparably to ground-based instruments. With the exception of a resonance around 100 Hz, the deck-mounted instruments recorded within 5 dB of ground-based instruments. The increased quality compared to the Gulkana site is partially due to

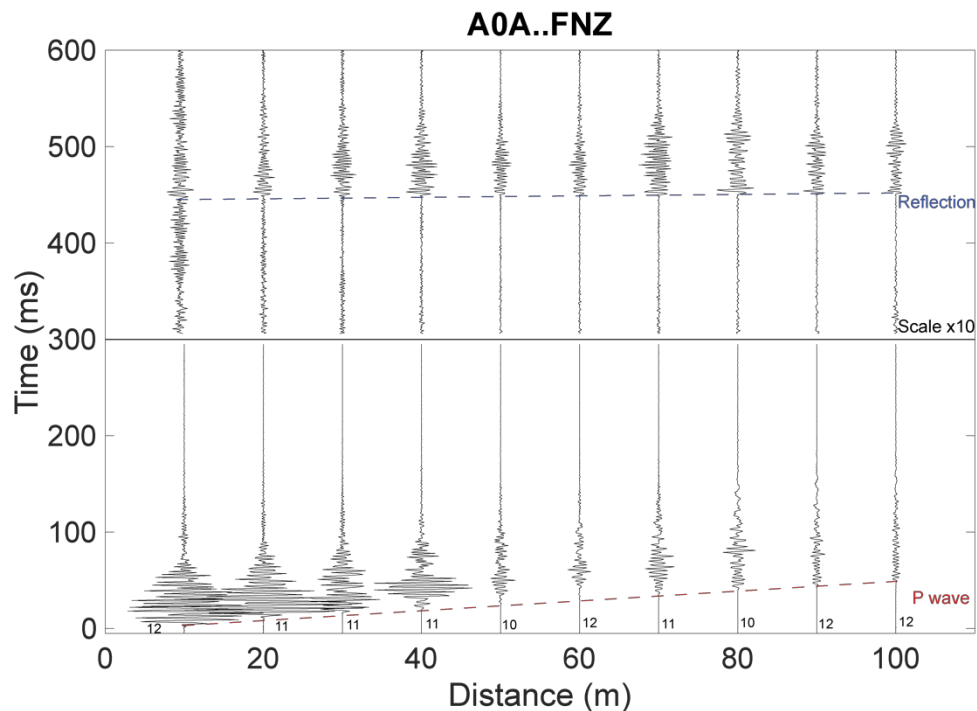


Figure 3.12. Active Source Moveout for Greenland deployment. The small number near the x-axis refers to the number of shots at each location. The first arriving P wave (red) was easily observed. After 300 ms the amplitudes are increased by a factor of 50. After this scaling the reflections off the lake (blue) are also observed.

the burial of instruments and enclosure within the aluminum vault. Improved coupling to the mock-lander likely also improved the signal-to-noise ratios. Lack of glacier movement also kept instruments level and unrotated, maintaining high quality data recordings until loss of power.

3.4 Data and Resources

Data can be obtained from the Incorporated Research Institutions for Seismology (IRIS) Data Management Center (DMC) using network code YH (2017) and DOI: https://doi.org/10.7914/SN/YH_2017 for Gulkana data and network code 9C (2018) for Greenland data. Maps and previous data on Gulkana are available through the USGS <https://www2.usgs.gov/landresources/lcs/glacierstudies/gulkana.asp>. Gulkana's weather data can be found via https://waterdata.usgs.gov/ak/nwis/uv?site_no=15478038. Data on the Greenland Environment, including ice thickness and elevation can be found on (<https://nsidc.org/data>, <https://doi.org/10.5067/GDQ0CUCVTE2Q>) and was last accessed in February 2020. Spectrograms and noise models were generated using the open source project, ObsPy (Beyreuther et al., 2010).

3.5 Summary

The results of our data analysis has important implications for future geophysical explorations of our solar system. While there have been some previous studies comparing deployments on mock landers versus ground placement (Panning & Kedar, 2019), and even using the InSight SEIS instrument while on Mars (Panning et al., 2020), these studies were not conducted for icy ocean worlds in an analog setting. By testing in two different analog settings, we were able to better understand the role of an atmosphere on seismic lander

deployments and how local seismic environment can also influence our science capabilities.

Gulkana Glacier was a better analog for a highly active environment with an atmosphere. The active seismic environment provided numerous signals and the opportunity to study many source mechanisms. Instruments deployed on Gulkana Glacier were able to record more tectonic earthquakes than Greenland partially due to a higher amount of global seismic activity, but also because our site was closer to a tectonic plate boundary. This allowed the instruments more opportunities to record regional events that may not be detectable at large distances.

Because our mock-lander instruments were exposed to the atmosphere, we could measure the detrimental reduction in signal-to-noise ratio. This is not the first time this phenomenon has been measured. The Viking missions to Mars carried two seismometers as part of their payloads. One seismometer failed to properly uncage, but the other was able to passively record. The working seismometer mostly recorded noise from the wind, the response of the lander, and one possible event (Nakamura & Anderson, 1979). The InSight mission to Mars recorded data while still on the lander deck, after initial ground deployment, and after the Wind and Thermal Shield (WTS) was deployed. The background noise recorded while on deck was significantly higher than the noise recorded on the ground, prior to the WTS deployment (Panning et al., 2020). It was shown that the noise levels were high enough that the SEIS instrument would not have been able to detect any of the events in InSight's current catalog had SEIS remained on deck. This finding agrees with our finding that our mock-lander stations at Gulkana recorded noise levels

significantly higher than ground-based stations. However, as Greenland shows, lander-based instrumentation can be useful in the right conditions.

By enclosing our instruments and burying them beneath the snow, we were successful in removing much of the background noise from wind itself and the lander's response to the wind. In this regard, Greenland is a better analog for an airless body and a landing site further from anticipated sources of seismic activity. Due to the quasi-random nature of earthquake occurrences, our instruments deployed on Greenland did not have the opportunity to record a large ($M_w > 6.0$) event. Our site was also far from plate boundaries which further reduced any opportunities to record smaller ($M_w < 4.0$) events but local events. However, because Greenland was a quieter site, we could record signals with relative high signal-to-noise ratios. When events did occur, they tended to be clearer than if they had been recorded at the Gulkana site. For an in-depth discussion of the detectability of tectonic events, see Chapter 4.

These results have important implications for future planetary missions. For airless bodies such as the Moon or Europa, a lander-coupled deployment could be viable. However, for an icy ocean world such as Titan, which has a thick atmosphere, a ground-based deployment would be required. The seismic signals recorded by future deployments will also be highly dependent on the local environment. For example, landing next to an active rift zone on Europa would likely lead to the detection of numerous events.

3.5 Acknowledgements

This project was supported by NASA PSTAR Grant #80NSSC17K0229 and NASA NESSF # 80NSSC18K1260. We thank the IRIS PASSCAL facility at the Instrument Center at New Mexico Tech, especially Pnina Miller and Noël Barstow, for

providing training on instruments and lending equipment to the project. We also thank Polar Field Services, Susan Detweiler, Emilie Sinkler, Ferderico Covi, and Andrew Johnson for their assistance in field logistics.

3.7 Appendices

Active Source Location No.	0	1	2	3	4	5	6	7	8	9	10	11	12
Distance To Array Center (m)	109	111	114.3	118.5	124	93.5	80.2	67	52	41.5	30	19	11.5
Azimuth (deg)	190	164.5	161	156	151	174	174	176	172	172	172	172.5	175
Latitude (N)	63.268014	63.268014	63.268025	63.268031	63.268034	63.267902	63.267765	63.267648	63.267648	63.267418	63.267315	63.267217	63.267151
Longitude (E)	-145.41307	-145.41329	-145.41344	-145.41366	-145.41389	-145.41429	-145.41288	-145.41281	-145.41281	-145.41284	-145.41281	-145.41279	-145.41276
Shot #	Time [s] since UTC 2017-253-21:50:00												
1	353.889543	2199.74072	2844.67945	3529.59491	4268.75404	5087.26934	5656.32877	6343.92023	6814.19982	7418.99216	7967.73782	8476.22421	8961.24836
2	1275.85945	2237.38953	2862.93172	3548.84947	4299.43463	5162.97552	5697.57092	6368.30108	6883.99362	7440.40693	7982.17358	8486.99989	8981.67732
3	1299.8771	2269.73454	2875.69679	3567.79796	4323.39301	5187.11638	5715.7468	6389.82634	6902.04743	7461.51278	7993.68028	8510.47761	8999.6874
4	1318.02716	2292.53711	2894.57889	3586.22698	4244.18779	5218.85213	5740.05663	6411.32813	6916.07424	7481.5586	8001.94758	8525.78605	9017.25998
5	1334.11583	2313.8733	2978.3497	3652.21685	4369.86154	5247.95537	5761.85066	6429.33687	6954.67124	7489.41864	8022.02801	8550.75328	9032.44053
6	1351.86053	2332.25968	2994.44998	3678.63663	4406.43286	5281.694	5778.29448	6443.35952	6966.05998	7521.01125	8032.69369	8566.9886	9057.66602
7	1363.35376	2342.35032	3015.50604	3695.02263	4421.75581	5306.84774	5796.8288	6457.57807	6987.64662	7540.42405	8045.38429	8583.88913	9072.70859
8	1384.4625	2365.47579	3065.33158	3766.9187	4438.22281	5339.88696	5837.09086	6482.69593	7005.81431	7558.92363	8059.42618	8599.03053	9092.01915
9	1410.79238	2389.4928	3081.76378	3785.4049	4454.17086	5368.83692	5903.55497	6499.38519	7019.51147	7580.60696	8076.1926	8613.50817	9118.3823
10	1438.31948	2421.35076	3115.06841	3805.43765	4480.04404	--	5931.55098	6512.33332	7036.92004	7659.52819	8101.89468	8622.53295	9127.27575
11	--	2443.63406	3130.00999	--	--	--	--	--	--	--	--	--	--
12	--	--	3149.35918	--	--	--	--	--	--	--	--	--	--
13	--	--	3165.8701	--	--	--	--	--	--	--	--	--	--

Table 3.A.1 Active Source Experiment Timings and Locations.

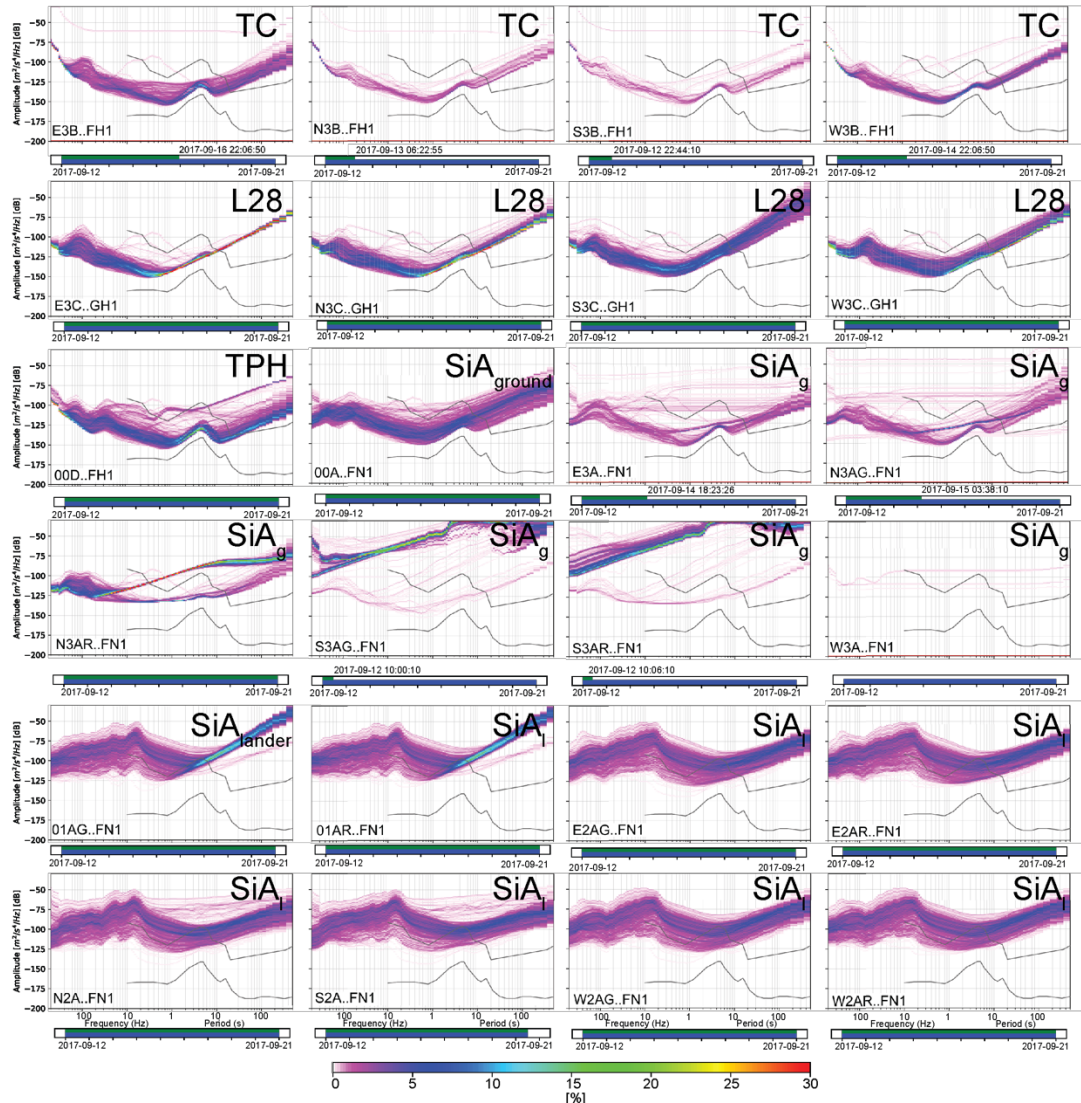


Figure 3.A.1 Component 1 Probability Density Functions. The first row are Trillium Compacts. The second row are L28 Geophones. The Trillium Posthole is the 1st plot of the 3rd row. The remaining 3rd and 4th rows are Silicon Audios that were deployed on the ground. The 5th and 6th rows are Silicon Audios placed on the table. The blue bar indicates the dates the instruments were on and collecting data. The green bar indicates the days that the component was within its dynamic range, properly recording signals. The text next to the green bar indicates the time and date that the instrument channel stopped reliably recording data.

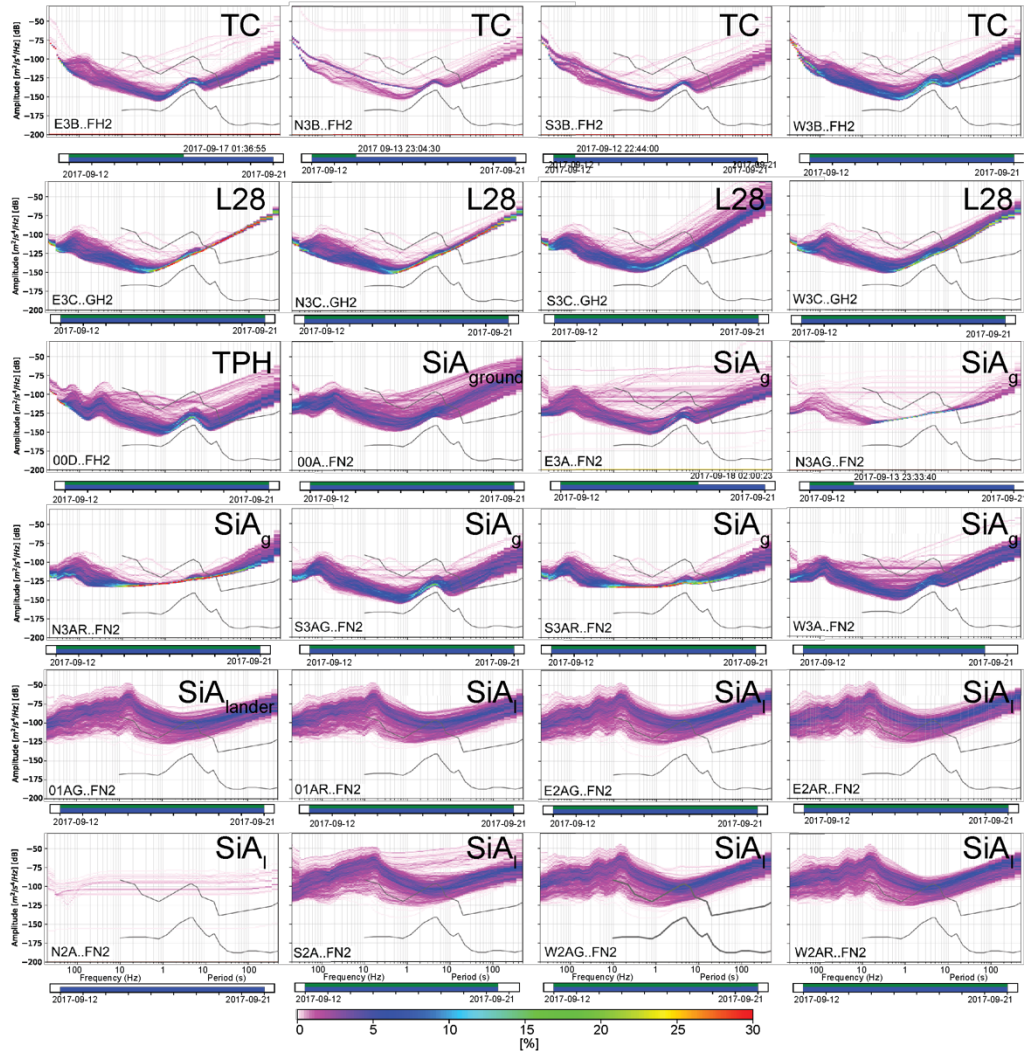


Figure 3.A.2 Component 2 Probability Density Functions. The first row are Trillium Compacts. The second row are L28 Geophones. The Trillium Posthole is the 1st plot of the 3rd row. The remaining 3rd and 4th rows are Silicon Audios that were deployed on the ground. The 5th and 6th rows are Silicon Audios placed on the table. The blue bar indicates the dates the instruments were on and collecting data. The green bar indicates the days that the component was within its dynamic range, properly recording signals. The text next to the green bar indicates the time and date that the instrument channel stopped reliably recording data.

Active Source Location Number	1	2	3	4	5	6	7	8	9	10
Distance to Array center (m)	10	20	30	40	50	60	70	80	90	100
Azimuth (deg)	45									
Latitude (N)	78.0543	78.0543	78.0544	78.0545	78.0545	78.0546	78.0546	78.0547	78.0548	78.0548
Longitude (E)	-68.4333	-68.433	-68.4327	-68.4324	-68.4321	-68.4318	-68.4314	-68.4311	-68.4308	-68.4305
Shot #	Time Since 01 June 2018 01:21:00.0000									
1	51.2175	649.6498	788.2228	942.3025	1088.6494	1264.2207	1454.9476	1634.3314	2002.3669	2002.3669
2	272.1571	655.7622	798.3735	949.4921	1095.6370	1269.7913	1460.8384	1640.1295	1849.9199	2017.9785
3	325.1733	661.7258	803.8616	956.6016	1100.9500	1275.5547	1466.6107	1645.1007	1855.5439	2030.9029
4	334.9175	668.0058	808.7156	963.6747	1106.5131	1280.9304	1472.6749	1650.4872	1864.8087	2042.1185
5	342.4236	674.9815	813.9662	969.5637	1112.6057	1286.5328	1478.7332	1656.2248	1870.1411	2054.5123
6	349.1723	681.5322	819.7674	976.0790	1118.3217	1292.5707	1485.3223	1662.2325	1875.9581	2064.5013
7	355.9836	687.8223	824.9899	983.2661	1124.0954	1300.0933	1492.4666	1668.2240	1882.0031	2073.8434
8	364.2631	693.4714	829.9784	990.1133	1130.1935	1315.3787	1498.9941	1673.6190	1887.7937	2083.4193
9	371.8770	699.0281	835.3942	996.8933	1137.0375	1321.5731	1505.5002	1678.9583	1893.3745	2094.2139
10	420.4359	715.5107	840.4510	1003.2166	1143.4159	1328.6854	1512.1024	1681.4942	1899.3513	2107.5101
11	427.7259	726.5590	861.8450	1010.4218	--	--	1522.5450	--	1905.0464	2198.4555
12	436.1484	--	--	--	--	--	--	--	1912.0914	2302.4095

Table 3.A.2 Active source experiment conducted on Greenland's ice sheet.

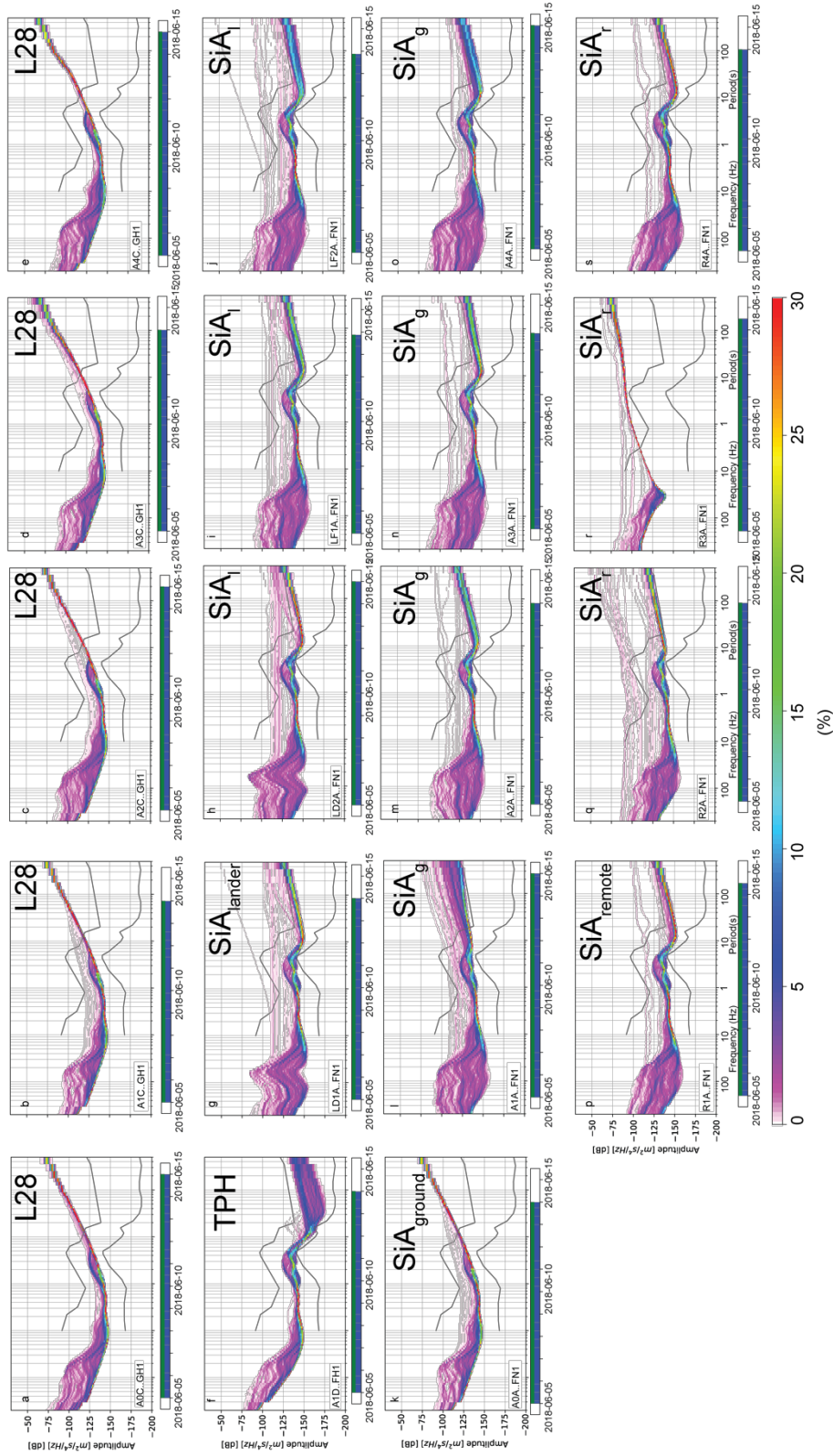


Figure 3.A.3. Power Density Functions for Component 1 for instruments deployed in the Greenland array.

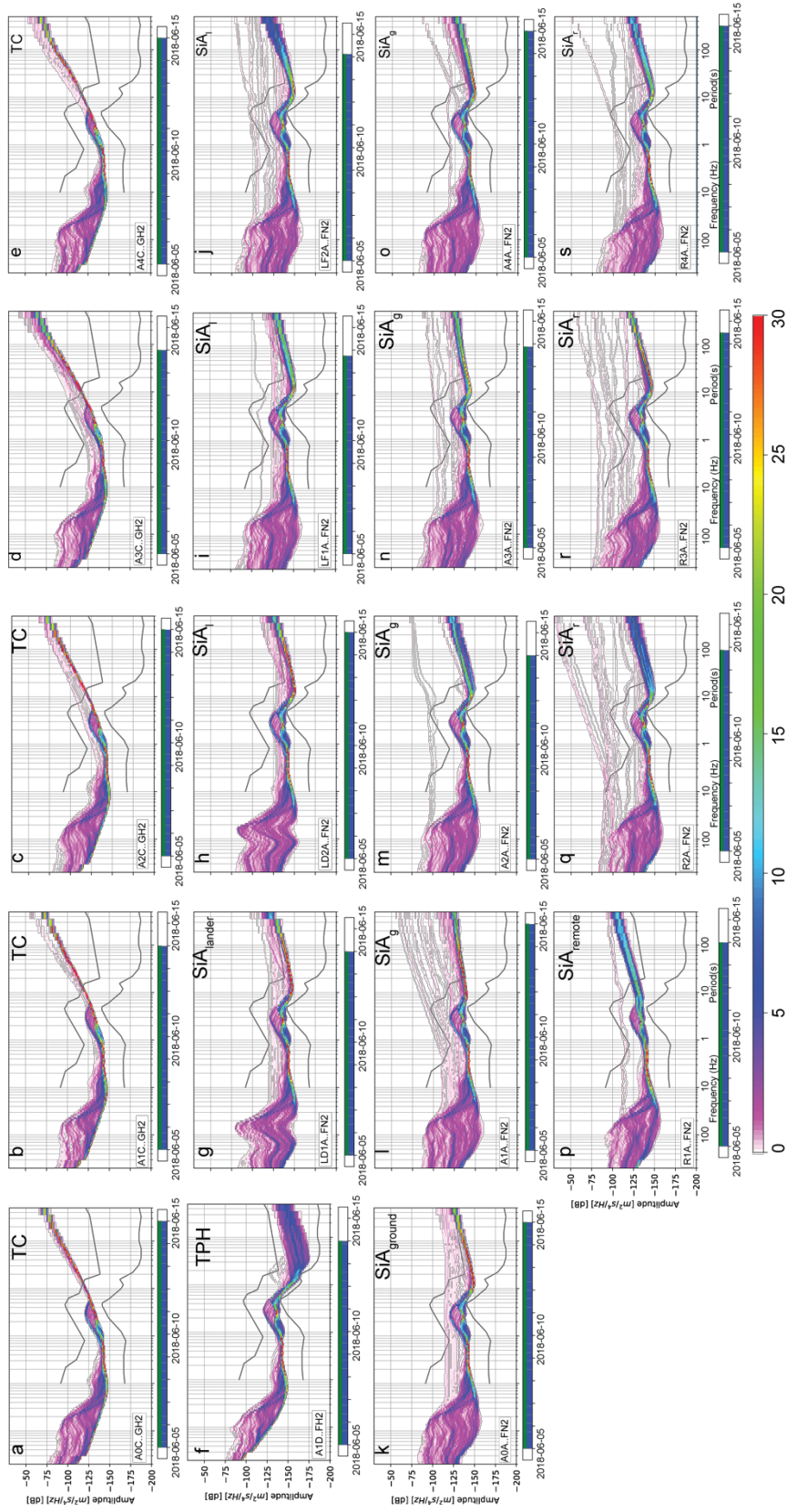


Figure 3.A.4. Power Density Functions for Component 2 for the Greenland Array.

Chapter 4: Detecting Passive Signals on Icy ocean World Analogs

Abstract

One major goal of an icy ocean world mission carrying a seismic payload, would be to measure global and local seismicity to determine where the ice shells are or are not active. Large events can further reveal global processes and help constrain deep interior structure while local seismicity reveals the behavior of the local environment and structure. In this chapter, I discuss some of the passively recorded signals observed at icy ocean world analog sites in the Alaska Range and in Northwest Greenland. The events were found in the passively recorded data using a Short-Term Average/ Long-Term Average (STA/LTA) technique. Detections of low-frequency events such as regional and teleseismic tectonic events were made using both a single-station and the small-aperture rays to quantitatively compare their detection capabilities. In addition to tectonic events, catalogs of high frequency (HF) and very high frequency (VHF) were created. The Alaskan site experienced a larger quantity of HF and VHF events than the site in Greenland. This is likely due to higher surface temperatures which fluctuated above and below freezing which allowed for increased moulin activity and surface runoff. Gulkana's SIIOS array was also located near a mountain range and closer to the glacier's terminus than the Greenland's array. The Greenland site had a higher rate of detection of tectonic events, likely due to the reduced background signal. At both sites, VHF events were detected using a template of events and a correlation technique. Cluster analysis of HF events compared differences in the waveform to categorized events. Polarization analysis constrained the azimuths from

which the different categories originated. Analysis of the VHF events suggests they were likely caused by bamboo poles near the seismic sensors at the Greenland sites, and a pole and tarped equipment left at the Gulkana site. Future missions to icy ocean worlds can use these techniques to detect, locate, and identify sources of seismic signals in their local environment. The signals can inform how the local structure responds to changes in the environment. The approaches can also be used to identify possible cultural effects from equipment, including the lander, near the landing sites.

4.1 Introduction

Icy ocean worlds are bodies in the outer solar system with thick ice shells overlying their subsurface oceans. Notable ocean worlds include Europa, Ganymede, and Callisto in the Jovian system, Enceladus and Titan in the Saturnian system, and the Pluto-Charon system. The ocean worlds come in a wide range of sizes from Enceladus which is only ~ 250 km in radius (Iess et al., 2010; Nimmo & Pappalardo, 2016), up to Titan, one of the largest moons in the solar system with a radius of ~ 2900 km (Smith, 1980; West et al., 1983). The internal structures of the icy ocean worlds also vary. Some bodies like Callisto or Ganymede have very thick ice crusts (>100 km) (Schubert et al., 2004b). Other bodies like Europa or Enceladus may have ice shells that are only several to tens of kilometers thick (Billings & Kattenhorn, 2005; Iess et al., 2014; Nimmo et al., 2003; Schubert et al., 2007, 2009). Larger moons like Titan may have multiple layers of liquid water and ice resulting in high-pressure ice layers (Sohl et al., 2003, 2010). While some moons like Ganymede are heavily cratered indicating old surface ages, some moons like Europa and Enceladus are more active and have younger surfaces (Zahnle et al., 2003).

A lack of craters on Europa, Enceladus, and Titan's surface suggests their surfaces are relatively young (Bierhaus et al., 2009). Additional evidence exists for their active surfaces. During Cassini flybys, plumes were seen erupting from Enceladus's southern pole (Porco, 2006). The Galileo mission imaged extensive faults on Europa's surface (Greeley et al., 2000). Both the faults and plumes are linked to tidal interactions between the moons and their host planets (Greeley et al., 2004; Greenberg et al., 2003; Rhoden et al., 2015; Sotin et al., 2009; Wahr et al., 2009). Tidal interactions in the form of diurnal cycles (Hoppa et al., 1999; Hurford et al., 2009) and non-synchronous rotation (Rhoden et al., 2012; Wahr et al., 2009) create stresses and tidal heating (Carr et al., 1998; Meyer & Wisdom, 2007; Roberts & Nimmo, 2008; Sotin et al., 2002, 2009; Tyler, 2008) in the ice shells. The stresses can manifest as strike-slip faulting (Prockter et al., 2000; Tufts et al., 1999) or normal faulting (Nimmo & Schenk, 2006) observed on the surface. Theories also suggest subsumption and convection may be possible within the ice shells (Bland & McKinnon, 2017; Kattenhorn & Prockter, 2014; Showman & Han, 2005), though this is disputed (Johnson et al., 2017). Tidal heating can also support liquid water oceans beneath their ice shells.

Icy ocean worlds have been listed as a top priority in the Decadal Survey (The National Academy of the Sciences, 2011) for several reasons. One is their potential habitability. Beneath their thick ice shells, lie subsurface oceans that could harbor life (Hand et al., 2009; Parkinson et al., 2008; Raulin, 2008; Reynolds et al., 1983). Tidal heating could help support long-lived oceans. The composition of observed plumes (Bouquet et al., 2015; Parkinson et al., 2008; Waite et al., 2017) and possible subsurface material on Europa's surface (McCord et al., 1999; Sohl et al., 2002, 2010) further suggest

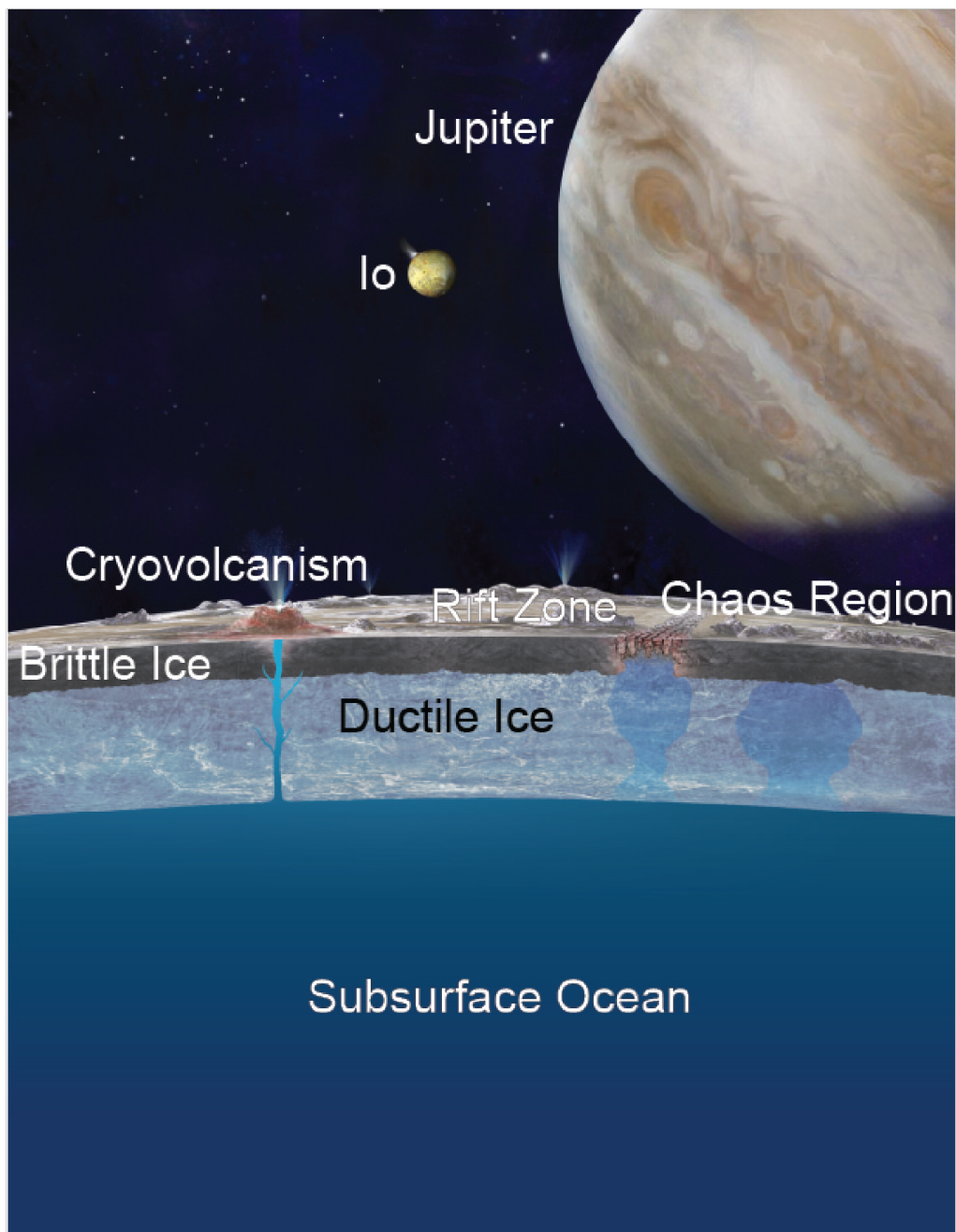


Figure 4.1 Image Credit: NASA/JPL. Possible interior structure of Europa. Seismic sources could be generated through cryovolcanism, faulting along rift zones, or during the break up of chaos terrain. Seismicity will likely occur only in the brittle regime of the ice shell.

habitable conditions exist in the subsurface oceans. Titan's observed atmospheric and surface composition from the Huygen's probe also suggests life could inhabit the subsurface (Raulin, 2008).

Another reason icy ocean worlds are intriguing is because they could be some of the most seismically active bodies in the solar system (Vance et al., 2018a). A future mission to an icy ocean world would investigate the seismicity of that body to better understand the response to tidal stresses and internally generated stresses (Figure 4.1). For example, events deep within the ice shell may indicate that subsumption is occurring (Bland & McKinnon, 2017; Katterhorn & Prockter, 2014; Katterhorn & Hurford, 2009). The events would also indicate where strike-slip or extensional faulting is actively occurring, and whether it agrees with current models (Hurford et al., 2020; Nimmo & Gaidos, 2002; Rhoden et al., 2012). Observed faults on Europa could have produced events with magnitudes above Mw 5.5 (Nimmo & Schenk, 2006; Panning et al., 2006; Vance et al., 2018a). A large teleseismic event might create multiple body wave orbits which can be used to determine the distance to event, even if the seismic velocity structure of the planet is not yet constrained (Bose et al., 2017; Khan et al., 2016; Panning et al., 2015). Numerous body waves might be observed which can help constrain internal layering such ice-ocean, ocean-mantle and other internal boundaries. Focal mechanisms of the large event can help explain the event's origins and the processes which create the events. The waveforms from seismic events could be used to determine the thickness of the ice shell, detect pockets of liquid water within the ice shell, and determine the depth of the subsurface ocean.

In addition to the large events, smaller local events are also likely. Small ice cracking (here referred to as icequakes) are likely going to occur throughout the tidal cycle.

There could also be events originating from cryovolcanic activity (Lopes et al., 2013; Porco, 2006; Quick et al., 2013). As liquid moves within the ice shell and erupts onto the surface, we would expect to see seismic signals similar to those of terrestrial volcanism. Additional seismic signals from ice-water interactions could produce seismic signals similar to those observed in cryosphere settings (Podolskiy & Walter, 2016). Beneath the chaos terrains on Europa, could lie entrained subsurface liquid water (Greenberg et al., 1999; O'Brien et al., 2002; Schmidt et al., 2011). These reservoirs of liquid water would be similar to subglacial lakes found in Antarctica and Greenland (Bowling et al., 2019; Isanina et al., 2009; Palmer et al., 2013; Peters et al., 2008). Like terrestrial investigations, seismic deployments on ocean worlds could reveal the presence and size and state of the subsurface liquid water pockets. Seismic signals originating near the liquid water may also indicate if and how the water remains stable and is exchanged within the ice shells.

Passively recorded seismology can reveal how a local or global environment responds to changes or added stresses. On Earth, different regions have different seismicity due to the locations relative to plate boundaries, the type of plate boundary, and local environmental conditions. For example, subduction zones experience deep earthquakes that are not typically seen elsewhere (Giardini & Woodhouse, 1984; Stauder, 1975). Subduction zones are also capable of producing the largest recorded events (Davies & House, 1979). Mid-ocean ridges have shallow events with focal mechanisms indicating shear or normal (extensional) motions (Atwater & MacDonald, 1977; Lachenbruch & Thompson, 1972). Focal mechanisms of earthquakes in general indicate relative fault motion which can reveal how a tectonic plate is moving relative to another one. For these reasons, seismology provided powerful evidence to support plate-tectonics theory. Similar

observations or lack thereof would provide necessary evidence to prove if Europa's ice shell behaves like plate tectonics. In addition to large-scale global implications, seismology can also investigate local phenomena. Seismic catalogs have been interpreted to provide seismic hazard analysis and forecast seismic risk (Field et al., 2003; National Research Council (US). Panel on Seismic Hazard Analysis et al., 1988; Schwartz & Coppersmith, 1986). Seismic hazards from anthropogenic sources have also been investigated (Majer et al., 2007; Segall & Lu, 2015; Shapiro & Dinske, 2009). Seismometers have also played a key role in remotely assessing environmental hazards (Goodling et al., 2018).

Volcanic processes produce a number of specific types of seismicity (McNutt & Roman, 2015). It is not uncommon for swarms of earthquakes to occur before eruptions indicating fluid motion within the near-surface. For this reason, many volcanoes are seismically monitored to help provide early-warning mechanisms (McNutt, 1996). On icy ocean worlds, seismometers may detect swarm activity prior to plume or cryovolcanic activity. The timing of the swarms relative to eruptions could indicate internal mechanisms and activity responsible for the plume activity.

In addition to volcanoes, the cryosphere and hydrosphere also host unique seismicity. Glaciers and ice-sheets have signature cryoseismic signals from basal motion, icequakes, and calving events (Podolskiy & Walter, 2016). Seismometers have been deployed to Arctic and Antarctic regions to monitor ice sheets, ice loss from climate change, and water-ice interactions (Amundson et al., 2012; Clinton et al., 2014; Mordret et al., 2016; Winberry et al., 2009). In addition to unique seismic sources, the cryosphere also has unique seismic waves. Crary and flexural waves are unique to the cryosphere and have been investigated to determine ice sheet thickness (Crary, 1955; Ewing et al., 1934;

MacAyeal et al., 2015). Seismometers on ocean worlds would likewise be used to monitor conditions of the ice shell and detect ice-water interactions within the ice shells. On Earth, the oceans are responsible for microseismic noise that can be detected anywhere on Earth (Ardhuin et al., 2001). Correspondingly, seismometers could monitor hydrocarbon lakes on Titan (Stähler et al., 2019).

Events, and specifically uniquely occurring events, can help characterize the local environment and reveal the inner workings of planetary environments. The Apollo seismic experiments revealed deep moonquakes, near-surface thermal events, contractional tectonic events, as well as meteorite impacts. The deep moonquakes, which are the most common type of lunar event, were caused by tidal interactions with the Earth (Bulow et al., 2007; Kawamura et al., 2017). Another type of identified event were contractional tectonic events which show the Moon is shrinking as it cools (Watters et al., 2019). Thermal moonquakes were temporally linked to sunrise and sunset and diurnal temperature cycles (Duennebier & Sutton, 1974). Together the events provide a picture of the Moon's seismic activity. Currently the InSight mission to Mars is building its catalog of events which fall into several categories. Early results indicate that Martian seismicity falls between the Earth and the Moon (Giardini et al., 2020). The Martian events tend to excite different frequency ranges, which may point to differences in their sources. Joint investigations between the SEIS instrumentation and meteorological instruments have investigated atmospheric phenomena such as daily changes in wind speed and direction, and dust devils (Banfield et al., 2020; Perrin et al., 2020). Missions to icy ocean worlds would like-wise benefit from seismic deployments.

One proposed mission, the Europa lander (Hand et al., 2017), and a selected mission, Dragonfly (Lorenz et al., 2019), will carry seismic payloads to Europa and Titan, respectively. The missions have several goals including constraining internal structure and investigating seismicity. Like all planetary missions, there are associated challenges. Titan has a thick atmosphere and lakes which could contribute to background noise (Stähler et al., 2017; Vance et al., 2018b). More significantly, Europa has a high level of radiation at its surface (Paranicas et al., 2007), thus the lifetime of a lander mission is limited to about a few weeks (Hand et al., 2017). Due to the short time frame of the mission, data would likely be sent using a low sampling rate, and if a detection is made, higher sampling rates can be sent back to Earth. It is also likely that the mission would have a single-station seismometer or be confined within a small-aperture array (< 2 m). This means there will be a location bias associated with detected events. For example, the Apollo experiments were only able to detect deep moonquakes on the near-side of the Moon. It is still uncertain whether a lack of far-side detections is due to the absence of events, or if the properties of the lunar interior inhibited their detection. Likewise for InSight, a blind test was able to show that the detection of an event is related to the size of the event and the distance from the source (van Driel et al., 2019) such that only larger events can be detected at greater distances.

The ability to detect both large teleseismic and smaller, local events will be critical for the success of future seismology-driven missions. Due to data and/or cost restrictions, a single-station may be preferred over a small array of stations. However, the array would provide additional data as well as necessary redundancy in the event of instrument failure. In this chapter, I test how single-stations and the small-aperture arrays detected tectonic

events through automated detection, and how many additional events were found through visual inspection. This allows me to quantify the advantages of a small array over a single-station, as well as investigate if automated detection algorithms are a reliable method compared to visual inspection. Here the small-aperture array is limited to a few square meters, mimicking deployment through use of a robotic arm. Previous stations in small-aperture arrays deployed on the Moon were separated by several tens of meters (Kovach & Watkins, 1973), and terrestrial small-aperture arrays are typically kilometers in scale (Manchee & Weichert, 1968). By deploying in two analog locations, I further quantify how detection rates vary between the more active site, Gulkana, and the quieter site in Greenland. Events were detected through a short-term average/long-term average (STA/LTA) approach after applying bandpass filters. For the small-aperture array, the same approach is applied, but the plausible detection needed to be made for the majority of the stations, meaning most stations needed to meet the conditions for detection. I then compared the results of the single-station and small-aperture array catalogs to known event catalogs (U.S. Geological Survey, 2020) to determine how many events were detected and how many were missed. Seismograms and spectrograms were visually inspected to search for events that were not included in the original catalog to determine how and why the algorithm failed. For the high frequency events, a cluster analysis was performed in order to help identify their potential sources. The cluster analysis compared waveforms to categorize events based on their envelopes. For each cluster category, the azimuth, average event duration, dominant frequencies, and preferred time of day were compared. These characteristics revealed if the clusters share characteristics that can help identify or locate them.

4.2 Analogs and Data

To determine how a single-station or small-aperture array could be used to detect and identify seismicity on an icy ocean world, I used passively recorded data at terrestrial analogs sites. The Seismometer to Investigate Ice and Ocean Structure (SIIOS) was funded in part to study how single-station or small-aperture arrays can achieve science objectives on icy ocean worlds using terrestrial analog locations. These sites were Gulkana Glacier in the Alaska Range and a site in northwest Greenland (Figure 4.2). For details on the deployment, data, and instruments at these sites, see Chapter 3.

Gulkana Glacier represented a noisier potentially active site. It was originally selected as an analog site for logistical reasons and its status as a benchmark glacier which meant it has been extensively studied (Baker et al., 2018; Van Beusekom et al., 2010). Its location near a subduction zone meant regional seismicity ($<20^\circ$ epicentral distance) could include large ($M_w > 4$) earthquakes. During deployment the largest teleseismic event was a $M_w 7.1$ that occurred in Mexico on 19 September 2017. There were four events with $M_w > 6.0$ that also occurred. More locally, Gulkana was also considered more active in several regards. Gulkana Glacier was located in the Alaska Range near Ogive Mountain and Skull Peak. The local topography ranged from ~ 1200 m to ~ 2000 m (March & Trabant, 1997; Ostenso et al., 1965) (See Fig 3.1 in previous chapter). The nearby mountains allowed for potential rockfall events and some were heard during installation. There were also several active moulins near the array. Moulins allowed water to drain from the surface of the glacier to the bedrock below, thus served as a semi-continuous source of background noise.

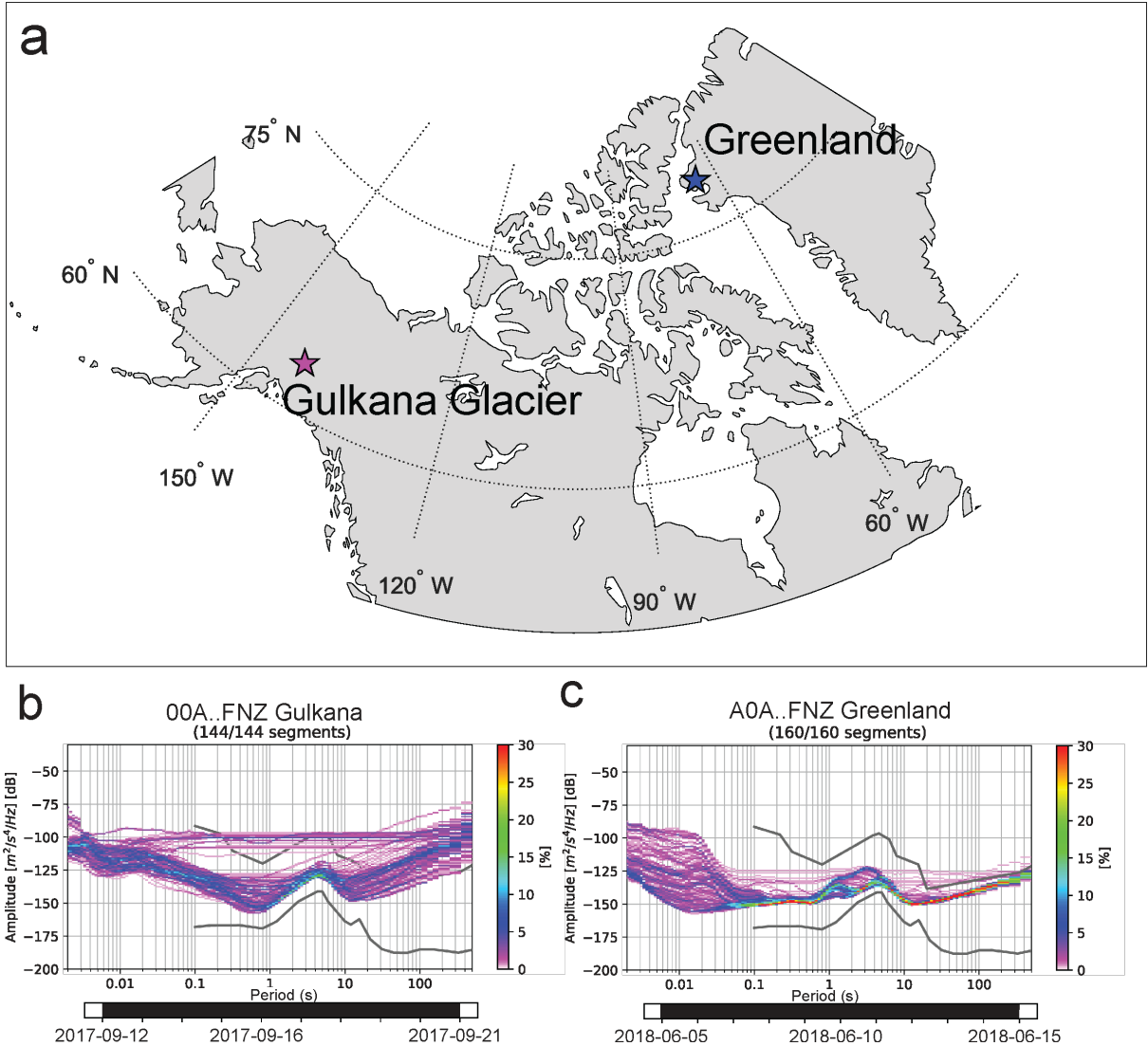


Figure 4.2 a) Map of SI IOS location on Gulkana Glacier (purple/pink star) and in Greenland (blue star). b) Gulkana is located close to the subduction zone around the Aleutians Islands and is in a more active local environment. Its power density function indicates higher levels of noise c) The Greenland site is relatively farther from active plate boundaries. The Greenland location was also colder (259 - 271° K vs 269-282°K) than the Alaska site reducing surface activity producing a quieter power density function.

We observed surface runoff as well as drainage at the terminus of the glacier. The variety of activity in the local area were capable of producing seismic signals.

Conversely, Greenland was considered the quieter site. The site was not near active plate boundaries, thus recorded far fewer regional events than Gulkana. During the deployment, there also happened to be fewer large teleseismic events. No events larger

than Mw 6 occurred. Locally, Greenland was also less active than Gulkana. The temperatures at Greenland remained below freezing for the duration of the experiment, eliminating surface runoff and reducing the possibility of active moulins. Due to its location at the ice divide, the ice sheet moved at less than 10 m a year (Joughin et al., 2010, 2020). The ice at Greenland was also much thicker than Gulkana (~850 m versus ~100 m) (March, 2000; Ostenso et al., 1965; Paden et al., 2010). Beneath the site in Greenland, lied a subsurface lake (Bowling et al., 2019; Palmer et al., 2013). The thicker ice and subglacial lake insulated sensors on the surface from basal motion, further reducing background signals.

Both of these sites passively recorded data for approximately two weeks. The small arrays consisted of one Silicon Audio in the center, with four additional sensors ~1 m away in each cardinal direction. Each station recorded with a sampling rate of 1000 Hz on three orthogonal components (FNZ, FH1, FH2). Instrument responses have been removed and different bandpass filters were later applied (see Section 4.3 for details). Some of the sensors in the Gulkana array became tilted and/or rotated over the course of the experiment which can impend azimuthal recovery and data quality. Most of the sensors still had power and were actively recording upon demobilization. Some of Greenland's sensors lost power sooner than others, up to several days. None of the instruments at Greenland had any tilts or rotations. For consistency across the field sites, when the single-station results were presented, the referred station was the center station. At both locations, these sensors experienced the least tilt and some of the longest deployment times. For details regarding the power density functions, tilt directions, rotations, and exact geometries see Chapter 3 or Marusiak et al., (2020).

4.3 Methods

Seismic sources were detected and in some instances, located using a suite of techniques. To detect events I used the vertical component of seismic data to implement a STA/LTA approach (Baer & Kradolfer, 1987; Withers et al., 1998) or in some cases, a template detector which takes advantage of cross-correlation detections (Forghani-Arani et al., 2013). The template used a short period (~0.5 seconds) of high quality signals that represented desired characteristics I was searching for. The cross-correlation technique was used with lunar data to detect additional lunar events with low signal-to-noise ratios (Bulow et al., 2005). Many of the approaches used built-in functions of the Python ObsPy module (Beyreuther et al., 2010). Results of the functions were then analyzed using original Matlab code. The first types of events the algorithms searched for were larger tectonic events. Teleseismic and regional events would be of high interest to planetary missions for several reasons. Due to their size and potentially wide-range of distances, they can provide numerous information that a small local event cannot. These events tend to have lower-frequencies (below 5 Hz) and have longer durations (several seconds to several minutes long) than local events such as icequakes (Podolskiy & Walter, 2016). To search for these events the STA/LTA approach was used on filtered time-series. The second type of event the algorithm searched for were high frequency (HF events) that could represent icequakes, moulin activity, or rockfalls. These events have been observed in arctic environments and can help reveal the stability of the glacier or ice sheet. Icequakes, for example, have characteristic frequencies between 5-20 Hz and typically have durations of 1.5 seconds (Lombardi et al., 2019). To detect these events the STA/LTA was also implemented but the parameters and filters were adjusted to better fit the expected characteristics of the local

events. The last event was an anomalous very high frequency (VHF) signal originally detected in the data from Greenland. This signal consisted of repeating signals at semi-regular intervals. As these events had characteristic repeating signals, the template detector approach was implemented. The algorithm determined when they occurred and for how long at a time. A polarization approach (Stachnik et al., 2012) was also implemented to determine azimuth with the goal of determining the source.

4.3.1 Short-Term Average/Long-Term Average

The first approach invoked the (STA/LTA) (Baer & Kradolfer, 1987; Withers et al., 1998). This approach was commonly used to automatically detect events in seismic data sets. It determined the short-term amplitude average and then divided by a longer-term average resulting in a ratio. To detect the events of high-interest, we bandpass filtered the data and then set the short-term and long-term average parameters (Trnkoczy, 1999). For teleseismic events which typically have long durations and dominant at low frequencies, the bandpass filter was set to 0.02-1 Hz, and the STA/LTA parameters were set to 1 and

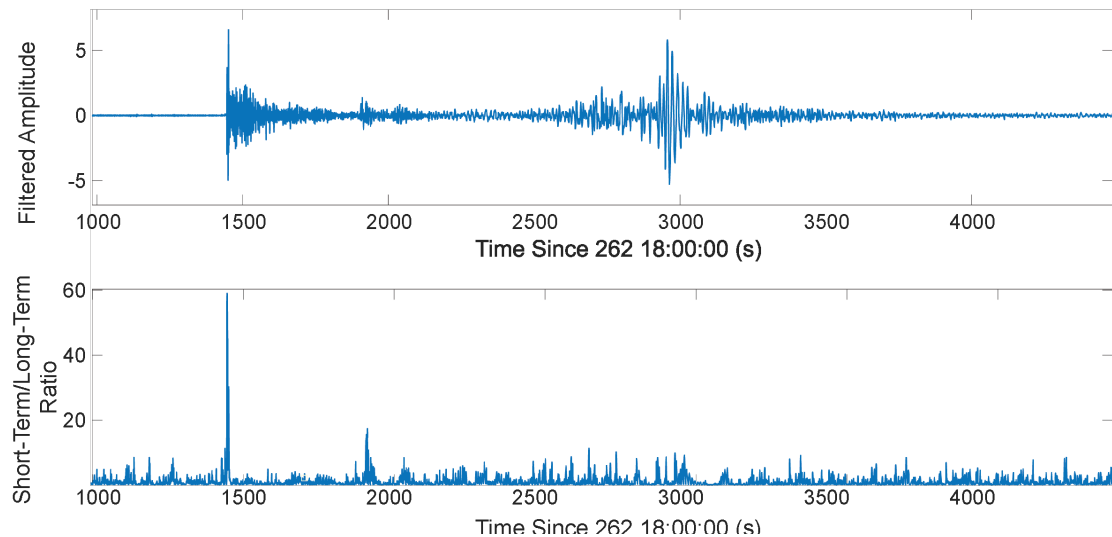


Figure 4.3 Time-Series of filtered (0.02-1 Hz) vertical component data collected at Gulkana Glacier (top). Corresponding values of the short-term average/long-term average ratio (bottom). The Mw 7.1 Event shows a clear arrival and resulting STA/LTA value.

60 seconds, respectively. A detection threshold was set at 20 for Gulkana, meaning the short-term average (1 second surrounding the event) had to be at least 20 times greater than the long-term average (60 seconds) to be triggered (Figure 4.3). In this example the *P* wave shows STA/LTA value of nearly 60, which initiated the detection trigger. Owing to a lower background noise, the threshold for Greenland was reduced to 10. For regional events, the bandpass filter was set to 0.1-5 Hz, and the STA/LTA parameters were set at 0.5 and 30 seconds, respectively. The threshold for regional event detection was set to 35 for Gulkana and 5 for Greenland. Greenland had lower thresholds because there were fewer potential recordings, and the potential recordings tended to be farther distance-wise, reducing signal-to-noise ratios. By looking for known events we were able to adjust the parameters to increase detections without over-producing false positives. The reported parameters were found to produce an optimal number of true positives while reducing false negatives and false positives. The false positives could come in the form of instrumental anomalies or glitches, discussed in more detail below. False positives could also be caused by other local signals.

Once the lists of potential detections were made, the candidate events in the STA/LTA catalog were read into another algorithm. The second algorithm examined spectrograms to determine the event duration once the onset of the event was triggered. The spectrogram of a candidate event needed to stay 5 dB over the average background value for approximately 2 seconds surrounding the start and end time of the event. Teleseismic and regional earthquakes have dominant frequencies below 1 Hz which is well below the frequency of local background noise which tends to dominant above 50 Hz. The events also tend to be longer in duration, lasting minutes for regional, or tens of minutes

for large teleseismic. The duration of the event was determined by time period that remained above 5dB over the background at frequencies below 10 Hz. The algorithm checked the end time with the next event in the catalog. If the previous event ended within 20 seconds for regional filters or 60 seconds for teleseismic filters, the events were merged. This helped with larger teleseismic events where the P wave and surface waves were separated by minutes. Spectral analysis helped to eliminate false positives especially from some glitches. To further reduce the number of false positives in the detection algorithm, events were removed from consideration if the event duration was under a minimum threshold. Minimum event length was set to 10 seconds for regional events and 15 seconds for teleseismic events which helped to remove some instrumental anomalies. Occasionally glitches in the sensors would produce a sharp spike in amplitudes and show increased power levels across the entire spectral range. These events would pass all the criteria, but visual inspection would eliminate them as plausible event candidates.

Once the candidate events passed the second algorithm, the events were visual inspected and a catalog was made that recorded the time of the event, the raw (unfiltered, but instrument response removed) amplitude, filtered amplitude, dominant frequency, and event duration. The events were then compared to a catalog generated using the USGS Advanced National Seismic System (ANSS) Comprehensive Catalog (ComCat) (U.S. Geological Survey, 2020). This service combined regional and global catalogs to create a more complete catalog of events. The minimum magnitude of this catalog was M_w 2.5. Using the cited locations and onset times, anticipated arrivals of surface waves and P waves were calculated using TauP software (Crotwell et al., 1999) with the PREM model (Dziewonski & Anderson, 1981). For the events in our catalog, azimuths were calculated

using a polarization approach (Stachnik et al., 2012). If the predicted arrival times reasonably matched the start times of our catalog (within ~1- 20 seconds depending on event distance) then the event was considered a match. There were times where an event was detected in the SIIOS catalog, but no event from the ComCat catalog had a predicted arrival time that matched. It is possible the events were relatively close to our stations but were a low magnitude (<2.5 Mw) and thus excluded from the ANSS generated catalog.

To search for potential thermal or other high frequency (HF) events a bandpass filter of 5-20 Hz was applied to the data (Lombardi et al., 2019). The STA/LTA parameters were set to 2.5 and 40 seconds for the short and long term averages, respectively. The required threshold for detection was an STA/LTA value of 20 and 5 for Gulkana and Greenland, respectively. This was based on visual inspection of the filtered time-series and returned values for the STA/LTA. Some trial and error was involved by testing a range of values from the literature (Lombardi et al., 2019; Trnkoczy, 1999; Withers et al., 1998) as well as the results of the visual inspection and outputted STA/LTA values. Because we assumed the events were more local due to the high frequency content, the amplitudes were relatively high compared to background, at least for Gulkana. Unlike lower frequency events, the secondary algorithm did not inspect the spectrograms. This was done for two reasons. The first was due to the higher limit of the bandpass filtered (20 Hz) which was close to where the background could be begin to dominant. It would be difficult to determine if the event was causing high values in the spectrogram, or if it was general background signals. Glitches were also common which would saturate across a wide frequency band further complicating automated techniques. The second reason was for efficiency. HF events such as icequakes are short in duration (< 2 seconds). To properly

assess the event duration, one would need to calculate the spectrogram in ~ 0.1 s increments. For datasets consisting of \sim two weeks with 1000 Hz sampling rates, the algorithm would become significantly slower. Instead of relying on spectrograms, the duration of the event relied on the STA/LTA values. The event duration was determined by the time-span that the STA/LTA minimum threshold (20 or 5) was exceeded. The minimum event duration was set to 0.25 seconds, and minimum event separation was set to 0.1 seconds, meaning events separated by less than 0.1 seconds would be merged. The initial catalog was then visually inspected to remove events with unclear arrivals, or events caused by VHF events or glitches. The final catalog recorded dominant frequencies from periodogram calculations, along with raw (unfiltered) amplitude, azimuth, time of event and duration of event.

In addition to single-station approaches I also tested small-aperture array approaches. For the lower frequency, potentially tectonic, events the STA/LTA results for all stations in the small-aperture arrays were compared. To become a candidate event, the majority of the stations in the small-aperture array needed to have STA/LTA values exceeding the minimum requirement. For most of the passive experiments 4 out of the 5 stations needed to have STA/LTA values that exceeded the threshold for candidate detection. Towards the end of the experiment, as stations began to lose power, 3 out of 4, or 2 out of 3 stations, needed to meet the requirements to trigger a candidate detection. To properly compare the single-station versus small-aperture array approach, the same length of short and long term averages and minimum thresholds used to compute the single-station STA/LTA were implemented.

4.3.2 Template Detection

A very high frequency (VHF) signal was originally visually detected when inspecting the Greenland data for potential misses of the high frequency events. The signal was visually identified by its repeating nature and spectral signature (Figure 4.4). Because of the repeating nature, a template was created to perform cross-correlation detections. This was preferred to STA/LTA approach because the events were very similar to one-another and had a signature repeating nature. Unlike regional or teleseismic events where arrivals times of body waves and surface waves vary, the waveforms of these VHF were nearly identical. Unlike the other HF events, the unique repeating nature of VHF made them more identifiable through a template detector. The python code used the template to perform a

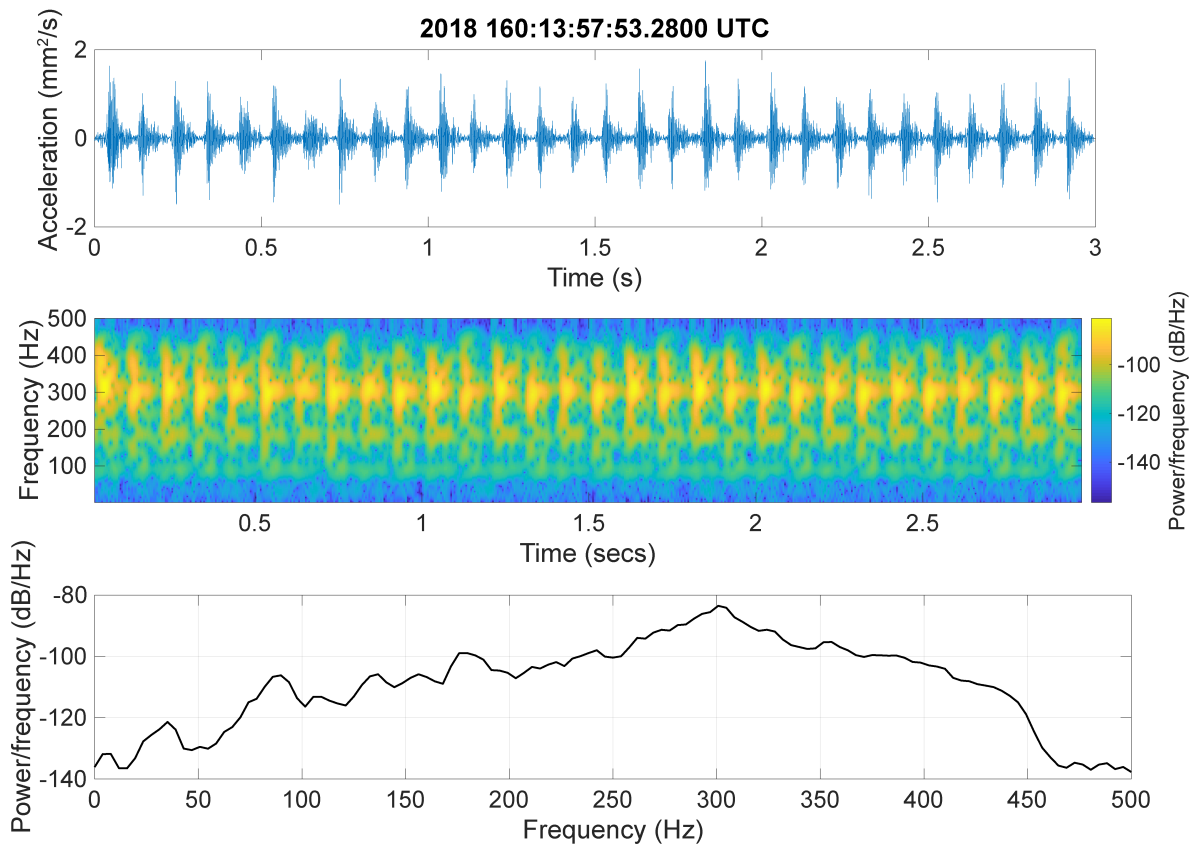


Figure 4.4. Example of the anomaly signal in temporal (top) and spectral (middle and bottom) domains. The signals repeat approximately 10 times per second. The dominant frequency is around 300 Hz with additional resonances at 175 and 90 Hz.

cross-correlation of the passively recorded data set. The template was set as the vertical component at time 2018-06-09 13:46:52.22 and lasted for 0.6 seconds, capturing about 5 of the individual signals. A secondary template made from a stack of ten of the individual signals was also tested but tended to retrieve a large number of false positive events. The template detector worked by calculating the similarity between the dataset and the template. If the similarity exceeded a threshold of 1.0, a candidate detection was made. For each possible detection, a second Matlab algorithm calculated the power spectral density (PSD). At the time of the detections, the PSD between 300-400 Hz must exceed 15 times the mean PSD values over all frequencies for 0.5 seconds before and after the event. The rationale for this criteria is based on the secondary algorithm for tectonic event detection. By setting a minimum required power level over the background, false positives can be eliminated. In most cases the false-positives were from other HF events. The maximum amplitude also has to exceed 0.04 mm/s^2 . This value is somewhat arbitrary but was determined by visually examining known signals and helped to eliminate false positive detections. If HF events occurred in rapid succession, the template finder would initiate a detection, but these event tended to fail to meet the amplitude criterion. Once a detection was made and met the initial criteria, the events were visually inspected to ensure only the desired waveforms were in the final catalog. This final catalog recorded the time of the signal, filtered and unfiltered amplitudes, and duration.

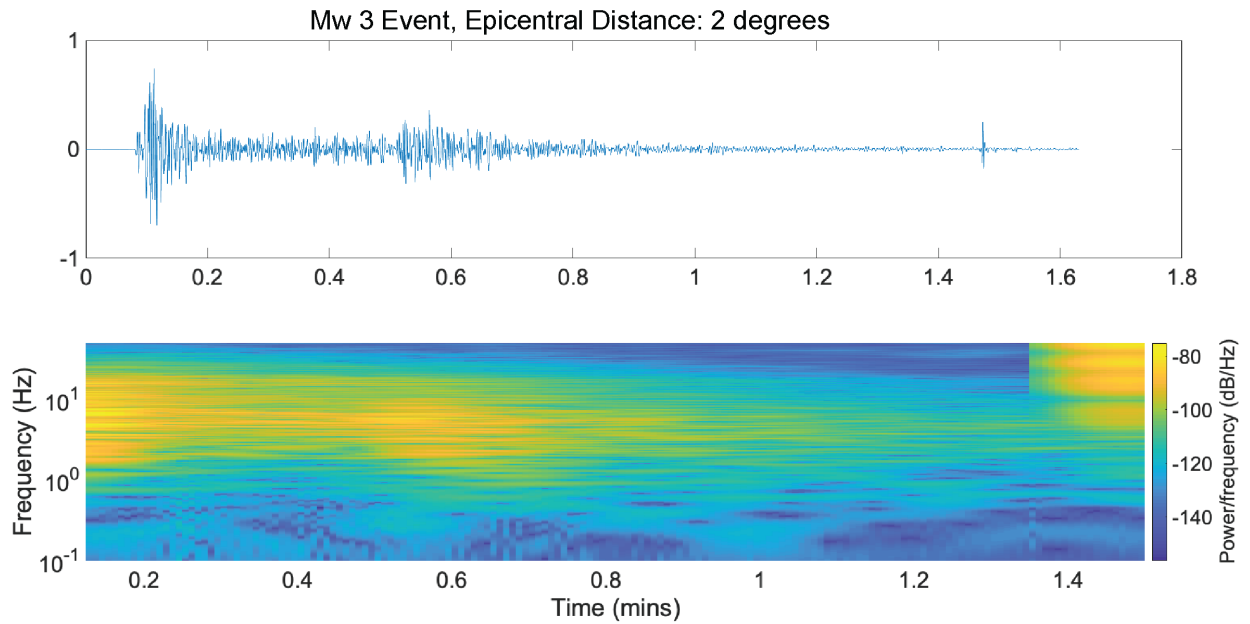


Figure 4.5. Example of a positive detection using the single-station approach at Gulkana Glacier. The time-series (top) shows a clear arrival. The spectral domain (bottom) also shows strong power in frequencies below 10 Hz.

4.4 Results

4.4.1 Regional and Teleseismic

The candidate catalog for Gulkana contained 81 possible teleseismic and 117 regional events using the single-station approach. Out of the 198 candidate events, 130 (66%) were matched to an event in the ComCat catalog. The Greenland candidate catalog contained 64 plausible teleseismic and 89 regional events. Of the 153 candidate events, 85 (56%) were matched to a ComCat event. Many of the candidate events at Gulkana were from instrumental anomalies (65 out 198, ~33%). Because the glitches were high amplitude in the time-series and high power (dB) across all spectral ranges it was difficult to remove them from the potential catalog without visual inspection. The algorithm was able to detect many of the large events and some of the small but nearby ($<10^\circ$) events (Figure 4.5, see

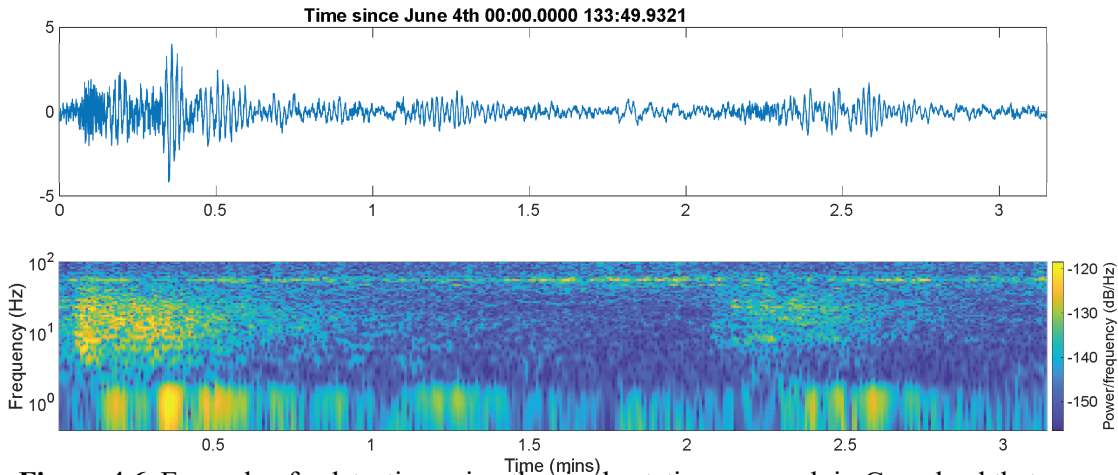


Figure 4.6. Example of a detection using the single-station approach in Greenland that could not be matched to a known event. There is one event that lasts about 45 seconds and a possible second event that occurs about 2 minutes later. The time-series (top) shows a distinct arrival, while the spectral domain (bottom) shows the events duration more clearly.

full catalog in Appendix 1). In addition to the events in the catalog, there were 3 events detected that were not in the catalog for Gulkana and 5 for Greenland (Figure 4.6).

Using the small-aperture array approach, the candidate catalog contained 135 plausible teleseismic events and 423 plausible regional events for the Gulkana site, and 246 teleseismic and 188 regional events for the Greenland site. Of the 558 candidate events at Gulkana, 214 (38%) were attributed to an event in ComCat. Of Greenland’s 434 candidate events, 226 (52%) were attributed to an event. Low-Frequency event detection rates at Gulkana ranged between about 0 an hour up to 5 per hour (Fig. 4.7a). Greenland detected one or two low-frequency events per hour (Fig. 4.7b). Like the single-station approach, the small-aperture array data included some (22 for Gulkana, 7 for Greenland) events that were not in the original catalog. There were less triggers from glitches, but larger HF events tended to trigger detections, especially for Gulkana where there were more high quality (signal-to-noise ratio) HF events. The dominant frequencies of HF events (5-20 Hz) were similar to the bandpass filter for the regional events. The HF events were identified by their

relatively short durations and higher frequency content (>20 Hz). In total 322 (58%) events in the Gulkana candidate catalog and 201 (46%) in the Greenland candidate catalog were attributed to HF events or instrumental anomalies.

Table 4.1. Results for the single-station and small-aperture array detections using data from Gulkana and Greenland sites. Percentage of Visually Observable Events refers to the percentage of ComCat Events that were visually observable. Percentage for STA/LTA and Small-Aperture Array Coincidence refer to the percentage of visually detected events that were detected by the respective algorithms. Both Methods refers to events detected by either or both STA/LTA Single-Stations and Small Array. The percentage refers to total automated detections out of the visually observable data.

Analog	Number of Events	Visually	Single-	Array	Either
	Mw >5 or distance	Observable	Station	Coincidence	Automated
	< 20° in ComCat	Events	STA/LTA	Triggered	Detections
			Detections	Detections	
Gulkana	127	75 (59%)	38 (51%)	45 (60%)	57 (76%)
Greenland	41	26 (63%)	9 (35%)	21 (81%)	22 (85%)

Events from the ComCat catalog greater than Mw 5 or closer than 20° were visually searched for to determine why they weren't included in the SIIOS catalogs. Of the 70 undetected ComCat events for Gulkana, an additional 18 events were found through visual inspection of the data (Table 4.1). For the Greenland site, of the possible 19 undetected ComCat events, visual inspection revealed 3 additional events. The events that were visually detected tended to occur near larger events or during high background noise periods, which made automated detections through amplitude alone difficult as the STA/LTA would fall below the threshold for detection (Fig 4.8). Once wind speeds exceed 4 m/s it became more likely the algorithm would fail to detect events. Some of the events that not detected at all were too small to be seen visually such as a Mw 6.1 event that

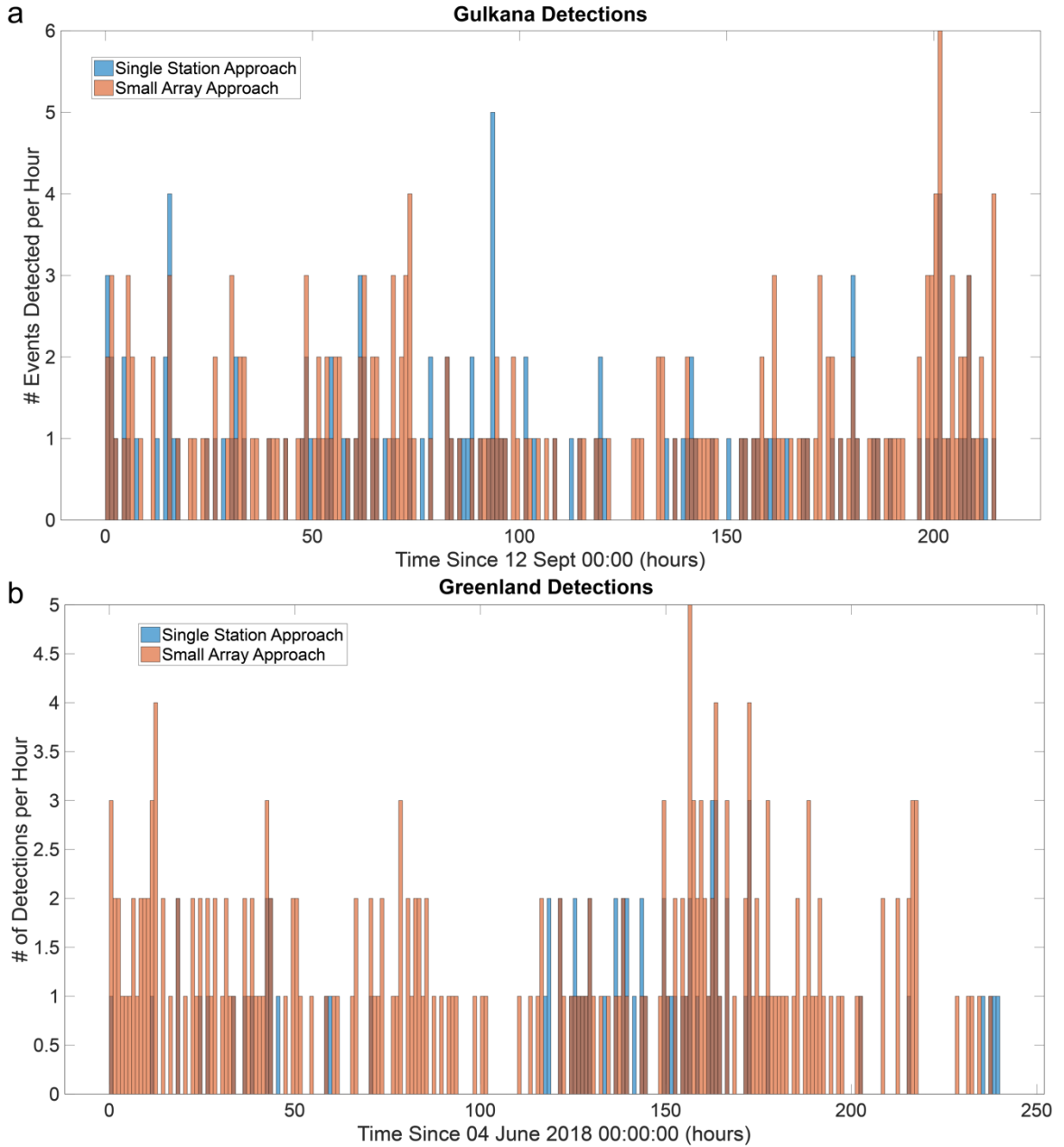


Fig. 4.7 Final catalogs for a) Gulkana site and b) Greenland site using the single-station approach (blue) and Array approach (orange). Detection rates ranged from 0-6 detected events per hour.

occurred 121° away, or a Mw 2.5 event that occurred 10° away from Gulkana. Both of these events happened when wind was particularly strong (~ 10 mph, 4 m/s) which created a strong background signal. Other undetectable events tended to occur during daylight hours when HF events and other local noise might have obscured their arrivals. Gulkana failed

to detect all 24 ComCat events that occurred between 9am and 1 pm local time. Small events tended to be obscured by larger concurrent events. Small events that occurred in clusters or within short intervals were also difficult to detect visually or with the automated algorithm.

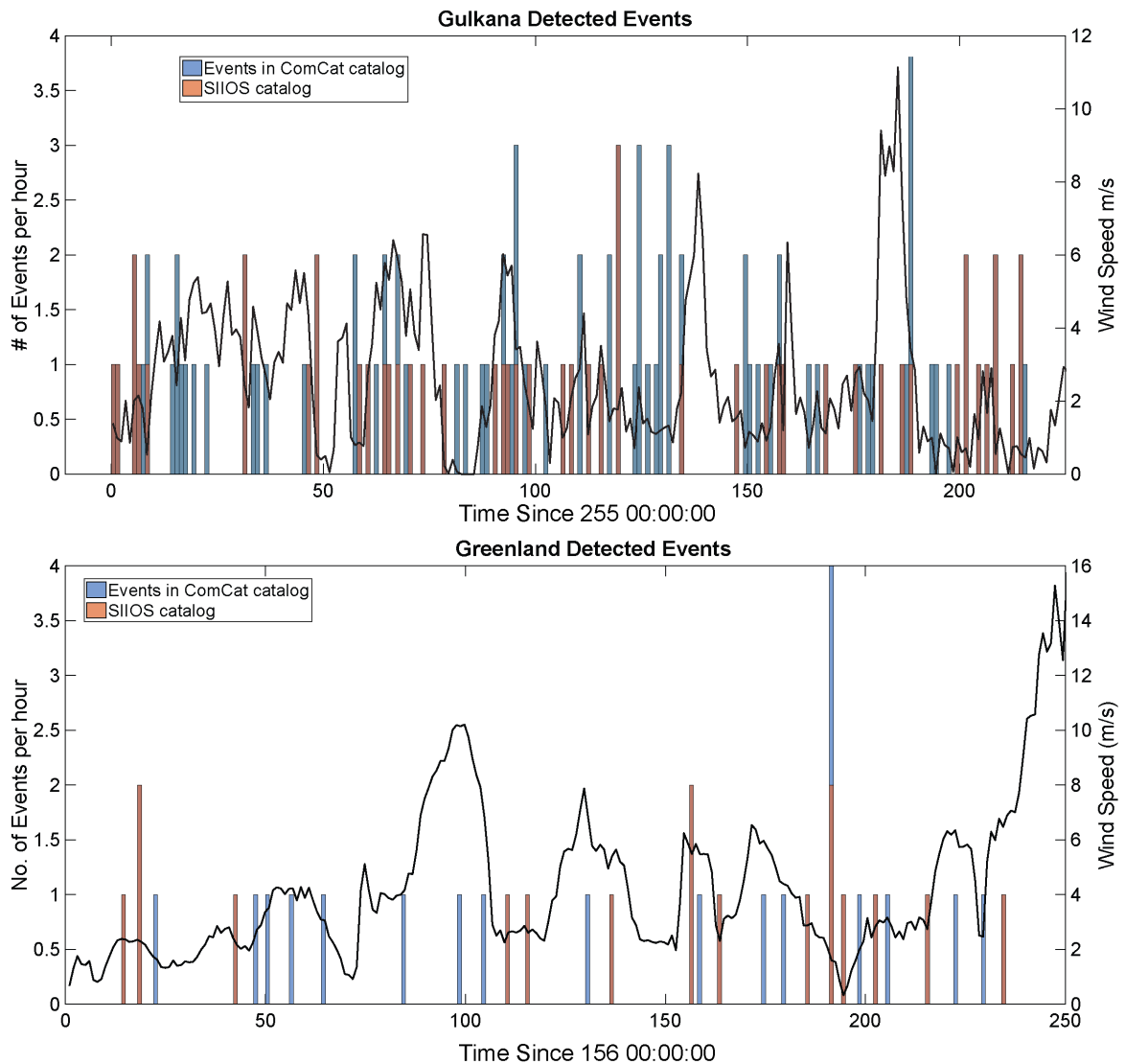


Fig 4.8. Comparison of $M_w > 5$ or Epicentral Distances $< 20^\circ$ from the ComCat catalogs (blue) and the SIOS automated detected catalog (orange). Many of the undetected ComCat events occurred when average hourly wind speeds exceeded 4 m/s which would increase the measured background noise.

4.4.2 HF event

Using the data from Gulkana, I initially detected 2,252 HF events of which 1456 (65%) made it to the final catalog. The removed events were either instrumental anomalies or had low signal-to-noise ratios. The events had a diurnal signal, with most events occurring between 6 am and 6 pm, local time (Figure 4.9). The event catalog was compared to weather data from MERRA satellites (Global Modeling and Assimilation Office (GMAO), 2015) and a local USGS weather station (Van Beusekom et al., 2010). The

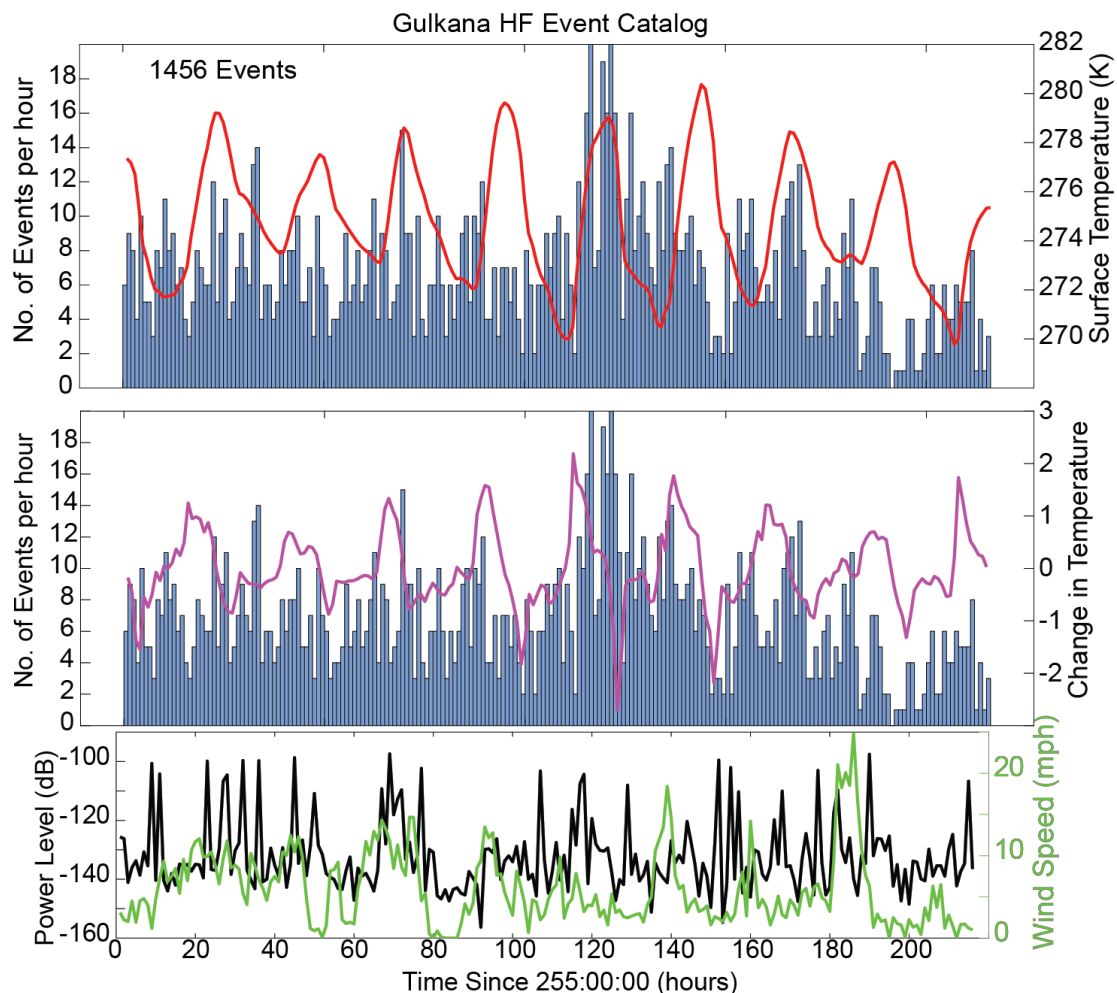


Figure 4.9 Comparison of number of detected events per hour (blue histogram) with a) temperature (K) (red), and b) change in temperature (pink). c) A lack of detections could be caused by high wind speeds (green) which tend to coincide with higher background noise (black).

events tended to coincide with increased temperature and changes in temperature. Occasionally, sharp rise in temperature were not indicative of detected events. These occurrences tended to happen when wind speeds were particularly high (>20 mph). Based on Pearson Correlation tests, however, the r value comparing number of detected events per hour with temperature and changes with temperature were 0.2 and 0.19, respectively. The corresponding p values were 0.003 and 0.006. Since the r values are not close to a value of 1, statistically temperature was not the primary control on their occurrence.

A cluster analysis was performed on the detected events to determine if there were any characteristics that could indicate their origin. A polarization approach was used to determine the likely azimuths of each event (Stachnik et al., 2012). Since it was difficult to distinguish between P , S , or surface waves, the entire waveform was used to determine likely azimuths. It's worth noting the station used for Gulkana (00A) was originally

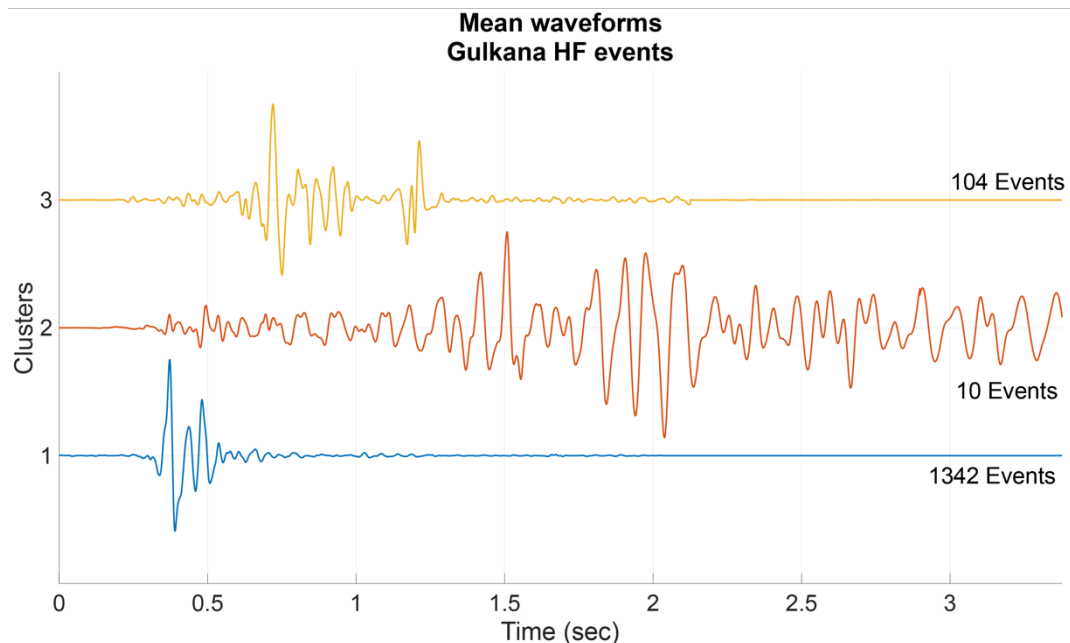


Fig. 4.10 Mean waveforms of clusters. Cluster 1 (blue) contained the majority of events and typically had high signal-to-noise and a single event per detection. Cluster 2 (red) had 10 events. The events had relatively small arrivals followed by larger amplitudes 1-2 seconds later. Cluster 3 (yellow) had 104 events. These events had a small arrival followed by a larger second arrival about 0.5 seconds later.

installed facing due north (0/360°). Upon demobilization the final azimuth was 335°, indicating it rotated 25° counterclockwise over the course of the experiment. To attempt to correct for this rotation, the recovered azimuth was adjusted by ~2.7° per day starting on 12 September 2017. The following cluster analysis compares waveforms to determine similarity and categorize the events. For Gulkana, there were 3 main categories (Figure 4.10).

The first cluster had the majority of the events (1342 events) and tended to originate with azimuths from between 150-180°, although there were events from nearly every direction. The waveforms exhibited a single clear arrival. The events tended to dominate at high frequencies dominant either between 15-40 Hz or 40-70 Hz. The events occurred

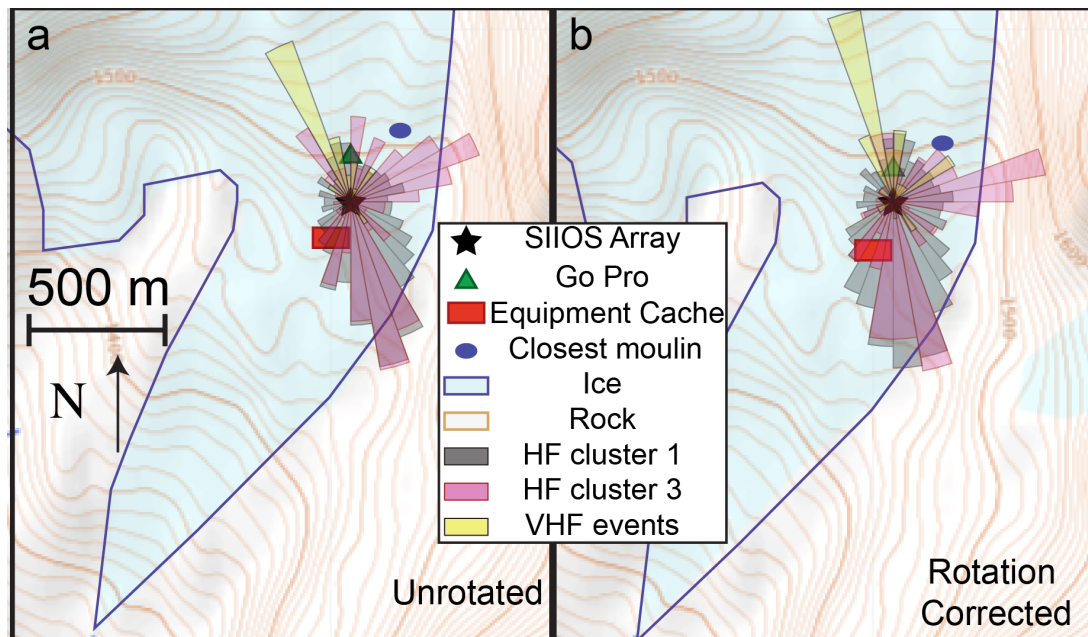


Fig. 4.11. Map of Gulkana and SIIOS array (black star). The location of the SIIOS array is well constrained, but the equipment cache (red rectangle), Go Pro camera (green triangle), and closest moulin (blue oval) are approximate locations. a) Before correcting for instrument rotation the first cluster of HF events (grey) and third cluster (pink) indicate the majority of events originate due South of the glacier. b) After correcting for rotation HF cluster 1 points mostly due south. HF cluster 3 points south and easterly. The VHF events tend to point due south towards the equipment cache and north towards the Go Pro camera.

during all times of day and were recorded throughout the passively recorded experiment. The southerly direction (azimuths 150-180°) and duration of events are consistent with events originating toward the ablation zone and terminus of the glacier (Fig. 4.11). The

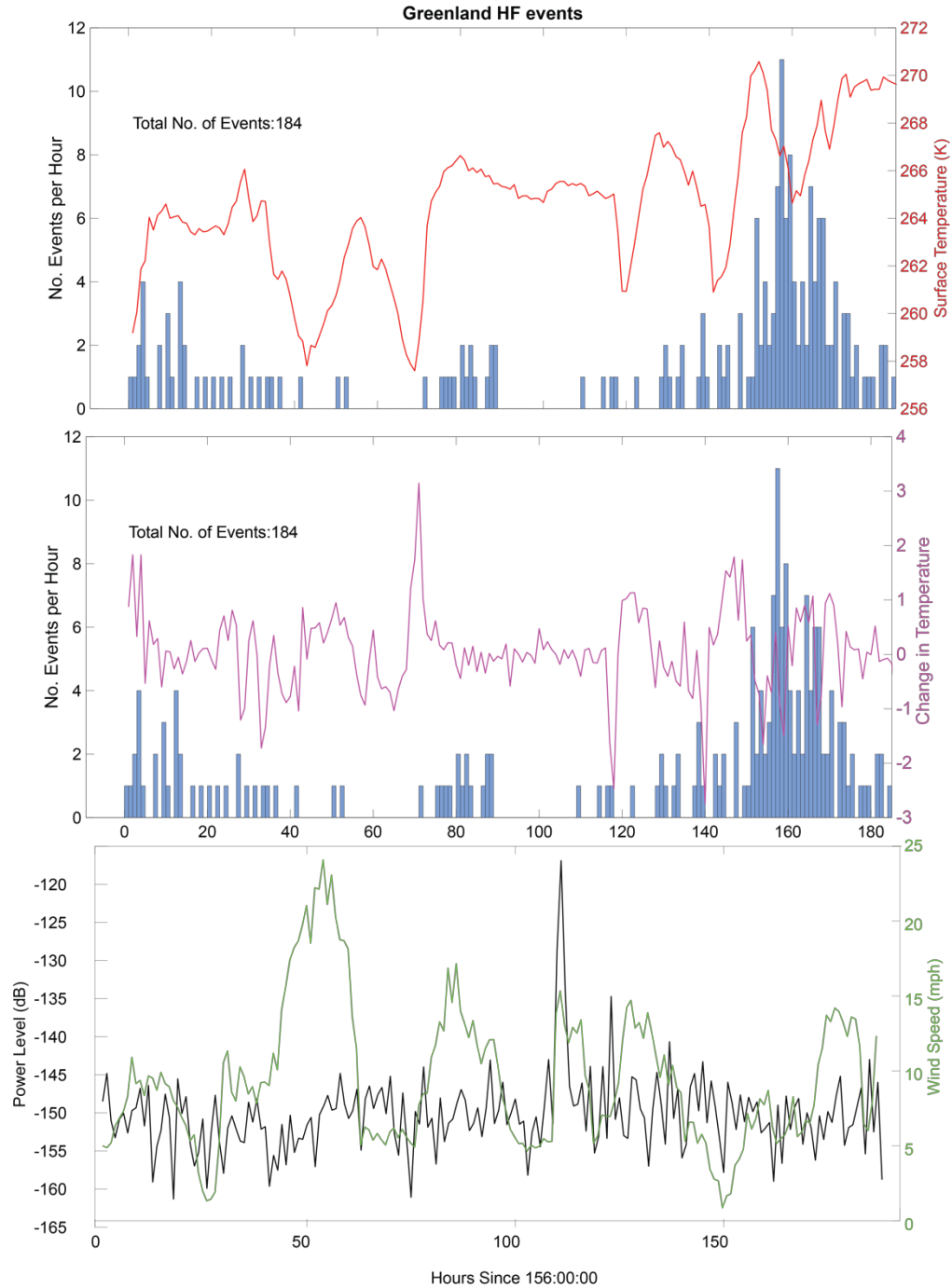


Figure. 4.12 Thermal events detected at the Greenland (blue histogram) site versus surface temperature (red, top) and changes in temperature (purple, middle). The power level (black) is compared to wind speeds (green).

second cluster contained 10 events. These events had a relatively small initial arrival with larger arrivals occurring within a second or two later. The events originated from a wide range of azimuths with no preferred direction suggesting their origins came from a wide range of locations. They also occurred throughout the experiment and at all times of day. The final cluster had 104 events. This cluster's waveforms typically had a small initial arrival followed by a larger arrival within 0.5 seconds. The events had azimuths from all directions but most occurred either due south (150-180°) or due east (50-80°).

In total there were 1778 detected HF events using the Greenland data of which 188 made it to the final catalog. Almost 500 of the automated detections were due to instrument anomalies. This mostly affected the data after 12 June 2018. For this reason the catalog stops 11 June 2018 at about 20:00 when the last positive HF event was detected. Another 50 events were also removed from the initial catalog because they were associated with VHF events discussed in the next section. Due to lower threshold for detection, the

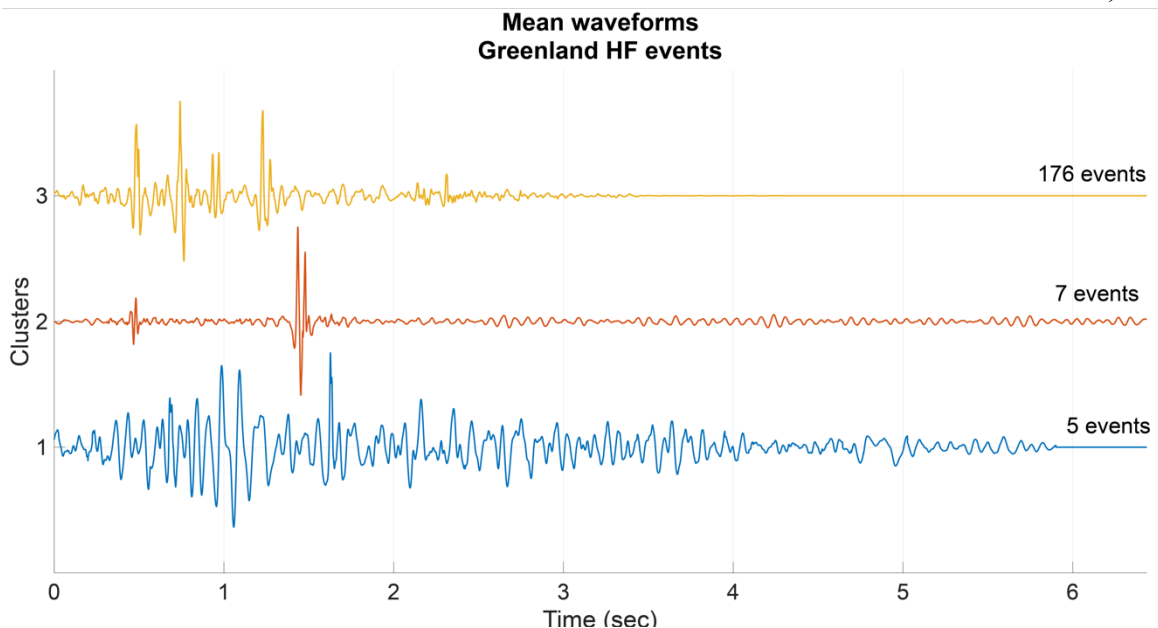


Figure 4.13 Greenland exhibited 3 clusters of events. The first cluster blue (1) had 5 events with low signal-to-noise ratios. The second cluster (red) had 7 events which tended to have higher signal-to-noise ratios. The third cluster (yellow) contained the majority of events. There were clear initial arrivals.

Greenland data tended to have noisier signals in the final catalog than Gulkana. Unlike the Gulkana events, there was no clear diurnal signal (Fig 4.12) although most events tended to occur between 09:00 and 15:00 local time. The Greenland events fell into 3 clusters with 5 events falling into the first cluster (Fig. 4.13). This cluster had frequencies that dominated above 40 Hz. The events azimuths indicated a southerly direction (Fig 4.14). The second cluster contained only 7 events. The events resembled glitches due to high signal-to-noise ratios and a wide range of dominant frequencies. These events came from a wide range of azimuths and occurred at all times of day. The third cluster consisted of 176 events preferentially occurred between the hours of 09:00-16:00 UTC (06:00-13:00 local). The events occurred throughout the experiment, but most occurred after 08 June 2018. The dominant frequencies were always below 20 Hz. The majority of the events had azimuths spanning 50-70°.

4.4.3 VHF Anomalies

During the inspection of HF events, a VHF signal was detected at both Gulkana and Greenland. Additional VHF signals were found using a template detector. The template was a section of the time-series which exhibited particularly high signal-to-noise events. The template found thousands of plausible events, many of which were then eliminated based on the additional criteria for amplitude and spectral characteristics. The initial autodetected catalog of events contained about 210 time series for Greenland of which 13 were included in the final catalog.

Due to the relatively low number of events in the catalog, a cluster analysis was not performed. The event lengths of the final catalog were typically only a few seconds long, although they could reach up to 10 seconds in length. Each of these detections contained

several of the individual signals. Many of the events occurred toward the end of the Greenland experiment with most occurring on 09 June 2018. The events tended to occur between 08:00-09:00 UTC, (04:00-05:00 local). The events tended to occur during periods of low wind when background noise was also low. Most of the detections had low signal-to-noise ratios which made azimuth recovery difficult. Using the highest quality events such as the time period used for the template, recovered azimuths pointed directly north. Analysis of different stations showed these events were detected not only in the small-aperture array but also by the remote stations. This was done to determine if the source of the signal was near the array or was also detected a kilometer away. One remote station

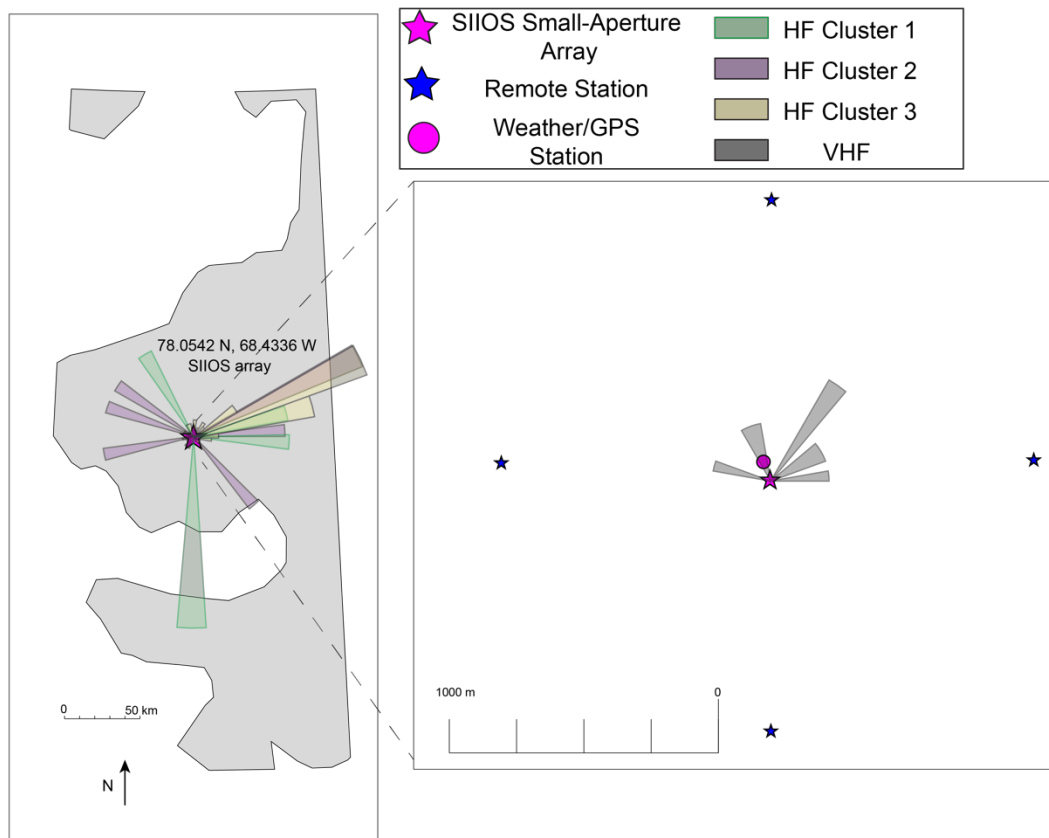


Fig 4.14 Map of SI IOS site in Greenland (purple star). In the left panel shaded gray indicates land versus ocean (white). Recovered azimuths of HF cluster 1 are shaded green, cluster 2 shaded purple and cluster 3 shaded yellow. The VHF events (grey) are plotted relative to remote stations (blue star) the center of the small-aperture array (purple star) and the GPS and weather stations (pink circle).

(R3A) was not used because it did not record usable data due to equipment malfunction. The other remote stations (R1A, R2A, R4A) did record the VHF signal. Each station recorded different azimuths of the signal.

A similar signal was found in the Gulkana data. A template of the events was created and used to search for additional events in the dataset set. About 2000 VHF candidate events were found through the initial template detector of which 34 were in the final catalog. The majority of the events occurred on 15 September 2017 between 04:00 and 06:00 UTC (20:00-22:00 local time). This time periods are all at night local time when temperatures were low and wind speeds were low (<5 m/s). The time series when the VHF were detected did not coincide with tectonic activity or high-rates of HF detections suggesting the VHF were not related to tectonic or HF activity. As with the Greenland VHF events, a cluster analysis was not performed due to the low number of events. Most of the events were several seconds long. The dominant frequency was between 380-400 Hz with additional resonances around 250 Hz and 125 Hz. After correcting for rotation effects, the events tended to originate from azimuths spanning 340-350°, and 50-60°. This signal was also converted into audio due to the high frequency content.

4.5 Discussion

For future missions to icy ocean worlds, expected seismicity should be considered when determining a landing site. Being close to a potentially active region would increase the number of local events and may help characterize the activity along an active area such as a fault, chaos terrain or nearby cryovolcanism. A lack of detected activity may indicate the area surrounding the landing is no longer active or less active than predicted. However,

a site farther from local events may detect a higher percentage of larger magnitude tectonic events. This may be preferred if the goals of the mission are to investigate larger scale structure or global-scale activity rather than a specific feature. The choice for a landing site would depend in part, on the anticipated mission duration. In the case of Europa, where the high levels of radiation would reduce the mission lifetime to a few weeks, a landing site near a potentially active area would be preferred. Such a landing site would have a better chance of detecting events which could characterize the local environment or possibly the global structure. For a mission to Enceladus or Titan where a mission may survive years, a landing site in a quieter area may be more suitable. Larger events would be more likely to be detected due to decreased background noise.

4.5.1 Regional and Teleseismic Detections

The low-frequency events were often associated with regional and tectonic activity. It was anticipated that the algorithm would not find every event in the catalog and would produce some false positives. Previous studies on single-station detection capabilities have shown limitations. The InSight MarsQuake Service (MQS) team created a blind test to determine how well a catalog could be built for Mars using InSight as a single-station. In that test, not every event was detected, even by the MQS team (van Driel et al., 2019). They showed that visually inspecting the time-series and spectrograms allowed for higher rates of detections than using only automated detections such as the STA/LTA approach. Furthermore, they illustrated only high magnitude events could be detected over a large range of distances resulting in the detection of about 50-60% of all events.

By visually inspecting the data, both temporally and spectrally, I was able to determine instances when detections failed. Many of the failed detections were not visible

in the data, as expected. This was due to high background noise compared to signal strength. For example, many of the small local events were not detected if they occurred during the daylight hours when local activity was high. Local weather events and background noise were also expected to obscure some of the arrivals of events. When winds were above 4 m/s, the tectonic events were difficult to detect. This phenomenon was not just restricted to just the dataset in this study. The InSight mission to Mars was able to detect more events during the evening hours than during the day when winds are increased (Giardini et al., 2020).

Events that occurred at great distances were also less likely to be detected as their energies were attenuated. Small events could also be obscured by larger events. For example, the large Mw 7.1 event obscured smaller events that occurred in the hour following the initial arrival. Occasionally it was difficult to determine which event the signal originated from. Small events tended to occur with short intervals between events so their waveforms could destructively interfere upon arrival, or it was difficult to identify the *P* wave onset. One additional complication that was also a problem for the MQS blindtest, was when events occur over 2 data files. Due to the size of the datasets, the time-series were divided into 6 hour segments for Gulkana and 3 hour segments for Greenland. This allowed the data files to be read-in more readily and for more efficient analysis. The algorithm was designed so that if an event was detected in one time segment, the search for the end of the event would continue into the second. However, due to the filtering and tapering effects applied to the time-series, the STA/LTA minimum thresholds were not always triggered as they should have been. This was a problem for both the single-station and small-aperture array approach.

The small-aperture array was more reliable in terms of false positive detections. The algorithm rarely detected glitches. The majority of the false-positives were actually local events such as thermal icequakes, moulin activity, or rockfalls. To reduce this number, the bandpass filter or thresholds for detections could be adjusted to a smaller range to prevent the detections of thermal icequakes. It should be noted that while increasing the threshold for detections would reduce false positives, the number of undetected events would also increase.

A future geophysical mission using this approach would want to assess the capacity to send data back to determine whether it is more acceptable to detect small local events, or to possibly reduce the overall number of detected events. Generally speaking, visually inspecting the data was the best way to detect all possible tectonic events. While time consuming, it can ensure no events are missed and eliminate false-positive detections. Data from the small-aperture array can also help confirm detections and improve data quality as not all stations would likely experience instrumental anomalies at the same time.

4.5.2 HF Detections

HF events were compared to local weather data to determine if changes in the environment could be driving the diurnal seismicity seen at Gulkana. Gulkana showed a clear diurnal signals where increased temperatures and changes in temperatures were linked to increased activity. Lack of detections tended to happen when wind speeds were particularly high (>20 mph) suggesting high background noise was reducing the detection capabilities. Since thermal icequakes are more likely to occur with decreased temperatures, not increased, at least some of the events are unlikely to be caused by tensional (expansional) cooling of the ice (Lombardi et al., 2019; Olinger et al., 2019). Previous studies in

Antarctica (Lombardi et al., 2019; Olinger et al., 2019) indicated there should generally be 1 thermally-driven events detected per hour, with higher rates occurring with decreasing temperatures. The detection rates were about 1-2 per hour and 3-14 per hour at our Greenland and Gulkana sites, respectively. A key distinction is that these studies used datasets spanning years and a wider range of temperatures (238-268° K), while ours were only deployed for ~ 2 weeks. Additionally, the temperatures at their field site in Antarctica ranged between 238-268°K while ours ranged 256-270° at the Greenland site and 270-280° at the Gulkana site. Because our events were similar in both time-series waveforms and spectral content, it is likely that at some of the detected events were caused by cooling and expansion of ice. However, not all of the detected events were likely caused by this effect.

One potential interpretation of the HF events is that they were related to increased surface and subsurface runoff. During installation of the Gulkana equipment, increased surface runoff was observed with increasing temperatures. As temperatures rose above freezing the surface of the glacier became more active (in terms of runoff) and more liquid water was drained through moulins. Studies on surface runoff suggested increased activity corresponded with increasing temperatures (Carmichael et al., 2012, 2015; MacAyeal et al., 2019). The event duration (~2 seconds) matched fluid resonances observed in volcanic-glacier systems (Métaxian et al., 2003), although the frequency content above 5 Hz suggested cracking. The directionality of the HF events detected at Gulkana indicated they might have originated toward the ablation zone of the glacier where melt and runoff flow downhill as stream. Although Europa or some icy ocean worlds are unlikely to have surface runoff, there could be water-ice interactions within the ice shells which could mimic the

observed drainage events. Titan, which does have liquid hydrocarbons on the surface (Hayes et al., 2008; Mitri et al., 2007) could exhibit similar signals to those we observed.

Another possible source for HF events at Gulkana were rockfalls. During the installation, numerous rockfalls were heard in the local vicinity. Previous studies (Norris, 1994; Zimmer & Sitar, 2015) detected rockfalls using similar filters and STA/LTA parameters that we used for HF detections. These studies also showed that rockfalls within a kilometer should be detectable. Many of the events detected in cluster 3 also pointed in the direction of greatest topography changes for the nearby range (Gesch et al., 2009) (Fig 4.11). On icy ocean worlds, there could be analogous signals from ice breaking near rifting zones or locally high topography.

The detection algorithm for the Greenland data found only a tenth of the number of events detected at Gulkana. Generally speaking, the events' occurrence rate was not coincident with surface temperature ($r=0.348$, $p=1.23 \times 10^{-6}$) or changes in temperature ($r=-0.112$, $p=0.132$). There was a periodicity to the detection rate of the events. Although the recovered azimuths suggested an easterly origin, there was a 180° ambiguity to the events. If the events did occur due west, that was the direction of the nearest coastline and terminus for some glaciers. The signal quality of the Greenland events were not as high as Gulkana, and it was difficult for a stack to produce a clear mean signal for each cluster (Figure 4.10). One reason the events at Greenland were noisier could be due to the local wind speeds. High winds were correlated with increased background noise, which reduced the ability to detect events. Previous studies have shown that the 5-15 Hz range can be particularly affected by wind speeds (Dybing et al., 2019). If an icy ocean world lander were to land on a Greenland analogous site, it may be more difficult to detect local events and determine

their sources but a higher percentage of tectonic events might be recorded. For a mission like InSight that has global scale goals, this tradeoff would be acceptable. If, however, a mission goal was to determine seismicity of a potentially active fault or investigate cryovolcanism, it would be better to have a landing site closer to the targeted area of study.

Two key differences between Gulkana and Greenland were the quantity and quality of events. There were far fewer detected events at the Greenland analog than in Gulkana. One possible reason for the discrepancy could be that the SIIOS site on Gulkana was relatively close to the ablation zone, while the SIIOS site in Greenland was far from the ablation zone. Proximity near the ablation zone would increase the number of detectable events. These findings indicated a single-station or small-aperture array deployed on an icy ocean world would be able to detect the diurnal influences of local events and determine the direction from which the events originate. Such a finding on an icy ocean world could help constrain the mechanisms driving local seismicity and regions of high activity.

4.5.3 VHF Detections

The VHF signals were found through the template detector. Similar signals were detected at both field sites. Due to the repetition of the signal, cultural (anthropogenic) sources were considered along with natural sources. Studies have shown that poles and equipment left in the field can have similar seismic signatures to moulins (Carmichael, 2019). To try and identify the events, we focused on the repeating nature of the signals, short reoccurrence rate, VHF content and event durations characteristics. Previous studies (Allstadt & Malone, 2014) have shown that repeating signals could be due to snow loading. While the Greenland site did accumulate ~1 meter of snow, Gulkana did not see significant precipitation. Furthermore, the previous study noted the repeating signals had a

reoccurrence rate of several minutes, not tenths of seconds and the frequency content of the repeating events was 1-5 Hz. While snow loading may have contributed to some signals seen at the Greenland site, snow loading was unlikely a contributing signal at the Gulkana site.

Moulins were known to exhibit HF energy and have short durations (Carmichael et al., 2015). However, they were more likely to contribute to the HF (<10 Hz) diurnal signals we observed, not the VHF content which dominated at frequencies above 100 Hz. Additionally, moulins signals tended to be observed during early morning hours when they become more active from increased melt while background noise is still low. Moulins were ruled out as a potential source for the Greenland site because none were observed near our site. At Gulkana, moulins might have contributed to some of the HF diurnal signals, but could not explain the repeating nature and very short duration of the VHF signals.

One plausible explanation would be the effect of cultural influences such as hard drive spinning, or effects of the lander. At the Greenland field site, the signal was detected by both the small array and the remote array. Because the remote stations also recorded the signal, the aluminum vault and mock-lander were eliminated as possible sources. Polarization analysis of the signals also indicated that the remote stations pointed in different directions, likely due to the different positioning of the poles relative to the station. Longer duration seismograms from day 09 June 2018 around 12:00 UTC, were converted to audio which revealed that the signals were likely caused by bamboo poles. Because the signals had very high dominant frequencies, the time-series of the data did not require resampling to “speed up” the amplitudes so they could be audible to human hearing. Audio files were also made using time-series when helicopters were in the vicinity. This

process indicated the signals caused by the helicopter were similar but not an exact match. The characteristic spectra of the events also helped to identify slight differences between helicopter signals and pole signals. This would explain why the helicopter signal was similar; the helicopters likely caused the poles to move as if there was a strong wind. A review of field notes did reveal that some poles had flags that were left in the field so the demobilization team could spot the field site from a helicopter. The flags were attached to bamboo poles that were roughly 1 meter in length. The 4th harmonic for a 1 meter cylinder with one fixed end is roughly 320 Hz, the same as the characteristic frequency. Based on these results, it was likely the VHF signals recorded at the Greenland site were caused by the poles moving in the wind. It was noted that when the winds were at the highest, these events were not detected. Visual inspection of the time-series data confirmed that no events had occurred during periods of high winds (>10 m/s). It is possible the winds were strong enough to cause the background noise to increase above the signal or were strong enough to force the poles to stop swaying.

At Gulkana there were no bamboo poles with flags, however there was a cache of equipment left at the field site that was covered with tarp and a bamboo pole with a GoPro camera attached to it. This pole was located due north of the small-aperture array and the equipment cache was due south of the array. Although the tarp was secured with tie lines, it was still able to flap from wind gusts. The azimuths tended point in the direction of 330-350° (due north). This direction was towards a nearby GoPro camera setup, and notably not a common azimuth for most HF detections (Fig. 4.12). As with the data recorded at the Greenland site, seismograms were converted to audio files to help identify possible sources. The signals sounded like a semi-regular thump. Background signals without the

VHF signals were also turned into audio to verify that the thumping noise was only heard when VHF events were recorded. The background signals sounded like blowing wind or static without any thumping or flapping noises. Based on this evidence we believe the VHF signals were caused by a combination the GoPro camera setup and equipment cache left behind in the field.

The detections of the VHF indicated the importance of distinguishing signal sources. Possible cultural sources should be considered for future geophysical missions. At both Greenland and Gulkana, equipment left in the field created sources that obscured other local, naturally occurring, events. This is not unique to our site. Poles have previously been shown to create seismic noise (Carmichael, 2019). Previous planetary missions have also detected cultural and anthropogenic influences on seismic signals. The Apollo missions recorded astronaut movements (Khatib et al., 2020; Nakamura, 1976) which were expected. Thermal moonquakes have also been associated with equipment left on the lunar surface (Weber et al., 2018) long after the astronauts left the surface. The InSight mission on Mars has also seen possible signals originating from the lander (Giardini et al., 2020). While future missions may not have bamboo poles, flags, or tarped covered equipment, the missions may include other instrumentation that can generate seismic signals. Titan, in particular does have an atmosphere which could produce wind and produce similar signals to those we observed. It will be vital for future missions to determine whether signals are from landers or anthropogenic origins, or if the events have a natural origin that can be used to characterize the local environment.

4.5 Summary

The SIIOS analog sites were able to provide data to investigate how single-station seismometers can detect and identify sources of seismicity. A geophysical mission to an icy ocean world not only care about large teleseismic or regional events, but also local events. In addition to naturally occurring sources, future missions would need to determine if anthropogenic sources are causing local events.

Both sites were able to illustrate a single-station was capable of detecting numerous teleseismic and regional events. Previous terrestrial studies have indicated this capability (Bose et al., 2017; Frohlich & Pulliam, 1999; Panning et al., 2015), but we have expanded on these studies by using a flight candidate instrument, in two analogous icy ocean world environments. Not only did we test single-station capabilities, but we were also able to quantify a small-aperture array designed to mimic a robotic deployment. The setups on Gulkana and in Greenland further allowed us to quantify capabilities in high activity and low activity locations. Despite high levels of local background noise at the Gulkana site, distant tectonic events were still detected. However, the small-aperture arrays were able to detect more events with less false positives from instrumental anomalies. Although the small-aperture array approach produced more detections, many of the detections made at Gulkana were from local events not tectonic events. Since the local events can still yield information regarding the local environment, it may be preferred to have more data from any natural event, than risk not detecting events to reduce false positives from glitches.

The HF and VHF events themselves were able to reveal characteristics of the environment. HF events at Gulkana could be linked to increases in temperature although increased wind may have reduced the ability to detect events. Wind-induced background

noise limiting detections has been observed both on Earth (Dybing et al., 2019) as well on Mars (Giardini et al., 2020). The HF events at Gulkana were likely due to cracking near the glacier terminus as well as runoff. Some of the events were likely caused by nearby rockfalls. The Greenland site HF data was also far noisier than the Gulkana data despite general lower levels of background noise at lower frequencies. Increased wind at Greenland could have increased the background noise. Thicker ice or increased distance from detected events would further reduce signal-to-noise ratios.

In addition to naturally occurring local events, both sites also exhibited a possible cultural signal. VHF events were detected at both sites and were likely caused in part by equipment left in the field. Future analog experiments as well as future missions should be aware of possible anthropogenic/cultural signals. While these signals could be used to constrain near-surface structure, they add to background noise and obscured naturally occurring signals.

4.6 Acknowledgements and Data Resources

This project was supported by NASA PSTAR Grant #80NSSC17K0229 and NASA NESSF # 80NSSC18K1260. SIOS data used in this study can be obtained from the Incorporated Research Institutions for Seismology (IRIS) Data Management Center (DMC) with network code YH (2017) and doi: 10.7914/SN/ YH_2017 for Gulkana and network code 9C (2018) for the Greenland data. Maps and previous data on Gulkana are available through the U.S. Geological Survey (USGS; https://alaska.usgs.gov/portal/project.php?project_id=108). Gulkana weather data can be found via https://waterdata.usgs.gov/ak/nwis/uv?site_no=15478038. Python code for STA/LTA and Coincidence triggers were generated using the open-source project, ObsPy (Beyreuther et

al., 2010). The reference catalog was built using the USGS ComCat web service provided by the ANSS.

Chapter 5: Conclusions and Future Work

Overview

This thesis has shown the utility of single-station and small-aperture seismic arrays in analog settings for meeting key science objectives. Given predicted seismicity rates, a single-station seismometer can recover the core-mantle boundary of large terrestrial (e.g. rocky) planets, and detect, identify, and locate tectonic and local seismicity. Environmental analog settings in icy ocean world settings presented the unique opportunity to study seismic sources and instrument capabilities in high-fidelity ways for future missions. In the following section I summarize my findings from Chapters 2-4 and discuss the broader implications of their results.

5.1 Summary of Conclusions

One of the most understudied aspects of planetary sciences has been the interior structures of rocky bodies. Dedicated geophysical missions can constrain internal layers and provide a wealth of information on the history and evolution of planetary bodies. Seismological observations would be a key component of these investigations. My dissertation outlines practical methodologies and can be adapted for a wide range of bodies in our solar system.

5.1.1 Deep Interior Structure Constraints with a Single-Station Seismometer

Chapter 2 focused on a single-station seismometer's ability to detect the core-mantle boundary of Earth and Mars. The key finding of this chapter was that the quantity of events detected will ultimately determine the uncertainty in core depth. Increasing the number of stackable events decreased uncertainty. By increasing the number of stackable events, a coherent signal was allowed to rise above the background signal. Increasing the quantity of events also likely decreased location bias effects, e.g. crustal variations or deep mantle velocity heterogeneities. Furthermore, source location uncertainty effects were diminished by increased event quantity. When five or less events were used to find the core depth, uncertainties increased by up to 10 km and 25 km for added 1° errors and 10% errors, respectively. However, when 15 events were stacked, the uncertainty in core depths only decreased by 2 km and 10 km for added 1° errors and 10% errors, respectively. Lastly, a larger quantity of events in the catalog might be useful for detecting heterogeneities within the mantle. It was shown that when events occur from diverse azimuths, different recovered core depths indicated the presence of deep mantle heterogeneities such as LLSVPs and ULVZs.

A somewhat surprising finding of this chapter was that increasing the quality of events did not necessarily reduce core depth uncertainties or increase the recovery rate. High quality events are still subjected to the causes of velocity variations and were more likely to have a source location bias. Utilizing *ScS* multiples also did not necessarily lead to a better core recovery. The multiples had low signal-to-noise ratios, in most cases below 1.0. While the multiples still produced positive stacks, the resulting stack was less coherent and tended to have larger uncertainties.

Based on this chapter's conclusions, a single-station seismometer deployed on rocky bodies would be able to recover the core depth provided a sufficient number of events were detected. The events are not required to have high signal-to-noise, so long as S and ScS can be identified. Source location errors can be overcome by a larger quantity of events. Numerous events from diverse locations may also reveal mantle heterogeneities.

While the chapter was tailored to fit predicted Martian seismicity rates due to the timeliness of the InSight mission, the algorithm can be adjusted for any rocky planetary surface. To adjust to other settings, the quantity of events should mimic seismicity rates and anticipated mission durations. For a body like Earth, which has higher anticipated seismicity, the investigated quantity of events would increase. For the Moon, which is anticipated to have lower rates of seismicity, the quantity of events would decrease. A mission to Venus would be more limited in expected mission lifetime and thus, would likely rely on a smaller number of events. While this chapter also focused on ScS and its multiples, additional phases such as PcP , SKS , or PKP could also be investigated to determine their abilities to constrain core properties.

5.1.2 Lessons Learned and Recommendations for Deployments on Icy Ocean Worlds

Chapter 3 presented datasets collected at two icy ocean world environmental geophysical analogs; Gulkana Glacier in Alaska and a site in Northwest Greenland. These geophysical analog sites allowed the Seismometer to Investigate Ice and Ocean Structure (SIOS) project to test deployment schemes and flight-candidate instruments in environments that mimic icy ocean worlds. A major finding from both field campaigns was the flight-candidate, Silicon Audio seismometer, performs comparably to traditional

terrestrial equipment across a wide range of frequencies and periods. An advantage of the flight-candidate instrument was that it was less effected by tilting in the field, was more compact, and low mass, qualities which would enhance its chances of selection for a future mission.

At the field site in Gulkana, the instruments were less protected from wind and thermal variations. For this reason, the instruments deployed on top of a mock-lander recorded noise up to 50 dB higher than the same instrumentation deployed on the ground. At Greenland, where the instruments were directly coupled to the lander and then contained in an aluminum vault and buried, the instruments recorded similar noise with the exception of the lander resonant frequency (~ 100 Hz). Both studies suggest that some isolation of the seismometer from the local environment and improved ground coupling are desirable regardless of the land environment.

The two field sites allowed me to study the difference between an icy ocean world analog site for a more seismically active area (Gulkana) and in a seismically quieter area (Greenland). This is comparable to being near a tidally modulated rift, or active plume on Europa or Enceladus, versus a region with no currently known surface activity that is tectonically inactive. Gulkana was situated closer to a tectonically active area (a major plate boundary and subduction zone) and experienced larger tectonic events during our passive experiment. Greenland was further from active plate boundaries and located in a more stable local environment. Furthermore, the site in Greenland was relatively far from the ice ablation zone and the local ice thickness was an order of magnitude thicker than Gulkana. These conditions meant the local Greenland seismicity was predicted to be lower than Gulkana seismicity resulting in an overall lower background noise. We would expect a

similar pattern on icy ocean worlds, where seismicity near an active region would increase the background noise of the icy ocean world environment for a future seismometer deployment.

5.1.3 Advantages and Recommendations for Single-Station and Small-Aperture Array Seismology

Chapter 4 utilized the datasets described in Chapter 3 to detect, identify and if possible, locate sources of seismicity. At both sites, the small-aperture array was able to detect more events than using only a single-station. The use of a coincidence trigger reduced the number of false positives from instrumental anomalies while finding smaller events that the single-station missed. However, the cost of a small-aperture array is not only financial but an increase in the amount of data, requiring increased bandwidth and data storage on future missions. The predicted differences in site locations manifested in catalogs of events for each site. The algorithm using Gulkana data detected more tectonic events in terms of quantity detected, but a larger percentage of known events were detected with the Greenland data. As Greenland was a quieter site, more events were able to trigger the detection algorithm.

Gulkana was in part noisier because there was more local seismicity than the Greenland site. Algorithms using data collected at Gulkana detected almost ten times the number of HF events than using data from the Greenland site. The HF events at Gulkana exhibited a diurnal behavior. A location algorithm was able to determine that most of the HF events at Gulkana originated south of the array, toward the glacier's terminus, suggesting the events were caused by a combination of ice cracking and drainage from the glacier. Some HF events could be rockfalls, as their azimuths were toward the direction of

greatest topographic change. The detected Greenland HF events were not strongly tied to changes in temperature and had azimuths suggesting origins due east of the SIIOS array. It was possible there is a 180° ambiguity and the events actually originated toward the closest coastline where the ice sheet terminated. HF events at Greenland were more difficult to detect than at Gulkana due to decreased signal-to-noise ratio and the presence of VHF events.

In addition to HF events, VHF events were detected at both sites. The signals were identified by characteristic frequencies and the repetition of occurrence intervals. Converting seismic signals to audio signals helped to identify the sources. At Greenland, the VHF source was likely bamboo poles left in the field to identify our equipment. The Gulkana VHF signals were likely tarps covering bins of equipment or a Go-Pro camera attached to a pole, as the recovered azimuths point in that direction.

The seismicity of both locations revealed that a small-aperture array can better detect tectonic signals than a single-station. A single-station is still capable of detecting events and can be used to characterize the local seismic environment. A more active site can increase the overall number of detected events, but increased noise from local seismicity may reduce the ability to detect all potentially detectable events. Future missions should consider whether their mission goals are best met using larger tectonic events or characterizing a specific local environment. In addition to naturally occurring events, non-seismic instrumentation and equipment are capable of producing seismically detectable signals. Glitches and cultural effects can reduce the detectability of naturally occurring events. Glitches were a common false-positive for single-station detection approaches, and in the case of the VHF events, obscured detection of HF events for period up to several

minutes. Although using the small-aperture array eliminated most false-positives from glitches, the VHF events were observed on most stations concurrently. Future missions will need to determine the origin of the sources to better understand natural phenomena and if possible, mitigate their effects.

5.2 Continued Work

5.2.1 Applications to InSight mission

InSight successfully landed in 2018 and as of May 2020, detected several hundred events. As the number of marsquakes from InSight increases, I can begin to apply my approach from Chapter 2 to investigate the Martian core-mantle boundary. To accomplish this task the most up-to-date interior structure models and constraints will need to be used. In addition to constraints from the SEIS instrumentation, constraints can also be provided by tidal measurements and the RISE instrumentation. As the MSS updates interior models, predicted arrival times of S and ScS will also be improved. A main conclusion of Chapter 2 was that the quantity of events used to find the core is a key factor in recovering the core and the resulting uncertainty. For this reason, the recovered core depth and associated uncertainty will be updated as more events are detected in the future. Thus, this work will likely continue for as InSight records data and the MQS catalog is updated.

The recovered core depth will have significant implications. The size and state of the core can further be used to help constrain the mineralogy and chemical composition of the lower mantle and core. These results provide parameters for modelling the internal evolution and state of the Martian mantle and magnetic dynamo. Results can further be

used to compare the evolutions Mars, Earth, and the Moon to help explain why the planets evolved so differently.

5.2.3 Future Icy Ocean World Deployments and Investigations

Chapter 4 focused on using STA/LTA approaches for detecting events. It was shown that while this method can find numerous events, visual inspection can still find more events. Additional approaches could be tested to determine how they perform compared to STA/LTA and visual inspection. Machine and deep learning tools could be implemented in order to find events. Neural networks could be trained to find events in the temporal (Perol et al., 2018) or in the spectral domain. Such approaches could automate the detection of seismicity on future missions, improving the science return of the seismic instrumentation.

While this thesis focused primarily on the small-aperture arrays in the SIOS deployments, the remote stations of the 1-km array in Greenland and other instruments could be used for additional analysis. The more remote array in particular could be used to further investigate how tectonic and local events could be located once stations are separated by more than ~ 1 m. The stations coupled to the mock-lander could also be tested to determine how their catalogs of events compares to the stations on the ground. Additional stations could be used to quantify how instrumental anomalies degrade seismic data and if there are any relationships between glitch occurrences and the local environment. If such relationship were found, it would have implications for sending this instrument into environments that would be colder and likely without wind.

In addition to the SIOS experiment, additional field work could be completed elsewhere, in similar analog environments that replicate other aspects of icy ocean worlds.

In particular, Antarctica and the Ross Ice Shelf are excellent candidate analogs for icy ocean worlds due to the large-scale ice decoupled from land and modulated by tidal forcing. Like the SIOS deployment, large teleseismic or regional tectonic events could mimic large icequakes in ice shells. Smaller HF events would mimic ice cracking, or interactions between liquid and solid water. VHF events created by field equipment would mimic seismic signals created by lander noise or other equipment. Since the Ross Ice Shelf has several hundred meters of ice overlying an ocean (Clough & Hansen, 1979; Thomas & MacAyeal, 1982) it would provide the opportunity to test methods for constraining ice shell thickness along with ocean depth. The effects of tides could also be studied (Olinger et al., 2019). Mount Erebus provides an analog for cryovolcanism. This site would have both glacial and volcanic sources.

5.4 Summary

This dissertation has illustrated how even a single-station seismometer can be a powerful tool for answering numerous science questions. Although the small-aperture seismic array had better detection capabilities than the single-station, this approach adds complexity and cost and data volume constraints that need to be considered. With a single-station, deep interior structure can be investigated and provide key parameters and constraints for additional modelling and understanding of how planets form and evolve through time. Seismicity studies can reveal where planets are most active and the processes generating seismicity. Such studies have provided support for plate-tectonics theory on Earth and shown the absence of such plate motion on the Moon. On a more local scale, seismicity can indicate where activity is concentrated and why it may become more active at different times.

The use of analog studies in relevant settings in relevant planetary settings is critical for future mission planning. This thesis showed that quantity of events has a greater impact than quality of events when trying to recover deep interior structure. High quality events had a location bias and were still subjected to velocity variations through the crust and mantle. Comparison of icy ocean world analogs quantified the trade-offs between an active and quiet site for detecting tectonic and local seismicity. The use of analog settings as opposed to modeling further showed the importance of potential cultural or instrument effects. Glitches and cultural noise hindered the detection of naturally occurring effects. The quantification of this effect would not be possible through modelling alone.

Future geophysical missions should consider sending single-station, and if possible, a small-aperture seismometer array to characterize global and local seismicity, and constrain local structure. Planetary analog studies provided unique opportunities to test approaches and instrumentation in planetary-like environments. By using planetary analog studies in appropriate settings prior to landing and data recording, future missions will be better prepared. *Ad astra.*

Appendices

A.1 Catalog of Events Detected by SIIOS Gulkana Array. The onset time, magnitude (Mw), Latitude, Longitude, and depth (km) are the values cited by the ComCat catalog. Epicentral distance and azimuth are calculated using the center of the small array as reference. Detection method refers to either approaches using either a single-station or the small-aperture array.

Time	Mw	Latitude	Longitude	Depth (km)	Epicentral distance	Azimuth	Detection Method
9/20/17 23:54	2.8	36.53	-98.97	5	38.67	111.28	Array
9/20/17 22:57	4.4	-19.99	-70.98	12.56	101.06	112.72	Array
9/20/17 22:36	4.6	-5.14	147.91	10	84.41	246.78	Array
9/20/17 22:17	5.2	-5.09	147.97	10	84.34	246.74	Single Station & Array
9/20/17 22:13	5.9	-5.08	147.83	10	84.4	246.87	Single Station
9/20/17 20:09	6.4	-18.79	169.09	197	89.37	222.47	Single Station & Array
9/20/17 19:56	2.5	36.62	-98.06	5.828	38.98	110.21	Array
9/20/17 19:42	4	-17.51	-178.79	518.75	84.87	211.79	Array
9/20/17 18:22	2.71	32.38	-115.39	15.18	36.18	134.29	Single Station & Array
9/20/17 17:10	3.65	40.89	-121.98	16.86	26.28	137.24	Single Station
9/20/17 16:54	3.18	36.83	-121.55	3.48	30.16	139.87	Array
9/20/17 16:37	6.1	37.98	144.66	11	47.83	272.72	Single Station & Array
9/20/17 16:25	5.3	-10.2	118.88	10.84	101.66	270.45	Single Station & Array

9/20/17 16:02	4.4	33.96	135.44	44.93	55.31	277.82	Array
9/20/17 15:08	4.4	36.59	70.9	194.83	76.03	330.66	Single Station & Array
9/20/17 15:06	4.1	5.13	-82.86	10	73.36	112.71	Array
9/20/17 14:37	4.1	15.77	-95.32	33.23	58.64	120.17	Array
9/20/17 14:29	5.4	23.33	121.78	20.22	70.52	283.39	Single Station & Array
9/20/17 14:29	2.76	40.25	-124.18	11.38	26.23	141.29	Array
9/20/17 13:22	4.6	1.23	132.57	10	85.32	263.41	Array
9/20/17 12:55	4.4	-2.93	139.82	47.94	85.85	255.05	Array
9/20/17 12:25	5.1	1.15	132.71	10	85.33	263.25	Array
9/20/17 12:24	2.7	42.61	-111.46	7.67	28.45	120.35	Single Station & Array
9/20/17 11:58	4.2	-5.95	154.8	175.48	82.38	240.13	Array
9/20/17 10:39	4.7	15.24	-93.39	68.02	59.88	118.45	Single Station & Array
9/20/17 9:59	3.6	51.68	-170.52	40.62	17.59	240.54	Single Station & Array
9/20/17 9:47	4.2	-10.18	162	56.91	83.61	231.87	Single Station & Array
9/20/17 9:37	3.8	55.34	-160.05	69.1	10.85	229.81	Array
9/20/17 9:17	4.2	13.54	144.61	124.19	68.97	258.13	Array
9/20/17 9:15	4.1	18.42	-68.15	172.14	67.9	92.77	Single Station & Array
9/20/17 9:01	4.8	30.61	141.04	38.85	55.64	270.78	Array
9/20/17 8:40	4.4	37.87	22.65	35.41	78.41	9.59	Single Station & Array
9/20/17 8:23	2.8	42.58	-111.43	7.76	28.48	120.34	Array
9/20/17 8:15	2.56	19.39	-155.28	2.782	44.4	193.36	Array

9/20/17 8:10	2.6	42.58	-111.43	7.57	28.48	120.35	Array
9/20/17 7:47	4.5	44.46	148.98	34.94	40.7	274.56	Array
9/20/17 7:31	2.7	53.33	-160.6	10	12.68	225.45	Array
9/20/17 7:10	4.6	-6.9	128.28	282.21	94.5	263.6	Array
9/20/17 6:59	4.6	14.02	146.64	10	67.66	256.47	Array
9/20/17 6:30	4.4	27.92	56.81	24.32	87.12	340.45	Single Station & Array
9/20/17 6:02	3	35.56	-96.74	5	40.44	109.65	Single Station & Array
9/20/17 4:49	4	15.98	-95.15	37.4	58.51	119.89	Array
9/20/17 4:15	4.5	15.57	-95.03	35	58.93	119.96	Array
9/20/17 0:44	4.5	-3.91	141.54	43.33	85.99	253.07	Array
9/19/17 23:26	3	42.59	-111.42	9.63	28.48	120.32	Array
9/19/17 22:17	3.1	36.46	-98.8	5.377	38.81	111.15	Array
9/19/17 21:31	4.3	2.98	96.84	59.69	99.37	296.39	Single Station
9/19/17 21:13	5	15.26	-94.73	22.51	59.34	119.8	Array
9/19/17 20:36	3.6	57.9	-156.48	244.9	7.62	230.29	Array
9/19/17 18:42	2.8	52.06	-178.83	206.12	20.74	253	Single Station
9/19/17 18:14	7.1	18.55	-98.49	48	54.87	122.15	Single Station & Array
9/19/17 17:12	4.6	-7.45	128.13	167.65	95.06	263.48	Array
9/19/17 16:45	2.7	42.61	-111.47	7.7	28.45	120.37	Single Station & Array
9/19/17 13:26	5.1	27.93	53.99	10	87.51	342.92	Single Station & Array
9/19/17 12:48	4.4	-2.13	-78.73	112.4	81.68	111.96	Single Station & Array
9/19/17 12:46	3	51.07	-179.16	6.09	21.59	251.52	Single Station

9/19/17 12:04	4.4	-20	-173.94	10	86.22	206.73	Array
9/19/17 11:57	4.5	17.53	-62.11	51.77	71.39	87.81	Single Station & Array
9/19/17 9:55	3.03	19.2	-67.72	9	67.4	91.98	Array
9/19/17 7:58	4.9	15.15	-94.2	18.1	59.64	119.32	Single Station
9/19/17 7:53	5.5	15.11	-94.14	29.73	59.7	119.28	Array
9/19/17 7:03	4.9	15.66	-94.65	55	59	119.54	Array
9/19/17 6:37	4.9	-11.05	162.56	26.64	84.23	231.04	Array
9/19/17 6:20	3.61	34.09	-118.48	10.48	33.63	137.35	Array
9/19/17 4:20	4.3	15.54	-94.74	33.94	59.08	119.69	Array
9/19/17 4:10	3.54	17.43	-68.66	35	68.54	93.73	Array
9/19/17 4:01	4.5	-29.02	-177.57	67.87	95.75	207.89	Array
9/19/17 3:11	4.6	-20.78	169.74	61.18	91.07	221.26	Array
9/19/17 1:23	4.3	15.31	-94.6	35	59.34	119.65	Single Station
9/19/17 1:12	2.67	41.27	-111.72	12.54	29.49	122.12	Single Station & Array
9/19/17 0:38	2.5	60.21	-152.02	73.3	4.37	228.61	Array
9/18/17 23:52	2.8	44.44	-105.46	0	29.36	110.77	Array
9/18/17 21:20	2.77	19.03	-66.5	9	68.11	90.97	Single Station
9/18/17 20:57	4.7	-52.83	-4.58	10	157.28	81.09	Array
9/18/17 19:51	4.9	15.3	-94.82	20.1	59.26	119.88	Array
9/18/17 18:24	3.51	31.03	-116.66	5.16	37.03	136.8	Array
9/18/17 17:49	4.3	15.69	-95.28	40.33	58.72	120.16	Array
9/18/17 17:25	4.2	16.1	-94.84	41.16	58.52	119.52	Single Station & Array
9/18/17 17:21	3.28	40.7	-111.61	10.96	30.03	122.56	Single Station

9/18/17 16:25	4.4	-20.47	-177.31	373.72	87.39	209.7	Single Station
9/18/17 15:35	4.3	-31.81	-72.17	10	111.13	119.26	Array
9/18/17 15:23	4.5	23.9	141.88	78.83	61.05	266.04	Array
9/18/17 14:19	5.6	15.26	-94.57	10	59.4	119.64	Array
9/18/17 14:06	4.6	-4.08	143.3	108.39	85.39	251.41	Single Station & Array
9/18/17 13:46	5.9	-31.82	-72.13	17	111.16	119.23	Single Station & Array
9/18/17 12:11	5	-30.31	-177.95	32.88	97.09	207.9	Single Station & Array
9/18/17 10:18	3.6	63.54	-149.54	107.9	1.87	280.28	Single Station & Array
9/18/17 9:41	4.2	39.15	43.67	10	77.33	352.79	Single Station
9/18/17 6:10	4.2	-11.36	-75.85	107.44	91.26	113.23	Array
9/18/17 3:50	3	55.77	-153.02	33	8.42	210.56	Single Station & Array
9/18/17 2:14	4.1	15.03	-94.35	10	59.69	119.53	Array
9/18/17 1:01	4	14.82	-94.52	18.19	59.81	119.8	Array
9/18/17 0:32	4.4	-8.13	119.36	41.72	99.61	270.99	Array
9/17/17 23:12	4.9	-4.64	149.57	588.19	83.27	245.47	Array
9/17/17 22:22	5	-30.28	-177.97	44.3	97.06	207.92	Single Station
9/17/17 22:16	5	-21.83	169.09	12.83	92.26	221.49	Single Station
9/17/17 21:54	4.7	-55.37	-28.34	10	148.34	105.38	Array
9/17/17 21:49	4.5	21.66	94.57	97.03	83.08	305.84	Single Station
9/17/17 21:21	4.7	-20.25	-69.27	99.2	102.01	111.37	Single Station
9/17/17 20:57	4.5	-19.54	-177.52	564	86.54	210.12	Array
9/17/17 20:29	4.9	-18.98	-174.95	129.26	85.44	207.88	Single Station

9/17/17 19:28	2.5	42.59	-111.43	4.84	28.48	120.33	Single Station & Array
9/17/17 17:53	4	15.42	-94.93	34.09	59.11	119.94	Single Station
9/17/17 15:16	4.3	-6.46	148.97	35	85.17	245.26	Array
9/17/17 14:50	5.4	-16.64	-173.64	30.39	82.88	207.18	Array
9/17/17 14:48	5	12.82	92.1	26.18	92.15	304.61	Array
9/17/17 13:30	4.9	-21.01	-11.76	10	127.59	58.48	Array
9/17/17 13:12	4	15.5	-94.45	7.94	59.22	119.41	Array
9/17/17 9:31	4.6	-59.69	-26.39	10	151.79	111.04	Array
9/17/17 8:17	2.54	42.58	-111.45	2	28.48	120.38	Array
9/17/17 7:49	4.6	-23.88	-66.74	236.16	106.31	110.91	Array
9/17/17 1:16	4.4	-25.77	-176.69	71.26	92.41	207.9	Single Station
9/17/17 0:41	4.3	-10.43	123.97	23.54	99.58	265.81	Array
9/16/17 23:56	2.7	59.86	-136.76	2.62	5.34	125.74	Single Station
9/16/17 23:43	2.5	59.87	-136.82	8.54	5.31	125.88	Single Station
9/16/17 23:38	5	59.87	-136.79	6.55	5.32	125.8	Single Station & Array
9/16/17 22:53	4.1	-6.77	130.24	121.27	93.52	261.91	Array
9/16/17 19:35	5.1	15.23	-94.7	12.76	59.38	119.79	Single Station
9/16/17 18:58	4.4	15.62	-94.78	10	58.99	119.69	Single Station
9/16/17 16:17	2.6	61.9	-150.79	60.5	2.83	243.44	Single Station & Array
9/16/17 12:36	5.1	-6.4	154.97	84.07	82.73	239.8	Array
9/16/17 10:11	5.4	42.21	83.52	16	67.6	322.84	Array
9/16/17 8:53	4	15.7	-95.46	31.39	58.65	120.35	Single Station
9/16/17 7:50	3.64	18.45	-64.05	34	69.71	89.08	Array

9/16/17 6:57	4.5	3.64	128.47	61.45	85.01	268.18	Single Station
9/16/17 5:43	4.4	17.6	-60.73	14.79	71.95	86.56	Single Station & Array
9/16/17 5:35	4	15.27	-94.19	54.83	59.54	119.25	Array
9/16/17 3:57	4.3	13.23	-89.74	55.35	63.17	115.72	Array
9/16/17 2:45	2.6	54.1	-165.58	122.11	13.82	237.82	Array
9/16/17 2:22	4.4	17.08	-100.03	10.86	55.64	124.49	Single Station & Array
9/16/17 0:44	4.6	-23.98	69.63	10	134.39	312.78	Array
9/15/17 23:30	2.5	64.77	-139.93	4.15	2.83	55.48	Single Station
9/15/17 23:13	4.9	67.62	142.98	14.89	28.37	310.51	Single Station & Array
9/15/17 22:43	4.2	-4.68	151.57	135.04	82.5	243.62	Array
9/15/17 22:10	2.8	37.28	-97.97	4.85	38.46	109.55	Single Station
9/15/17 21:55	2.6	51.56	178.67	10	22.18	255.05	Single Station & Array
9/15/17 21:48	4.6	-5.91	147.56	108.71	85.25	246.77	Single Station
9/15/17 21:21	3.36	42.61	-111.44	5.28	28.46	120.32	Single Station
9/15/17 21:21	2.61	42.61	-111.44	5.68	28.46	120.32	Single Station
9/15/17 21:17	3	64.78	-139.89	8.2	2.85	55.56	Single Station & Array
9/15/17 20:08	3.2	59.87	-152.83	91.8	4.89	229.46	Array
9/15/17 19:58	3.43	19.19	-64.63	40	68.8	89.22	Single Station & Array
9/15/17 18:48	5.5	-55.44	-28.36	9	148.38	105.5	Single Station & Array
9/15/17 16:54	4.7	-31.32	-178.99	62.61	98.28	208.52	Single Station
9/15/17 16:46	4.6	-32.64	-178.55	28.94	99.47	207.82	Single Station

9/15/17 15:55	4.7	-51.95	140.49	10	128.85	229.56	Single Station
9/15/17 14:07	4	-7.03	118.28	10	99.11	272.46	Single Station & Array
9/15/17 13:04	3	37.28	-97.97	4.9	38.46	109.55	Single Station & Array
9/15/17 11:12	3.23	35.03	-119.3	11.48	32.5	137.88	Single Station & Array
9/15/17 10:39	3	42.59	-111.45	5.25	28.47	120.36	Single Station & Array
9/15/17 10:23	3.3	18.72	-65.04	49	69.03	89.82	Single Station
9/15/17 6:51	4.4	-21.92	179.58	639.82	89.51	212.16	Single Station
9/15/17 6:22	2.8	60.11	-153.5	151.7	4.96	234.17	Array
9/15/17 6:19	2.6	37.41	-121.81	-0.14	29.54	139.84	Single Station
9/15/17 4:59	2.78	37.42	-121.8	2.65	29.54	139.82	Array
9/15/17 2:45	4.4	15.26	-93.52	63.36	59.81	118.57	Array
9/15/17 1:45	3.04	19.2	-155.47	35.437	44.6	193.58	Array
9/15/17 1:44	3.9	15.27	-94.81	53.62	59.29	119.88	Array
9/15/17 1:38	5.2	-26.67	-112.29	10	93.68	150.71	Single Station & Array
9/15/17 1:11	4.3	15.31	-94.73	35.58	59.29	119.78	Array
9/15/17 0:48	4	-18.24	-178.75	601.11	85.56	211.57	Array
9/15/17 0:20	4.4	24.47	141.72	93.7	60.62	266.51	Array
9/15/17 0:07	4.1	-31.91	-67.31	136.67	113.16	115.38	Array
9/14/17 23:32	4.1	15.27	-93.67	45.83	59.74	118.72	Array
9/14/17 23:06	4.7	-15.33	-172.74	10	81.42	206.6	Array
9/14/17 22:21	5.2	-13.83	170.1	10	84.37	223.13	Array
9/14/17 21:58	4.1	-7.15	129.18	129.67	94.33	262.68	Array

9/14/17 21:26	4.4	-12.93	122.17	10	102.61	266.25	Single Station & Array
9/14/17 21:15	3.03	18.96	-67.86	5	67.55	92.23	Array
9/14/17 20:43	3.1	18.78	-67.54	5	67.85	92.02	Single Station
9/14/17 19:06	3.5	53.17	-166.74	45.14	14.98	237.54	Array
9/14/17 17:41	5.8	18.69	145.75	166	63.9	259.66	Single Station & Array
9/14/17 17:32	3.28	37.41	-121.81	-0.21	29.54	139.84	Array
9/14/17 16:37	4.3	37.97	142.58	32.79	48.78	274.52	Single Station & Array
9/14/17 16:03	3	57.73	-154.43	15	7.09	222.71	Single Station & Array
9/14/17 14:36	4.2	15.16	-93.69	50.96	59.84	118.79	Single Station & Array
9/14/17 14:33	4.4	15.31	-95.04	25.42	59.17	120.1	Array
9/14/17 14:14	3.8	17.72	-60.64	12.38	71.89	86.42	Single Station
9/14/17 13:54	3.32	17.9	-68.4	89	68.24	93.25	Single Station & Array
9/14/17 13:32	4.2	-10.55	34.26	10	127.28	0.41	Single Station & Array
9/14/17 13:11	4.3	-16.17	-176.29	393.23	82.99	209.78	Array
9/14/17 12:28	2.8	58.61	-155.1	140.4	6.61	229.64	Single Station
9/14/17 12:14	4.4	15.14	-94.2	34.35	59.65	119.32	Single Station
9/14/17 10:41	3.7	52.34	-168	9.91	16.09	237.81	Array
9/14/17 10:03	4.2	9.87	-78.47	10	70.93	106.44	Single Station
9/14/17 9:25	4.4	25.03	128.19	10	66.2	278.77	Array
9/14/17 8:54	2.53	40.12	-108.83	-3.25	31.6	119.56	Array
9/14/17 8:19	4.6	-12	-76.43	10	91.59	114.02	Array

9/14/17 7:38	4	15.73	-95.25	34.84	58.7	120.12	Array
9/14/17 7:04	4.1	-34.29	-72.7	12.58	113.13	120.93	Single Station
9/14/17 6:24	4	15.55	-94.69	43.43	59.08	119.63	Single Station
9/14/17 6:10	4.5	15.13	-94.32	35.74	59.61	119.45	Array
9/14/17 6:05	4.4	15.49	-94.71	25.87	59.13	119.68	Single Station & Array
9/14/17 5:49	3	36.74	-98.37	7.992	38.75	110.44	Array
9/14/17 5:36	3.2	51.6	-178.4	12.8	20.89	251.56	Array
9/14/17 4:14	3.4	37.28	-97.97	4.96	38.46	109.55	Array
9/14/17 3:41	4.4	18.22	145.67	141.07	64.35	259.49	Single Station & Array
9/14/17 3:40	4.32	18.22	-68.79	133	67.78	93.45	Array
9/14/17 2:54	3.2	42.54	-111.42	8.91	28.52	120.37	Single Station
9/14/17 1:53	3.1	42.66	22.93	10	73.67	8.91	Array
9/14/17 0:57	4	15.61	-94.97	32.32	58.92	119.89	Single Station
9/14/17 0:42	2.8	54.45	-161.24	14.85	11.97	229.89	Single Station & Array
9/14/17 0:27	4.6	35.82	139.6	53.24	51.89	275.52	Array
9/14/17 0:07	2.8	52.11	-174.28	78.84	18.78	247.08	Single Station & Array
9/13/17 23:21	4.3	-18.06	-69.44	143.42	99.98	110.52	Array
9/13/17 22:12	2.5	61.67	-146.39	29.1	1.66	196.17	Single Station & Array
9/13/17 19:37	4.6	-6.1	112.95	590.53	100.67	277.68	Array
9/13/17 17:33	3.2	37.47	-80.7	17.77	45.9	92.33	Array
9/13/17 16:59	4.4	15.8	-94.68	43.13	58.86	119.5	Single Station & Array
9/13/17 15:33	4.3	-4.88	152.13	54.06	82.46	243.02	Array

9/13/17 12:48	4.5	15.85	-93.7	95.22	59.2	118.48	Array
9/13/17 11:51	4.1	2.99	128.18	58.22	85.71	268.14	Single Station & Array
9/13/17 9:46	4.5	15.54	-94.74	31.41	59.07	119.68	Array
9/13/17 9:18	3.9	15.27	-94.24	42	59.52	119.3	Array
9/13/17 8:48	2.5	42.59	-111.45	6.05	28.46	120.36	Array
9/13/17 8:34	4.4	15.58	-95.19	10	58.86	120.13	Single Station
9/13/17 7:55	4.1	-2.43	139.25	26.3	85.65	255.78	Array
9/13/17 7:22	3.4	61.65	-145.59	24.8	1.62	182.94	Single Station
9/13/17 7:22	4.2	62.9	-149.92	79.6	2.07	261.78	Single Station & Array
9/13/17 6:39	4.6	-22.09	-179.06	539.95	89.36	210.89	Array
9/13/17 6:26	4.7	13.55	147.56	10	67.67	255.38	Array
9/13/17 6:20	2.62	37.49	-118.8	2.5	30.38	135.36	Array
9/13/17 5:02	4.2	-20.26	-70.96	11.75	101.32	112.82	Single Station
9/13/17 4:05	4.2	15.26	-94.45	35	59.44	119.52	Single Station & Array
9/13/17 2:43	4.4	15.29	-94.57	34.84	59.37	119.63	Array
9/13/17 2:17	3.12	19.09	-66.51	21	68.04	90.95	Single Station & Array
9/13/17 0:51	4.1	15.6	-95.32	29.98	58.8	120.25	Array
9/12/17 23:10	4.9	58.1	-32.46	10	48.28	40.69	Array
9/12/17 21:04	4.9	58.06	-32.37	10	48.33	40.66	Array
9/12/17 20:38	4.8	-15.08	-174.23	148.04	81.47	208.07	Single Station
9/12/17 17:59	4.1	15.79	-94.48	33.96	58.95	119.3	Array
9/12/17 17:33	4.3	-5.21	129.62	217.1	92.4	263.17	Single Station

9/12/17 16:58	4.5	15.28	-93.24	73.2	59.9	118.28	Single Station & Array
9/12/17 15:58	4.5	-7.57	129.32	115.97	94.64	262.38	Single Station & Array
9/12/17 15:28	5	15.06	-93.92	37.96	59.83	119.07	Single Station
9/12/17 15:25	4.4	15.87	-94.46	40.82	58.88	119.24	Array
9/12/17 15:23	2.51	42.51	-111.41	7.97	28.55	120.4	Single Station
9/12/17 15:09	4.5	-30.43	-177.29	12.38	97.06	207.31	Single Station
9/12/17 14:48	4.7	-14.1	167.65	43.3	85.4	225.31	Single Station
9/12/17 14:36	3.11	18.07	-67.89	112	68.33	92.71	Single Station
9/12/17 12:22	2.5	42.57	-111.42	8.3	28.5	120.34	Array
9/12/17 11:26	4.7	27.91	101.69	32.74	74.73	302.45	Array
9/12/17 11:06	4.2	15.89	-95.06	33.09	58.63	119.85	Array
9/12/17 8:26	3	52.11	-174.28	228.97	18.78	247.08	Single Station
9/12/17 7:10	4.5	-40.68	175.92	35.49	108.41	209.96	Array
9/12/17 6:43	4.6	55.2	-157.06	8.4	10	221.6	Array
9/12/17 6:00	4.9	-26.13	70.83	10	135.97	310.2	Array
9/12/17 5:20	4.6	15.03	-94.13	34.94	59.78	119.3	Single Station & Array
9/12/17 5:17	3.3	53.14	-166.72	25.6	14.99	237.45	Array
9/12/17 5:08	5.4	15.11	-93.97	42.49	59.77	119.1	Single Station & Array
9/12/17 4:04	2.8	21.63	-157.32	8.469	42.4	196.53	Single Station
9/12/17 4:00	2.63	18.53	-67.39	19	68.14	92.03	Array
9/12/17 2:53	4.4	-6.79	125.29	525.3	95.75	266.3	Single Station
9/12/17 2:09	4.7	15.9	-95.11	27.97	58.6	119.9	Single Station & Array

9/12/17 1:47	4.6	15.23	-94.36	48.87	59.51	119.44	Array
9/12/17 1:12	5.1	15.3	-94.47	17.32	59.4	119.52	Single Station & Array
9/12/17 1:00	4.6	15.05	-94.13	67.28	59.76	119.29	Array
9/12/17 0:52	2.8	42.58	-111.42	7.47	28.49	120.33	Single Station & Array
9/12/17 0:21	2.9	62.8	-152.17	8.1	3.1	264.34	Single Station
9/12/17 0:14	2.7	42.6	-111.45	6.65	28.46	120.35	Single Station
9/12/17 0:00	3.1	42.59	-111.46	9.11	28.46	120.38	Array

A.2 Catalog of Events from SIIOS Deployment in Greenland. The onset time, magnitude (Mw), Latitude, Longitude, and depth (km) are the values cited by the ComCat catalog.

Epicentral distance and azimuth are calculated using the center of the Array as reference.

Time	Mw	Latitude	Longitude	Depth (km)	Epicentral Distance	Azimuth	Detections
6/14/18 23:18	4.1	-18.20	-177.91	580.05	112.60	285.32	Single-Station
6/14/18 22:27	4.5	-12.70	-73.88	77.28	112.01	185.31	Single-Station
6/14/18 21:08	4.4	-14.89	-173.59	31.26	110.19	281.75	Single-Station & Array
6/14/18 19:15	4.1	-34.26	179.25	131.76	127.70	284.00	Single-Station
6/14/18 18:12	5.5	0.85	-26.13	10	90.11	136.95	Array
6/14/18 16:57	4.5	36.53	70.38	168.61	41.55	36.51	Array
6/14/18 15:04	4.7	64.70	-17.56	10	27.04	103.04	Array
6/14/18 12:17	2.75	19.39	-155.32	1.8	79.40	271.13	Array
6/14/18 1:46	4.3	36.61	71.36	96.37	41.48	35.62	Array
6/14/18 1:26	2.55	19.40	-155.28	-0.46	79.40	271.09	Array
6/14/18 1:16	2.55	19.40	-155.26	0.78	79.40	271.07	Array
6/14/18 0:42	4.4	30.86	78.28	10	47.41	30.24	Array
6/14/18 0:28	2.99	19.33	-155.15	2.26	79.49	270.95	Array
6/14/18 0:25	2.5	51.13	-179.55	22.41	44.52	303.14	Array
6/13/18 23:54	5.2	7.43	-80.57	10	92.83	192.75	Array
6/13/18 23:54	2.63	19.42	-155.27	-0.18	79.38	271.09	Array
6/13/18 23:06	4.9	-1.83	98.63	10	81.52	13.30	Single-Station
6/13/18 20:56	4.6	-20.24	-70.96	10	119.07	182.40	Array

6/13/18 20:21	4.3	1.99	126.23	30.02	81.72	345.14	Array
6/13/18 16:47	4.6	31.50	57.65	10	46.81	48.98	Array
6/13/18 16:20	2.7	56.15	-149.84	20.76	43.77	279.32	Array
6/13/18 10:33	5.1	-18.88	169.45	220.82	110.73	297.95	Single- Station & Array
6/13/18 9:28	4.3	14.61	-94.38	10	86.81	207.92	Array
6/13/18 5:05	2.59	18.14	-66.73	20	80.48	178.13	Array
6/13/18 4:14	2.72	19.44	-155.17	2.28	79.38	270.99	Array
6/13/18 2:07	5.4	-1.93	98.67	10	81.62	13.27	Array
6/13/18 0:14	2.6	34.41	-96.28	5	67.15	212.85	Array
6/12/18 23:46	5.6	-1.95	98.69	10	81.64	13.25	Array
6/12/18 23:45	5.2	50.59	156.35	84.62	40.48	323.33	Array
6/12/18 22:23	4.7	-20.74	-69.16	104.07	119.29	180.69	Array
6/12/18 21:24	2.8	56.42	-149.93	20.54	43.50	279.58	Array
6/12/18 20:57	4.3	23.97	122.31	16.98	59.41	349.96	Array
6/12/18 20:56	4.2	-20.16	-69.20	96.83	118.73	180.73	Array
6/12/18 20:35	3.8	51.69	-173.50	48.98	44.98	298.13	Array
6/12/18 19:23	4.5	8.68	-104.12	10	93.16	217.40	Array
6/12/18 17:53	4	-2.92	129.59	10	87.15	341.41	Array
6/12/18 17:17	5.3	-13.07	45.84	10	92.02	68.77	Array
6/12/18 16:24	3.1	56.32	-148.58	10	43.73	278.26	Array
6/12/18 14:14	3.3	51.33	-168.50	35	46.11	293.57	Array
6/12/18 13:08	4.2	26.33	96.47	116.86	53.31	13.97	Array
6/12/18 12:31	2.95	19.41	-155.26	3.91	79.39	271.08	Array
6/12/18 11:24	2.88	19.40	-155.26	0.49	79.40	271.07	Array

6/12/18 10:52	2.75	19.41	-155.24	-0.37	79.39	271.06	Array
6/12/18 9:58	2.7	19.42	-155.26	1.35	79.38	271.08	Array
6/12/18 9:49	2.75	19.40	-155.27	0.71	79.40	271.08	Array
6/12/18 9:45	2.76	19.40	-155.28	-0.33	79.40	271.09	Array
6/12/18 9:35	4.9	1.07	-77.27	11.55	98.78	189.06	Single-Station
6/12/18 8:53	3.49	19.41	-155.28	0.57	79.39	271.09	Array
6/12/18 7:27	2.59	19.41	-155.26	-0.22	79.39	271.08	Array
6/12/18 6:52	3.4	19.32	-155.11	8.32	79.50	270.91	Array
6/12/18 6:13	2.78	19.42	-155.27	0.7	79.38	271.09	Array
6/12/18 5:07	2.57	19.38	-155.30	5.25	79.42	271.11	Array
6/12/18 4:53	4.6	-17.98	-174.45	60.35	113.06	281.91	Single-Station & Array
6/12/18 4:45	4.2	16.05	-95.18	35	85.42	208.93	Single-Station & Array
6/12/18 4:30	4.2	17.57	122.18	111.03	65.67	349.83	Array
6/12/18 4:22	4.8	14.65	52.08	10	63.93	57.41	Single-Station & Array
6/12/18 3:39	2.98	19.39	-155.27	1.1	79.41	271.08	Array
6/12/18 3:24	4.7	-30.26	-176.97	10	124.57	281.35	Single-Station & Array
6/12/18 0:20	2.57	19.53	-68.66	29	79.38	180.25	Array
6/11/18 22:50	2.53	19.41	-155.27	-0.6	79.39	271.09	Array
6/11/18 22:34	4.4	36.40	71.17	119.27	41.68	35.83	Single-Station & Array
6/11/18 22:16	3	52.35	-170.47	11.17	44.82	295.77	Single-Station & Array

6/11/18 20:09	4.9	35.11	140.55	35	52.07	334.18	Single-Station & Array
6/11/18 19:56	4.8	31.36	131.63	35	53.93	341.83	Single-Station & Array
6/11/18 19:54	5.4	31.30	131.37	30	53.94	342.06	Single-Station & Array
6/11/18 19:20	3.1	36.49	-98.62	5.851	65.18	215.98	Array
6/11/18 19:05	4.2	-19.02	-177.54	562.58	113.48	284.76	Single-Station & Array
6/11/18 18:22	4.9	-5.32	145.81	72.33	92.62	324.52	Single-Station & Array
6/11/18 18:14	2.8	37.30	-122.14	10	64.46	242.39	Single-Station
6/11/18 18:00	3.16	18.44	-67.58	122	80.31	179.06	Single-Station & Array
6/11/18 17:14	2.52	33.51	-116.80	4.18	68.39	235.54	Single-Station & Array
6/11/18 16:13	4.4	12.41	144.22	37.21	74.94	328.17	Array
6/11/18 16:01	2.91	19.40	-155.27	0.4	79.40	271.08	Array
6/11/18 15:50	4.5	-14.89	-173.29	25.23	110.25	281.45	Array
6/11/18 15:42	4.5	24.00	121.72	10.29	59.28	350.52	Array
6/11/18 15:05	4.2	-24.21	-67.20	187.53	122.42	178.85	Array
6/11/18 14:24	4.7	-0.09	129.95	36.43	84.43	341.23	Single-Station
6/11/18 14:20	2.53	19.41	-155.27	0.58	79.40	271.09	Array
6/11/18 13:57	2.54	19.39	-155.26	2.78	79.41	271.07	Array
6/11/18 13:51	2.91	19.41	-155.26	1.51	79.40	271.08	Array
6/11/18 13:03	2.51	19.40	-155.26	0.29	79.40	271.07	Array

6/11/18 12:42	3.03	19.41	-155.28	0.49	79.39	271.09	Array
6/11/18 12:36	4.4	70.85	-4.74	16.35	19.29	79.75	Array
6/11/18 12:34	5.3	-20.74	169.63	84.32	112.58	297.36	Single-Station & Array
6/11/18 12:23	2.57	19.39	-155.27	0.03	79.41	271.08	Array
6/11/18 12:13	4.3	-5.09	129.97	208.41	89.35	340.87	Single-Station & Array
6/11/18 11:34	4.4	1.80	99.57	175.65	78.01	12.17	Single-Station & Array
6/11/18 10:09	4.4	-5.65	154.45	128.97	94.70	315.66	Single-Station & Array
6/11/18 10:07	2.57	19.40	-155.26	0.29	79.40	271.07	Array
6/11/18 8:18	2.6	19.43	-155.28	0.25	79.37	271.10	Array
6/11/18 8:05	4.6	-19.99	-174.91	10	114.94	281.91	Single-Station & Array
6/11/18 7:53	2.83	19.41	-155.28	1.04	79.39	271.09	Single-Station
6/11/18 6:49	4.2	-5.19	149.93	156.2	93.33	320.33	Single-Station & Array
6/11/18 5:44	2.78	19.43	-155.29	-0.47	79.37	271.11	Single-Station & Array
6/11/18 5:41	2.53	19.40	-155.26	0.6	79.40	271.07	Single-Station & Array
6/11/18 5:10	3.47	19.41	-155.27	0.5	79.39	271.09	Array
6/11/18 4:34	4.2	-21.35	-68.78	137.57	119.84	180.33	Array
6/11/18 0:06	2.99	19.39	-155.26	-0.35	79.41	271.07	Single-Station & Array

6/10/18 23:56	2.68	36.27	-81.10	2.1	64.21	195.28	Single-Station & Array
6/10/18 23:30	4.3	-7.24	120.28	437.39	89.81	350.85	Single-Station
6/10/18 21:25	2.8	55.96	-150.02	7.26	43.94	279.36	Single-Station
6/10/18 19:43	4.3	13.91	-91.45	60.23	87.33	204.72	Single-Station
6/10/18 19:20	4.5	6.49	126.41	96.28	77.31	345.20	Single-Station & Array
6/10/18 18:52	4.3	-16.21	-173.11	39.08	111.57	280.98	Single-Station & Array
6/10/18 18:32	4.6	-16.31	-173.17	10	111.67	281.02	Single-Station & Array
6/10/18 17:45	2.5	19.66	-155.21	4.9	79.15	271.08	Array
6/10/18 16:16	2.57	19.41	-155.25	0.11	79.39	271.07	Single-Station
6/10/18 16:11	4.4	83.89	-1.54	10	11.38	30.71	Single-Station & Array
6/10/18 14:55	5	27.29	143.39	10	60.25	330.66	Array
6/10/18 13:04	4.6	-13.20	45.63	10	92.17	69.01	Single-Station
6/10/18 12:41	2.8	56.35	-149.28	21.07	43.63	278.93	Array
6/10/18 10:42	3.93	19.40	-155.27	0.61	79.40	271.08	Array
6/10/18 9:27	2.58	19.40	-155.26	0.63	79.40	271.07	Single-Station
6/10/18 9:11	2.81	19.40	-155.27	0.65	79.40	271.08	Single-Station & Array
6/10/18 9:09	2.61	19.40	-155.27	0.06	79.40	271.08	Array
6/10/18 8:21	4.5	6.68	126.24	74.58	77.10	345.37	Array
6/10/18 8:18	3.1	23.59	120.54	10	59.47	351.60	Single-Station
6/10/18 7:37	2.65	19.40	-155.27	0.12	79.40	271.08	Single-Station

6/10/18 7:01	3.27	19.39	-155.27	0.99	79.41	271.08	Array
6/10/18 6:11	2.61	19.43	-155.29	0.37	79.37	271.11	Array
6/10/18 6:06	2.78	19.40	-155.27	0.77	79.40	271.08	Single-Station
6/10/18 5:25	3.8	52.04	178.20	196.63	43.25	305.44	Single-Station
6/10/18 5:24	2.58	19.40	-155.28	0.4	79.40	271.09	Single-Station
6/10/18 5:13	2.5	19.40	-155.26	0.24	79.40	271.07	Array
6/10/18 4:17	4.7	-12.51	166.83	131.98	103.97	301.90	Single-Station & Array
6/10/18 2:01	2.7	61.75	-146.27	26	38.62	280.37	Array
6/10/18 1:36	4.2	-21.27	-68.86	132.54	119.77	180.40	Single-Station & Array
6/10/18 1:03	4.5	15.06	-94.14	35	86.35	207.71	Single-Station & Array
6/9/18 22:36	4.9	-13.06	45.54	10	92.04	69.07	Single-Station
6/9/18 22:19	2.5	19.30	-155.25	7.95	79.51	271.04	Single-Station
6/9/18 21:45	4.7	43.82	145.93	84.43	44.78	330.71	Single-Station
6/9/18 20:59	4.3	-20.53	-178.28	553.22	114.81	285.15	Array
6/9/18 20:53	4.5	-5.92	152.09	10	94.48	318.02	Array
6/9/18 19:49	5.2	-5.88	151.91	10	94.41	318.21	Array
6/9/18 17:09	2.51	36.95	-117.74	-1.51	64.92	237.54	Array
6/9/18 14:48	5.2	19.41	-155.28	0.61	79.39	271.09	Array
6/9/18 5:16	2.97	19.42	-155.29	0.29	79.38	271.11	Array
6/9/18 4:13	5	-14.90	-173.22	10	110.28	281.38	Array
6/9/18 2:43	3.12	18.53	-64.88	99	79.84	176.09	Array
6/8/18 21:28	4.4	-2.71	119.15	7.01	85.15	352.17	Array
6/8/18 20:28	3.18	19.39	-155.26	0.59	79.41	271.07	Array

6/8/18 19:27	4.2	36.27	22.77	10	45.95	80.22	Array
6/8/18 17:26	4.2	36.47	71.17	235.14	41.61	35.82	Array
6/8/18 15:08	4.1	18.93	145.39	196.09	68.80	327.80	Array
6/8/18 13:58	4.3	-18.59	-174.42	166.14	113.66	281.75	Array
6/8/18 13:26	4.6	-5.81	142.57	10	92.45	327.79	Array
6/8/18 12:03	4.9	-12.93	45.50	10	91.90	69.08	Array
6/8/18 11:44	4.4	-5.62	154.78	147.96	94.75	315.33	Array
6/8/18 11:12	4.5	-8.16	-13.71	10	96.36	126.07	Array
6/8/18 10:30	2.59	19.41	-155.28	-1.11	79.39	271.09	Array
6/8/18 10:01	4.5	-15.07	167.72	121.9	106.65	300.50	Array
6/8/18 9:31	2.63	19.39	-155.27	-0.14	79.41	271.08	Array
6/8/18 8:54	2.93	39.75	-122.84	12.63	61.99	243.96	Array
6/8/18 8:32	4	-24.20	-67.17	185.53	122.40	178.82	Array
6/8/18 6:19	3	51.37	-174.07	11.79	45.20	298.49	Array
6/8/18 6:07	4.9	-2.27	68.24	10	80.33	44.28	Array
6/8/18 6:04	4.2	34.70	24.09	9.62	47.26	79.44	Array
6/8/18 5:48	2.7	55.92	-149.79	7.51	44.00	279.12	Array
6/8/18 4:42	2.97	19.40	-155.28	0.47	79.40	271.09	Array
6/8/18 1:31	2.58	19.42	-155.27	1.07	79.38	271.09	Array
6/8/18 1:21	2.73	19.40	-155.26	1.25	79.40	271.07	Array
6/8/18 0:27	4.8	-7.30	105.96	44.6	87.80	5.89	Array
6/7/18 23:06	2.9	65.39	-143.83	15.7	35.25	281.96	Array
6/7/18 22:58	2.63	19.42	-155.27	0.76	79.38	271.09	Array
6/7/18 22:11	2.7	52.19	-170.32	30.58	45.00	295.57	Single- Station & Array
6/7/18 18:51	3.17	18.24	-68.06	96	80.58	179.59	Array
6/7/18 18:32	2.7	55.80	-161.65	183.8	42.72	289.79	Array
6/7/18 17:26	2.88	19.43	-154.91	4.81	79.42	270.74	Array
6/7/18 13:15	4.6	-4.81	151.71	161.96	93.32	318.57	Array

6/7/18 12:18	4.6	35.77	140.84	46.19	51.49	334.00	Array
6/7/18 11:12	4.2	13.40	144.86	91.16	74.10	327.66	Single- Station
6/7/18 10:56	4	55.73	162.19	35	36.79	320.10	Single- Station
6/7/18 10:51	2.7	36.28	-97.51	6.298	65.34	214.65	Array
6/7/18 6:51	4.4	34.23	78.05	10	44.03	30.00	Array
6/7/18 3:04	2.6	56.79	-149.24	6.7	43.21	279.19	Array
6/7/18 2:44	4.9	-18.70	-174.38	58.15	113.77	281.68	Array
6/7/18 2:03	2.72	19.40	-155.28	0.4	79.40	271.09	Array
6/7/18 1:22	2.61	37.66	-118.84	2.54	64.19	238.95	Array
6/7/18 1:02	2.6	55.93	-149.81	6.92	44.00	279.15	Array
6/6/18 23:54	4.4	-18.10	-178.36	581.76	112.43	285.79	Array
6/6/18 21:19	4.3	22.15	121.48	10	61.06	350.67	Single- Station
6/6/18 19:16	2.7	19.40	-155.27	0.26	79.40	271.08	Array
6/6/18 19:04	3.64	19.41	-155.28	0.51	79.39	271.09	Single- Station
6/6/18 19:03	2.7	40.90	44.25	10	38.45	58.90	Single- Station & Array
6/6/18 18:55	2.89	19.50	-155.50	-1.45	79.27	271.33	Array
6/6/18 18:51	5.6	-58.36	-25.76	31	147.23	147.28	Single- Station & Array
6/6/18 18:15	5	35.79	78.35	23.01	42.49	29.52	Single- Station & Array
6/6/18 17:42	4.8	-0.79	-21.91	10	90.84	132.97	Array
6/6/18 16:19	2.73	19.40	-155.27	1.68	79.40	271.08	Array
6/6/18 15:44	2.91	19.41	-155.26	1.23	79.39	271.08	Array
6/6/18 14:29	2.55	19.40	-155.28	1.06	79.40	271.09	Array
6/6/18 14:17	4.3	-12.75	45.61	10	91.72	68.93	Single- Station
6/6/18 14:11	4.3	-7.84	-13.55	10	96.02	125.86	Array

6/6/18 13:11	2.72	19.41	-155.52	5.19	79.35	271.33	Array
6/6/18 12:36	2.55	19.37	-155.35	11.64	79.42	271.15	Array
6/6/18 12:25	3	36.23	-97.29	7.069	65.38	214.38	Single- Station & Array
6/6/18 9:47	3	16.87	-68.19	35	81.95	179.73	Array
6/6/18 9:37	4.9	-12.87	45.74	10	91.82	68.83	Single- Station
6/6/18 8:30	2.57	19.42	-155.27	0.83	79.38	271.09	Array
6/6/18 7:49	4.4	-23.54	-66.83	210.23	121.70	178.50	Array
6/6/18 7:32	3.1	39.40	-119.98	7.5	62.42	240.75	Array
6/6/18 6:23	3.25	19.32	-65.12	58	79.09	176.34	Array
6/6/18 4:53	5	-1.34	135.21	10	86.63	335.78	Array
6/6/18 4:08	4.7	-29.90	-179.41	346.95	123.74	283.91	Array
6/6/18 3:15	4.4	-52.32	16.62	10	134.12	109.47	Array
6/6/18 2:56	2.53	19.39	-155.29	2.96	79.41	271.10	Array
6/6/18 2:34	4.3	18.52	145.91	175.82	69.31	327.25	Single- Station & Array
6/6/18 0:48	4.4	26.98	143.74	10	60.62	330.30	Single- Station
6/6/18 0:07	4	34.56	46.10	10	44.56	58.90	Array
6/5/18 23:12	4.7	23.86	94.49	82.01	55.55	15.96	Array
6/5/18 22:28	4.7	-18.01	-171.96	10	113.55	279.44	Array
6/5/18 22:23	2.66	19.45	-154.88	5.64	79.41	270.71	Array
6/5/18 20:46	4.2	2.25	128.31	242.46	81.83	343.05	Array
6/5/18 18:40	5.3	41.53	46.79	22.65	37.58	56.44	Single- Station & Array
6/5/18 18:09	4.9	76.70	7.45	10	12.78	56.72	Single- Station & Array
6/5/18 16:33	4.8	24.60	95.10	110.91	54.88	15.35	Array
6/5/18 14:47	3.31	18.14	-68.57	95	80.74	180.15	Array
6/5/18 14:32	5.4	19.40	-155.29	-0.83	79.40	271.10	Array
6/5/18 12:52	3.22	18.61	-64.61	33	79.72	175.79	Array

6/5/18 12:17	2.76	19.40	-155.28	0.49	79.40	271.09	Array
6/5/18 12:14	4.7	8.25	-38.00	10	85.27	148.09	Array
6/5/18 12:03	4.2	52.17	160.71	35	39.86	320.16	Array
6/5/18 11:38	4.2	27.31	140.11	371.54	59.56	333.69	Array
6/5/18 11:27	3.04	19.34	-155.25	0.25	79.46	271.05	Single- Station & Array
6/5/18 11:08	4.3	-38.12	176.59	10	130.90	285.46	Array
6/5/18 10:49	4.2	9.25	123.20	10	74.04	348.51	Array
6/5/18 10:19	2.73	19.40	-155.27	0.97	79.40	271.08	Array
6/5/18 9:57	3.26	18.98	-65.02	31	79.41	176.24	Array
6/5/18 9:36	4.4	-8.61	-74.25	137.61	108.01	185.76	Array
6/5/18 8:52	4.9	36.58	22.59	10	45.67	80.29	Array
6/5/18 8:18	2.56	17.98	-67.29	7	80.72	178.75	Array
6/5/18 7:09	4.2	-18.94	-177.81	449.49	113.36	285.05	Array
6/5/18 6:57	2.63	19.41	-155.28	0.76	79.38	271.09	Array
6/5/18 6:57	2.65	19.39	-155.27	0.58	79.41	271.08	Array
6/5/18 5:20	3	56.51	-148.65	21.47	43.54	278.45	Array
6/5/18 4:45	4.2	-21.61	-68.50	125.95	120.05	180.06	Array
6/5/18 3:19	2.6	62.98	-150.35	88.6	37.03	285.15	Array
6/5/18 2:53	4.5	-12.98	45.65	10	91.94	68.94	Array
6/5/18 2:03	4.4	-4.58	101.84	39.85	84.60	10.11	Array
6/5/18 1:45	2.54	19.40	-155.28	0.36	79.40	271.09	Array
6/5/18 1:34	4.7	29.65	81.68	10	48.78	27.29	Array
6/5/18 0:56	2.9	56.18	-149.76	22.2	43.75	279.27	Array
6/5/18 0:55	2.65	19.40	-155.26	0.62	79.40	271.07	Array
6/5/18 0:18	4	-5.76	151.28	68.39	94.16	318.87	Single- Station & Array

Bibliography

- Agnew, D., Berger, J., Buland, R., Farrell, W., & Gilbert, F. (1976). International deployment of accelerometers: a network for very long period seismology. *EOS, Transactions American Geophysical Union*, 57(4), 180–188. <https://doi.org/10.1029/EO057i004p00180>
- Allstadt, K., & Malone, S. D. (2014). Swarms of repeating stick-slip icequakes triggered by snow loading at Mount Rainier volcano. *Journal of Geophysical Research: Earth Surface*, 119(5), 1180–1203. <https://doi.org/10.1002/2014JF003086>
- Amundson, J. M., Clinton, J. F., Fahnestock, M., Truffer, M., Luthi, M. P., & Motyka, R. J. (2012). Observing calving-generated ocean waves with coastal broadband seismometers, Jakobshavn Isbrae, Greenland. *Annals of Glaciology*, 53(60), 79–84. <https://doi.org/10.3189/2012/AoG60A200>
- Anderson, D. L. (1965). Recent evidence concerning the structure and composition of the Earth's mantle. *Physics and Chemistry of the Earth*, 6, 1–131. [https://doi.org/10.1016/0079-1946\(65\)90013-3](https://doi.org/10.1016/0079-1946(65)90013-3)
- Anderson, D. L., & Dziewonski, A. M. (1984). Seismic Tomography. *Scientific American*, 251(4), 60–71.
- Anderson, D. L., Duennebieer, F. K., Latham, G. V., Toksöz, M. F., Kovach, R. L., Knight, T. C. D., et al. (1976). The Viking seismic experiment. *Science*, 194(4271), 1318–1321. <https://doi.org/10.1126/science.194.4271.1318>
- Andrews-Hanna, J. C., Zuber, M. T., & Banerdt, W. B. (2008). The Borealis basin and the origin of the martian crustal dichotomy. *Nature*, 453(7199), 1212–1215. <https://doi.org/10.1038/nature07011>
- Ardhuin, F., Stutzmann, E., Schimmel, M., & Mangeney, A. (2001). Ocean wave sources of seismic noise. *Journal of Geophysical Research: Oceans*, 116(C9). <https://doi.org/10.1029/2011JC006952>
- Atwater, T., & MacDonald, K. C. (1977). Are spreading centers perpendicular to their transform faults? *Nature*, 270(5639), 715–719. <https://doi.org/10.1038/270715a0>
- Baer, M., & Kradolfer, U. (1987). An automatic phase picker for local and teleseismic events. *Bulletin of the Seismological Society of America*, 77(4), 1437–1445.
- Baker, E. H., O'Neel, S., Fagre, D. B., Whorton, E. N., Sass, L. C., McNeil, C. J., et al. (2018). USGS Benchmark Glacier Mass Balance and Project Data: 1966-2016: U.S. Geological Survey data release. <https://doi.org/10.5066/F7BG2N8R>
- Banerdt, W. B., & Landis, M. E. (2010). Getting Under Mars' Skin: The InSight Mission to the Deep Interior of Mars. In *American Geophysical Union Fall Meeting*
- Banerdt, W. B., Smrekar, S. E., Hoffman, T., Spath, S., Lognonné, P., Spohn, T., et al. (2017). The InSight Mission for 2018. *LUNAR AND PLANETARY SCIENCE CONFERENCE 48*, 1896. <https://doi.org/10.1029/2007JE002905>.
- Banerdt, W. B., Smrekar, S. E., Lognonné, P., Pike, W. T., Giardini, D., & Christensen, U. (2020). Initial results from the InSight mission on Mars. *Nature Geoscience*. <https://doi.org/10.1038/s41561-020-0544-y>
- Banfield, D., Spiga, A., Newman, C., Forget, F., Lemmon, M., Lorenz, R., et al. (2020). The atmosphere of Mars as observed by InSight. *Nature Geoscience*, 13(3), 190–198. <https://doi.org/10.1038/s41561-020-0534-0>

- Banks, M. E., Daubar, I. J., Schmerr, N. C., & Golombek, M. P. (2015). Predicted Seismic Signatures of Recent Dated Maritan Impact Events: Implications for the InSight Lander. *LUNAR AND PLANETARY SCIENCE CONFERENCE XLVI*. Houston, TX.
- Barazangi, M., & Isacks, B. L. (1976). Spatial distribution of earthquakes and subduction of the Nazca plate beneath South America. *Geology*, *4*(11), 686. [https://doi.org/10.1130/0091-7613\(1976\)4<686:SDOEAS>2.0.CO;2](https://doi.org/10.1130/0091-7613(1976)4<686:SDOEAS>2.0.CO;2)
- Barker, B., Clark, M., Davis, P., Fisk, M., Hedlin, M., Israelsson, H., et al. (1998). Monitoring Nuclear Tests. *Science*, *281*(5385), 1967–1968. <https://doi.org/10.1126/science.281.5385.1967>
- Beals, C. S., Ferguson, G. M., & Landau, A. (1956). Canadian scientists report (II. A search for analogies between lunar and terrestrial topography on photographs of the Canadian shield, part I. *Journal of the Royal Astronomical Society of Canada*, *50*, 203.
- Van Beusekom, A. E., O’Neel, S. R., March, R. S., Sass, L. C., & Cox, L. H. (2010). *Re-analysis of Alaskan Benchmark Glacier Mass-Balance Data Using the Index Method Scientific Investigations Report 2010-5247*. Retrieved from <http://www.usgs.gov/pubprod>
- Beyreuther, M., Barsch, R., Krischer, L., Megies, T., Behr, Y., & Wassermann, J. (2010). ObsPy: A Python Toolbox for Seismology. *Seismological Research Letters*, *81*(3), 530–533. <https://doi.org/10.1785/gssrl.81.3.530>
- Bierhaus, E. B., Zahnle, K., Chapman, C. R., Pappalardo, R. T., McKinnon, W. R., & Khurana, K. K. (2009). Europa’s crater distributions and surface ages. In *Europa* (pp. 161–180). University of Arizona Press Tucson, AZ.
- Billings, S. E., & Kattenhorn, S. A. (2005). The great thickness debate: Ice shell thickness models for Europa and comparisons with estimates based on flexure at ridges. *Icarus*, *177*(2), 397–412. <https://doi.org/10.1016/j.icarus.2005.03.013>
- Bills, B. G., Neumann, G. A., Smith, D. E., & Zuber, M. T. (2005). Improved estimate of tidal dissipation within Mars from MOLA observations of the shadow of Phobos. *Journal of Geophysical Research*, *110*(E7), E07004. <https://doi.org/10.1029/2004JE002376>
- Binder, A. B., & Oberst, J. (1985). High stress shallow moonquakes: evidence for an initially totally molten moon. *Earth and Planetary Science Letters*. [https://doi.org/10.1016/0012-821X\(85\)90018-4](https://doi.org/10.1016/0012-821X(85)90018-4)
- Bland, M. T., & McKinnon, W. B. (2017). Breaking the shell: Initiating plate tectonic-like subduction on Europa. In *AAS/Division for Planetary Sciences Meeting Abstracts* (Vol. 49).
- Bondár, I., & Engdahl, E. R. (2019). Seismological Networks BT - Encyclopedia of Solid Earth Geophysics. In H. K. Gupta (Ed.) (pp. 1–11). Cham: Springer International Publishing. https://doi.org/10.1007/978-3-030-10475-7_16-1
- Bose, M., Clinton, J. F., Ceylan, S., Euchner, F., van Driel, M., Khan, A., et al. (2017). A probabilistic framework for single-station location of seismicity on Earth and Mars. *Physics of the Earth and Planetary Interiors*, *262*, 48–65. <https://doi.org/10.1016/j.pepi.2016.11.003>
- Bouquet, A., Mousis, O., Waite, J. H., & Picaut, S. (2015). Possible evidence for a methane source in Enceladus’ ocean. *Geophysical Research Letters*, *42*(5), 1334–1339. <https://doi.org/10.1002/2014GL063013>
- Bowling, J. S., Livingstone, S. J., Sole, A. J., & Chu, W. (2019). Distribution and dynamics of Greenland subglacial lakes. *Nature Communications*, *10*(1), 2810. <https://doi.org/10.1038/s41467-019-10821-w>

- Bray, V. J., Weber, R. C., DellaGiustina, D. N., Bailey, H., Schmerr, N. C., Marusiak, A. G., et al. (2017). SIIOS in Alaska – Testing an ‘In-Vault’ Option for a Europa Lander Seismometer. In *American Geophysical Union Fall Meeting*.
- Buffett, B. A., Garnero, E. J., & Jeanloz, R. (2000). Sediments at the Top of Earth’s Core. *Science*, 290(5495), 1338–1342. <https://doi.org/10.1126/science.290.5495.1338>
- Bulow, R. C., Johnson, C. L., & Shearer, P. M. (2005). New events discovered in the Apollo lunar seismic data. *Journal of Geophysical Research*, 110(E10), E10003. <https://doi.org/10.1029/2005JE002414>
- Bulow, R. C., Johnson, C. L., Bills, B. G., & Shearer, P. M. (2007). Temporal and spatial properties of some deep moonquake clusters. *Journal of Geophysical Research: Planets*, 112(9), 1–12. <https://doi.org/10.1029/2006JE002847>
- Burke, K., Steinberger, B., Torsvik, T. H., & Smethurst, M. A. (2008). Plume Generation Zones at the margins of Large Low Shear Velocity Provinces on the core–mantle boundary. *Earth and Planetary Science Letters*, 265(1), 49–60. <https://doi.org/10.1016/j.epsl.2007.09.042>
- Cammarano, F., Goes, S., Deuss, A., & Giardini, D. (2005). Is a pyrolitic adiabatic mantle compatible with seismic data? *Earth and Planetary Science Letters*, 232(3–4), 227–243. <https://doi.org/10.1016/j.epsl.2005.01.031>
- Carmichael, J. D. (2019). Narrowband signals recorded near a moulin that are not moulin tremor: a cautionary short note. *Annals of Glaciology*, 60(79), 231–237. <https://doi.org/10.1017/aog.2019.23>
- Carmichael, J. D., Pettit, E. C., Hoffman, M., Fountain, A., & Hallet, B. (2012). Seismic multiplet response triggered by melt at Blood Falls, Taylor Glacier, Antarctica. *Journal of Geophysical Research: Earth Surface*, 117(F3). <https://doi.org/10.1029/2011JF002221>
- Carmichael, J. D., Joughin, I., Behn, M. D., Das, S., King, M. A., Stevens, L., & Lizarralde, D. (2015). Seismicity on the western Greenland Ice Sheet: Surface fracture in the vicinity of active moulins. *Journal of Geophysical Research: Earth Surface*, 120(6), 1082–1106. <https://doi.org/10.1002/2014JF003398>
- Carr, M. H., Belton, M. J. S. S., Chapman, C. R., Davies, A. S., Geissler, P., Greenberg, R., et al. (1998). Evidence for a subsurface ocean on Europa. *Nature*, 391(6665), 363–365. <https://doi.org/10.1038/34857>
- Ceylan, S., van Driel, M., Euchner, F., Khan, A., Clinton, J., Krischer, L., et al. (2017). From Initial Models of Seismicity, Structure and Noise to Synthetic Seismograms for Mars. *Space Science Reviews*, 211(1–4), 595–610. <https://doi.org/10.1007/s11214-017-0380-6>
- Chaput, J., Campillo, M., Aster, R. C., Roux, P., Kyle, P. R., Knox, H., & Czoski, P. (2015). Multiple scattering from icequakes at Erebus volcano, Antarctica: Implications for imaging at glaciated volcanoes. *Journal of Geophysical Research-Solid Earth*, 120(2), 1129–1141. <https://doi.org/10.1002/2014jb011278>
- Christensen, N. I., & Mooney, W. D. (1995). Seismic velocity structure and composition of the continental crust: A global view. *Journal of Geophysical Research: Solid Earth*, 100(B6), 9761–9788. <https://doi.org/10.1029/95JB00259>
- Clinton, John F., Nettles, M., Walter, F., Anderson, K., Dahl-Jensen, T., Giardini, D., et al. (2014). Seismic Network in Greenland Monitors Earth and Ice System. *Eos, Transactions American Geophysical Union*, 95(2), 13–14. <https://doi.org/10.1002/2014EO020001>
- Clinton, John Francis, Giardini, D., Lognonné, P., Banerdt, W. B., van Driel, M., Drilleau, M., et al. (2017). Preparing for InSight: An Invitation to Participate in a Blind Test for Martian

- Seismicity. *Seismological Research Letters*, 88(5), 1290–1302.
<https://doi.org/10.1785/0220170094>
- Clough, J. W., & Hansen, B. L. (1979). The Ross Ice Shelf Project. *Science*, 203(4379), 433 LP – 434. <https://doi.org/10.1126/science.203.4379.433>
- Crary, A. P. (1955). A brief study of Ice Tremors. *Bulletin of the Seismological Society of America*, 45(1), 1–9.
- Creager, K. C., & Jordan, T. H. (1986). Aspherical structure of the core-mantle boundary from PKP travel times. *Geophysical Research Letters*, 13(13), 1497–1500.
<https://doi.org/10.1029/GL013i013p01497>
- Crotwell, H. P., Owens, T. J., & Ritsema, J. (1999). The TauP Toolkit: Flexible Seismic Travel-time and Ray-path Utilities. *Seismological Research Letters*, 70(2), 154–160.
<https://doi.org/10.1785/gssrl.70.2.154>
- Davies, G. F., & Richards, M. A. (1992). Mantle Convection. *The Journal of Geology*, 100(2), 151–206. <https://doi.org/10.1086/629582>
- Davies, J. N., & House, L. (1979). Aleutian subduction zone seismicity, volcano-trench separation, and their relation to great thrust-type earthquakes. *Journal of Geophysical Research*, 84(B9), 4583. <https://doi.org/10.1029/JB084iB09p04583>
- Dimech, J.-L., Knapmeyer-Endrun, B., Phillips, D., & Weber, R. C. (2017). Preliminary analysis of newly recovered Apollo 17 seismic data. *Results in Physics*, 7, 4457–4458.
<https://doi.org/10.1016/j.rinp.2017.11.029>
- Doornbos, D. J., & Hilton, T. (1989). Models of the core-mantle boundary and the travel times of internally reflected core phases. *Journal of Geophysical Research: Solid Earth*, 94(B11), 15741–15751. <https://doi.org/10.1029/JB094iB11p15741>
- van Driel, M., Ceylan, S., Clinton, J. F., Giardini, D., Alemany, H., Allam, A., et al. (2019). Preparing for InSight: Evaluation of the Blind Test for Martian Seismicity. *Seismological Research Letters*, 90(4), 1518–1534. <https://doi.org/10.1785/0220180379>
- Drilleau, M., Beucler, É., Mocquet, A., Verhoeven, O., Moebs, G., Burgos, G., et al. (2013). A Bayesian approach to infer radial models of temperature and anisotropy in the transition zone from surface wave dispersion curves. *Geophysical Journal International*, 195(2), 1165–1183. <https://doi.org/10.1093/gji/ggt284>
- Duennebieer, F., & Sutton, G. H. (1974). Thermal moonquakes. *Journal of Geophysical Research*, 79(29), 4351–4363. <https://doi.org/10.1029/JB079i029p04351>
- Dybing, S. N., Ringler, A. T., Wilson, D. C., & Anthony, R. E. (2019). Characteristics and Spatial Variability of Wind Noise on Near-Surface Broadband Seismometers. *Bulletin of the Seismological Society of America*, 109(3), 1082–1098. <https://doi.org/10.1785/0120180227>
- Dziewonski, A. M. (1984). Mapping the lower mantle: Determination of lateral heterogeneity in P velocity up to degree and order 6. *Journal of Geophysical Research: Solid Earth*, 89(B7), 5929–5952. <https://doi.org/10.1029/JB089iB07p05929>
- Dziewonski, A. M., & Anderson, D. L. (1981). Preliminary reference Earth model. *Physics of the Earth and Planetary Interiors*, 25(4), 297–356. [https://doi.org/10.1016/0031-9201\(81\)90046-7](https://doi.org/10.1016/0031-9201(81)90046-7)
- Dziewonski, A. M., Hager, B. H., & O’Connell, R. J. (1977). Large-scale heterogeneities in the lower mantle. *Journal of Geophysical Research*, 82(2), 239–255.
<https://doi.org/10.1029/JB082i002p00239>

- Edelmann, G. F., & Gaumond, C. F. (2011). Beamforming using compressive sensing. *The Journal of the Acoustical Society of America*, *130*(4), EL232–EL237. <https://doi.org/10.1121/1.3632046>
- Efron, B., & Tibshirani, R. (1997). Improvements on Cross-Validation: The 632+ Bootstrap Method. *Journal of the American Statistical Association*, *92*(438), 548–560. <https://doi.org/10.1080/01621459.1997.10474007>
- Elkins-Tanton, L. T., Parmentier, E. M., & Hess, P. C. (2003). Magma ocean fractional crystallization and cumulate overturn in terrestrial planets: Implications for Mars. *Meteoritics & Planetary Science*, *38*(12), 1753–1771. <https://doi.org/10.1111/j.1945-5100.2003.tb00013.x>
- Ewing, M., Crary, A. P., & Thorne, A. M. J. (1934). Propagation of elastic waves in ice. Part II. *Physics*, *5*(7), 181–184. <https://doi.org/10.1063/1.1745249>
- Field, E. H., Jordan, T. H., & Cornell, C. A. (2003). OpenSHA: A Developing Community-modeling Environment for Seismic Hazard Analysis. *Seismological Research Letters*, *74*(4), 406–419. <https://doi.org/10.1785/gssrl.74.4.406>
- Folkner, W. M., Yoder, C. F., Yuan, D. N., Standish, E. M., & Preston, R. A. (1997). Interior structure and seasonal mass redistribution of Mars from radio tracking of Mars Pathfinder. *Science*, *278*(5344), 1749–1752. <https://doi.org/10.1126/science.278.5344.1749>
- Forghani-Arani, F., Behura, J., Haines, S. S., & Batzle, M. (2013). An automated cross-correlation based event detection technique and its application to a surface passive data set. *Geophysical Prospecting*, *61*(4), 778–787. <https://doi.org/10.1111/1365-2478.12033>
- de Franco, R., & Musacchio, G. (2001). Polarization filter with singular value decomposition. *Geophysics*, *66*(3), 932–938. <https://doi.org/10.1190/1.1444983>
- Friederich, W., & Dalkolmo, J. (1995). Complete synthetic seismograms for a spherically symmetric earth by a numerical computation of the Green's function in the frequency domain. *Geophysical Journal International*, *122*(2), 537–550. <https://doi.org/10.1111/j.1365-246X.1995.tb07012.x>
- Frohlich, C., & Pulliam, J. (1999). Single-station location of seismic events: a review and a plea for more research. *Physics of the Earth and Planetary Interiors*, *113*(1–4), 277–291. [https://doi.org/10.1016/S0031-9201\(99\)00055-2](https://doi.org/10.1016/S0031-9201(99)00055-2)
- Fukao, Y. (1984). Evidence from Core-Reflected Shear-Waves for Anisotropy in the Earth's Mantle. *Nature*, *309*(5970), 695–698. <https://doi.org/10.1038/309695a0>
- Garcia, R. F., & Souriau, A. (2000). Amplitude of the core–mantle boundary topography estimated by stochastic analysis of core phases. *Physics of the Earth and Planetary Interiors*, *117*(1–4), 345–359. [https://doi.org/10.1016/S0031-9201\(99\)00106-5](https://doi.org/10.1016/S0031-9201(99)00106-5)
- Garcia, R. F., Gagnepain-Beyneix, J., Chevrot, S., & Lognonne, P. (2011). Very preliminary reference Moon model. *Physics of the Earth and Planetary Interiors*, *188*(1–2), 96–113. <https://doi.org/10.1016/j.pepi.2011.06.015>
- Garcia, R. F., Khan, A., Drilleau, M., Margerin, L., Kawamura, T., Sun, D., et al. (2019). Lunar Seismology: An Update on Interior Structure Models. *Space Science Reviews*, *215*(8), 50. <https://doi.org/10.1007/s11214-019-0613-y>
- Garnero, E. J. (2000). Heterogeneity of the Lowermost Mantle. *Annual Review of Earth and Planetary Sciences*, *28*(1), 509–537. <https://doi.org/10.1146/annurev.earth.28.1.509>
- Garnero, E. J., & McNamara, A. K. (2008). Structure and dynamics of Earth's lower mantle.

- Science*, 320(5876), 626–628. <https://doi.org/10.1126/science.1148028>
- Garnero, E. J., Revenaugh, J., Williams, Q., Lay, T., & Kellogg, L. H. (1998). Ultralow velocity zone at the core-mantle boundary. In *Core-Mantle Boundary Region* (Vol. 28, pp. 319–334). <https://doi.org/10.1029/GD028p0319>
- Gellert, R., Rieder, R., Anderson, R. C., Brückner, J., Clark, B. C., Dreibus, G., et al. (2004). Chemistry of Rocks and Soils in Gusev Crater from the Alpha Particle X-ray Spectrometer. *Science*, 305(5685), 829 LP – 832. <https://doi.org/10.1126/science.1099913>
- Gesch, D., Evans, G., Mauck, J., Hutchinson, J., & Carswell Jr, W. J. (2009). The national map—Elevation. *US Geological Survey Fact Sheet*, 3053(4).
- Giardini, D., & Woodhouse, J. H. (1984). Deep seismicity and modes of deformation in Tonga subduction zone. *Nature*, 307(5951), 505–509. <https://doi.org/10.1038/307505a0>
- Giardini, D., Lognonné, P., Banerdt, W. B., Pike, W. T., Christensen, U., Ceylan, S., et al. (2020). The seismicity of Mars. *Nature Geoscience*, 13(3), 205–212. <https://doi.org/10.1038/s41561-020-0539-8>
- Gleeson, D. F., Pappalardo, R. T., Grasby, S. E., Anderson, M. S., Beauchamp, B., Castaño, R., et al. (2010). Characterization of a sulfur-rich Arctic spring site and field analog to Europa using hyperspectral data. *Remote Sensing of Environment*, 114(6), 1297–1311. <https://doi.org/10.1016/j.rse.2010.01.011>
- Gleeson, D. F., Pappalardo, R. T., Anderson, M. S., Grasby, S. E., Mielke, R. E., Wright, K. E., & Templeton, A. S. (2012). Biosignature Detection at an Arctic Analog to Europa. *Astrobiology*, 12(2), 135–150. <https://doi.org/10.1089/ast.2010.0579>
- Global Modeling and Assimilation Office (GMAO). (2015). MERRA-2 tavg1_2d_slv_Nx: 2d,1-Hourly,Time-Averaged,Single-Level,Assimilation,Single-Level Diagnostics V5.12.4. <https://doi.org/10.5067/VJAFPLI1CSIV>
- Golabek, G. J., Keller, T., Gerya, T. V., Zhu, G., Tackley, P. J., & Connolly, J. A. D. (2011). Origin of the martian dichotomy and Tharsis from a giant impact causing massive magmatism. *Icarus*, 215(1), 346–357. <https://doi.org/10.1016/J.ICARUS.2011.06.012>
- Goldstein, P., Dodge, D., Firpo, M., & Lawrence, L. M. (2003). *SAC2000: Signal Processing and Analysis Tools for Seismologists and Engineers*. Retrieved from <http://www.llnl.gov/sac>.
- Golombek, M. P. (2002). A revision of Mars seismicity from surface faulting. *LUNAR AND PLANETARY SCIENCE CONFERENCE XXXIII*. Houston, TX.
- Goodling, P. J., Lekic, V., & Prestegard, K. (2018). Seismic signature of turbulence during the 2017 Oroville Dam spillway erosion crisis. *Earth Surface Dynamics*, 6(2), 351–367. <https://doi.org/10.5194/esurf-6-351-2018>
- Gouly, N. R. (1979). Tidal triggering of deep moonquakes. *Physics of the Earth and Planetary Interiors*, 19(1), 52–58. [https://doi.org/10.1016/0031-9201\(79\)90089-X](https://doi.org/10.1016/0031-9201(79)90089-X)
- Grand, S. P., van der Hilst, R. D., & Widiyantoro, S. (1997). Global Seismic Tomography: A Snapshot of Convection in the Earth. *GSA Today*, 7(4), 1–7. <https://doi.org/10.1130/GSAT01707GW.1>
- Greeley, R., Sullivan, R. J., Coon, M. D., Geissler, P., Tufts, B. R., Head, J. W., et al. (1998). Terrestrial Sea Ice Morphology: Considerations for Europa. *Icarus*, 135, 25–40. <https://doi.org/10.1006/icar.1998.5977>
- Greeley, R., Figueredo, P. H., Williams, D. A., Chuang, F. C., Klemaszewski, J. E., Kadel, S. D., et al. (2000). Geologic mapping of Europa. *Journal of Geophysical Research-Planets*,

- 105(E9), 22559–22578. <https://doi.org/10.1029/1999je001173>
- Greeley, R., Chyba, C. F., Head, J. W., McCord, T., McKinnon, W. B., Pappalardo, R. T., & Figueredo, P. H. (2004). Geology of Europa. *Jupiter: The Planet, Satellites and Magnetosphere*, 329–362.
- Greenberg, R., Hoppa, G. V., Tufts, B. R., Geissler, P., Riley, J., & Kadel, S. (1999). Chaos on Europa. *Icarus*, 141(2), 263–286. <https://doi.org/10.1006/icar.1999.6187>
- Greenberg, R., Hoppa, G. V., Bart, G., & Hurford, T. A. (2003). Tidal stress patterns on Europa's crust. *Celestial Mechanics & Dynamical Astronomy*, 87(1–2), 171–188. <https://doi.org/10.1023/A:1026169424511>
- Grover, F. H. (1979). The collection and analysis of seismological data to detect possible violations of a nuclear test ban treaty. *Physics of the Earth and Planetary Interiors*, 18(2), 135–142. [https://doi.org/hro10.1016/0031-9201\(79\)90142-0](https://doi.org/hro10.1016/0031-9201(79)90142-0)
- Gudkova, T. V., & Zharkov, V. N. (2004). Mars: interior structure and excitation of free oscillations. *Physics of the Earth and Planetary Interiors*, 142(1–2), 1–22. <https://doi.org/10.1016/j.pepi.2003.10.004>
- Gutenberg, B. (1913). Über die Konstitution des Erdinnern, erschlossen aus Erdbebenbeobachtungen. *Phys. Z*, 14, 1217–1218.
- Gutenberg, B. (1914). Ueber Erdbebenwellen. VII A. Beobachtungen an Registrierungen von Fernbeben in Göttingen und Folgerung über die Konstitution des Erdkörpers (mit Tafel). *Nachrichten von Der Gesellschaft Der Wissenschaften Zu Göttingen, Mathematisch-Physikalische Klasse*, 1914, 125–176.
- Gutenberg, B. (1959). *Physics of the Earth's Interior*, Acad. Press, New York, 240.
- Guy, M. R., Patton, J. M., Fee, J., Hearne, M., Martinez, E., Ketchum, D., et al. (2015). National Earthquake Information Center systems overview and integration. *Open-File Report*. Reston, VA. <https://doi.org/10.3133/ofr20151120>
- Hager, B. H., & Clayton, R. W. (1989). Constraints on the structure of mantle convection using seismic observations, flow models, and the geoid. *Mantle Convection, Plate Tectonics and Global Dynamics*, 657–763.
- Hall, R. C. (1977). *Lunar impact: A history of Project Ranger* (Vol. 4210). Scientific and Technical Information Office, National Aeronautics and Space Agency
- Hand, K. P., Chyba, C. F., Priscu, J. C., Carlson, R. W., & Nealson, K. H. (2009). Astrobiology and the potential for life on Europa. In R. T. Pappalardo, W. B. McKinnon, & K. Khurana (Eds.), *Europa* (1st ed., pp. 589–629). University of Arizona Press Tucson.
- Hand, K. P., Murray, A. E., Garvin, J. B., Brinckerhoff, W. B., Christner, B. C., Edgett, K. S., et al. (2017). *Report of the Europa Science Definition Team*.
- Hannon, W. J. (1985). Seismic Verification of a Comprehensive Test Ban. *Science*, 227(4684), 251–257. <https://doi.org/10.1126/science.227.4684.251>
- Harri, A. M., Marsal, O., Lognonne, P., Leppelmeier, G. W., Spohn, T., Glassmeier, K. H., et al. (1999). Network science landers for Mars. *Moon and Mars*, 23(11), 1915–1924. [https://doi.org/10.1016/S0273-1177\(99\)00279-3](https://doi.org/10.1016/S0273-1177(99)00279-3)
- Hartmann, W. K. (1973). Ancient lunar mega-regolith and subsurface structure. *Icarus*, 18(4), 634–636. [https://doi.org/10.1016/0019-1035\(73\)90066-3](https://doi.org/10.1016/0019-1035(73)90066-3)
- Hayes, A., Aharonson, O., Callahan, P., Elachi, C., Gim, Y., Kirk, R., et al. (2008). Hydrocarbon lakes on Titan: Distribution and interaction with a porous regolith. *Geophysical Research*

- Letters*, 35(9), L09204. <https://doi.org/10.1029/2008GL033409>
- Hecht, M. H., Kounaves, S. P., Quinn, R. C., West, S. J., Young, S. M. M., Ming, D. W., et al. (2009). Detection of Perchlorate and the Soluble Chemistry of Martian Soil at the Phoenix Lander Site. *Science*, 325(5936), 64 LP – 67. <https://doi.org/10.1126/science.1172466>
- Heffels, A., Knapmeyer, M., Oberst, J., & Haase, I. (2017). Re-evaluation of Apollo 17 Lunar Seismic Profiling Experiment data. *Planetary and Space Science*, 135, 43–54. <https://doi.org/10.1016/J.PSS.2016.11.007>
- Hernlund, J. W., Thomas, C., & Tackley, P. J. (2005). A doubling of the post-perovskite phase boundary and structure of the Earth's lowermost mantle. *Nature*, 434(7035), 882–886. <https://doi.org/10.1038/nature03472>
- van der Hilst, R. D., Widiyantoro, S., & Engdahl, E. R. (1997). Evidence for deep mantle circulation from global tomography. *Nature*, 386(6625), 578–584. <https://doi.org/DOI10.1038/386578a0>
- van der Hilst, R. D., de Hoop, M. V., Wang, P., Shim, S.-H., Ma, P., & Tenorio, L. (2007). Seismostratigraphy and Thermal Structure of Earth's Core-Mantle Boundary Region. *Science*, 315(5820), 1813–1817. <https://doi.org/10.1126/science.1137867>
- Hoppa, G. V., Tufts, B. R., Greenberg, R., & Geissler, P. (1999). Strike-slip faults on Europa: Global shear patterns driven by tidal stress. *Icarus*, 141(2), 287–298. <https://doi.org/10.1006/icar.1999.6185>
- Horowitz, N. H., Cameron, R. E., & Hubbard, J. S. (1972). Microbiology of the dry valleys of Antarctica. *Science*, 176(4032), 242–245. <https://doi.org/10.1126/science.176.4032.242>
- Hurford, T. A., & Brunt, K. M. (2014). Antarctic Analog for dilational bands on Europa. *Earth and Planetary Science Letters*, 401, 275–283. <https://doi.org/10.1016/j.epsl.2014.05.015>
- Hurford, T. A., Sarid, A. R., Greenberg, R., & Bills, B. G. (2009). The influence of obliquity on european cycloid formation. *Icarus*, 202(1), 197–215. <https://doi.org/10.1016/j.icarus.2009.02.036>
- Hurford, T. A., Henning, W. G., Maguire, R., Lekic, V., Schmerr, N., Panning, M., et al. (2020). Seismicity on tidally active solid-surface worlds. *Icarus*, 338, 113466. <https://doi.org/10.1016/j.icarus.2019.113466>
- Hutko, A. R., Lay, T., Garnero, E. J., & Revenaugh, J. (2006). Seismic detection of folded, subducted lithosphere at the core-mantle boundary. *Nature*, 441(7091), 333–336. <https://doi.org/10.1038/nature04757>
- Iess, L., Rappaport, N. J., Jacobson, R. A., Racioppa, P., Stevenson, D. J., Tortora, P., et al. (2010). Gravity Field, Shape, and Moment of Inertia of Titan. *Science*, 327(5971), 1367–1369. <https://doi.org/10.1126/science.1182583>
- Iess, L., Stevenson, D. J., Parisi, M., Hemingway, D., Jacobson, R. A., Lunine, J. I., et al. (2014). The Gravity Field and Interior Structure of Enceladus. *Science*, 344(6179), 78–80. <https://doi.org/10.1126/science.1250551>
- Isacks, B., Oliver, J., & Sykes, L. R. (1968). Seismology and the New Global Tectonics. *Journal of Geophysical Research*, 75(18), 5855–5899. <https://doi.org/10.1029/JB073i018p05855>
- Isanina, E. V., Krupnova, N. A., Popov, S. V., Masolov, V. N., & Lukin, V. V. (2009). Deep structure of the Vostok Basin, East Antarctica as deduced from seismological observations. *Geotectonics*, 43(3), 221–225. <https://doi.org/10.1134/S0016852109030042>
- Ishii, M., & Tromp, J. (2004). Constraining large-scale mantle heterogeneity using mantle and

- inner-core sensitive normal modes. *Physics of the Earth and Planetary Interiors*, 146(1–2), 113–124. <https://doi.org/10.1016/J.PEPI.2003.06.012>
- Iyer, H. M., & Hirahara, K. (1993). *Seismic tomography : theory and practice*. Chapman & Hall.
- Johnson, B. C., Sheppard, R. Y., Pascuzzo, A. C., Fisher, E. A., & Wiggins, S. E. (2017). Porosity and Salt Content Determine if Subduction Can Occur in Europa’s Ice Shell. *Journal of Geophysical Research: Planets*, 122(12), 2765–2778. <https://doi.org/10.1002/2017JE005370>
- Josberger, E. G., Bidlake, W. R., March, R. S., & Kennedy, B. W. (2007). Glacier mass-balance fluctuations in the Pacific Northwest and Alaska, USA. *Annals of Glaciology*, 46, 291–296. <https://doi.org/10.3189/172756407782871314>
- Joughin, I., Smith, B. E., Howat, I. M., Scambos, T., & Moon, T. (2010). Greenland flow variability from ice-sheet-wide velocity mapping. *Journal of Glaciology*, 56(197), 415–430. <https://doi.org/10.3189/002214310792447734>
- Joughin, I., Smith, B. E., & Howat, I. (2018). Greenland Ice Mapping Project: ice flow velocity variation at sub-monthly to decadal timescales. *The Cryosphere*, 12(7), 2211–2227. <https://doi.org/10.5194/tc-12-2211-2018>
- Joughin, I., Howat, I., Smith, B., & Scambos, T. (2020). No MEaSURES Greenland Ice Velocity: Selected Glacier Site Velocity Maps from InSAR, Version 2 Title. Boulder, CO: NASA National Snow and Ice Data Center Distributed Active Archive Center. <https://doi.org/10.5067/JQHJUOYCF2TE>
- Kapitsa, A. P., Ridley, J. K., de Q. Robin, G., Siegert, M. J., & Zotikov, I. A. (1996). A large deep freshwater lake beneath the ice of central East Antarctica. *Nature*, 381(6584), 684–686. <https://doi.org/10.1038/381684a0>
- Kattenhorn, S. A., & Prockter, L. M. (2014). Evidence for subduction in the ice shell of Europa. *Nature Geoscience*, 7(10), 762–767. <https://doi.org/10.1038/ngeo2245>
- Katterhorn, S. A., & Hurford, T. A. (2009). Tectonics of Europa. In R. Pappalardo, W. B. McKinnon, & K. Khurana (Eds.), *Europa* (pp. 199–236). The University of Arizona Press.
- Kawamura, T., Lognonné, P., Nishikawa, Y., & Tanaka, S. (2017). Evaluation of deep moonquake source parameters: Implication for fault characteristics and thermal state. *Journal of Geophysical Research: Planets*, 122(7), 1487–1504. <https://doi.org/10.1002/2016JE005147>
- Kellogg, L. H., Hager, B. H., & van der Hilst, R. D. (1999). Compositional Stratification in the Deep Mantle. *Science*, 283(5409), 1881–1884. <https://doi.org/10.1126/science.283.5409.1881>
- Kendall, J.-M., & Silver, P. G. (1996). Constraints from seismic anisotropy on the nature of the lowermost mantle. *Nature*, 381(6581), 409–412. <https://doi.org/10.1038/381409a0>
- Kennett, B. L. N., & Engdahl, E. R. (1991). Traveltimes for Global Earthquake Location and Phase Identification. *Geophysical Journal International*, 105(2), 429–465. <https://doi.org/10.1111/j.1365-246X.1991.tb06724.x>
- Kennett, B. L. N., Engdahl, E. R., & Buland, R. (1995). Constraints on seismic velocities in the Earth from traveltimes. *Geophysical Journal International*, 122(1), 108–124. <https://doi.org/10.1111/j.1365-246X.1995.tb03540.x>
- Khan, A., & Connolly, J. A. D. (2008). Constraining the composition and thermal state of Mars from inversion of geophysical data. *Journal of Geophysical Research- Planets*, 113(E7).

<https://doi.org/Artn E07003 10.1029/2007je002996>

- Khan, A., Mosegaard, K., & Rasmussen, K. L. (2000). A new seismic velocity model for the Moon from a Monte Carlo inversion of the Apollo lunar seismic data. *Geophysical Research Letters*, 27(11), 1591–1594. <https://doi.org/10.1029/1999GL008452>
- Khan, A., Connolly, J. A. D., Pommier, A., & Noir, J. (2014). Geophysical evidence for melt in the deep lunar interior and implications for lunar evolution. *Journal of Geophysical Research: Planets*, 119(10), 2197–2221. <https://doi.org/10.1002/2014JE004661>
- Khan, A., van Driel, M., Bose, M., Giardini, D., Ceylan, S., Yan, J., et al. (2016). Single-station and single-event marsquake location and inversion for structure using synthetic Martian waveforms. *Physics of the Earth and Planetary Interiors*, 258, 28–42. <https://doi.org/10.1016/j.pepi.2016.05.017>
- Khan, A., Liebske, Rozel, A., Rivoldini, A., Nimmo, F., Connolly, J. A. D., et al. (2017). A geophysical perspective on the bulk composition of Mars. *Journal of Geophysical Research: Planets*. <https://doi.org/10.1002/2017JE005371>
- Khatib, A. S., Schmerr, N. C., Feist, B., Plescia, J. B., & Petro, N. E. (2020). Active-Source Seismology from anthropogenic sources during th Apollo 11 Lunar Mission. *LUNAR AND PLANETARY SCIENCE CONFERENCE I*
- Knapmeyer, M., Oberst, J., Hauber, E., Wahlich, M., Deuchler, C., & Wagner, R. (2006). Working models for spatial distribution and level of Mars' seismicity. *Journal of Geophysical Research-Planets*, 111(E11). <https://doi.org/Artn E11006 10.1029/2006je002708>
- Kochan, H., Feibig, W., Konopka, U., Kretschmer, M., Möhlmann, D., Seidensticker, K. J., et al. (2000). CASSE - The Rosetta Lander Comet Acoustic Surface Sounding Experiment - Status of some aspects, the technical realisation and laboratory simulations. *Planetary and Space Science*, 48(5), 385–399. [https://doi.org/10.1016/s0032-0633\(00\)00013-1](https://doi.org/10.1016/s0032-0633(00)00013-1)
- Konopliv, A. S., Asmar, S. W., Folkner, W. M., Karatekin, Ö., Nunes, D. C., Smrekar, S. E., et al. (2011). Mars high resolution gravity fields from MRO, Mars seasonal gravity, and other dynamical parameters. *Icarus*, 211(1), 401–428. <https://doi.org/10.1016/j.icarus.2010.10.004>
- Konopliv, A. S., Park, R. S., & Folkner, W. M. (2016). An improved JPL Mars gravity field and orientation from Mars orbiter and lander tracking data. *Icarus*, 274, 253–260. <https://doi.org/10.1016/J.ICARUS.2016.02.052>
- Konstantinidis, K., Flores Martinez, C. L., Dachwald, B., Ohndorf, A., Dykta, P., Bowitz, P., et al. (2015). A lander mission to probe subglacial water on Saturn's moon Enceladus for life. *Acta Astronautica*, 106, 63–89. <https://doi.org/10.1016/j.actaastro.2014.09.012na>
- Kooistra Jr, J. A., Mitchell, R. B., & Strughold, H. (1958). The behavior of microorganisms under simulated Martian environmental conditions. *Publications of the Astronomical Society of the Pacific*, 70, 64.
- Kovach, R. L., & Anderson, D. L. (1964). Attenuation of shear waves in the upper and lower mantle. *Bulletin of the Seismological Society of America*, 54(6A), 1855–1864.
- Kovach, R. L., & Chyba, C. F. (2001). Seismic detectability of a subsurface ocean on Europa. *Icarus*, 150(2), 279–287. <https://doi.org/10.1006/icar.2000.6577>
- Kovach, R. L., & Watkins, J. S. (1973). The structure of the lunar crust at the Apollo 17 site. In *LUNAR AND PLANETARY SCIENCE CONFERENCE IV*

- Krüger, F., Weber, M., Scherbaum, F., & Schlittenhardt, J. (1995). Evidence for normal and inhomogeneous lowermost mantle and core-mantle boundary structure under the Arctic and northern Canada. *Geophysical Journal International*, 122(2), 637–657. <https://doi.org/10.1111/j.1365-246X.1995.tb07017.x>
- Ksanfomaliti, L. V., Zubkova, V. M., Morozov, N. A., & Petrova, E. V. (1982). Microseisms at the VENERA-13 and VENERA-14 Landing Sites. *Soviet Astronomy Letters*, 8, 241–242.
- Lachenbruch, A. H., & Thompson, G. A. (1972). Oceanic ridges and transform faults: Their intersection angles and resistance to plate motion. *Earth and Planetary Science Letters*, 15(2), 116–122. [https://doi.org/10.1016/0012-821X\(72\)90051-9](https://doi.org/10.1016/0012-821X(72)90051-9)
- Laneuville, M., Wiczeorek, M. A., Breuer, D., Aubert, J., Morard, G., & Rückriemen, T. (2014). A long-lived lunar dynamo powered by core crystallization. *Earth and Planetary Science Letters*, 401, 251–260. <https://doi.org/10.1016/J.EPSL.2014.05.057>
- Latham, G. V, Ewing, M., Press, F., Sutton, G., Dorman, H. J., Nakamura, Y., et al. (1970b). Passive Seismic Experiment. *Science*, 167(3918), 455–457. <https://doi.org/10.1126/science.167.3918.455>
- Latham, G. V, Ewing, M., Dorman, J., Press, F., Toksoz, N., Sutton, G., et al. (1970a). Seismic Data from Man-Made Impacts on the Moon. *Science*, 170(3958), 620–626. <https://doi.org/10.1126/science.170.3958.620>
- Lawrence, J. F., & Wyssession, M. E. (2006). QLM9: A new radial quality factor (Q_{μ}) model for the lower mantle. *Earth and Planetary Science Letters*, 241(3–4), 962–971. <https://doi.org/10.1016/J.EPSL.2005.10.030>
- Lay, T., & Garnero, E. J. (2004). Core-mantle boundary structures and processes. In *Geophysical Monograph Series* (Vol. 150, pp. 25–41). American Geophysical Union (AGU). <https://doi.org/10.1029/150GM04>
- Lay, T., Williams, Q., & Garnero, E. J. (1998). The core-mantle boundary layer and deep Earth dynamics. *Nature*, 392(6675), 461–468. <https://doi.org/10.1038/33083>
- Lay, T., Garnero, E. J., & Russell, S. A. (2004). Lateral variation of the D'' discontinuity beneath the Cocos Plate. *Geophysical Research Letters*, 31(15), L15612. <https://doi.org/10.1029/2004GL020300>
- Lee, S. W., Zanolin, M., Thode, A. M., Pappalardo, R. T., & Makris, N. C. (2003). Probing Europa's interior with natural sound sources. *Icarus*, 165(1), 144–167. [https://doi.org/10.1016/S0019-1035\(03\)00150-7](https://doi.org/10.1016/S0019-1035(03)00150-7)
- Lehmann, I. (1936). P'. *Bureau Central Séismologique International Strasbourg: Publications Du Bureau Central Scientifiques*, 14, 87–115.
- Lekic, V., Cottaar, S., Dziewonski, A. M., & Romanowicz, B. (2012). Cluster analysis of global lower mantle tomography: A new class of structure and implications for chemical heterogeneity. *Earth and Planetary Science Letters*, 357–358, 68–77. <https://doi.org/10.1016/J.EPSL.2012.09.014>
- Léveillé, R. (2010). A half-century of terrestrial analog studies: From craters on the Moon to searching for life on Mars. *Planetary and Space Science*, 58(4), 631–638. <https://doi.org/10.1016/j.pss.2009.04.001>
- Li, M., McNamara, A. K., Garnero, E. J., & Yu, S. (2017). Compositionally-distinct ultra-low velocity zones on Earth's core-mantle boundary. *Nature Communications*, 8(1), 177. <https://doi.org/10.1038/s41467-017-00219-x>

- Li, X.-D., Giardini, D., & Woodhouses, J. H. (1991). Large-scale three-dimensional even-degree structure of the Earth from splitting of long-period normal modes. *Journal of Geophysical Research*, 96(B1), 551. <https://doi.org/10.1029/90JB02009>
- Lockman, A. B., & Allen, R. M. (2005). Single-station earthquake characterization for early warning. *Bulletin of the Seismological Society of America*, 95(6), 2029–2039. <https://doi.org/10.1785/0120040241>
- Lognonné, P., & Mosser, B. (1993). Planetary seismology. *Surveys in Geophysics*, 14(3), 239–302. <https://doi.org/10.1007/BF00690946>
- Lognonné, P., Giardini, D., Banerdt, W. B., Gagnepain-Beyneix, J., Mocquet, A., Spohn, T., et al. (2000). The NetLander very broad band seismometer. *Planetary and Space Science*, 48(12), 1289–1302.
- Lognonné, P., Banerdt, W. B., Hurst, K., Mimoun, D., Garcia, R. F., Lefeuvre, M., et al. (2012). InSight and single-station broadband seismology: From signal and noise to interior structure determination. *LUNAR AND PLANETARY SCIENCE CONFERENCE XLIII*.
- Lognonné, P., Banerdt, W. B., Giardini, D., Pike, W. T., Christensen, U., Laudet, P., et al. (2019). SEIS: Insight's Seismic Experiment for Internal Structure of Mars. *Space Science Reviews*, 215(1), 12. <https://doi.org/10.1007/s11214-018-0574-6>
- Lombardi, D., Gorodetskaya, I., Barruol, G., & Camelbeeck, T. (2019). Thermally induced icequakes detected on blue ice areas of the East Antarctic ice sheet. *Annals of Glaciology*, 60(79), 45–56. <https://doi.org/10.1017/aog.2019.26>
- Loper, D. E., & Lay, T. (1995). The core-mantle boundary region. *Journal of Geophysical Research: Solid Earth*, 100(B4), 6397–6420. <https://doi.org/10.1029/94JB02048>
- Lopes, R. M. C., Kirk, R. L., Mitchell, K. L., LeGall, A., Barnes, J. W., Hayes, A., et al. (2013). Cryovolcanism on Titan: New results from Cassini RADAR and VIMS. *Journal of Geophysical Research: Planets*, 118(3), 416–435. <https://doi.org/10.1002/jgre.20062>
- Lorenz, R. D., Prieto-Ballesteros, O., Gomez, F., Hand, K., & Bulat, S. (2011). Analog environments for a Europa lander mission. *Advances in Space Research*, 48, 689–696. <https://doi.org/10.1016/j.asr.2010.05.006>
- Lorenz, R. D., Nakamura, Y., & Murphy, J. (2016). A bump in the night: wind statistics point to Viking 2 Sol 80 seismometer event as a real marsquake. *LUNAR AND PLANETARY SCIENCE CONFERENCE XLVII*
- Lorenz, R. D., Nakamura, Y., & Murphy, J. R. (2017). Viking-2 Seismometer Measurements on Mars: PDS Data Archive and Meteorological Applications. *Earth and Space Science*, 4(11), 681–688. <https://doi.org/10.1002/2017EA000306>
- Lorenz, R. D., Panning, M. P., Stähler, S., Shiraishi, H., Yamada, R., Turtle, E. P., et al. (2019). Titan Seismology with Dragonfly: Probing the Internal Structure of the Most Accessible Ocean World. *LUNAR AND PLANETARY SCIENCE CONFERENCE L*, Abstract #2173.
- Lucchetti, A., Pozzobon, R., Mazzarini, F., Cremonese, G., & Massironi, M. (2017). Brittle ice shell thickness of Enceladus from fracture distribution analysis. *Icarus*, 297, 252–264. <https://doi.org/10.1016/j.icarus.2017.07.009>
- Lunar Exploration Roadmap Steering Committee. (2016). *The Lunar Exploration Roadmap: Exploring the Moon in the 21st Century: Themes, Goals, Objectives, Investigations, and Priorities*. Retrieved from <http://www.lpi.usra.edu/leag>
- MacAyeal, D. R., Wang, Y. T., & Okal, E. A. (2015). Ambient seismic, hydroacoustic, and

- flexural gravity wave noise on a tabular iceberg. *Journal of Geophysical Research-Earth Surface*, 120(2), 200–211. <https://doi.org/10.1002/2014jf003250>
- MacAyeal, D. R., Banwell, A. F., Okal, E. A., Lin, J., Willis, I. C., Goodsell, B., & MacDonald, G. J. (2019). Diurnal seismicity cycle linked to subsurface melting on an ice shelf. *Annals of Glaciology*, 60(79), 137–157. <https://doi.org/10.1017/aog.2018.29>
- Magotra, N., Ahmed, N., & Chael, E. (1987). Seismic event detection and source location using single-station (three-component) data. *Bulletin of the Seismological Society of America*, 77(3), 958–971.
- Magotra, N., Ahmed, N., & Chael, E. (1989). Single-station seismic event detection and location. *Ieee Transactions on Geoscience and Remote Sensing*, 27(1), 15–23. <https://doi.org/10.1109/36.20270>
- Majer, E. L., Baria, R., Stark, M., Oates, S., Bommer, J., Smith, B., & Asanuma, H. (2007). Induced seismicity associated with Enhanced Geothermal Systems. *Geothermics*, 36(3), 185–222. <https://doi.org/10.1016/j.geothermics.2007.03.003>
- Manchee, E. B., & Weichert, D. H. (1968). Epicentral uncertainties and detection probabilities from the Yellowknife seismic array data. *Bulletin of the Seismological Society of America*, 58(5), 1359–1377.
- March, R. S. (2000). Mass balance, meteorological, ice motion, surface altitude, runoff, and ice thickness data at Gulkana glacier, Alaska, 1995 balance year. Fairbanks, AK. Water-Resources Investigations Report 00-4074
- March, R. S., & Trabant, D. C. (1997). Mass Balance, Meteorological, Ice Motion, Surface Altitude, and Runoff Data at Gulkana Glacier, Alaska, 1993 Balance Year. Water-Resources Investigations Report 96-429
- Marusiak, A. G., Schmerr, N. C., Weber, R. C., DellaGiustina, D. N., Bailey, S. H., Bray, V. J., et al. (2018). SIIOS in Alaska- Active Source Comparative Test for an Europa Lander Seismometer. *LUNAR AND PLANETARY SCIENCE CONFERENCE XLIX*, 8.
- Marusiak, A. G., Schmerr, N. C., DellaGiustina, D., Bailey, H., Bray, V., Broadbeck, J., et al. (2018). The Seismometer to Investigate Ice and Ocean Structure (SIIOS) in Greenland: Testing Instrument Performance on an Icy World Analog. In *American Geophysical Union Fall Meeting*. Washington D.C.
- Marusiak, A. G., Schmerr, N. C., Avenson, B., Bailey, H., Bray, V. J., DellaGiustina, D. N., et al. (2019). Ambient Seismicity on European Analogs using the Seismometer to Investigate Ice and Ocean Structure (SIIOS). In *American Geophysical Union Fall Meeting 2019*. AGU.
- Marusiak, A. G., Schmerr, N. C., Bailey, H., DellaGiustina, D., Bray, V. J., Dahl, P., et al. (2019). Location of Seismicity with a Small-Aperture Seismometer Array: Implication for Seismology with an Ocean-World Lander. In *LUNAR AND PLANETARY SCIENCE CONFERENCE L*.
- Marusiak, A. G., Schmerr, N. C., DellaGiustina, D. N., Pettit, E. C., Dahl, P. H., Avenson, B., et al. (2020). The Deployment of the Seismometer to Investigate Ice and Ocean Structure (SIIOS) on Gulkana Glacier, Alaska. *Seismological Research Letters*. <https://doi.org/10.1785/0220190328>
- McCord, T. B., Hansen, G. B., Matson, D. L., Johnson, T. V., Crowley, J. K., Fanale, F. P., et al. (1999). Hydrated salt minerals on Europa's surface from the Galileo near-infrared mapping spectrometer (NIMS) investigation. *Journal of Geophysical Research-Planets*, 104(E5), 11827–11851. <https://doi.org/10.1029/1999je900005>

- McKenzie, D. P., & Parker, R. L. (1967). The North Pacific: an Example of Tectonics on a Sphere. *Nature*, 216(5122), 1276–1280. <https://doi.org/10.1038/2161276a0>
- McLennan, S. M., Anderson, R. B., Bell, J. F., Bridges, J. C., Calef, F., Campbell, J. L., et al. (2014). Elemental Geochemistry of Sedimentary Rocks at Yellowknife Bay, Gale Crater, Mars. *Science*, 343(6169), 1244734. <https://doi.org/10.1126/science.1244734>
- McNamara, D. E., & Buland, R. P. (2004). Ambient noise levels in the continental United States. *Bulletin of the Seismological Society of America*, 94(4), 1517–1527. <https://doi.org/10.1785/012003001>
- McNutt, S. R. (1996). Seismic monitoring and eruption forecasting of volcanoes: a review of the state-of-the-art and case histories. In *Monitoring and mitigation of volcano hazards* (pp. 99–146). Springer.
- McNutt, S. R., & Roman, D. C. (2015). Volcanic Seismicity. *The Encyclopedia of Volcanoes*, 1011–1034. <https://doi.org/10.1016/B978-0-12-385938-9.00059-6>
- McSween, H. Y. (1985). SNC meteorites: Clues to Martian petrologic evolution? *Reviews of Geophysics*, 23(4), 391. <https://doi.org/10.1029/RG023i004p00391>
- McSween, H. Y. (1994). What we have learned about Mars from SNC meteorites. *Meteoritics*, 29(6), 757–779. <https://doi.org/10.1111/j.1945-5100.1994.tb01092.x>
- McSween, H. Y., Taylor, G. J., & Wyatt, M. B. (2009). Elemental Composition of the Martian Crust. *Science*, 324(5928), 736 LP – 739. <https://doi.org/10.1126/science.1165871>
- Mégnin, C., & Romanowicz, B. (2000). The three-dimensional shear velocity structure of the mantle from the inversion of body, surface and higher-mode waveforms. *Geophysical Journal International*, 143(3), 709–728. <https://doi.org/10.1046/j.1365-246X.2000.00298.x>
- Métaxian, J.-P., Araujo, S., Mora, M., & Lesage, P. (2003). Seismicity related to the glacier of Cotopaxi Volcano, Ecuador. *Geophysical Research Letters*, 30(9). <https://doi.org/10.1029/2002GL016773>
- Meyer, J., & Wisdom, J. (2007). Tidal heating in Enceladus. *Icarus*, 188(2), 535–539. <https://doi.org/10.1016/j.icarus.2007.03.001>
- Mimoun, D., Murdoch, N., Lognonné, P., Hurst, K., Pike, W. T., Hurley, J., et al. (2017). The Noise Model of the SEIS Seismometer of the InSight Mission to Mars. *Space Science Reviews*, 211(1), 383–428. <https://doi.org/10.1007/s11214-017-0409-x>
- Mitchell, B. J., & Helmberger, D. V. (1973). Shear velocities at the base of the mantle from observations of S and ScS. *Journal of Geophysical Research*, 78(26), 6009–6020. <https://doi.org/10.1029/JB078i026p06009>
- Mitri, G., Showman, A. P., Lunine, J. I., & Lorenz, R. D. (2007). Hydrocarbon lakes on Titan. *Icarus*, 186(2), 385–394. <https://doi.org/10.1016/j.icarus.2006.09.004>
- Mitsuru, Y., & Tsujiura, M. (1975). Spectrum and attenuation of multiply reflected core phases. *Journal of Physics of the Earth*, 23(1), 31–42. <https://doi.org/10.4294/jpe1952.23.31>
- Mocquet, A., Vacher, P., Grasset, O., & Sotin, C. (1996). Theoretical seismic models of Mars: The importance of the iron content of the mantle. *Planetary and Space Science*, 44(11), 1251–1268. [https://doi.org/10.1016/S0032-0633\(96\)00086-4](https://doi.org/10.1016/S0032-0633(96)00086-4)
- Mohorovicic, A. (1909). Das Beben vom 8. x. *Jb. Met. Obs. Zagreb (Agram)*, 9, 1–63.
- Molnar, P., & Sykes, L. R. (1969). Tectonics of the Caribbean and Middle America regions from focal mechanisms and seismicity. *Geological Society of America Bulletin*, 80(9), 1639–1684. [https://doi.org/10.1130/0016-7606\(1969\)80\[1639:TOTCAM\]2.0.CO;2](https://doi.org/10.1130/0016-7606(1969)80[1639:TOTCAM]2.0.CO;2)

- Montési, L. G. J., & Zuber, M. T. (2003). Clues to the lithospheric structure of Mars from wrinkle ridge sets and localization instability. *Journal of Geophysical Research: Planets*, 108(E6). <https://doi.org/10.1029/2002JE001974>
- Mordret, A., Mikesell, T. D., Harig, C., Lipovsky, B. P., & Prieto, G. A. (2016). Monitoring southwest Greenland's ice sheet melt with ambient seismic noise. *Science Advances*, 2(5), e1501538. <https://doi.org/10.1126/sciadv.1501538>
- Morelli, A., & Dziewonski, A. M. (1987). Topography of the core–mantle boundary and lateral homogeneity of the liquid core. *Nature*, 325(6106), 678–683. <https://doi.org/10.1038/325678a0>
- Morgan, W. J. (1968). Rises, trenches, great faults, and crustal blocks. *Journal of Geophysical Research (1896-1977)*, 73(6), 1959–1982. <https://doi.org/10.1029/JB073i006p01959>
- Morgan, W. J. (1972). Deep Mantle Convection Plumes and Plate Motions1. *AAPG Bulletin*, 56(2), 203–213. <https://doi.org/10.1306/819A3E50-16C5-11D7-8645000102C1865D>
- Moulik, P., & Ekstrom, G. (2014). An anisotropic shear velocity model of Earth's mantle using normal modes, body waves, surface waves and long-period waveforms. *Geophysical Journal International*, 199, 1713–1738. <https://doi.org/10.1093/gji/ggu356>
- Murphy, J. R. (1977). Seismic source functions and magnitude determinations for underground nuclear detonations. *Bulletin of the Seismological Society of America*, 67(1), 135–158.
- Nakamura, Y. (1976). Seismic energy transmission in the lunar surface zone determined from signals generated by movement of lunar rovers. *Bulletin of the Seismological Society of America*, 66(2), 593–606.
- Nakamura, Y. (1977a). HFT events: Shallow moonquakes? *Physics of the Earth and Planetary Interiors*, 14(3), 217–223. [https://doi.org/10.1016/0031-9201\(77\)90174-1](https://doi.org/10.1016/0031-9201(77)90174-1)
- Nakamura, Y. (1977b). Seismic energy transmission in an intensively scattering environment. *Journal of Geophysics Zeitschrift Geophysik*, 43, 389–399.
- Nakamura, Y. (2003). New identification of deep moonquakes in the Apollo lunar seismic data. *Physics of the Earth and Planetary Interiors*, 139(3), 197–205. <https://doi.org/10.1016/j.pepi.2003.07.017>
- Nakamura, Y. (2005). Farside deep moonquakes and deep interior of the Moon. *Journal of Geophysical Research*, 110(E1), E01001. <https://doi.org/10.1029/2004JE002332>
- Nakamura, Y., & Anderson, D. L. (1979). Martian wind activity detected by a seismometer at Viking lander 2 site. *Geophysical Research Letters*, 6(6), 499–502. <https://doi.org/10.1029/GL006i006p00499>
- Nakamura, Y., Latham, G. V., & Dorman, H. J. (1982). Apollo lunar seismic experiment-final summary. In *LUNAR AND PLANETARY SCIENCE CONFERENCE XIII* (Vol. 13, pp. A117–A123).
- Nanometrics. (2015). *Trillium Compact User Guide*. Kanata, Canada. Retrieved from https://www.nanometrics.ca/sites/default/files/2019-03/trillium_compact_datasheet.pdf
- NASA. (2018). Mars InSight Launch Kit. Retrieved from https://www.jpl.nasa.gov/news/press_kits/insight/download/mars_insight_launch_presskit.pdf
- National Research Council (US). Panel on Seismic Hazard Analysis, Aki, K., National Research Council (US). Committee on Seismology, National Research Council (US). Board on Earth Sciences, & National Research Council (US). Commission on Physical Sciences

- Mathematics Resources. (1988). *Probabilistic seismic hazard analysis*. National Academies.
- Navarro-González, R., Rainey, F. A., Molina, P., Bagaley, D. R., Hollen, B. J., de la Rosa, J., et al. (2003). Mars-like soils in the Atacama Desert, Chile, and the dry limit of microbial life. *Science*, *302*(5647), 1018–1021. <https://doi.org/10.1126/science.1089143>
- Nimmo, F., & Faul, U. H. (2013). Dissipation at tidal and seismic frequencies in a melt-free, anhydrous Mars. *Journal of Geophysical Research: Planets*, *118*(12), 2558–2569. <https://doi.org/10.1002/2013JE004499>
- Nimmo, F., & Gaidos, E. (2002). Strike-slip motion and double ridge formation on Europa. *Journal of Geophysical Research*, *107*(E4), 5021. <https://doi.org/10.1029/2000JE001476>
- Nimmo, F., & Pappalardo, R. T. (2016). Ocean worlds in the outer solar system. *Journal of Geophysical Research: Planets*, *121*(8), 1378–1399. [https://doi.org/10.1002/2016JE005081@10.1002/\(ISSN\)2169-9100.JGRE25](https://doi.org/10.1002/2016JE005081@10.1002/(ISSN)2169-9100.JGRE25)
- Nimmo, F., & Schenk, P. (2006). Normal faulting on Europa: implications for ice shell properties. *Journal of Structural Geology*, *28*(12), 2194–2203. <https://doi.org/10.1016/j.jsg.2005.08.009>
- Nimmo, F., & Stevenson, D. J. (2000). Influence of early plate tectonics on the thermal evolution and magnetic field of Mars. *Journal of Geophysical Research: Planets*, *105*(E5), 11969–11979. <https://doi.org/10.1029/1999JE001216>
- Nimmo, F., Giese, B., & Pappalardo, R. T. (2003). Estimates of Europa’s ice shell thickness from elastically-supported topography. *Geophysical Research Letters*, *30*(5). <https://doi.org/10.1029/2002gl016660>
- Norris, R. D. (1994). Seismicity of Rockfalls and Avalanches at Three Cascade Range Volcanoes: Implications for Seismic Detection of Hazardous Mass Movements. *Bulletin of the Seismological Society of America* (Vol. 84).
- O’Brien, D. P., Geissler, P., & Greenberg, R. (2002). A melt-through model for chaos formation on Europa. *Icarus*, *156*(1), 152–161. <https://doi.org/10.1006/icar.2001.6777>
- Oberst, J. (1987). Unusually high stress drops associated with shallow moonquakes. *Journal of Geophysical Research*. <https://doi.org/10.1029/JB092iB02p01397>
- Oberst, J., & Nakamura, Y. (1991). A search for clustering among the meteoroid impacts detected by the Apollo lunar seismic network. *Icarus*, *91*(2), 315–325. [https://doi.org/10.1016/0019-1035\(91\)90027-Q](https://doi.org/10.1016/0019-1035(91)90027-Q)
- Oldham, R. D. (1906). The Constitution of the Interior of the Earth, as Revealed by Earthquakes. *Quarterly Journal of the Geological Society*, *62*, 456–475.
- Olinger, S. D., Lipovsky, B. P., Wiens, D. A., Aster, R. C., Bromirski, P. D., Chen, Z., et al. (2019). Tidal and Thermal Stresses Drive Seismicity Along a Major Ross Ice Shelf Rift. *Geophysical Research Letters*, *46*(12), 6644–6652. <https://doi.org/10.1029/2019GL082842>
- Oliver, J., & Murphy, L. (1971). WWNSS: Seismology’s Global Network of Observing Stations. *Science*, *174*(4006), 254–261. <https://doi.org/10.1126/science.174.4006.254>
- Ostenso, N. A., Sellmann, P. V., & Péwé, T. L. (1965). The Bottom Topography of Gulkana Glacier, Alaska Range, Alaska. *Journal of Glaciology*, *5*(41), 651–660. <https://doi.org/10.3189/S0022143000018669>
- Paden, J., Li, J., Leuschen, C., Rodriguez-Morales, F., Hale, R., Gogineni, P., et al. (2010). IceBridge MCoRDS L2 Ice Thickness, Version 1. *NASA National Snow and Ice Data Center Distributed Active Archive Center*. Boulder, CO: NASA National Snow and Ice Data

- Center Distributed Actice Archive Center. <https://doi.org/10.5067/GDQ0CUCVTE2Q> (date accessed 2016)
- Palmer, S. J., Dowdeswell, J. A., Christoffersen, P., Young, D. A., Blankenship, D. D., Greenbaum, J. S., et al. (2013). Greenland subglacial lakes detected by radar. *Geophysical Research Letters*, *40*, 6154–6159. <https://doi.org/10.1002/2013GL058383>
- Pandit, B. I., & Tozer, D. C. (1970). Anomalous Propagation of Elastic Energy within the Moon. *Nature*, *226*(5243), 335–335. <https://doi.org/10.1038/226335a0>
- Panning, M. P., & Kedar, S. (2019). Seismic response of the Mars Curiosity Rover: Implications for future planetary seismology. *Icarus*, *317*, 373–378. <https://doi.org/10.1016/j.icarus.2018.06.017>
- Panning, M. P., Lekic, V., Manga, M., Cammarano, F., & Romanowicz, B. (2006). Long-period seismology on Europa: 2. Predicted seismic response. *Journal of Geophysical Research-Planets*, *111*(E12). <https://doi.org/Artn E12008 10.1029/2006je002712>
- Panning, M. P., Beucler, E., Drilleau, M., Mocquet, A., Lognonne, P., & Banerdt, W. B. (2015). Verifying single-station seismic approaches using Earth-based data: Preparation for data return from the InSight mission to Mars. *Icarus*, *248*, 230–242. <https://doi.org/10.1016/j.icarus.2014.10.035>
- Panning, M. P., Lognonné, P., Bruce Banerdt, W., Garcia, R. F., Golombek, M., Kedar, S., et al. (2017). Planned Products of the Mars Structure Service for the InSight Mission to Mars. *Space Science Reviews*, *211*(1), 611–650. <https://doi.org/10.1007/s11214-016-0317-5>
- Panning, M. P., Stähler, S. C., Vance, S. D., Kedar, S., Tsai, V. C., Pike, W. T., et al. (2018). Expected seismicity and the seismic noise environment of Europa. *Journal of Geophysical Research: Planets*, *123*(1), 163–179. <https://doi.org/10.1002/2017JE005332>
- Panning, M. P., Pike, W. T., Lognonné, P., Banerdt, W. B., Murdoch, N., Banfield, D., et al. (2020). On-deck seismology: Lessons from InSight for future planetary seismology. *Journal of Geophysical Research: Planets*, e2019JE006353. <https://doi.org/10.1029/2019JE006353>
- Pappalardo, R. T., & Coon, M. D. (1996). A Sea Ice Analog for the Surface of Europa. In *LUNAR AND PLANETARY SCIENCE CONFERENCE XXIII*.
- Pappalardo, R. T., Vance, S. D., Bagenal, F., Bills, B. G., Blaney, D. L., Blankenship, D. D., et al. (2013). Science potential from a Europa lander. *Astrobiology*, *13*(8), 740–773. <https://doi.org/10.1089/ast.2013.1003>
- Pappalardo, R. T., Senske, D. A., Prockter, L. M., Paczkowski, B., Vance, S. D., Rhoden, A. R., et al. (2015). Science Objectives for Europa Clipper Mission Concept: Investigating Potential Habitability of Europa. *European Planetary Science Congress 2015*.
- Paranicas, C., Mauk, B. H., Khurana, K., Jun, I., Garrett, H., Krupp, N., & Roussos, E. (2007). Europa's near-surface radiation environment. *Geophysical Research Letters*, *34*(15). <https://doi.org/10.1029/2007GL030834>
- Parkinson, C. D., Liang, M.-C., Yung, Y. L., & Kirschvink, J. L. (2008). Habitability of Enceladus: Planetary Conditions for Life. *Origins of Life and Evolution of Biospheres*, *38*(4), 355–369. <https://doi.org/10.1007/s11084-008-9135-4>
- Perol, T., Gharbi, M., & Denolle, M. (2018). Convolutional neural network for earthquake detection and location. *Science Advances*, *4*(2), e1700578. <https://doi.org/10.1126/sciadv.1700578>
- Perrin, C., Rodriguez, S., Jacob, A., Lucas, A., Spiga, A., Murdoch, N., et al. (2020). Monitoring

- of Dust Devil Tracks Around the InSight Landing Site, Mars, and Comparison with in-situ Atmospheric Data. *Geophysical Research Letters*. <https://doi.org/10.1029/2020GL087234>
- Peters, L. E., Anandakrishnan, S., Holland, C. W., Horgan, H. J., Blankenship, D. D., & Voigt, D. E. (2008). Seismic detection of a subglacial lake near the South Pole, Antarctica. *Geophysical Research Letters*, *35*(23), L23501. <https://doi.org/10.1029/2008GL035704>
- Peterson, J. (1993). *Observations and modeling of seismic background noise*. Albuquerque, New Mexico: US Geological Survey Albuquerque NM. <https://doi.org/Open-File-Report-93-322>
- Phillips, C. B., & Pappalardo, R. T. (2014). Europa Clipper mission concept: exploring Jupiter's ocean moon. *Eos, Transactions American Geophysical Union*, *95*(20), 165–167. <https://doi.org/10.1002/2014EO200002>
- Le Pichon, X. (1968). Sea-floor spreading and continental drift. *Journal of Geophysical Research (1896-1977)*, *73*(12), 3661–3697. <https://doi.org/10.1029/JB073i012p03661>
- Plesa, A.-C., Knappmeyer, M., Golombek, M. P., Breuer, D., Grott, M., Kawamura, T., et al. (2018). Present-Day Mars' Seismicity Predicted From 3-D Thermal Evolution Models of Interior Dynamics. *Geophysical Research Letters*. <https://doi.org/10.1002/2017GL076124>
- Podolskiy, E. A., & Walter, F. (2016). Cryoseismology. *Reviews of Geophysics*, *54*(4), 708–758. <https://doi.org/10.1002/2016RG000526>
- Porco, C. C. (2006). Cassini Observes the Active South Pole of Enceladus. *Science*, *311*(5766), 1393–1401. <https://doi.org/10.1126/science.1123013>
- Prockter, L. M., Pappalardo, R. T., & Head, J. W. (2000). Strike-slip duplexing on Jupiter's icy moon Europa. *Journal of Geophysical Research: Planets*, *105*(E4), 9483–9488. <https://doi.org/10.1029/1999je001226>
- Quick, L. C., Barnouin, O. S., Prockter, L. M., & Patterson, G. W. (2013). Constraints on the detection of cryovolcanic plumes on Europa. *Planetary and Space Science*, *86*, 1–9. <https://doi.org/10.1016/J.PSS.2013.06.028>
- Raulin, F. (2008). Astrobiology and habitability of Titan. *Space Science Reviews*, *135*(1–4), 37–48. <https://doi.org/10.1007/s11214-006-9133-7>
- Razzaghi, A. I., Di Pietro, D. A., Quinn, D. A., Simon-Miller, A. A., & Tompkins, S. D. (2008). Mission Concepts for Studying Enceladus. *AIP Conference Proceedings*, *969*(1), 388–395. <https://doi.org/10.1063/1.2844992>
- Reynolds, R. T., Squyres, S. W., Colburn, D. S., & McKay, C. P. (1983). On the habitability of Europa. *Icarus*, *56*(2), 246–254. [https://doi.org/10.1016/0019-1035\(83\)90037-4](https://doi.org/10.1016/0019-1035(83)90037-4)
- Rhoden, A. R., Wurman, G., Huff, E. M., Manga, M., & Hurford, T. A. (2012). Shell tectonics: A mechanical model for strike-slip displacement on Europa. *Icarus*, *218*(1), 297–307. <https://doi.org/10.1016/j.icarus.2011.12.015>
- Rhoden, A. R., Hurford, T. A., Roth, L., & Retherford, K. (2015). Linking Europa's plume activity to tides, tectonics, and liquid water. *Icarus*, *253*, 169–178. <https://doi.org/10.1016/j.icarus.2015.02.023>
- Ritsema, J., Lekić, V., & Lekić, V. L. (2020). Heterogeneity of Seismic Wave Velocity in Earth's Mantle. *Annual Review of Earth and Planetary Sciences*, *48*. <https://doi.org/10.1146/annurev-earth-082119>
- Rivera, A., Corripio, J. G., Brock, B., Clavero, J., & Wendt, J. (2008). Monitoring ice-capped active Volcán Villarrica, southern Chile, using terrestrial photography combined with automatic weather stations and global positioning systems. *Journal of Glaciology*, *54*(188),

920–930. <https://doi.org/10.3189/002214308787780076>

- Rivoldini, A., Van Hoolst, T., Verhoeven, O., Mocquet, A., & Dehant, V. (2011). Geodesy constraints on the interior structure and composition of Mars. *Icarus*, *213*(2), 451–472. <https://doi.org/10.1016/j.icarus.2011.03.024>
- Roberts, J. H., & Nimmo, F. (2008). Tidal heating and the long-term stability of a subsurface ocean on Enceladus. *Icarus*, *194*(2), 675–689. <https://doi.org/10.1016/j.icarus.2007.11.010>
- Roberts, R. G., Christoffersson, A., & Cassidy, F. (1989). Real-Time Event Detection, Phase Identification and Source Location Estimation Using Single Station Three-Component Seismic Data. *Geophysical Journal International*, *97*(3), 471–480. <https://doi.org/10.1111/j.1365-246X.1989.tb00517.x>
- Romanowicz, B. A., & Dziewonski, A. M. (1986). Toward a federation of broadband seismic networks. *Eos, Transactions American Geophysical Union*, *67*(25), 541–542.
- Rost, S., Garnero, E. J., & Williams, Q. (2008). Seismic array detection of subducted oceanic crust in the lower mantle. *Journal of Geophysical Research-Solid Earth*, *113*(B6). <https://doi.org/Artn B06303> 10.1029/2007jb005263
- Rudnick, R. L., McDonough, W. F., & O’Connell, R. J. (1998). Thermal structure, thickness and composition of continental lithosphere. *Chemical Geology*, *145*(3–4), 395–411. [https://doi.org/10.1016/S0009-2541\(97\)00151-4](https://doi.org/10.1016/S0009-2541(97)00151-4)
- Ruedas, T., Tackley, P. J., & Solomon, S. C. (2013). Thermal and compositional evolution of the martian mantle: Effects of phase transitions and melting. *PHYSICS OF THE EARTH AND PLANETARY INTERIORS*, *216*, 32–58. <https://doi.org/10.1016/j.pepi.2012.12.002>
- Russell, S. A., Lay, T., & Garnero, E. J. (1999). Small-scale lateral shear velocity and anisotropy heterogeneity near the core-mantle boundary beneath the central Pacific imaged using broadband ScS waves. *Journal of Geophysical Research: Solid Earth*, *104*(B6), 13183–13199. <https://doi.org/10.1029/1999JB900114>
- Scarpetta, S., Giudicepietro, F., Ezin, E. C., Petrosino, S., Del Pezzo, E., Martini, M., & Marinaro, M. (2005). Automatic Classification of Seismic Signals at Mt. Vesuvius Volcano, Italy, Using Neural Networks. *Bulletin of the Seismological Society of America*, *95*(1), 185–196. <https://doi.org/10.1785/0120030075>
- Schimmel, M., & Gallart, J. (2004). Degree of Polarization Filter for Frequency-Dependent Signal Enhancement Through Noise Suppression. *Bulletin of the Seismological Society of America*, *94*(3), 1016–1035. <https://doi.org/10.1785/0120030178>
- Schimmel, M., & Paulssen, H. (1997). Noise reduction and detection of weak, coherent signals through phase-weighted stacks. *Geophysical Journal International*, *130*(2), 497–505. <https://doi.org/10.1111/j.1365-246X.1997.tb05664.x>
- Schlaphorst, D., Thomas, C., Holme, R., & Abreu, R. (2016). Investigation of core-mantle boundary topography and lowermost mantle with P4KP waves. *Geophysical Journal International*, *204*(2), 1060–1071. <https://doi.org/10.1093/gji/ggv496>
- Schmerr, N. C., Banks, M. E., & Daubar, I. J. (2016). The Seismic Signatures of Impact Events on Mars: Implications for the InSight Lander. *Lunar and Planetary Science Conference*. Retrieved from <http://adsabs.harvard.edu/abs/2016LPI....47.1320S>
- Schmidt, B. E., Blankenship, D. D., Patterson, G. W., & Schenk, P. M. (2011). Active formation of ‘chaos terrain’ over shallow subsurface water on Europa. *Nature*, *479*(7374), 502–505. <https://doi.org/10.1038/nature10608>

- Schubert, G., Turcotte, D. L., & Olson, P. (2001). *Mantle convection in the Earth and planets*. Cambridge University Press.
- Schubert, G., Anderson, J. D., Spohn, T., & McKinnon, W. B. (2004). Interior composition, structure and dynamics of the Galilean satellites. In F. Bagenal, T. E. Dowling, & W. B. McKinnon (Eds.), *Jupiter: The planet, satellites and magnetosphere* (1st ed., Vol. 1, pp. 281–306). Cambridge, UK: Cambridge University Press.
- Schubert, G., Masters, G., Olson, P., & Tackley, P. (2004). Superplumes or plume clusters? *Physics of the Earth and Planetary Interiors*, 146(1), 147–162. <https://doi.org/10.1016/j.pepi.2003.09.025>
- Schubert, G., Anderson, J. D., Travis, B. J., & Palguta, J. (2007). Enceladus: Present internal structure and differentiation by early and long-term radiogenic heating. *Icarus*, 188(2), 345–355. <https://doi.org/10.1016/J.ICARUS.2006.12.012>
- Schubert, G., Sohl, F., & Hussmann, H. (2009). Interior of Europa. In *Europa* (pp. 353–368). University of Arizona Press. <https://doi.org/10.2307/j.ctt1xp3wdw.20>
- Schwartz, D. P., & Coppersmith, K. J. (1986). Seismic hazards: new trends in analysis using geologic data, 22(11). Retrieved from https://inis.iaea.org/search/search.aspx?orig_q=RN:22037154
- Segall, P., & Lu, S. (2015). Injection-induced seismicity: Poroelastic and earthquake nucleation effects. *Journal of Geophysical Research: Solid Earth*, 120(7), 5082–5103. <https://doi.org/10.1002/2015JB012060>
- Shapiro, S. A., & Dinske, C. (2009). Fluid-induced seismicity: Pressure diffusion and hydraulic fracturing. *Geophysical Prospecting*, 57(2), 301–310. <https://doi.org/10.1111/j.1365-2478.2008.00770.x>
- Showman, A. P., & Han, L. J. (2005). Effects of plasticity on convection in an ice shell: Implications for Europa. *Icarus*, 177(2), 425–437. <https://doi.org/10.1016/j.icarus.2005.02.020>
- Simmons, N. A., & Grand, S. P. (2002). Partial melting in the deepest mantle. *Geophysical Research Letters*, 29(11), 1552. <https://doi.org/10.1029/2001GL013716>
- Smith, D. E., & Zuber, M. T. (1996). The shape of Mars and the topographic signature of the hemispheric dichotomy. *Science*, 271(5246), 184. <https://doi.org/10.1126/science.271.5246.184>
- Smith, J. C., & Born, G. H. (1976). Secular acceleration of Phobos and Q of Mars. *Icarus*, 27(1), 51–53. [https://doi.org/10.1016/0019-1035\(76\)90183-4](https://doi.org/10.1016/0019-1035(76)90183-4)
- Smith, P. H. (1980). The radius of Titan from Pioneer Saturn data. *Journal of Geophysical Research*, 85(A11), 5943. <https://doi.org/10.1029/JA085iA11p05943>
- Smrekar, S. E., Lognonné, P., Spohn, T., Banerdt, W. B., Breuer, D., Christensen, U., et al. (2018). Pre-mission InSights on the Interior of Mars. *Space Science Reviews*, 215(1), 3. <https://doi.org/10.1007/s11214-018-0563-9>
- Sohl, F., & Spohn, T. (1997). The interior structure of Mars: Implications from SNC meteorites. *Journal of Geophysical Research-Planets*, 102(E1), 1613–1635. <https://doi.org/10.1029/96je03419>
- Sohl, F., Spohn, T., Breuer, D., & Nagel, K. (2002). Implications from Galileo observations on the interior structure and chemistry of the Galilean satellites. *Icarus*, 157(1), 104–119. <https://doi.org/10.1006/icar.2002.6828>

- Sohl, F., Hussmann, H., Schwentker, B., Spohn, T., & Lorenz, R. D. (2003). Interior structure models and tidal Love numbers of Titan. *Journal of Geophysical Research: Planets*, 108(E12). <https://doi.org/10.1029/2003JE002044>
- Sohl, F., Schubert, G., & Spohn, T. (2005). Geophysical constraints on the composition and structure of the Martian interior. *Journal of Geophysical Research-Planets*, 110(E12). <https://doi.org/Artn E12008> 10.1029/2005je002520
- Sohl, F., Choukroun, M., Kargel, J., Kimura, J., Pappalardo, R. T., Vance, S. D., & Zolotov, M. (2010). Subsurface Water Oceans on Icy Satellites: Chemical Composition and Exchange Processes. *Space Science Reviews*, 153(1–4), 485–510. <https://doi.org/10.1007/s11214-010-9646-y>
- Sotin, C., Head, J. W., & Tobie, G. (2002). Europa: Tidal heating of upwelling thermal plumes and the origin of lenticulae and chaos melting. *Geophysical Research Letters*, 29(8), 74. <https://doi.org/10.1029/2001GL013844>
- Sotin, C., Tobie, G., Wahr, J., & McKinnon, W. B. (2009). Tides and Tidal Heating on Europa. In R. Pappalardo, W. B. McKinnon, & K. Khurana (Eds.), *Europa* (pp. 85–118). The University of Arizona Press.
- Spencer, J. R., Tamppari, L. K., Martin, T. Z., & Travis, L. D. (1999). Temperatures on Europa from Galileo Photopolarimeter-Radiometer: Nighttime Thermal Anomalies. *Science*, 284(5419), 1514 LP – 1516. <https://doi.org/10.1126/science.284.5419.1514>
- Stachnik, J. C., Sheehan, A. F., Zietlow, D. W., Yang, Z., Collins, J., & Ferris, A. (2012). Determination of New Zealand Ocean Bottom Seismometer Orientation via Rayleigh-Wave Polarization. *Seismological Research Letters*, 83(4), 704–713. <https://doi.org/10.1785/0220110128>
- Stähler, S. C., Panning, M. P., Vance, S. D., Lorenz, R. D., van Driel, M., Nissen-Meyer, T., et al. (2017). Seismic Wave Propagation in Icy Ocean Worlds. *Journal of Geophysical Research: Planets*, 123(1), 206–232. <https://doi.org/10.1002/2017JE005338>
- Stähler, S. C., Panning, M. P., Hadziioannou, C., Lorenz, R. D., Vance, S., Klingbeil, K., & Kedar, S. (2019). Seismic signal from waves on Titan's seas. *Earth and Planetary Science Letters*, 520, 250–259. <https://doi.org/10.1016/j.epsl.2019.05.043>
- Stauder, W. (1975). Subduction of the Nazca Plate under Peru as evidenced by focal mechanisms and by seismicity. *Journal of Geophysical Research*, 80(8), 1053–1064. <https://doi.org/10.1029/JB080i008p01053>
- Stone, W. C., Siegel, V., Richmond, K., Stone, C., Siegel, ; V., & Richmond, ; K. (2019). Europa Station: Developing a concept for higher fidelity analog-environment testing of candidate ocean world technologies. In *Ocean Worlds*. USRA. Retrieved from <https://www.hou.usra.edu/meetings/oceanworlds2019/pdf/6039.pdf>
- Stutzmann, E., Schimmel, M., Patau, G., & Maggi, A. (2009). Global climate imprint on seismic noise. *Geochemistry, Geophysics, Geosystems*, 10(11), n/a-n/a. <https://doi.org/10.1029/2009GC002619>
- Su, W., Woodward, R. L., & Dziewonski, A. M. (1994). Degree 12 model of shear velocity heterogeneity in the mantle. *Journal of Geophysical Research*, 99(B4), 6945. <https://doi.org/10.1029/93JB03408>
- Tanaka, S. (2010). Constraints on the core-mantle boundary topography from P_4 KP-PcP differential travel times. *Journal of Geophysical Research*, 115(B4), B04310. <https://doi.org/10.1029/2009JB006563>

- Tanimoto, T., Eitzel, M., & Yano, T. (2008). The noise cross-correlation approach for Apollo 17 LSPE data: Diurnal change in seismic parameters in shallow lunar crust. *Journal of Geophysical Research: Planets*, *113*(E8). <https://doi.org/10.1029/2007JE003016>
- Teanby, N. A. (2015). Predicted detection rates of regional-scale meteorite impacts on Mars with the InSight short-period seismometer. *Icarus*, *256*(2015), 49–62. <https://doi.org/10.1016/j.icarus.2015.04.012>
- Teanby, N. A., & Wookey, J. (2011). Seismic detection of meteorite impacts on Mars. *Physics of the Earth and Planetary Interiors*, *186*(1–2), 70–80. <https://doi.org/10.1016/j.pepi.2011.03.004>
- The National Academy of the Sciences. (2011). *Visions and Voyages for Planetary Science in the Decade 2013-2022*. (N. R. C. of the N. Academies, Ed.). Washington, D.C.: The National Academy of Sciences. <https://doi.org/10.17226/13117>
- Thiriet, M., Michaut, C., Breuer, D., & Plesa, A.-C. (2018). Hemispheric Dichotomy in Lithosphere Thickness on Mars Caused by Differences in Crustal Structure and Composition. *Journal of Geophysical Research: Planets*. <https://doi.org/10.1002/2017JE005431>
- Thomas, E., & Frechette, K. (2003). JEvalResp. Instrumental Software Technologies, Inc. Retrieved from <http://www.isti.com/JEvalResp/>
- Thomas, R. H., & MacAyeal, D. R. (1982). Derived characteristics of the ross ice shelf, Antarctica. *Journal of Glaciology*, *28*(100), 397–412. <https://doi.org/10.3189/S0022143000005025>
- Thorne, M. S., & Garnero, E. J. (2004). Inferences on ultralow-velocity zone structure from a global analysis of SPdKS waves. *Journal of Geophysical Research: Solid Earth*, *109*(B8). <https://doi.org/10.1029/2004JB003010>
- Thorne, M. S., Lay, T., Garnero, E. J., Jahnke, G., & Igel, H. (2007). Seismic imaging of the laterally varying D" region beneath the Cocos plate. *Geophysical Journal International*. <https://doi.org/10.1111/j.1365-246X.2006.03279.x>
- Toksöz, M. N., Dainty, A. M., Solomon, S. C., & Anderson, K. R. (1974). Structure of the Moon. *Reviews of Geophysics*, *12*(4), 539–567. <https://doi.org/10.1029/RG012i004p00539>
- Trnkoczy, A. (1999). Topic Understanding and parameter setting of STA/LTA trigger algorithm. *New Manual of Seismological Observatory Practice*, *2*, 1–20. https://doi.org/10.2312/GFZ.NMSOP-2_IS_8.1
- Tufts, B. R., Greenberg, R., Hoppa, G. V., & Geissler, P. (1999). Astypalaea Linea: A large-scale strike-slip fault on Europa. *Icarus*, *141*(1), 53–64. <https://doi.org/10.1006/icar.1999.6168>
- Turtle, E. P., & Pierazzo, E. (2001). Thickness of European Ice Shell from Impact Crator Simulations. *Science*, *294*, 1326. <https://doi.org/10.1126/science.1062492>
- Turtle, E. P., Barnes, J. W., Trainer, M. G., Lorenz, R. D., MacKenzie, S. M., Hibbard, K. E., et al. (2017). Dragonfly: Exploring Titan's Prebiotic Organic Chemistry and Habitability. In *Lunar and Planetary Science Conference XLVIII* (p. Abstract #1958). Houston:
- Tyler, R. H. (2008). Strong ocean tidal flow and heating on moons of the outer planets. *Nature*, *456*(7223), 770–772. <https://doi.org/10.1038/nature07571>
- U.S. Geological Survey, E. H. P. (2020). Advanced National Seismic System (ANSS) Comprehensive Catalog of Earthquake Events and Products. <https://doi.org/10.5066/F7MS3QZH>

- Vance, S. D., Panning, M. P., Stähler, S., Cammarano, F., Bills, B. G., Tobie, G., et al. (2018a). Geophysical Investigations of Habitability in Ice-Covered Ocean Worlds. *Journal of Geophysical Research: Planets*, 123(1), 180–205. <https://doi.org/10.1002/2017JE005341>
- Vance, S. D., Kedar, S., Panning, M. P., Stähler, S. C., Bills, B. G., Lorenz, R. D., et al. (2018b). Vital Signs: Seismology of Icy Ocean Worlds. *Astrobiology*. <https://doi.org/10.1089/ast.2016.1612>
- Vance, S. D., Behoukova, M., Bills, B. G., Cadek, O., Castillo-Rogez, J., Choblet, G., et al. (2019). Enceladus Distributed Geophysical Exploration. *Lunar and Planetary Science Conference L*. The Woodlands, Texas:
- Vidale, J. E. (1986). Complex Polarization Analysis of Particle Motion. *Bulletin of the Seismological Society of America*, 76(5), 1393–1405.
- Vidale, J. E., & Benz, H. M. (1992). A sharp and flat section of the core–mantle boundary. *Nature*, 359(6396), 627–629. <https://doi.org/10.1038/359627a0>
- Wahr, J., Selvans, Z. A., Mullen, M. E., Barr, A. C., Collins, G. C., Selvans, M. M., & Pappalardo, R. T. (2009). Modeling stresses on satellites due to nonsynchronous rotation and orbital eccentricity using gravitational potential theory. *Icarus*, 200(1), 188–206. <https://doi.org/10.1016/j.icarus.2008.11.002>
- Waite, J. H., Glein, C. R., Perryman, R. S., Teolis, B. D., Magee, B. A., Miller, G., et al. (2017). Cassini finds molecular hydrogen in the Enceladus plume: Evidence for hydrothermal processes. *Science*, 356(6334), 155–159. <https://doi.org/10.1126/science.aai8703>
- Watkins, J. S., & Kovach, R. L. (1972). Apollo 14 Active Seismic Experiment. *Science*, 175(4027), 1244–1245. <https://doi.org/10.1126/science.175.4027.1244>
- Watters, T. R., Weber, R. C., Collins, G. C., Howley, I. J., Schmerr, N. C., & Johnson, C. L. (2019). Shallow seismic activity and young thrust faults on the Moon. *Nature Geoscience* 2019, 1. <https://doi.org/10.1038/s41561-019-0362-2>
- Weber, R. C., Lin, P. Y., Garnero, E. J., Williams, Q., & Lognonne, P. (2011). Seismic Detection of the Lunar Core. *Science*, 331(6015), 309–312. <https://doi.org/10.1126/science.1199375>
- Weber, R. C., Garcia, R., & Lin, P.-Y. (2017). Recent Re-Analyses of the Apollo Lunar Seismic Data: InSight into the Moons Deep Interior. In *Forum on Lunar and Planetary Seismology*.
- Weber, R. C., Dimech, J.-L., Phillips, D., Molaro, J., Schmerr, N. C., & Fassett, C. (2018). Thermal Moonquakes: Implications for Surface Properties. In *Lunar and Planetary Science Conference XL*
- Weiss, B. P., & Tikoo, S. M. (2014). The lunar dynamo. *Science*, 346(6214). <https://doi.org/10.1126/science.1246753>
- West, R. A., Lane, A. L., Hart, H., Simmons, K. E., Hord, C. W., Coffeen, D. L., et al. (1983). Voyager 2 photopolarimeter observations of Titan. *Journal of Geophysical Research: Space Physics*, 88(A11), 8699–8708. <https://doi.org/10.1029/JA088iA11p08699>
- Wilhelms, D. E., & Squyres, S. W. (1984). The martian hemispheric dichotomy may be due to a giant impact. *Nature*, 309(5964), 138–140. <https://doi.org/10.1038/309138a0>
- Williams, Q., & Garnero, E. J. (1996). Seismic evidence for partial melt at the base of Earth’s mantle. *Science*, 273(5281), 1528–1530. <https://doi.org/10.1126/science.273.5281.1528>
- Williams, Q., Revenaugh, J., & Garnero, E. J. (1998). A Correlation Between Ultra-Low Basal Velocities in the Mantle and Hot Spots. *Science*, 281(5376), 546–549. <https://doi.org/10.1126/science.281.5376.546>

- Winberry, J. P., Anandkrishnan, S., & Alley, R. B. (2009). Seismic observations of transient subglacial water-flow beneath MacAyeal Ice Stream, West Antarctica. *Geophysical Research Letters*, 36(11), L11502. <https://doi.org/10.1029/2009GL037730>
- Withers, M., Aster, R., Young, C., Beiriger, J., Harris, M., Moore, S., & Trujillo, J. (1998). A Comparison of Select Trigger Algorithms for Automated Global Seismic Phase and Event Detection. *Bulletin of the Seismological Society of America*, 88(1), 95–106.
- Woodward, R. L., & Masters, G. (1991). Lower-mantle structure from ScS–S differential travel times. *Nature*, 352(6332), 231–233. <https://doi.org/10.1038/352231a0>
- Wu, M., Yen, H.-Y. H., Zhao, L., Huang, B. B.-S., Liang, W.-T. W., Wu, Y., et al. (2006). Magnitude determination using initial P waves: A single-station approach. *Geophysical Research Letters*, 33(5). <https://doi.org/10.1029/2005GL025395>
- Wyssession, M. E., Okal, E. A., & Bina, C. R. (1992). The structure of the core-mantle boundary from diffracted waves. *Journal of Geophysical Research: Solid Earth*, 97(B6), 8749–8764. <https://doi.org/10.1029/92JB00511>
- Yoder, C. F., & Standish, E. M. (1997). Martian precession and rotation from Viking lander range data. *Journal of Geophysical Research: Planets*, 102(E2), 4065–4080. <https://doi.org/10.1029/96JE03642>
- Young, A. (2007). *Lunar and planetary rovers: the wheels of Apollo and the quest for Mars*. Springer Science & Business Media.
- Young, C. J., & Lay, T. (1987). The Core-Mantle Boundary. *Annual Review of Earth and Planetary Sciences*, 15, 25–46.
- Yuan, K., & Romanowicz, B. (2017). Seismic evidence for partial melting at the root of major hot spot plumes. *Science*, 357(6349), 393–397. <https://doi.org/10.1126/science.aan0760>
- Zahnle, K., Schenk, P., Levison, H., & Dones, L. (2003). Cratering rates in the outer Solar System. *Icarus*, 163(2), 263–289. [https://doi.org/10.1016/S0019-1035\(03\)00048-4](https://doi.org/10.1016/S0019-1035(03)00048-4)
- Zheng, Y., Nimmo, F., & Lay, T. (2015). Seismological implications of a lithospheric low seismic velocity zone in Mars. *Physics of the Earth and Planetary Interiors*, 240, 132–141. <https://doi.org/10.1016/j.pepi.2014.10.004>
- Zimmer, V. L., & Sitar, N. (2015). Detection and location of rock falls using seismic and infrasound sensors. *Engineering Geology*, 193, 49–60. <https://doi.org/10.1016/j.enggeo.2015.04.007>
- Zuber, M. T. (2001). The crust and mantle of Mars. *Nature*, 412(6843), 220–227. <https://doi.org/10.1038/35084163>
- Zuber, M. T., Smith, D. E., Watkins, M. M., Asmar, S. W., Konopliv, A. S., Lemoine, F. G., et al. (2013). Gravity field of the Moon from the Gravity Recovery and Interior Laboratory (GRAIL) mission. *Science*, 339(6120), 668–671. <https://doi.org/10.1126/science.1231507>
- Zuber, M. T., Smith, D. E., Lehman, D. H., Hoffman, T. L., Asmar, S. W., & Watkins, M. M. (2013). Gravity Recovery and Interior Laboratory (GRAIL): Mapping the lunar interior from crust to core. *Space Science Reviews*, 178(1), 3–24. <https://doi.org/10.1007/s11214-012-9952-7>

